PONTIFICIA UNIVERSIDAD CATOLICA DE CHILE
ESCUELA DE INGENIERIA

ASSESSMENT AND MITIGATION OF CONCRETE THERMAL MICROCRACKING DUE TO EARLY-AGE TIME-TEMPERATURE CYCLES

FRANCO ZUNINO SOMMARIVA

Thesis submitted to the Office of Research and Graduate Studies in partial fulfillment of the requirements for the Degree of Master of Science in Engineering

Advisor:
MAURICIO LÓPEZ CASANOVA

Santiago de Chile, July 2014.

PONTIFICIA UNIVERSIDAD CATOLICA DE CHILE
ESCUELA DE INGENIERIA

ASSESSMENT AND MITIGATION OF CONCRETE THERMAL MICROCRACKING DUE TO EARLY-AGE TIME-TEMPERATURE CYCLES

FRANCO ZUNINO SOMMARIVA

Members of the Committee:

MAURICIO LÓPEZ CASANOVA

CARLOS VIDELA CIFUENTES

JAVIER CASTRO SEPÚLVEDA

LUIS EBENSPERGER MORALES

GLORIA ARANCIBIA HERNÁNDEZ

Thesis submitted to the Office of Research and Graduate Studies in partial fulfillment of the requirements for the Degree of Master of Science in Engineering

Santiago de Chile, July 2014

A mis padres, familiares y amigos por su constante apoyo, paciencia y ánimo aportado durante este proceso.

ACKNOWLEDGMENTS

I would like to begin acknowledging my parents and brother for their support, patience and comprehension during the research process that ends in this thesis. Fundamentally, I believe that my parents are responsible for my early curiosity and interest in research, and without that curiosity the experience would not been the same.

I acknowledge in the same manner to my friends and school mates during these years at the faculty, with their support and encouraging words, kept the human component that allowed this long learning and challenging process.

I cannot forget to acknowledge the supporting comments, collaboration, patience and stimulation that my partners and friends of the research group gave me during these years. Since I have been in these group for a long time, I had the opportunity to met and share with two generations of graduate students, each one with a particular and special contribution to my formation as a researcher. I acknowledge Daniel Moreno, Ariela Astorga, Fernando Bustos, Álvaro Paul y Gastón Jalil for sharing with me their meetings and results when I was starting my path in the School of Engineering, and for believing from the first minute in my work. To Claudia Stuckrath, Melissa Soto, José Carlos Remesar, Iván Navarrete, Omar Ríos and Ricardo Serpell for their important contributions to this work, encouraging words in the difficult times and fundamentally, for being the source of motivation that kept my research work ongoing for such a long time. In special, I would like to acknowledge the work and contributions of Sebastián Calderón to the results and experimental development of this research project.

I want to acknowledge the unconditional support an mainly, the confidence that professor Javier Castro put into my work, even considering that we did not have a chance of meeting before and we have no previous experience of working together. In the same way, and cannot forget the invaluable contribution, patience and friendship of the actual technical team of the research lab, Mauricio Guerra and Patricio Pinilla, and as well to its former

members, Patricio García and Fernando Palma. With no doubts, any of the results and contributions of this thesis would have been possible without their support. I also acknowledge the RESMAT lab team, specially to Karina Tobar and the team of the cement and hardened concrete lab.

Finally, I cant end without acknowledging professor Mauricio López, for his support and uninterested guide, inspiration, friendship and mainly, for believing in me, without having strong reasons to do it in the beginning. I'm convinced that the success of an academic research process is an indivisible combination of motivation and interests of a student and an advisor, the trust that professor López put in myself contributed significantly to the achievements that we made during this research project. It has been four years since we started working together; personally, I hope that we would be able to increase that number in the future.

AGRADECIMIENTOS

Quisiera comenzar agradeciendo a mis padres y hermano por su constante apoyo, paciencia y compresión durante el proceso de investigación que culmina en esta tesis. Fundamentalmente, creo que el rol de mis padres es crucial en el despertar temprano de mi curiosidad por la investigación, sin la cual la experiencia no hubiese sido la misma.

Agradezco de la misma forma a mis amigos y compañeros de aula durante largos años, que con su apoyo y palabras de aliento, mantuvieron en pie la componente humana que permitió desarrollar con éxito este proceso de formación y de investigación.

No puedo dejar de agradecer los comentarios de apoyo, colaboración, paciencia y estímulo que mis compañeros y amigos del grupo de investigación me otorgaron durante los años. Debido a mi prolongada permanencia en dicho grupo, pude compartir con dos generaciones de estudiantes de postgrado, cada una de las cuales marcó de forma particular mi formación inicial como investigador. Quiero agradecer a Daniel Moreno, Ariela Astorga, Fernando Bustos, Álvaro Paul y Gastón Jalil por abrirme las puertas en sus reuniones y equipo de investigación cuando aún iniciaba mi camino en la Escuela de Ingeniería, y por creer desde el primer día en el trabajo que realizaba. A Claudia Stuckrath, Melissa Soto, José Carlos Remesar, Iván Navarrete, Omar Ríos y Ricardo Serpell por sus importantes contribuciones al trabajo que esta tesis presenta, palabras de aliento en los momentos difíciles y fundamentalmente, por ser motores de la motivación que mantuvo en curso el trabajo constante en investigación por tanto tiempo. En especial, quiero agradecer el trabajo y contribuciones de Sebastián Calderón a los resultados y desarrollo experimental de esta investigación.

Quiero agradecer el apoyo incondicional y principalmente, la confianza que el profesor Javier Castro depositó en mi trabajo, a pesar de no conocernos y no tener experiencia de trabajo previo. En la misma línea, no puedo dejar de agradecer el aporte invaluable, paciencia y amistad de el equipo actual del Laboratorio Docente, Mauricio Guerra y

Patricio Pinilla, como también de sus integrantes que ya no están, Patricio García y Fernando Palma. Sin duda, nada de lo que esta tesis presenta hubiese sido posible sin su constante apoyo y consejo. Agradezco también al equipo del Laboratorio RESMAT, en especial a Karina Tobar y el equipo del laboratorio de cemento y de hormigón endurecido, por la buena disposición y colaboración prestada en tantas oportunidades durante estos años.

Finalmente, no puedo dejar de agradecer al profesor Mauricio López, por su apoyo y guía desinteresada, inspiración, amistad y principalmente, por haber creído en mi, sin tener quizá en ese momento argumentos tangibles para hacerlo. Convencido de que el éxito de un proceso de investigación académica es una combinación indivisible de motivación e interés de un estudiante y de un profesor, la confianza que el profesor López depositó en mi contribuyeron en gran parte a los logros que alcanzamos en investigación, como también al curso que mi formación como ingeniero tomó desde entonces. Han pasado más de 4 años desde que comenzamos a investigar juntos, personalmente, espero continuar incrementando ese número en el futuro.

TABLE OF CONTENTS

Page

LIST OF TABLES

Page

LIST OF FIGURES

Page

RESUMEN

La búsqueda constante de procesos constructivos más veloces ha impulsado el uso de hormigones de mayor resistencia temprana en las últimas décadas. Este tipo de mezclas se caracterizan en general por la magnitud y rapidez con que generan calor de hidratación. Lo anterior hace que el material sea vulnerable a agrietarse en edades tempranas por efecto de gradientes de temperatura en su interior, comprometiendo la resistencia y la durabilidad de la estructura.

En paralelo, la industria de la construcción comienza a vivir un proceso de transformación en donde la sustentabilidad está tomando un papel preponderante. Lo anterior ha motivado generar alternativas que permitan reducir la huella de carbono del hormigón, que en la actualidad es la mayor de origen antropogénico a nivel global.

Este trabajo de investigación explora los aspectos fundamentales que explican la generación de tensiones por gradientes térmicos a edades tempranas en el hormigón, mediante la utilización de un modelo micromecánico simple y de una caracterización termo-mecánica de las fases constituyentes del material. En una segunda etapa, se explora el uso de cenizas de cascarilla de arroz y puzolanas naturales como adiciones minerales con dos propósitos. El primero, reducir el calor de hidratación generado por la mezcla y así reducir la generación de tensiones por gradiente térmicos y el segundo, evaluar el impacto de las sustituciones en las propiedades mecánicas y de durabilidad.

Los resultados permiten concluir que el modelo micromecánico propuesto permite predecir satisfactoriamente el impacto en resistencia a compresión, módulo elástico y permeabilidad de un determinado esfuerzo térmico estimado por el modelo, con valores de R^2 que alcanzan 0.916, 0.845 y 0.990 respectivamente para cada una de las propiedades mencionadas y que validan al modelo como una herramienta predictiva confiable.

La ceniza de cascarilla de arroz demostró ser una alternativa técnicamente factible para reducir el calor de hidratación y la huella de carbono del hormigón, sin impactos negativos en resistencia a compresión y reduciendo la permeabilidad del material. Reemplazos de cemento por ceniza de cascarilla de arroz de un 50% mostraron valores de resistencia a compresión estadísticamente superiores a 90 días comparadas con el control de cemento Portland puro.

El modelo micromecánico para agrietamiento sienta las bases de una metodología de diseño de mezcla que incorpore elementos de evaluación de compatibilidad termo-mecánica *a priori* entre los materiales constituyentes. Así, podría diseñarse una mezcla con menores presiones de interfase esperables y por ende, con menor riesgo de agrietamiento por ciclos tiempo-temperatura a edad temprana. Por otro lado, el uso de materiales cementicios suplementarios como la ceniza de cascarilla de arroz permite el desarrollo de mezclas de hormigón con menor generación de calor de hidratación, sin sacrificio de propiedades mecánicas y con mejor desempeño de durabilidad.

Palabras Clave: termo-mecánico, hidratación, calor, temperatura, microagrietamiento, tensión, gradiente, fluorescencia, adiciones minerales, materiales cementicios suplementarios, durabilidad, permeabilidad, sustentabilidad, filler, hidratación, resistencia, degradación, compatibilidad, sustitución, micromecánico, madurez, ciclo térmico.

ABSTRACT

The pursuit of faster construction processes has promoted the use of high early-age strength concrete. These mixtures had higher heat of hydration rates at early ages, leading to higher generated temperatures and an overall increased risk of cracking due to gradients inside the structure, compromising overall strength and durability.

Simultaneously, construction industry has undergone substantial transformations where sustainability has taken a relevant role. This fact had lead in the past decades to develop new alternatives to reduce concrete's carbon footprint, the highest of anthropic origin at a global scale.

This study explores the fundamental variables controlling thermal stress generation in concrete due to early-age temperature exposure, using a simple two-phase micromechanical model and thermo-mechanical characteristics of concrete constituents. In a second research stage, the use of natural pozzolans and rice husk ash as supplementary cementitious materials was explored with two purposes. The first one is related to a reduction of heat of hydration generation while, simultaneously, assess the impact of these substitutions on mechanical properties and durability.

From the results analysis it is concluded that the proposed micromechanical model accurately predicts the impact on compressive strength, elastic modulus and permeability of a certain computed thermal stress level, with R^2 values that reach 0.916, 0.845 y 0.990 respectively for each property and that validates the model as an accurate predictive tool.

Rice husk ash showed to be a technically feasible alternative to reduce heat of hydration rates and carbon footprint of concrete, without negative impacts on compressive strength and, at the same time, improving material's durability. Mixtures with up to 50%

replacement level of cement by rice husk ash showed higher strength at 90 days compared to reference pure Portland cement mixtures.

The can be considered as a useful tool to develop a future mixture proportion design procedure that includes thermo-mechanical compatibility analysis of concrete constituents, in order to minimize thermal cracking risk. In addition, the use of high performance supplementary cementitious materials such as riche husk ash allows designing concrete mixtures with lower heat of hydration generation, without sacrifice of strength and improving durability.

Keywords: thermo-mechanical, hydration, heat, temperature, microcracking, stress, gradient, fluorescence, mineral admixtures, supplementary cementitious materials, durability, permeability, sustainability, filler, hydration, strength, degradation, compatibility, substitution, micromechanical, maturity, time-temperature cycles.

1 INTRODUCTION

The main driving force during the last decades of concrete construction industry has been to achieve faster construction. This fact has pushed the use of concrete mixtures designed to provide early-age strength qualities, allowing faster formwork stripping, strand release and loading of structures (Mehta & Monteiro, 2005). High early-age strength concrete mixtures usually incorporates high amounts of ordinary Portland cement (OPC), lower water-to-cement (w/c) ratios, cements with higher calcium aluminate (C_3A) content, finer cements, use of water reducing admixtures among others (Mehta, 1997), and are usually referred as high performance concretes (HPCs). Unfortunately, these mixtures are usually more prone to cracking, because they contain a higher cement paste fraction, develop more heat of hydration and exhibit a more pronounced self-dissecation, chemical shrinkage (Jensen & Hansen, 2001) and autogenous shrinkage (D.P. Bentz & Jensen, 2004; Holt, 2005; Jensen & Hansen, 2001).

Concrete industry is facing new challenges regarding environmental concerns, energy consumption and sustainability. US Environmental Protection Agency rates cement production as the most carbon intensive industry (E.P.A., 2007). This socio-economical turn has promoted the use of mineral alternatives to reduce cement content an thus, improve the environmental footprint of concrete (Schneider, Romer, Tschudin, & Bolio, 2011). Supplementary cementitious materials (SCMs) had been used extensively for this reason (Chungsangunsit, Gheewala, & Patumsawad, 2005; Lothenbach, Scrivener, & Hooton, 2011).

In addition to environmental and durability benefits of the use of SCMs partial substitution of OPC for one or more SCMs reduce the thermal load of the concrete element because less cement is available to react and release heat of hydration per unit volume. Therefore, SCMs can be also considered as an alternative to control hydration heat release and thus, design mixtures less prone to thermal cracking.

1.1 Portland cement production and chemistry

The American Society for Testing and Materials (ASTM) standard C-150 defines Portland cement as a hydraulic cement produced by pulverizing clinkers consisting essentially of hydraulic calcium silicates, and a small amount of one or more forms of calcium sulfate (gypsum) as an interground addition (ASTM C150, 2009). Cements fulfilling this definition with no special modifications are referred as OPC.

Since calcium silicates are the primary constituent, the raw materials for cement production must provide suitable forms of this components (Mehta & Monteiro, 2005; Neville, 1995). Natural carbonates such as limestone, chalk and marl are common industrial sources of calcium. Clay minerals contain alumina (Al_2O_3), iron oxide (Fe_2O_3) and alkalis (mainly Na and K). Components are grinded together and homogenized before entering a rotary kiln, which heats the mineral mixture to temperatures of the order of 1400ºC. The heating process consumes high amounts of energy, between 800-1400 kcal/kg of heated material (Mehta & Monteiro, 2005). At these high temperatures, carbonates decompose releasing CO_2 and combines with the other mineral raw materials, forming hydraulic phases (Neville, 1995). The clinkering operation ends with a reactive material know as clinker, which combined and grinded with about 5% by weight of gypsum is then called Portland cement. Considering the complete Portland cement manufacturing process, for the production of one ton of OPC, nearly one ton of CO_2 is released to the environment (E.P.A., 2007; Schneider et al., 2011). The manufacturing process is summarized schematically in Figure 1-1.

In cement chemistry, usually abbreviations regarding main compounds formed during clinkering are used. Also, chemical analyses of OPC are expressed as oxide contents (Taylor, 1997). This nomenclature will be used further in this document, and is summarized in Table 1-1 along with names of the mineral phases of cement (Mehta & Monteiro, 2005).

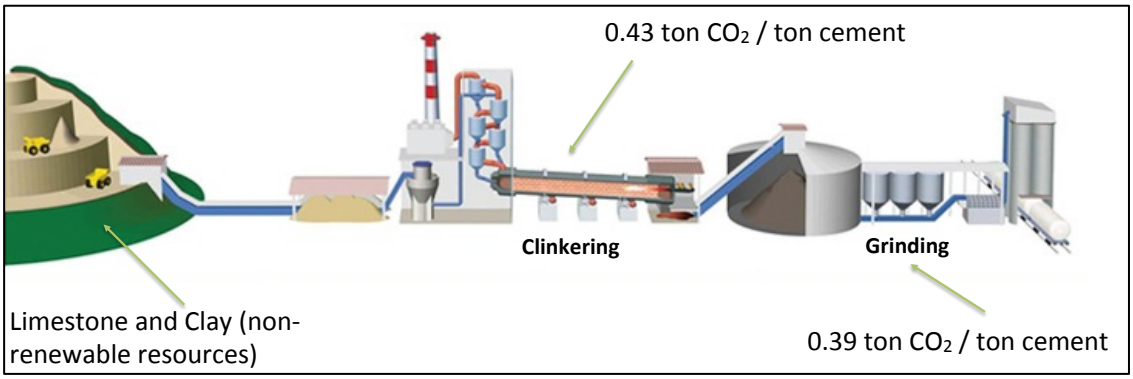

Figure 1-1: Portland cement production process and CO_2 generation (Source of data: E.P.A., 2007).

Table 1-1: Cement composition abbreviations and main phases present in OPC (Source of data: Mehta & Monteiro, 2005).

Oxide	Abbreviation	OPC Phase	Name	Abbreviation
CaO	C	$3CaO \cdot SiO_2$	Alite	C_3S
SiO_2	S	$2CaO \cdot SiO_2$	Belite	C_2S
Al_2O_3	A	$3CaO \cdot Al_2O_3$	Aluminate	C_3A
Fe_2O_3	F	$4CaO \cdot Al_2O_3 \cdot Fe_2O_3$	Ferrite	C_4AF
MgO	M	$CaSO_4 \cdot 2H_2O$	Gypsum	$C\bar{S}H_2$
SO_3	$\bar{S}$			
H_2O	H			

The most abundant phase in OPC is C_3S (55-70% by wt.), followed by C_2S (10-25% by wt.) and finally, C_3A and C_4AF with abundances commonly below 10%. As stated previously, gypsum is added at final stages of cement manufacturing, and is intended to control C_3A reaction and prevent flash setting (Taylor, 1997). The actual compositions of the main phases in OPC are not exactly as expressed in Table 1-1. This is due to impurities of the raw materials such as magnesium, alkalis and sulfur, which enter in

solid solution with the previously stated phases. The source of magnesium in Portland cement is usually dolomite, which is present as an impurity of most limestones. Part of the total magnesium can enter in solid solution with the main phases in OPC, the rest occurring as crystalline MgO, known as Periclase (Mehta & Monteiro, 2005).

1.2 Hydration of Portland cement

OPC is stated as hydraulic cement because in combination with water a chemical reaction takes place, forming hydration products that possess setting and hardening characteristics. This behavior allows binding rocks and sand into one consolidated material known as concrete (Mehta & Monteiro, 2005; Neville, 1995). The chemical reaction of OPC with water is known as cement hydration. The reaction is exothermic, and the released heat is usually referred as heat of hydration. Since OPC is a combination of different phases, hydration is not a single chemical reaction but a series of simultaneous different reactions of OPC components and water.

Cement hydration chemical reactions take place at different rates. Thus, OPC phases contribute differently to heat release and strength development over time. Typical heat of hydration values of the main OPC phases, along with contribution to strength in time are given in Table 1-2, based on data presented by Neville (1995).

Table 1-2: Heat of hydration of OPC phases, strength development rate and general contribution (Neville, 1995).

OPC Phase	Heat of Hydration [J/g]	Rate of reaction	Common Abundance [% by wt.]	Relative contribution to strength
C_3S	502	First 7 days	50-55	High
C_2S	260	1-4 months	15-20	Medium
C_3A	867	Instantaneous	5-12	Low
C_4AF	419	Months	6-10	Very Low

Hydration products of C_3S and C_2S phases are calcium silicate hydrates (CSH) and calcium hydroxide (CaOH, CH in cement chemistry notation). CH is responsible for the alkaline pH of concrete, which enables reinforcing steel passivation (Mehta & Monteiro, 2005). The microstructure of CSH is, in general, poorly crystalline and forms a porous solid, which exhibit characteristics of a rigid gel (Taylor, 1997). Stoichiometric full hydration reactions of C_3S and C_2S are shown in equations (1.1) and (1.2) (Mehta & Monteiro, 2005). Variations to this stoichiometric balance can occur due to variations in water availability during the hydration process.

$$2C_3S + 6H \longrightarrow C_3S_2H_3 + 3CH \quad (1.1)$$

$$2C_2S + 4H \longrightarrow C_3S_2H_3 + CH \quad (1.2)$$

Hydration reactions require a certain amount of energy to take place, known as activation energy (E_a). The relevance of heat of hydration in cement hydration can adopt different characters: while in mass concrete is a problem due to the difficulties to dissipate heat and temperature gradients that can lead to cracking, in cold weather concrete can provide the required activation energy for reactions to occur (ACI 207-2R, 2007). Therefore, the rate of heat evolution of the reaction is an indication of the reactivity and reaction progress of cement phases.

A general heat flow versus time plot, obtained using and isothermal calorimeter, of an OPC sample is shown in Figure 1-2. As seen in the figure, different sections of the heat flow evolution curve (in black) represent different stages an reactions occurring (Mehta & Monteiro, 2005). Stage 1 represents the descending portion of a rapid heat evolution in the first minutes after mixing OPC with water, corresponding to heat of solution of aluminates and sulfates. The valley denoted in the figure by stage 2 is known as induction period, where almost none reaction occurs. This is due to the formation of hydration products surrounding cement particles that prevents further dissolution. Stage 3 follows with a rapid increase in heat generation, attributable to C_3S hydration and subsequent nucleation and growth of hydration products (Scrivener & Nonat, 2011). At

the end of stage 3 almost 30% of the cement has reacted, and cement paste has undergone both initial and final set. This is also evidenced on the significant slope increase of the total heat curve shown on Figure1-2. Stage 4, known as diffusion limited hydration period, depends on the availability of water next to cement. Since porosity of hydrated cement matrix decreases significantly during stage 3, in some cases not all the OPC will be able to react (Neville, 1995). In this final stage, C_2S and C_4AF reactions takes place, and total heat release is decreased, as evidenced by the reduction in slope of the blue line in Figure 1-2.

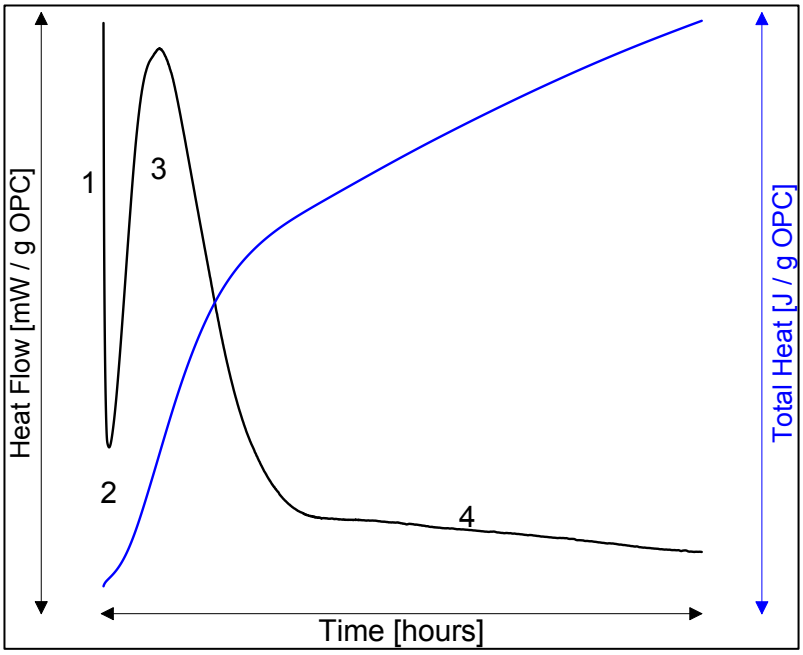

Figure 1-2: Heat flow rate (black) and total heat (blue) over time of a typical OPC sample.

1.3 Supplementary cementitious materials

Cost saving was probably the original reason to explore mineral additions and the first blended Portland cements were developed (Mehta & Monteiro, 2005). Today, these addition, commonly referred as supplementary cementitious materials (SCMs), are widely used either in blended cements or added separately in the concrete mixer

(Siddique, 2008). The use of these materials, were no additional clinkering process is involved, leads to a significant reduction of CO_2 emissions per ton of cementitious material (Mehta, 1977), and also means to use significant amounts of by-products of industrial products of the industry (Lothenbach et al., 2011).

Among the most used SCMs are:

- Fly ash, a by-product from the coal-fired power plants.
- Natural pozzolans, which are usually volcanic ashes.
- Granulated ground blast furnace slag (GGBS), a by-product of steel production process.
- Rice husk ash, a by-product of the agricultural and production of rice.
- Metakaolin, a mineral form found in clays.

1.3.1 Pozzolanic materials

Even the fact that by definition an SCM can be considered as any mineral addition in a cementitious matrix, a particular group, pozzolans, requires further understanding. A pozzolanic material is defined as a siliceous or siliceous and aluminous material (Mehta & Monteiro, 2005; Taylor, 1997), which by itself posses little or none cementing properties but will, in the presence of moisture, react with CH at ambient temperature to form hydration products such as CSH. Pozzolans were employed by Romans in combination with lime to build structures such as the Pantheon or the Port du Gard that last to nowadays, and are named after *Puzzuoli*, an Italian town from where the material was extracted.

The reaction of a pozzolan with CH is known as the pozzolanic reactions, an takes place simultaneously to cement hydration in a cementitious material (Kaid, Cyr, Julien, & Khelafi, 2009; Lothenbach et al., 2011; Yu, Sawayama, Sugita, Shoya, & Isojima, 1999).

With respect to the main hydration reaction (Eqs. (1.1) and (1.2)), the cement hydration and pozzolanic reaction can be simplified as shown in Eq. (1.3) and (1.4) respectively (Mehta & Monteiro, 2005).

Cement hydration: $$C_3S + H \xrightarrow{\text{fast}} CSH + CH \quad (1.3)$$

Pozzolanic reaction: $$Pozzolan + CH + H \xrightarrow{\text{slow}} CSH \quad (1.4)$$

Three major advantages can be concluded from the use of pozzolans. First, the reaction is slow, thus, heat generation from the pozzolanic reaction is extremely slow compared to OPC hydration, being an alternative to reduce maximum temperatures in concrete elements an reduce thermal cracking risk (Pane & Hansen, 2005). Second, the reaction needs lime; thus, makes concrete less alkaline (Mehta & Monteiro, 2005). Finally, researchers have concluded that concrete incorporating pozzolans exhibit better durability performance, since pore size and connectivity is reduced and thus, permeability of concrete is lower than concrete made only with OPC (A L G Gastaldini, Isaia, Gomes, & Sperb, 2007; Jain, 2012; Kaid et al., 2009; Mostafa, Mohsen, El-Hemaly, El-Korashy, & Brown, 2010; Nair, Fraaij, Klaassen, & Kentgens, 2008; Saraswathy & Song, 2007; Sensale, 2010).

Regarding the first advantage of pozzolans, Figure 1-3 shows heat flow evolution and total heat of pastes incorporating 20% of rice husk ash (RHA) and natural pozzolans (NP). These plots were obtained during this investigation using and isothermal calorimeter at 23ºC, and show the decrease in maximum heat release when pozzolanic SCMs are incorporated. Therefore, the maximum expectable temperature in a concrete structure using SCMs is lower compared to that containing 100% OPC concrete. This makes pozzolans a reliable method to manage peak temperature in a concrete element.

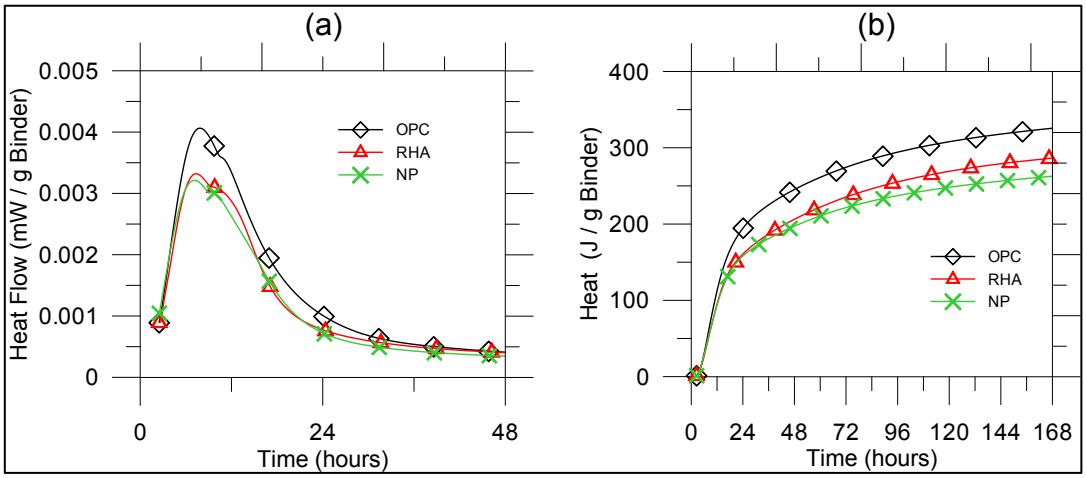

Figure 1-3: a) Heat flow of 100% OPC and 20% RHA and NP substitutions. b) Total heat plot of 100% OPC and 20% RHA and NP substitutions.

1.3.2 Supplementary cementitious materials interaction

The effects of supplementary cementitious materials can be analyzed as two non-divisible contributions, occurring simultaneously, in a cementitious system:

1. **Chemical contribution**, referred as pozzolanic effect, which relates to the formation of hydration products during the pozzolanic reaction (Lothenbach et al., 2011; Mehta & Monteiro, 2005). Rate of reaction depends on particle size (finer materials have more specific surface to react) and amorphous silica content, moisture and CH availability.
2. **Physical contribution**, referred as filler effect, related to changes in particle spacing and surface availability for hydration products nucleation (Lawrence, Cyr, & Ringot, 2003; Lothenbach et al., 2011).

As stated in the literature (Lawrence et al., 2003; Lothenbach et al., 2011), filler effect can be decomposed as a dual opposing physical interaction of the inert material with the cementitious matrix (Cyr, Lawrence, & Ringot, 2005). First, the dilution effect, which is equivalent to an increase in the water-to-cement ratio (at constant water to solids ratio),

generates more space between solid particles for hydration product formation. The second effect, related to the additional surface added by fine material particles, which acts as nucleation sites for hydration products (Lothenbach et al., 2011), referred as heterogeneous nucleation effect.

Chilean cements have incorporated SCMs since 1960's decade. In fact, the Chilean standard for cement classification (NCh148.Of68) criteria is based on cement composition and strength. This fact is attributed mainly to economic and technical issues, related to the lack of high quality limestone available for cement manufacture. This classification and chemical requirements for each type of cement is presented in Table 1-3 (I.N.N., 1968).

Table 1-3: Cement classification according to NCh148.Of68 based on SCMs content.

	CHILEAN CEMENT CLASSIFICATION				
	100% OPC	OPC + Pozzolan		OPC + GGBS	
Chem. requirements [Máx. %]	Portland	Portland Pozzolanic	Pozzolanic	Portland + Slag	Slag Cement
Mineral Addition	-----	30	50	30	75
Loss on Ignition	3.0	4.0	5	5.0	5.0
Insoluble Residue	1.5	30	50	3.0	4.0
SO_3	4.0	4.0	4.0	4.0	4.0
MgO	5.0	-----	-----	-----	-----

1.4 Thermal stresses, deformations and cracking

It is widely accepted that the major causes of concrete cracking are related to externally restrained thermal and shrinkage deformations, humidity gradients, structural overloads and chemical attacks (Mehta & Monteiro, 2005). Crack widths ranging from 0.1-1 mm

can be expected due to the exposed causes (ACI 224.1R, 2007). In addition, Bentz (2008) identified that autogenous shrinkage and thermal strains due to temperature gradients were the main causes of early-age cracking (D.P. Bentz, 2008).

1.4.1 Thermal cracking generation

In general terms, thermal cracking occurs when concrete strains due to temperature gradients exceed concrete's tensile strength. Figure 1-4 shows a typical temperature-strain development relation at early ages (ACI 231R, 2010), based on a slender concrete element externally restrained. After final set temperature (time A), concrete temperature rises beyond ambient temperature to its maximum (time B). If the expansion of the element is restrained, compressive stresses are generated. At this stage, concrete is still developing strength, thus, important stress relaxation occurs, setting zero-stress temperature beyond ambient temperature (time C). If concrete continues cooling down, tensile stresses will be generated. If those stresses exceeds concrete developing tensile strength, thermal cracking will occur (line D) (ACI 231R, 2010).

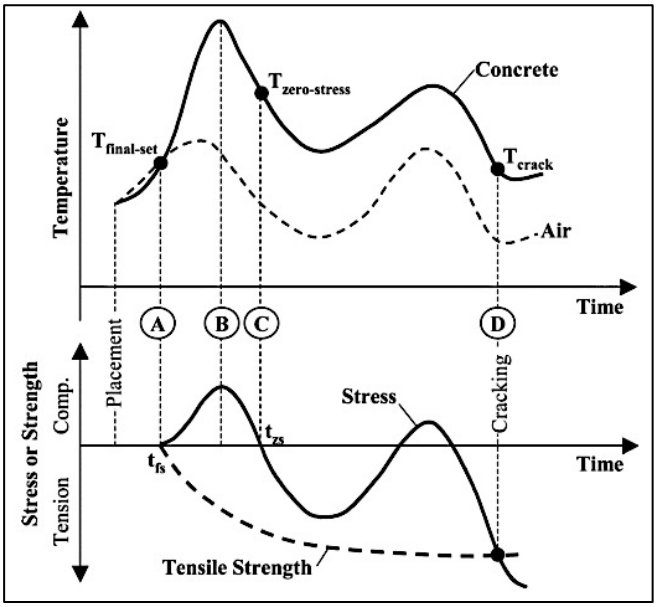

Figure 1-4: Concrete strength and thermal stress development diagram at early ages (ACI 231R, 2010).

As presented in section 1.2, cement hydration is an exothermic reaction, which is also promoted by an increase in temperature. Therefore, an increase in temperature will accelerate cement hydration, more heat of hydration will be generated and the reaction will keep increasing its rate in a self-powered manner (Schindler, 2004; Tank & Carino, 1991). While thermal cracking problems were attributed only to mass concrete structures in the past, actual concrete dosages intended for HPC generates high amounts of heat at early ages and, consequently, are prone to cracking for this reason (ACI 231R, 2010; Mehta & Monteiro, 2005). This explains the generalization of the definition of mass concrete given by ACI Committee 207: *any volume of concrete with dimensions large enough to require that measures be taken to cope with generation of heat from the hydration of the cement and attendant volume change, to minimize cracking"* (ACI 207-2R, 2007). The definition given by ACI considers the fact that smaller concrete elements made with high early-age concrete should be considered as possible candidates to apply control and mitigation strategies for thermal cracking.

1.4.2 Temperature gradients

In order to generate thermal strains and stresses that can lead to thermal cracking, temperature gradients inside concrete elements must occur. These gradients induce expansions with magnitude controlled by the coefficient of thermal expansion (CTE) of concrete constituents (Mukhopadhyay & Zollinger, 2009).

ACI committee 207 defines two kinds of thermal gradients (ACI 207-2R, 2007):

- **Surface gradient,** which is the difference in temperature between two locations at the concrete element at a fixed time.
- **Mass gradient***,* which is the difference in temperature between two periods of time, usually between the internal peak temperature and approximately the annual average ambient temperature.

Surface gradient usually generates cracking due to differential expansion between the center and the edges of the structure, due to differences in temperature between them at a certain instant (ACI 207-2R, 2007). These stresses can occur at early-ages, due to heat of hydration release, or later-ages, due to ambient temperature variations (ACI 224.1R, 2007). ACI 207 Committee defines mass gradient considering a slender element externally restrained to deformations at early ages. However, this definition can be extended to internal restraint between concrete phases due to temperature variations over time, and will be denoted as internal mass gradient. Cracking due to internal mass gradient has its origin on thermo-mechanical mismatches between concrete components: petrous aggregates and cementitious matrix (Alexander, 1996; Bremner & Holm, 1986; Selsing, 1961; Zhou et al., 2013), which lead to generation of thermal stresses. These stresses occur at early age in the interfacial transition zone (ITZ) between aggregates and cementitious matrix, which has lower strength and higher porosity compared to the bulk matrix (K. M. Lee & Park, 2008; Nilsen & Monteiro, 1993; Scrivener, Crumbie, & Laugesen, 2004). Thermal stresses at early-age occur simultaneously to other phenomena such as autogenous shrinkage (D.P. Bentz, 2008). Surface and mass gradients definitions and effects are summarized in Figure 1-5 based on the source of restraint that generates thermal cracking.

<table>
<tr><td rowspan="1">External Restraint</td><td>Mass Gradient</td><td>Difference in temperature of concrete between two periods of time
(External restraint to thermal deformation)</td><td>SERVICE LIFE</td></tr>
<tr><td rowspan="2">Internal Restraint</td><td rowspan="2">Surface Gradient</td><td rowspan="2">Difference in temperature between two points of the concrete element at a time instant t
(Geometrical effect)</td><td>SERVICE LIFE</td></tr>
<tr><td>EARLY AGE</td></tr>
<tr><td>Internal Mass Gradient</td><td>Difference in temperature of concrete between two periods of time
(Thermo-mechanical effect)</td><td>EARLY AGE</td></tr>
</table>

Figure 1-5: Temperature gradients definition and effects on thermal cracking as stated by ACI 207 Committee (2007) and proposed internal mass gradient.

Several studies and efforts have been made to control and mitigate surface gradient effects (Y. Lee, Choi, Yi, & Kim, 2009; Noumowe, Siddique, & Debicki, 2009; Qian & Gao, 2012), less information is available regarding mass gradient effects at early ages and on the effects of internal mass gradients on thermal microcracking. Moreover, lack of knowledge regarding effects of internal restraint and thermo-mechanical mismatch between concrete composites on key design parameters, such as compressive strength and elastic modulus, leads to uncertainty about the actual stresses, and load bearing capacity of concrete structures that had been subjected to high temperatures at early-age. Also, the uncertainty to establish permeability increases of damaged concrete elements expands the problem to durability considerations.

1.4.3 Concrete phases and thermal cracking

It is widely accepted that concrete is most accurately represented as a three-phase material (Nilsen & Monteiro, 1993): the petrous aggregates, cement paste and the interfacial transition zone (ITZ) between them. The ITZ is a high porosity zone (Zhu & Bartos, 1997) of size comparable to cement grains (0.1 to 100 microns), and has been described as the explanation for the quasi-ductile behavior of concrete (Scrivener et al., 2004), which differs from the linear-elastic behavior of its constituents, as seen in Figure 1-6. This behavior is believed to be due to extensive microcrack propagation through the ITZ (Mehta & Monteiro, 2005).

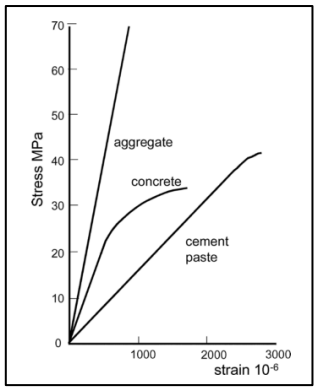

Figure 1-6: Idealized stress-strain curves of concrete constituents, showing the non-linear behavior of concrete due to the presence of the ITZ (Scrivener et al., 2004).

The origin of the ITZ is the so-called *wall effect*. Aggregate particles are several orders of magnitude larger than cement grains. This difference in size means that every aggregate particle acts as a wall to cement grains, disrupting its packing (Erdem, Dawson, & Thom, 2012; Scrivener et al., 2004). The *wall effect* can be illustrated as shown in Figure 1-7. If a large object, such as an aggregate particle, is placed in the middle of a cement grain distribution, it will cut through many grains (Figure 1-7a). As this is physically impossible for cement grains, the original packing is disrupted (Figure 1-7b). The result is a zone of small cement grains surrounding the aggregates, with higher porosity, leaving larger grains further out (Nilsen & Monteiro, 1993; Scrivener et al., 2004).

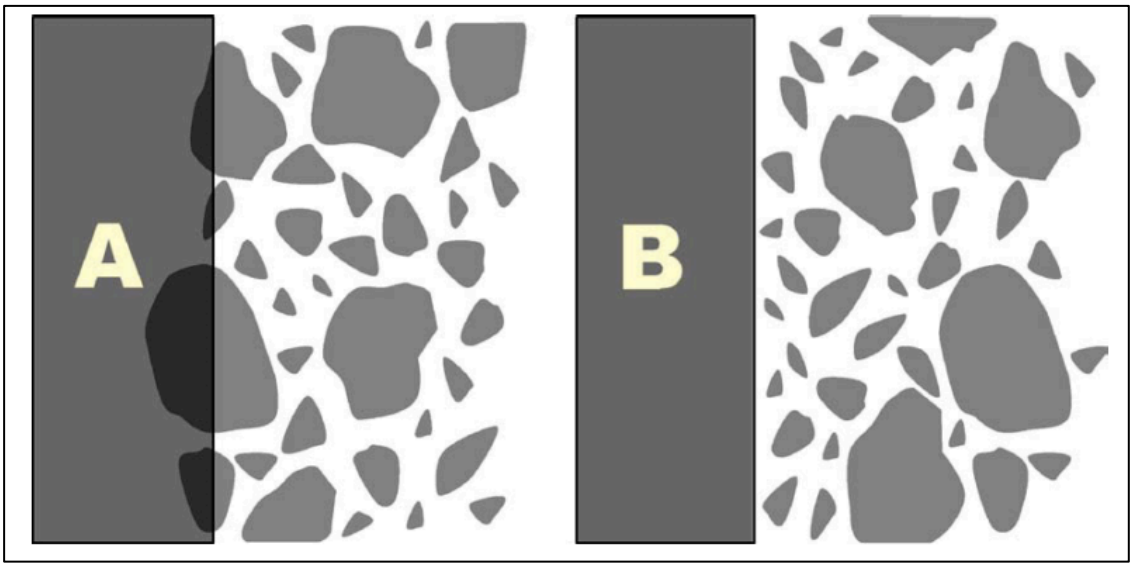

Figure 1-7: Illustration of the wall effect of aggregates which affects cement grains packing, forming the ITZ (Scrivener et al., 2004).

The formation, grow and propagation of microcracks occurring at the ITZ are the reason that this third phase has been found to be a controlling factor in concrete porosity and permeability (Samaha & Hover, 1992). In previous research, it has been concluded that if ITZ cracks forms a network, the transport properties of the material may be greatly modified (Konin, François, & Arliguie, 1998a, 1998b). They concluded that chloride

diffusivity is greatly increased by microcracking at the ITZ, which is consistent with the findings by other researchers (Gowripalan, Sirivivatnanon, & Lim, 2000). Increases up to 60% were measured in chloride ion penetration when subjected to damage at the ITZ. The impact of ITZ on concrete transport properties, which determines durability, is complex because ITZ is not a discrete zone but a region of gradually changing microstructure (Scrivener et al., 2004). Several efforts had been made to characterize and understand this particular phase (Erdem et al., 2012; Trtik & Bartos, 1999; Xiao, Li, Sun, Lange, & Shah, 2013; Zhu & Bartos, 2000).

Thermal cracking can affect significantly the ITZ, since the elastic and CTE incompatibility between the aggregate and the bulk cementitious matrix leaves the ITZ as the portion subjected to stresses generated due to these mismatches. In addition, the ITZ has been described as a higher porosity zone, thus, lower strength and more prone to cracking. A low quality ITZ can affect, as stated, transport properties an overall durability of concrete but also significant engineering properties, such as elastic modulus and strength (Erdem et al., 2012; K. M. Lee & Park, 2008). Since studies on thermal cracking had focused on the effects of surface gradient and mass gradient due to external restraint, there is lack of knowledge regarding the effects of ITZ cracking, related to internal mass gradient, on durability and engineering properties of concrete.

1.4.4 Thermo-mechanical mismatch between concrete phases

Despite of the recognized relevance of the ITZ to explain concrete behavior, the inherent difficulties in measuring mechanical and thermal properties at a micro-scale stills makes impractical to fully incorporate the ITZ in models. For this reason, a widely adopted approach has been to consider concrete as a two-phase material: coarse petrous aggregates and a bulk matrix of mortar (cement paste plus fine sand aggregate particles) surrounding them. This simplification has been successfully used to model and predict relevant properties of concrete such as elastic modulus and coefficient of thermal

expansion (Chen, Yen, & Chen, 2003; Hirsch, 1962; Nilsen, Monteiro, & Gjcrv, 1995; Zhou et al., 2013).

Based on the general formulation presented by Zhou et al. (Zhou et al., 2013), a two-phase model is presented to assess thermal stresses between concrete composites in different thermo-mechanical mismatch scenarios. As shown in Figure 1-8, the micromechanical model consists on a spherical aggregate particle of radius a surrounded by an infinite thickness spherical shell matrix. This model experiments a temperature change from T_0 to T_1, which will be denoted as ΔT.

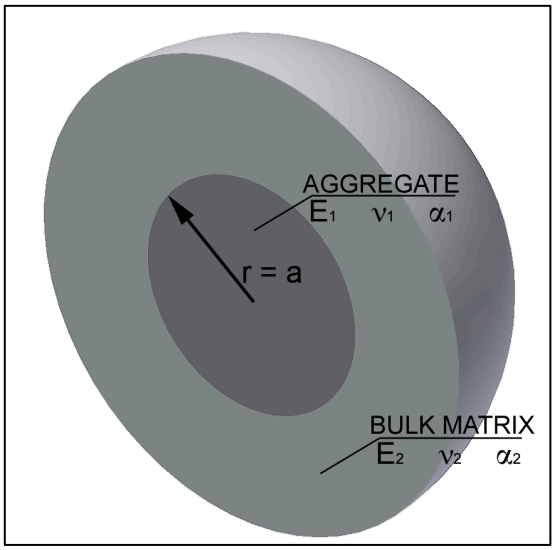

Figure 1-8: Two-phase model of concrete consisting of an aggregate particle surrounded by an infinite mortar matrix.

As shown in Section 4.3 of this thesis, this formulation makes clear the linear relationship between CTE mismatch between the aggregate and the matrix, represented by the coefficient $(\alpha_1 - \alpha_2)$, with the thermal stresses generated in the interfacial zone between phases.

The model is proposed to assess the effect of CTE and elastic mismatch between concrete phases on the computed stresses and strains generated. A novel approach of this

research is to apply the micromechanical model and the computed stresses, based on characterization of actual constituents used, as a comparative reference to observed impact on engineering and transport properties of thermally damaged concrete samples. This approach bridges the gap between microstructure damage, understood as microcracking through the ITZ, and macro-mechanical behavior on key properties.

1.5 Thermal cracking mitigation strategies

Thermal cracking mitigation has been a constant concern and motivating to develop new techniques focused on this issue (Neville, 1995). Since heat of hydration release peaks occur at early stages of cement hydration, many of these mitigation strategies focus on dissipate energy over a longer period of time. This allows concrete to gain strength to withstand these thermal stresses (ACI 231R, 2010). In addition, previous studies have been oriented on reinforcement design criteria to control early-age cracking (Hughes & Videla, 1992).

Three major factors that make concrete prone to thermal cracking can be identified based on the literature available:

1. Cementitious materials develop heat during hydration, which produces an increment in concrete temperature.
2. Changes in concrete temperature produces deformations, with magnitudes controlled by the particular CTE of the phases.
3. During hydration, concrete develops stiffness, thus, thermal deformations induce thermal stresses if any kind of restraint is imposed.

Any mitigation strategy should focus on one or more of these factors. In this section, the major available strategies to mitigate thermal cracking occurrence are summarized.

1.5.1 Heat of hydration reduction

Since temperature changes in concrete at early-ages can be manly attributed to heat of hydration release, a reduction of the total amount of heat or heat release rate can be naturally deduced as an initial approach to mitigation (D P Bentz, 1995; Mehta & Monteiro, 2005; Neville, 1995). As stated in Section 1.3.2, SCMs can be used as a reliable way to reduce heat release during early stages of concrete hardening (Pane & Hansen, 2005). These materials are usually available locally and allows a considerable reduction in OPC content per unit volume, still delivering acceptable levels of strength and stiffness (Jain, 2012; Neithalath, Persun, & Hossain, 2009; Rodríguez de Sensale, 2006).

Another approach to heat of hydration control is the reduction of the total amount of cementitious material. However, concrete design standards usually limits this reduction (ACI 318M, 2011). In addition, strength is strongly related to cementitious material content and thus, this makes the reduction unsuitable to obtain the HPC mixtures required by the industry.

Finally, a widely adopted technique used for mass concrete has been the pre-cooling of constituents prior to mixing or the use of a fraction of ice instead of water (Mehta & Monteiro, 2005; Neville, 1995). Pre-cooling strategy has dual effects. First, it reduces temperature surface gradients by cooling the hotter core of the mass element and making it closer to the ambient temperature. This effect will be discussed in more detail in the next section. The other effects relates to hydration. Since cement hydration is a reaction promoted by higher temperatures, a reduction in the initial temperature of concrete constituents slows down the reaction. Thus, heat release rate is reduced and mass gradients generated are smaller. However, strength gain of concrete is also slower. Therefore, this technique should be studied carefully both from an economical and technical feasibility perspective (Neville, 1995).

1.5.2 Temperature gradient reduction

As presented in previous sections, most o the strategies and research efforts regarding thermal cracking had focused in surface gradient mitigation (ACI 207-2R, 2007). Thermal cracking due to surface gradient takes place when internal restraint, which arises when concrete surface lose heat to the atmosphere. This generates a differential thermal expansion due to temperature differences between the hotter core and the cooler surface, inducing compressive stresses in one portion (core) and tensile in the other (surface). If the tensile stresses at the surface due to expansion of the core exceeds the tensile strength of concrete, cracking will occur (Neville, 1995).

Neville (1995) includes a reference of maximum allowable temperature gradient between the core and the surface to avoid thermal cracking. This limit is 20ºC, and was included in the European Standard ENV 206:1992 (EN206, 2002). For a temperature difference of 20ºC, taking concrete CTE as 10×10^{-6} per ºC as a typical value (Karadeniz & Kumlutas, 2007; Mukhopadhyay & Zollinger, 2009; Zhou et al., 2013), the differential strain is 200×10^{-6} . As stated in ACI design code, this is a realistic estimate of tensile strain at cracking of concrete (ACI 318M, 2011; Neville, 1995). The critical temperature difference occurs during cooling, as shown in Figure 1-9.

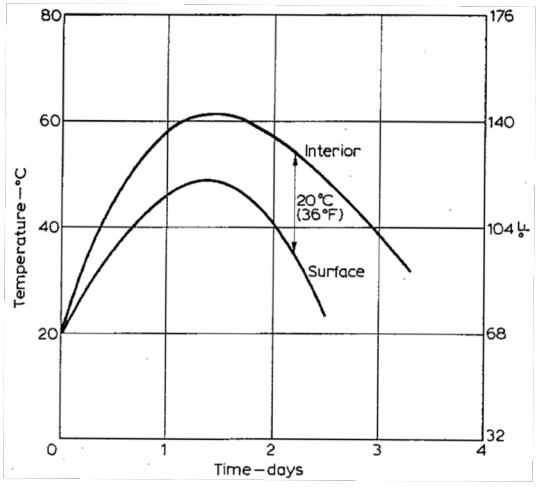

Figure 1-9: Pattern of temperature during cement hydration and critical temperature gradient during cooling. (Neville, 1995)

Since critical temperature difference occurs at the cooling stage, methods such as formwork selection between steel or wood, had been used to unsure that this gradient is kept below the critical value of 20ºC (Mehta & Monteiro, 2005). This technique actually reduces the gradient between the core and the surface by retaining heat and maintaining warm the surface, but it keeps concrete at higher temperatures for a longer period of time. This could have a negative impact from a mass gradient cracking perspective, which has not been covered by the available literature. Apart from cracking risks, concrete elements kept warm for long periods are vulnerable to delayed ettringite formation (DEF), which can significantly damage concrete microstructure (Escadeillas, Aubert, Segerer, & Prince, 2007; Pavoine, Brunetaud, & Divet, 2012; Taylor, Famy, & Scrivener, 2001; Z. Zhang, Olek, & Diamond, 2002). Ettringite is and expansive compound, which occupies 8 times the volume of the original phases that leads to its formation. Thus, in a hardened concrete structure this phenomenon can lead to significant cracking.

Another methods consist on circulating cold water using pipelines inside the concrete element. This method has proved to be effective, but is expensive and requires special and permanent modifications to the concrete structure (Neville, 1995).

1.5.3 Phase changing materials (PCMs)

Concrete is well known as a material with a high thermal mass, which refers to the ability to retain large amounts of heat inside the material without significant changes in temperature. This fact may be an advantage in moderate climates, where concrete stores heat during the day and releases it during the night, reducing the need of cooling/heating. The energy storage capacity of concrete can be further modified by the addition of phase changing materials (PCMs) (Dale P. Bentz & Turpin, 2007). Two major applications for PCMs incorporation to concrete has been described:

1. Increase of concrete thermal mass to improve insulating properties of the material (Alqallaf & Alawadhi, 2013; Dale P. Bentz & Turpin, 2007; Cabeza et al., 2007).
2. Reduction of early-age temperature rise, by storing heat of hydration on a phase change process and thus, mitigating thermal cracking risk (Fernandes et al., 2014; Qian & Gao, 2012).

Common PCMs used in concrete industry are paraffin microcapsules and butyl stereate. The first kind of PCM is incorporated directly to the mixture in the form of a mineral addition. The second type is used to impregnate lightweight aggregates, creating PCM capsules inside the pores of the aggregate (Dale P. Bentz & Turpin, 2007). Several research efforts have been made to understand and characterize thermal properties of different materials suitable to be used as PCMs (Jeong, Jeon, Cha, Kim, & Kim, 2013; Pomianowski, Heiselberg, Jensen, Cheng, & Zhang, 2014).

The basic concept of PCMs operation is described in Figure 1-10. This figure summarizes the phenomena involved, and is valid for either ambient temperature variation or heat of hydration release as inputs of the system.

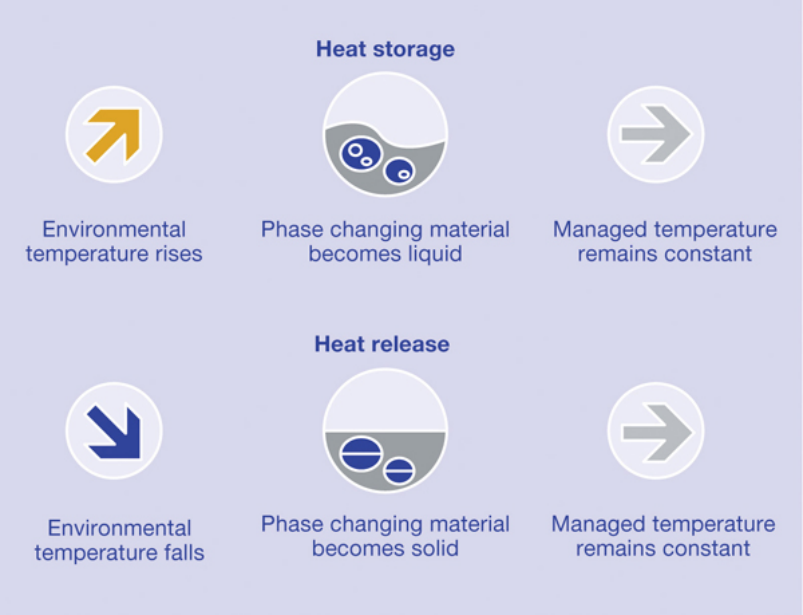

Figure 1-10: PCM physical principle that allows energy storage and temperature management. Source: sbec.eu.com.

1.5.4 Thermo-mechanical compatibilization

The variety of aggregates that are used in concrete mixtures sets inherent challenges to characterize and engineer key properties to improve performance and mechanical behavior in a cementitious matrix (Alexander, 1996). Each aggregate type has a mineralogical composition that conditions the fundamental thermo-mechanical parameters, E_1 and α_1, of that particular rock. This fact makes an individual assessment of the CTE and elastic mismatch between the aggregate and the bulk matrix phase impossible, since both variables varies necessarily together when the aggregate mineralogy changes.

A variation in the aggregate CTE, α_1, has relevance in the thermal stress problem while it generates aggregate thermal strain with a certain temperature variation, strain that can simply be denoted as $\alpha_1 \Delta T$, and increases or decreases the CTE mismatch with the

matrix. In parallel, a variation in the aggregate elastic modulus, E_1, has an exponential impact on the magnitude of the thermal stress induced by the strains generated due to a temperature change.

The magnitude of these parameters and the difference between them an the characteristic thermo-mechanical parameters of the bulk matrix (α_2, E_2), are the controlling factors of the magnitude of the stresses generated at the ITZ, according to the proposed micromechanical model. Engineering design of the CTE and elastic mismatch between the bulk paste and the aggregates sets a new alternative in the mitigation strategies for thermal cracking, associated with mass gradient effects. Since the effects of mass gradient cracking have not been explored extensively, the relevance of this alternative is subjected to the magnitude of damage expected on different mixture design scenarios. This fact sets a new opportunity to explore a new mitigation strategy based on mixture design, rather than heat release or temperature gradient control.

Interaction between thermo-mechanical parameters and computed stress development and the impact of these stresses on engineering and durability properties of concrete will be explored on this thesis.

2 OBJECTIVES, METHODOLOGY AND OUTLINE

2.1 Objectives and hypotheses

This thesis focuses on understanding the effects of elastic modulus and CTE mismatch of concrete phases on thermal cracking, and on the assessment of the benefits of using SCMs on the heat of hydrations and concrete properties. Based on literature review and preliminary research, three main hypotheses are formulated:

1. The incompatibility of thermal strains between concrete phases generates internal thermal microcracking, which can increase permeability at extents comparable with water-to-cementitious materials ratio variations and ongoing hydration.
2. A two-phase micromechanical model based on thermo-mechanical properties of concrete phases is able to model and predict impacts of thermal strains in relevant engineering parameters of concrete, such as compressive strength, elastic modulus and permeability.
3. Rice husk ash used as supplementary cementitious material in cementitious composites effectively reduces heat of hydration release, while improving durability and sustainable footprint of the material.

The main goal of this thesis is to assess and quantify the driving variables controlling thermal cracking expression due to internal mass gradients, and how this phenomena impacts on concrete design parameters and durability.

Based on this main research scope, four specific goals were in alignment with a validation process of the formulated hypotheses.

a) To understand the relation between elastic modulus and coefficient of thermal expansion of cementitious matrix and petrous aggregates on the expression of thermal microcracking.

b) To quantify the effects of different levels of imposed temperature gradients on compressive strength, elastic modulus and permeability.
c) To establish relations between fundamental mechanical indicators, derived from a two-phase micromechanical model of concrete, and thermal cracking damage measures as changes in particular properties of concrete.
d) To evaluate the feasibility of using rice husk ash to decrease heat release, while preserving strength compared to standard OPC mixtures and reducing embodied CO_2 emissions per unit volume of material.

2.2 Research methodology

The first stage of this study was an extensive literature review of the state-of-the-art knowledge related to thermal cracking and mitigation strategies. The scope was initially based on the proposal presented to CONICYT, which funded this project, and then on further requirements of the experimental design based on the hypotheses and questions to answer that derived from this process.

The second stage focused on understanding thermal microcracking due to internal mass gradients as a phenomena related to thermomechanical mismatch between concrete phases. For this reason, different types of natural and artificial aggregates were selected to cover a broad range of mismatch values. Externally imposed time-temperature cycles to concrete samples manufactured with these aggregates were intended to simulate heating and cooling conditions in the core of a mass concrete element. A micromechanical model was used to derive relations between thermomechanical mismatch and degradation of concrete properties due to thermal microcracking. The results of this stage are presented in Section 4 (paper 1) of this thesis.

The third stage of this study focused on thermal cracking mitigation strategies. In particular, the use of high performance SCMs was explored based on the traditional use of these materials in Chile and the opportunity to incorporate waste materials and by-

products from other industries in concrete. Rice husk ash and natural pozzolans were selected as SCMs and a multi-scale experimental program was designed to assess the chemical and physical contributions of each material to strength and durability. Extensive characterization of the composition and structures present on these materials was conducted using X-Ray diffraction (XRD), X-Ray fluorescence and particle size distribution (PSD). In addition, isothermal calorimetry was used to assess the effects of SCMs on OPC hydration. The results of this stage are presented in Section 5 (paper 2) of this thesis.

The research methodology is presented schematically on Figure 2-1.

2.3 Document Outline

The first section of this thesis corresponds to a general introductory chapter and the literature review of this study. Section 2 describes the hypothesis, goals and research methodology that was formulated based on the literature review and formulated research questions. Section 3 briefly describes the content of each one of the original research papers contained in this thesis. Section 4 and 5 are the manuscripts of the original research papers, which contents are described in Section 3. Finally, Section 6 presents general conclusions related to the hypotheses and goals formulated in Section 2. After section 6, a complete list of references is presented, including references from Section 1 and also from both research papers. In addition, Section 4 and 5 concludes with a reference list particular to each paper presented.

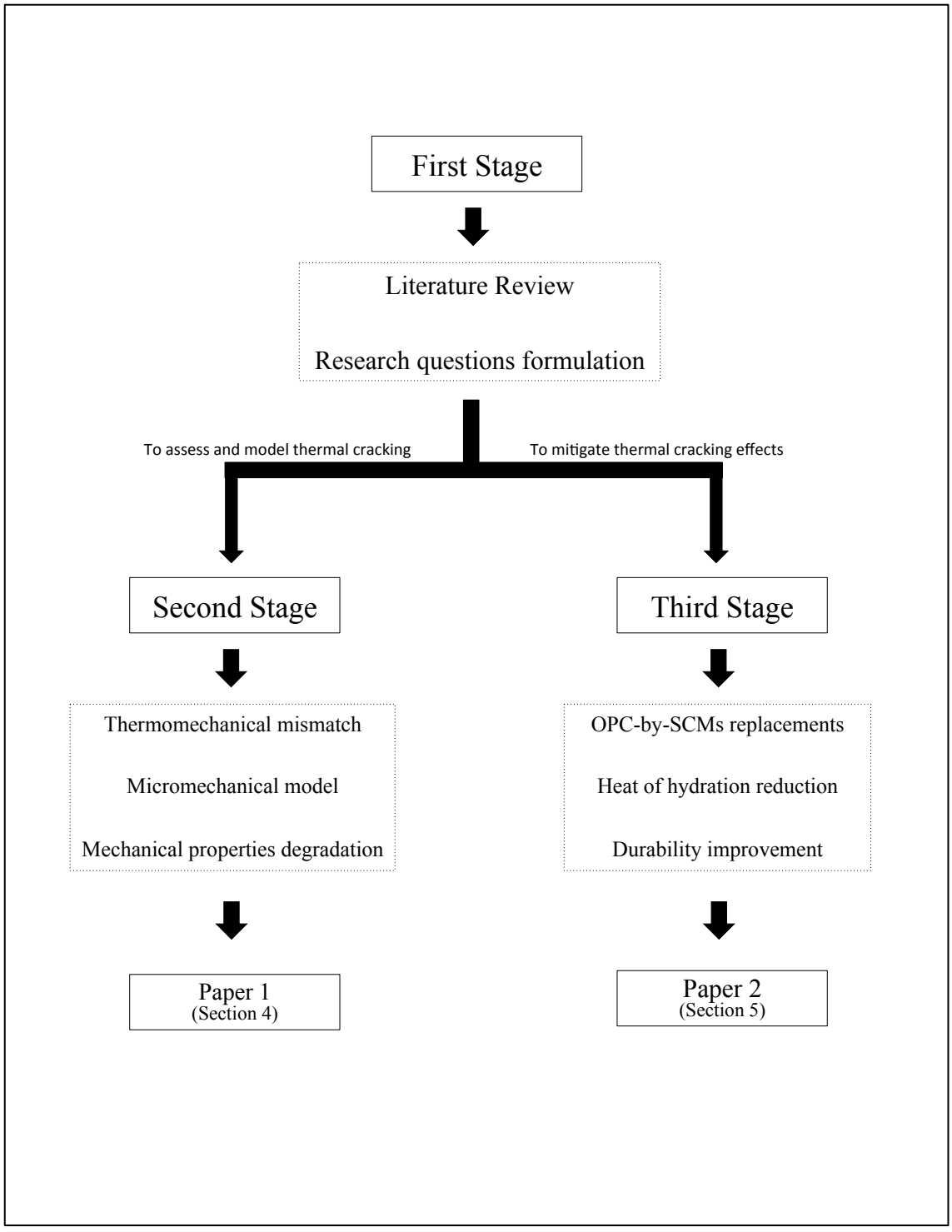

Figure 2-1: Research methodology schematic representation.

3 ORIGINAL RESEARCH PAPERS GENERAL OUTLINE

3.1 Paper 1: Thermo-mechanical assessment of concrete micro-cracking due to early-age temperature rise

This paper focuses on modeling and assessment of thermal stresses at the ITZ in concrete due to externally imposed time-temperature cycles. Four types of aggregates were used to cover a broad spectrum of elastic and CTE mismatch between concrete phases. Damage was evaluated based on compressive strength, dynamic elastic modulus and electrical resistivity measurements on damaged and undamaged samples. In addition, fluorescence microscopy was used to confirm the generation of thermal microcracks in a direct manner. Regression models from the results obtained presents strong relations between predicted stresses computed using the micro-mechanical model and observed impacts on measured properties.

This research article focuses on hypotheses 1 and 2, covering specific goals a), b) and c).

This paper was submitted to Construction and Building Materials from Elsevier on July 17th, 2014.

3.2 Paper 2: Decoupling the chemical and physical effects of supplementary cementitious materials in strength and permeability: a multi-scale approach

This paper assesses the effect on rice husk ash and natural pozzolans on strength and durability of cementitious materials. The experimental design considers a multi-scale approach, covering fundamental hydration characterization on cement paste, mortar compressive strength and concrete durability properties. In addition to the reactive

materials studied, inert fillers were made from ground quartz sand, in order to determinate physical and chemical contributions of the SCMs in the overall hydration process.

This research article focuses on hypothesis 3, and covers specific goal d).

This paper was submitted to Cement and Concrete Composites from Elsevier on June 28th, 2014.

4 THERMO-MECHANICAL ASSESSMENT OF CONCRETE MICRO-CRACKING DAMAGE DUE TO EARLY-AGE TEMPERATURE RISE

Franco Zunino, Javier Castro and Mauricio Lopez

ABSTRACT

The pursuit of high early-age strength concrete has led to mixtures with higher heat of hydration rates at early ages with produces higher temperatures and an overall increased risk of cracking. This study uses a two-phase micromechanical model to compute thermal stresses based on both coefficient of thermal expansion (CTE) and elastic modulus (E) mismatches between aggregates and the cementitious matrix. Concrete specimens were prepared using four types of aggregates (different CTE and E), and subjected to temperature cycles to generate thermal cracking. Fluorescence microscopy, compressive strength, dynamic elastic modulus, and electrical resistivity were used to characterize the effect of this induced thermal cracking. Experimental results were in agreement with the two-phase model and it was concluded that the interaction pressure (P) between phases could be used to estimate the impact on the mechanical and transportation properties of a temperature gradient at early age.

Keywords: temperature, microcracking, micromechanics, degradation, strain effect

4.1 Introduction

The main driving force in concrete construction over the last few decades has been construction speed, which has pushed the industry to develop high early-age strength concrete. These mixture designs promote the use of high cement contents, a low water-to-cement ratio (w/c), finer cements, and high-C_3A, contents, among others (Mehta & Monteiro, 2005).The resulting materials are commonly referred to as high-strength concretes (D.P. Bentz & Jensen, 2004). Unfortunately, these mixtures are more prone to cracking (Mehta, 1997) mainly because they tend to contain a higher paste fraction and exhibit more pronounced self-desiccation, chemical shrinkage (Jensen & Hansen, 2001), and autogenous shrinkage (D.P. Bentz & Jensen, 2004; Holt, 2005).

In addition, the higher cement content per unit volume and the use of finer cements increases both the initial rate and the total released heat of hydration, which can lead to an increase in temperature gradients inside the material. Differential thermal expansion of the concrete constituents may produce stresses and cracking that negatively affect the mechanical properties and durability of concrete (Gowripalan et al., 2000; Konin et al., 1998b; Samaha & Hover, 1992; Wang, Jansen, Shah, & Karr, 1997). These stresses occur in the early stages of the concrete, when it is more vulnerable to cracking (ACI 231R, 2010; Holt, 2005). Furthermore, the increased temperature that accelerates cement hydration (Schindler, 2004), produces lower quality and more porous calcium silicate hydrates (CSH) (Gallucci, Zhang, & Scrivener, 2013). Moreover, concrete temperatures greater than 70ºC can induce chemical modifications of the hardened phases and lead to expansion due to delayed ettringite formation (DEF) (Escadeillas et al., 2007; Taylor et al., 2001; Z. Zhang et al., 2002).

The ACI committee 207 defines two types of thermal gradients: a "*surface gradient*", which is the difference in temperature between two locations in the concrete element, and a "*mass gradient*", which is the difference in temperature between two periods of time, usually between the internal peak temperature and the annual average ambient

temperature (ACI 207-2R, 2007).

The surface gradient usually generates cracking due to differential expansion between the center and the edges of the structural elements due to differences in temperature at a certain instant (ACI 207-2R, 2007). These stresses can occur at early ages due to the heat of hydration release or at later-ages due to ambient temperature variations (ACI 224.1R, 2007). Cracking due to mass gradients has its origin in thermo-mechanical mismatches between concrete components, i.e., petrous aggregates and cementitious matrix (Alexander, 1996; Bremner & Holm, 1986; Selsing, 1961; Zhou et al., 2013), which lead to generation of thermal stresses. These stresses occur at early ages in the interfacial transition zone (ITZ) between the aggregates and cementitious matrix, which exhibits lower strength and higher porosity compared with those of the bulk matrix (K. M. Lee & Park, 2008; Nilsen & Monteiro, 1993; Scrivener et al., 2004). Thermal stresses at early ages occur simultaneously with other phenomena. It has been demonstrated that if proper curing is ensured, autogenous shrinkage and thermal stresses are the main driving forces in early-age cracking (D.P. Bentz, 2008).

Although several studies and efforts have been carried out in order to control and mitigate surface gradient effects (Y. Lee et al., 2009; Noumowe et al., 2009; Qian & Gao, 2012), less information is available on mass gradient effects. Moreover, a lack of knowledge of the effects of internal restraint and thermo-mechanical mismatches between concrete phases on key design parameters (i.e., compressive strength and elastic modulus), leads to uncertainty in the actual load-bearing capacity of concrete subjected to high temperatures at early age. Few studies exist in the assessment of permeability of damaged concrete (Dale P. Bentz et al., 2013; Pourasee, Peled, Weiss, & Asce, 2011; Yang, Weiss, & Olek, 2006), which further affects durability, but still not directly related to thermal cracking by mass gradient. Understanding how the aggregate and cementitious matrix properties affect the thermo-mechanical mismatches is crucial in assessment and design of concrete mixtures with reduced microcracking risk for the purpose of ensuring mechanical and durability performance.

4.2 Objective

The aim of this study is assessment of the impact of thermal stresses on mechanical and transport properties of concrete by imposing early-age "mass gradients" with external time-temperature cycles on specimens with a variety of combinations of the two fundamental thermo-mechanical parameters (CTE and elastic modulus) of the phases (aggregate and matrix). This approach allows assessment of the effect of these parameters mismatches in the thermal damage of concrete. In addition, this approach facilitates the estimate of expected stress and strain levels using the proposed micromechanical model.

4.3 Proposed Two-Phase Micromechanical Model

It is widely accepted that concrete is most accurately represented as a three-phase material (Nilsen & Monteiro, 1993), including the petrous aggregates, cement paste, and the ITZ between them. The ITZ has been described as the explanation for the quasi-ductile behavior of concrete (Scrivener et al., 2004), and several studies attempted to characterize and understand this particular phase (Erdem et al., 2012; Trtik & Bartos, 1999; Xiao et al., 2013; Zhu & Bartos, 2000). Despite the recognized relevance of the ITZ in explaining concrete behavior, the inherent difficulties in measuring the mechanical and thermal properties at a micro-scale makes it impractical to fully incorporate the ITZ in models. For this reason, a widely adopted approach considers concrete as a two-phase material: the coarse petrous aggregates and the bulk matrix of mortar surrounding them. This simplification has been successfully used to model and predict relevant properties of concrete, i.e., elastic modulus and coefficient of thermal expansion (Chen et al., 2003; Hirsch, 1962; Nilsen et al., 1995; Zhou et al., 2013).

Due to the composite nature of concrete, understanding the elastic and thermal compatibility of its components is crucial for predicting and modeling concrete behavior with reasonable accuracy (Bremner & Holm, 1986). In particular, temperature

fluctuations in concrete during cement hydration produce differential strains between the concrete phases and thus the thermally induced stresses that generate microcracking. Assuming a uniform temperature distribution in all concrete phases, the main thermo-mechanical variables that control the magnitude of these stresses are the elastic modulus (E) and the coefficient of thermal expansion (CTE, α) of the aggregates and the matrix (Selsing, 1961; Zhou et al., 2013). The occurrence of differential strains is well explained by the mismatch between the thermo-mechanical parameters of the aggregates and the matrix.

Based on the general formulation presented by Zhou et al. (2013), a two-phase model is proposed in this work to assess the thermal stresses between concrete composites in different thermo-mechanical mismatch scenarios. As shown in Figure 4-1, the micromechanical model consists of a spherical aggregate particle of radius a surrounded by an infinite thickness spherical shell matrix. This model applies a temperature change from T_0 to T_1, which will be denoted as ΔT. This parameter represents the temperature variation of a particular place at two different time periods.

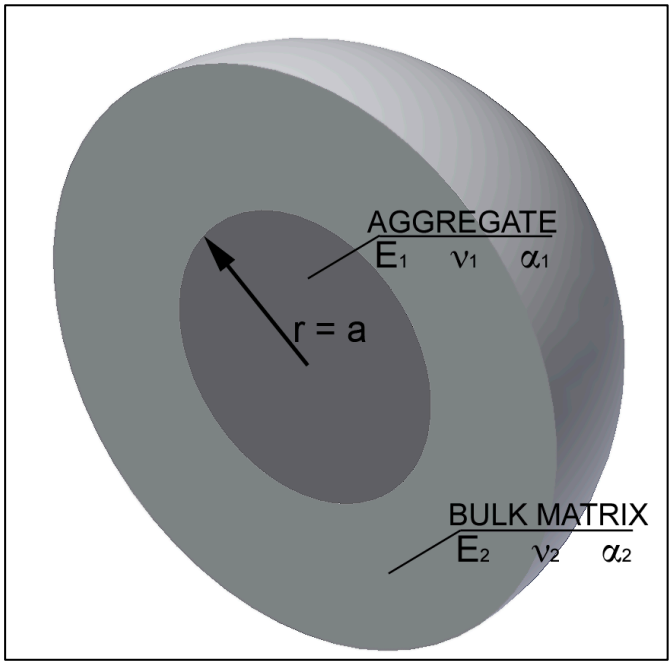

Figure 4-1: Two-phase model of concrete consisting of an aggregate particle surrounded by an infinite mortar matrix.

Properties and values related to the aggregate and matrix phase will be denoted with the subscripts 1 and 2, respectively. The radial strain (ε_r) and the tangential strain (ε_t) generated in the interface between the aggregate and the bulk matrix are given by (Burgreen, 1971):

$$\varepsilon_{ri} = \frac{1}{E_i}(\sigma_{ri} - 2\nu_i\sigma_{ti}) + \alpha_i\Delta T \tag{1}$$

$$\varepsilon_{ti} = \frac{1}{E_i}\left((1-\nu_i)\sigma_{ti} - \nu_i\sigma_{ri}\right) + \alpha_i\Delta T \tag{2}$$

where the subscript i refers to the considered phase (1 or 2), σ_r and σ_t are the radial and tangential stress, respectively, and ν_i is the Poisson ratio of phase i. It can be assumed that the differential thermal deformations of the concrete phases are represented by an equivalent thermal interaction pressure (P) present in the interface between them (Figures 4-2a and 4-2b). It should be noted that in a 2D formulation at the equator of the spherical aggregate the external shell is equivalent to a cylindrical section. As derived from a simple spherical model of internal radius a and infinite wall thickness with interaction pressure P applied on its cavity (Figure 4-2b) at a distance r from the center, the stresses are represented as described in (Selsing, 1961):

$$\sigma_{r2} = -2\sigma_{t2} = -P\frac{a^3}{r^3} \tag{3}$$

In this convention, positive values represent tensile stresses. Similarly, for a solid sphere of radius a subjected to an external pressure P (Figure 4-2a), the radial and tangential stresses are given by:

$$\sigma_{r1} = \sigma_{t1} = -P \tag{4}$$

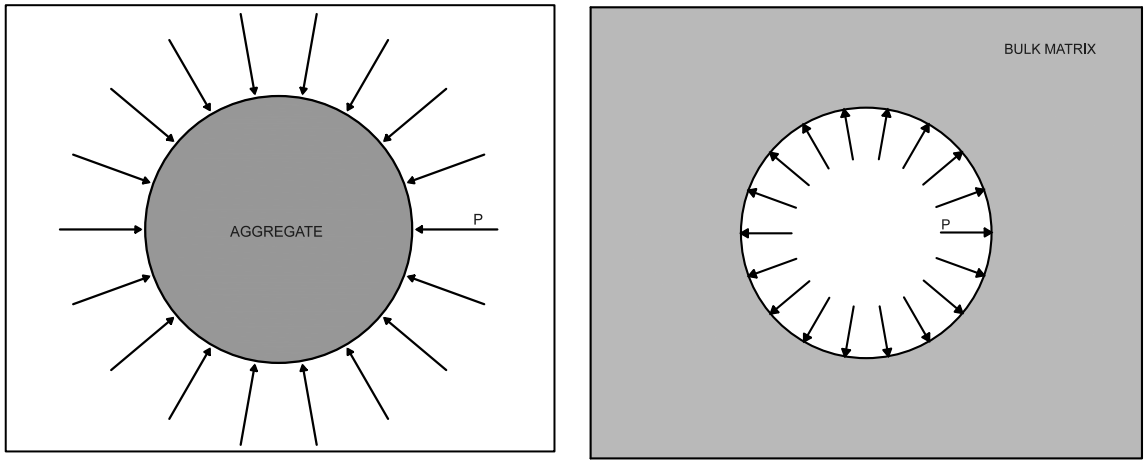

a) b)

Figure 4-2: a) Solid sphere of radius $\boldsymbol{a}$ with applied external pressure $\boldsymbol{P}$ applied; b) Spherical shell of infinite thickness with internal pressure $\boldsymbol{P}$.

Substituting Eqs. (3) and (4) into Eqs. (1) and (2) and applying the strain compatibility conditions at $r = a$ ($\varepsilon_{t1} = \varepsilon_{t2}|_{r=a}$), the value of the thermal interaction pressure P is obtained as:

$$P = \frac{\Delta T(\alpha_1 - \alpha_2)}{\frac{1+\nu_2}{2E_2} + \frac{1-2\nu_1}{E_1}} \tag{5}$$

The radial and tangential stress and strain for both phases can be obtained by substituting the obtained value of P into Eqs. (1) through (4).

As expected, Eq. (5) clarifies the linear relationship of P with the CTE mismatch between the aggregate and the matrix represented by the coefficient $(\alpha_1 - \alpha_2)$, and the non-linear relationship of P with the elastic mismatch between the aggregate and the matrix represented by E_1 and E_2. From analysis of Eqs. (3) through (5), it can be

observed that with a positive value of ΔT (temperature increment), if $\alpha_1 > \alpha_2$, tensile stresses are generated in the tangential direction of the second phase (matrix), and thus microcracks are more likely to be generated in the radial direction from the aggregate particle (Figure 4-3a). Similarly, if $\alpha_1 < \alpha_2$, the tensile stresses are oriented in the radial direction in both phases, and microcracks are prone to appear with a tangential orientation between the phases surrounding the aggregate particle (Figure 4-3b).

The interaction between fine aggregate particles and cement paste is not considered because they are modeled as a unified bulk matrix phase. It has been stated that an ITZ is most likely to occur in the area surrounding large aggregate particles (Nilsen & Monteiro, 1993); therefore, microcracks are more likely to occur in the area surrounding large aggregate particles, where a higher porosity and lower strength matrix is observed.

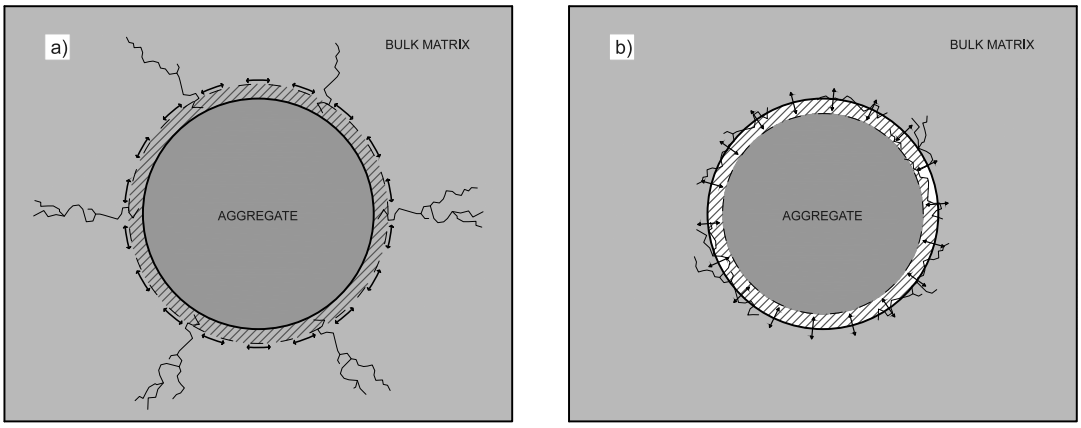

Figure 4-3: a) Tangential tensile stresses and radial microcracks induced when $\boldsymbol{\alpha_1 > \alpha_2}$ and $\boldsymbol{\Delta T > 0}$; b) Radial tensile stresses and tangential microcracks induced when $\boldsymbol{\alpha_1 < \alpha_2}$ and $\boldsymbol{\Delta T > 0}$.

4.4 Thermal History and Cement Hydration

The time-temperature cycles in concrete, especially at early ages, significantly affect the strength development due to an increase in the hydration reaction rate of cement (Mehta

& Monteiro, 2005). For this reason, many researchers have focused their efforts on developing relationships between temperature and strength (Tank & Carino, 1991). In addition, the hydration products generated at accelerated rates due to higher temperatures exhibit a coarser and more porous structure (Gallucci et al., 2013), which explains the lower long-term strength reached by concrete cured at higher temperatures (Abdel-Jawad, 2006; Neville, 1995) compare with those cured at 20 °C.

Saul (1951) introduced the maturity concept 60 years ago to account for this effect. According to his research, maturity is the product of temperature cycle ($\theta(t)$) and time (Eq. 6), accounting for a datum temperature (θ_0) below which hydration is unlikely to occur (Chengju, 1989; Deschutter, 2004):

$$M = \int_0^t (\theta(t) - \theta_0)dt \tag{6}$$

The ASTM C1074 (2004) recommends use of a datum temperature of 0 ºC for Type I Portland cement cured between 0 ºC and 40 ºC. An alternative approach to the maturity function is the equivalent age concept (t_{eq}), defined as the curing time required at a reference temperature (θ_R) to achieve the same maturity level as a concrete that undergoes the actual time-temperature cycle (Abdel-Jawad, 2006; Deschutter, 2004; Yi, Moon, & Kim, 2005). The most widely used function for computing equivalent age at a reference temperature θ_R is based on the Arrhenius equation (ASTM C1074, 2004; Poole et al., 2011):

$$t_{eq}(\theta_R) = \sum_{t=0}^{t} e^{-\frac{E_a}{R}\left(\frac{1}{\theta_C}-\frac{1}{\theta_R}\right)} \times \Delta t \tag{7}$$

where $t_{eq}(\theta_R)$ is the equivalent age at the reference temperature $\theta_R\,(K)$, $\theta_C\,(K)$ is the concrete temperature, Δt is the time interval (days or hours), R is the natural gas constant (8.314 J/mol/K), and E_a is the apparent activation energy (in J/mol), which combines the temperature sensitivity of the several chemical reactions occurring during

cement hydration into one parameter (Poole et al., 2011). The same study presents a method used to determine E_a using isothermal calorimetry, which provides a useful tool for accurately modeling the cement hydration kinetics.

4.5 Experimental Program

The variety of aggregates used in concrete mixtures poses inherent challenges to characterization and engineering of key properties required to improve performance and mechanical behavior in a cementitious matrix (Alexander, 1996). Each type of aggregate type contains a mineralogical composition that conditions the fundamental thermo-mechanical parameters E_1 and α_1, of that particular rock. This fact makes an individual assessment of the CTE and elastic mismatch between the aggregate and the bulk matrix phase impossible because both variables necessarily vary together when the aggregate mineralogy changes.

Temperature variations generate aggregate thermal strain that can be simply denoted as $\alpha_1 \Delta T$, where α_1 is the aggregate CTE. A variation in α_1 changes the thermal stress, increasing or decreasing the CTE mismatch $(\alpha_1 - \alpha_2)$ with the matrix. In parallel, a variation in the aggregate elastic modulus E_1 has an non-linear impact on the magnitude of the thermal stress induced by the strains generated due to a temperature change, as shown in Eq. (5). Because E_1 and α_1 are given for a certain aggregate and cannot be varied independently, different time-temperature cycles were used to artificially hold the aggregate thermal strain constant ($\alpha_1 \Delta T$). Thus, the same aggregate expansion scenario can be achieved over a wide range of E_1 values.

Similarly, for a given aggregate, time-temperature cycle adjustments can be used to simulate aggregate thermal strain variations while holding E_1 constant. This goal is achieved by modification of the ΔT term in the $\alpha_1 \Delta T$ expression. The effects of this external simulation on the stresses generated between the concrete phases are equivalent to an apparent α_1 modification for a given aggregate of known elastic modulus E_1.

The values of ν_1 and ν_2 were assumed as 0.2 (Zhou et al., 2013). Because the value of *P* represents a uniform stress in the aggregate and bulk matrix surfaces, the effect of this assumption has low relevance compared with the elastic modulus and CTE mismatches. A representation of the thermo-mechanical experimental design is shown in Figure 4-4.

4.5.1 Design of time-temperature cycles

Four different types of coarse aggregates were selected to explore a wide range of thermo-mechanical properties: expanded shale (LA, lightweight aggregate), calcareous gravel (CA, normalweight aggregate), siliceous gravel (SA, normalweight aggregate), and magnetite (HA, heavyweight aggregate).

Four experimental points were defined in the iso-thermal strain axis, one for each type of aggregate used. Temperature adjustments were chosen accordingly to account for the different α_1 value of each aggregate while holding $\alpha_1 \Delta T$ constant in all cases (determination of aggregate properties will be presented in next section). To explore the effects of the apparent α_1 variation (iso-stiffness axis), the LA and SA were selected due to their significantly different stiffnesses as well as the broad use and availability in the SA case. The experimental points are presented schematically in Figure 4-4.

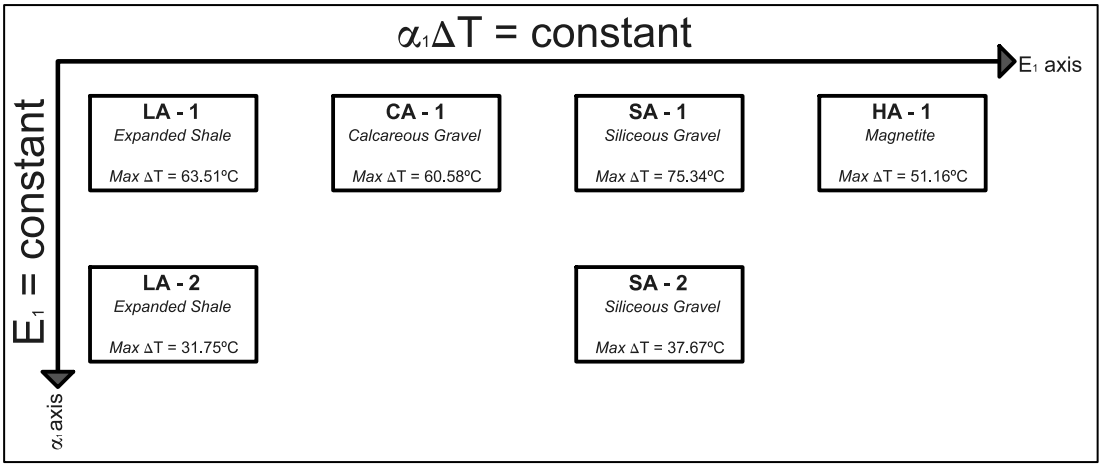

Figure 4-4: Experimental points explored over a conceptual two-axis thermo-mechanical design.

The time-temperature cycles were based on a real temperature record obtained from a massive concrete foundation. The cooling portion was adjusted to exhibit symmetry with the starting heating ramp, and the general shape of the thermal cycle is shown in Figure 4-5. The values of T_0, T_1,, and T_{MAX} (initial, 1-day, and maximum temperature, respectively) and the aggregate maximum thermal strains are presented in Table 4-1 for each of the experimental points. Max ΔT was computed as the difference between T_{MAX} and T_0 (20 ºC).

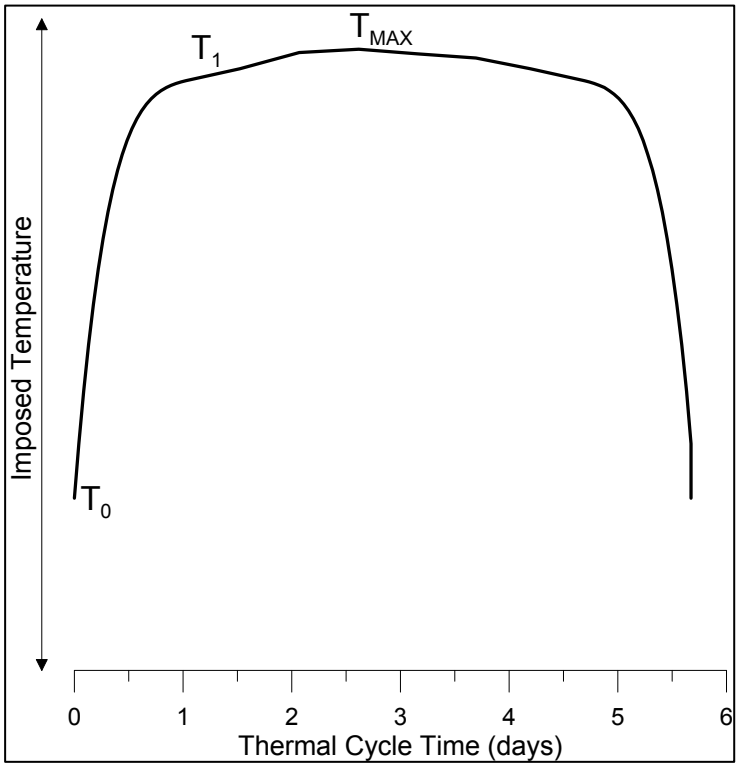

Figure 4-5: Basic shape of the time-temperature cycle applied to the concrete specimens.

Table 4-1: Temperature parameters for each experimental point.

Experimental Point	T_1 [ºC]	T_{MAX} [ºC]	Max ΔT [ºC]	Max $\alpha_1 \Delta T$ [$\mu\varepsilon$]
LA – 1	79.4	83.5	63.5	356
CA – 1	76.7	80.6	60.6	356
SA – 1	90.5	95.3	75.3	356
HA – 1	67.9	71.2	51.2	356
LA – 2	49.7	51.8	31.8	178
SA – 2	55.3	57.7	37.7	178

4.5.2 Concrete mixture proportions

The concrete mixtures were produced using four different types of coarse aggregates. The same base mortar matrix was used for all mixtures and was based on siliceous fine aggregate and Type I ordinary Portland cement (OPC). In all cases, the coarse aggregate volume fraction was 37.5 %, and a water to cement ratio of 0.55 was selected based on the literature to minimize the effects of autogenous shrinkage (Barcelo, Moranville, & Clavaud, 2005; Holt, 2005; Pichler, Lackner, & Mang, 2007; M. . Zhang, Tam, & Leow, 2003). OPC and fine aggregate dosage was fixed at 350 kg/m^3 and 820 kg/m^3, respectively.

Fifteen 10x20 cm cylinders, six 10x10x30 cm prism specimens, and eight 2.5x5.0 cm cylinders were cast for each of the six experimental points studied (Figure 4). The specimens were placed at an environmental chamber for 24 h at (20 ± 3) ºC and covered with plastic sheet to avoid evaporation until removed from the molds.

4.6 Thermal damage testing

After removal from the molds, the specimens were weighed and randomly assigned to the thermal cycle (TC) and equivalent age curing (TE) groups. Five10x20 cm cylinders, three 10x10x30 cm prisms, and four 2.5x5.0 cm cylinders each composed the TC and TE specimen groups.

The TC group refers to specimens subjected to the time-temperature cycles described in Table 4-1 and were intended to measure the effect of thermal stresses on the concrete properties. The TE group consisted of a set of specimens identical to the TC group and intended to serve as a non-damaged material reference; the specimens in this group were cured at (20 ± 3) ºC for the equivalent age calculated using Eq. (7), and the time-temperature cycle of the TC group. The initial tests on instrumented specimens showed that the maximum temperature gradients between the core and surface (surface gradient) was only 1.5 ºC regardless of the specimen size and shape, which was sufficient to neglect the surface gradient effect and to consider damage produced by a pure mass gradient effect (Neville, 1995). Specimens from the TC and TE groups were sealed using aluminum tape before undergoing thermal cycles and curing at 20 ºC, respectively. This method proved to be effective in avoiding water losses at high temperatures, which was relevant to avoid the concrete swelling and drying/shrinkage effects present in other curing methods.

4.6.1 Fluorescence microscopy

Fluorescence optical microscopy has been proven as a powerful technique for performing qualitative and quantitative measurements of microcracking in concrete (Jakobsen & Brown, 2006; Litorowicz, 2006; Soroushian, Elzafraney, & Nossoni, 2003; Soroushian & Elzafraney, 2005). In this study, fluorescence microscopy was used as a tool for qualitative identification of the crack density and morphology in specimens subjected to the time-temperature cycle and the equivalent-age curing. Samples of 1 cm

in height were cut from the 2.5x5.0 cm cylinder specimens of the TC and TE groups using a low-speed saw. The samples were cleaned in an ultrasonic bath for 10 min using iso-propanol as cleaning medium. After removal from the bath, the samples were cleaned with compressed air, dried at 35 ºC and 720-mmHg vacuum, and stored under those conditions for 2 h. The samples were finally impregnated using an ultra-low viscosity and high-hardness resin combined with fluorescein (FITC) as a fluorochrome. To avoid additional exposure of the samples to temperatures that could result in unintended microcracking, the resin was cured using UV radiation for 48 h at a laboratory temperature of 20 ºC. After curing, the samples were polished using a standard grinding machine prior to observation. The TE samples were prepared using the same procedure as the TC samples and were intended to provide a reference for cracking generated by the preparation method and other phenomena unrelated to the thermal cycle.

4.6.2 Compressive strength

The compressive strength was measured on 10x20 cm cylinder specimens of each TC and TE group. For the TC and TE specimens, tests were performed after the thermal cycle and equivalent age curing periods, respectively. After completion of electrical resistivity testing, the specimens were also tested for compressive strength. It should be noted that no significant difference in results were observed between the saturated and non-saturated specimens.

4.6.3 Dynamic elastic modulus

The dynamic elastic modulus was measured on 10x10x30 cm prism specimens of the TC and TE groups according to the ASTM C215 procedure (ASTM C215, 2008). This method was selected due to its suitability and sensitivity to measurement of concrete damage due to microcracking in freeze-thaw tests. It should be mentioned that the

dynamic elastic modulus test is based on measurement of the fundamental resonant frequencies of the specimen and is therefore non-destructive.

4.6.4 Electrical resistivity

The electrical resistivity was measured in 10x20 cm cylinder specimens of the TC and TE groups based on the axial-measurement method described by Spragg et al. (Spragg, Castro, Nantung, Paredes, & Weiss, 2012) to compare changes in the concrete pore percolation due to the presence of microcracks. In this method, two stainless steel plates are placed at the ends of the 10x20 cm cylinder and connected to the same surface resistivity meter used in the Wenner probe apparatus (Morris, Moreno, & Sagüés, 1996). The obtained electrical resistance values are normalized by the cross-sectional area-to-length ratio of the cylinder to calculate the bulk resistivity of the specimen. Three cylinder specimens were randomly selected, the aluminum tape was removed, and the specimens were submerged in water for 24 h at 20 ºC to achieve saturation of cracks before testing.

4.7 Materials Characterization

4.7.1 Cementitious matrix constituents

The Type I OPC chemical composition presented in terms of oxides measured with X-ray fluorescence (XRF) is shown in Table 4-2, and the particle size distribution (PSD) is presented in Figure 4-6.

Table 4-2: Cement chemical characterization.

Composition as oxides (%)	OPC
SiO_2	20.39
Al_2O_3	6.01
Fe_2O_3	3.15
CaO	63.25

Na_2O	0.15
K_2O	0.75
MnO	0.07
TiO_2	0.27
MgO	1.30
P_2O_5	0.08
SrO	0.03
SO_3	2.35
LOI	1.72
Specific gravity (g/cm^3)	3.122

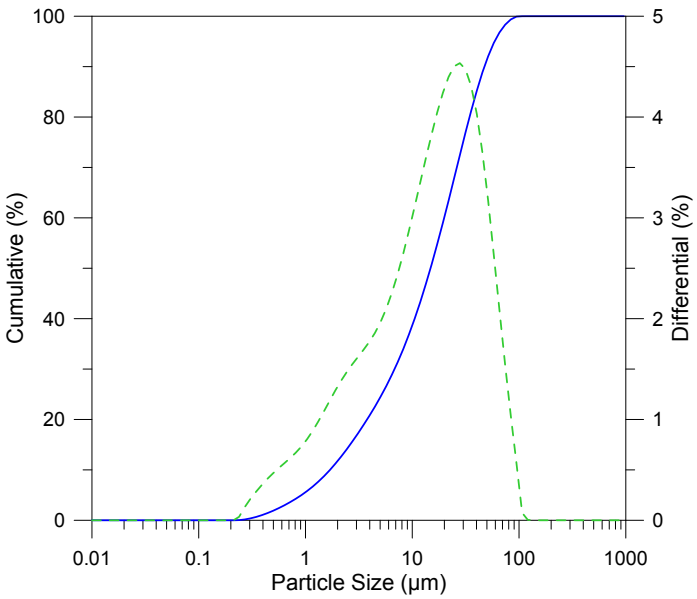

Figure 4-6: OPC particle size distribution. The solid line represents the cumulative PSD, and the dashed line corresponds to the differential results.

To accurately predict the cement hydration using the Arrhenius equation and calculate the equivalent age (Eq. 7), an accurate measure of the activation energy (E_a) is required. The procedure based on isothermal calorimetry described by Poole et al. (Poole et al., 2011) was used. The OPC phase composition was determined using X-ray diffraction (XRD) and Rietveld refinement analysis. Fluorite was used as an internal standard to account for the amorphous fraction and to correct the Rietveld results based on the procedure proposed by Chancey et al. (Chancey, Stutzman, Juenger, & Fowler, 2010).

The diffraction pattern with the identified main phases and the phase composition are shown in Figure 4-7 and Table 4-3, respectively.

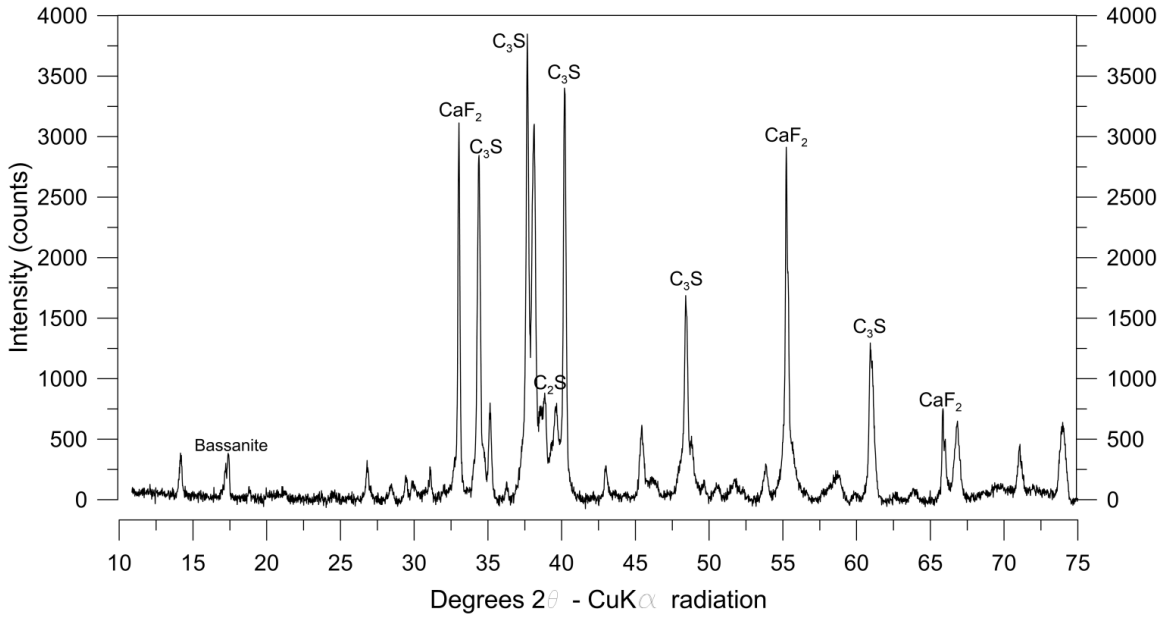

Figure 4-7: X-ray diffraction pattern of the OPC used for the Rietveld refinement.

Table 4-3: QXRD analysis of the OPC using the Rietveld refinement and fluorite as an internal standard.

Mineral Name	Formula	Rietveld Presence (% by wt.)
Quartz	SiO_2	1.0
Bassanite	$CaSO_4(H_2O)$	3.1
Anhydrite	$CaSO_4$	1.1
Calcite	$CaCO_3$	1.8
Fluorite (I.S.)	CaF_2	11.5
Lime	$CaCO_3$	0.7
C_3A cubic	$3CaOxAl_2O_3$	8.6
Alpha C_2S	$2CaOxSiO_2$	5.3
Beta C_2S	$2CaOxSiO_2$	1.7
Ferrite (C_4AF)	$4CaOxAl_2O_3xFe2O3$	6.8
Alite (C_3S)	$3CaOxSiO_2$	58.4

I.S. = Internal Standard

Isothermal calorimetry tests were carried out using TAM Air isothermal calorimeter at 10 ºC, 20 ºC, 32 ºC and 40 ºC. In all cases, a 0.55 w/c cement paste was used. The maximum heat of hydration (H_u) used to normalize the heat curves and obtain the degree of hydration plots was calculated using the equation proposed by Bogue (Bogue, 1947):

$$H_u = 500 \cdot p_{C_3S} + 260 \cdot p_{C_2S} + 866 \cdot p_{C_3A} + 420 \cdot p_{C_4AF} + 624 \cdot p_{SO_3} + 1186 \cdot p_{FreeCa} + 850 \cdot p_{MgO} \quad (8)$$

where p_x represents the mass ratio of phase x to the total cement material. A commercial non-linear regression package was employed to adjust the model presented in (Poole et al., 2011) with the obtained degree-of-hydration plots. The apparent activation energy was subsequently calculated using the equation proposed by Schindler (Schindler, 2004), and the resulting value was 45,880 J/mol. This parameter was used to compute the equivalent ages using Eq. (7) for all experimental points. The heat plots together with the regression fit at each temperature and the Arrhenius plot of the applied OPC are presented in Figure 4-8.

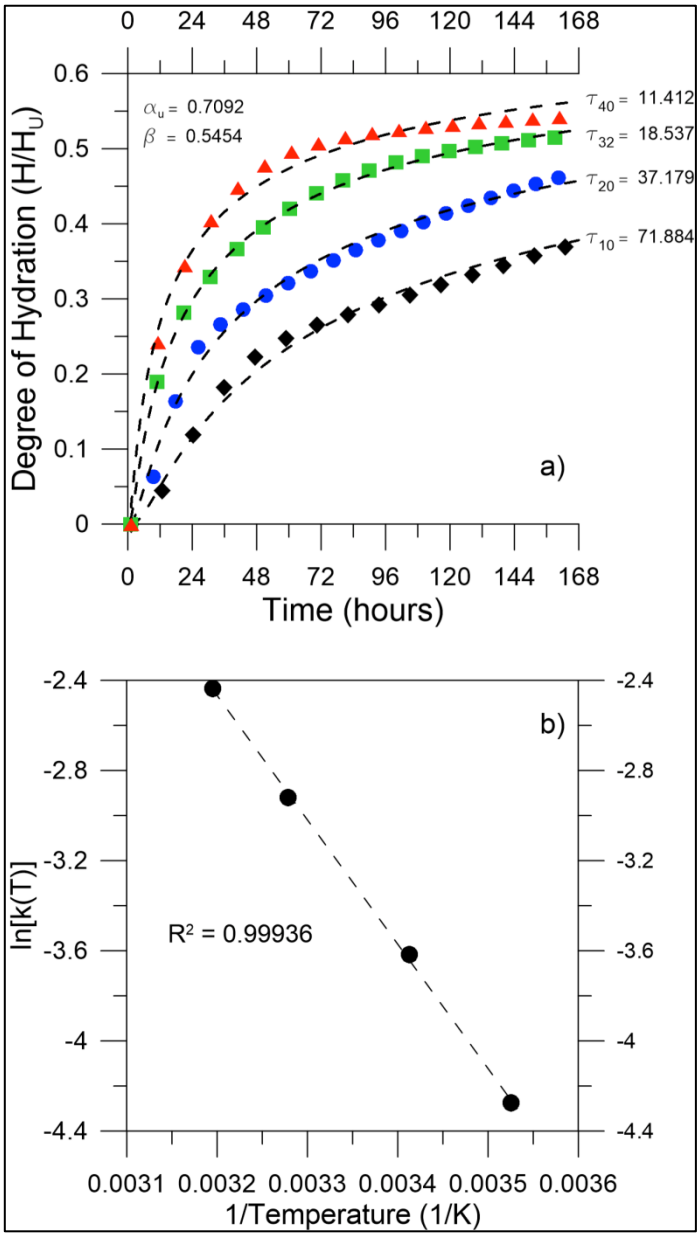

Figure 4-8: a) Isothermal calorimetry results (dots) and exponential regression (dashed line); b) Arrhenius plot of OPC.

The bulk matrix CTE (α_2) was measured over time using 2.54x2.54x25.4 cm prismatic specimens and a digital length comparator. The applied mixture proportions were the same as those used for concrete but without the coarse aggregate. Because the matrix CTE is influenced by the relative humidity content (Maruyama & Teramoto, 2012), the

specimens were sealed using aluminum tape after removal from the molds. Fifteen specimens were prepared, and three of each type were tested daily from 2 d to 28 d in age and every week up to 66 d. The specimens were heated to 50 ºC, measured in the length comparator (L_{50}), and subsequently cooled to room temperature (T_{LAB}) for a new length measurement (L_{LAB}). The temperature was recorded using a thermocouple embedded within one specimen subjected to the same time-temperature cycle and used exclusively for temperature recording. The CTE of the matrix (α_2) was computed using Eq. (9):

$$\alpha_2 = \frac{\frac{L_{50} - L_{LAB}}{L_{LAB}}}{50 - T_{LAB}} \tag{9}$$

The results for CTE tests of the bulk matrix are presented in Figure 4-9 in which a clear increasing trend is observed during the first 20 d. This observation is consistent with previous results (Maruyama & Teramoto, 2012) and is attributed to the reduction in internal relative humidity due to ongoing hydration. However, after 40 d of curing, the CTE change with time stabilizes, presumably due to a reduction in the hydration rate at lower internal relative humidity levels.

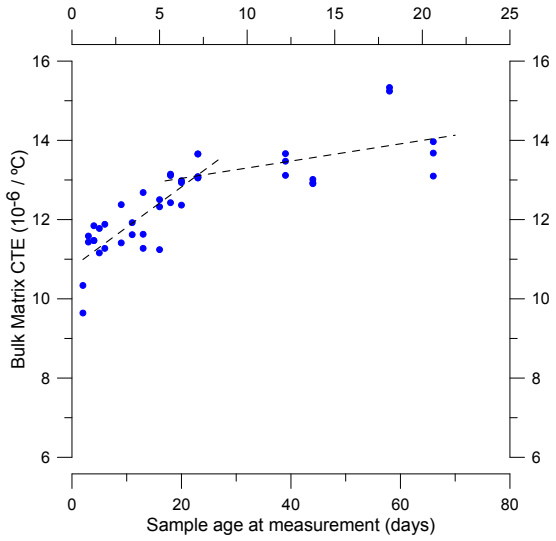

Figure 4-9: Bulk matrix CTE ($\boldsymbol{\alpha_2}$) measured over time.

4.7.2 CTE and E of coarse aggregates

The aggregate CTE (α_1) was measured using thermo-mechanical analysis (TMA) using a TA 943 instrument. Tests were carried out between -20 ºC and 120 ºC in samples with four different grains for each type of aggregate. For the LA aggregate, eight grains were considered in four tests parallel to the cleavage plane and four tests perpendicular to the cleavage plane. The grains were cooled from room temperature (approximately 25 °C) to -30 °C and held until the temperature stabilized. The specimen was heated to 130 °C at a rate of 5 °C/min. The test was performed under a load of 1 g (10 mN) and a flow of dry nitrogen at 25 mL/min. If the data showed excessive noise, extreme discontinuities, or outlier behavior due to sample placement or outer vibration, the data collection process was halted, the grain was re-cooled, and the test was restarted. The averages and standard deviations of the measured CTE values are summarized in Table 4-4.

The aggregate elastic modulus (E_1) of the aggregate grains is difficult to measure due to the irregular shapes that they present. Several composite models were proposed for estimating the concrete elastic modulus based on matrix and aggregate properties (Chen et al., 2003). The Hirsch model was selected due to good agreement between the predicted and theoretical values (Hirsch, 1962). In this study, the concrete and bulk matrix elastic moduli (E_C and E_m, respectively) were measured to compute the aggregate elastic modulus using Eq. (10) with knowledge of the volume fraction of the aggregate (V_a). The concrete mixtures were assembled following the procedure proposed by Moreno et al. (Moreno, Martinez, & Lopez, 2014) using a V_a equal to 0.4. The x parameter was experimentally adjusted using steel and aluminum chunks as coarse aggregates and was estimated at 0.5. Values for each aggregate type are presented in Table 4-4:

$$E_C = \frac{1}{x\left[\frac{V_a}{E_1} + \frac{1-V_a}{E_m}\right] + (1-x)\left[\frac{1}{V_a E_1 + (1-V_a)E_m}\right]} \tag{10}$$

Table 4-4: Aggregate CTE ($\boldsymbol{\alpha_1}$) and elastic modulus ($\boldsymbol{E_1}$) computed using the compound Hirsch model.

Aggregate Type	Specific gravity (SSD) ρ_a	Average α_1 [10^{-6}/ºC]	STD [10^{-6}/ºC]	Average E_1 [GPa]	STD [GPa]
LA	1.628	5.61	0.52	12.48	0.45
CA	2.566	5.88	2.73	50.24	8.37
SA	2.698	4.73	0.74	55.45	2.80
HA	4.220	6.96	0.52	85.70	2.40

4.8 Results and Discussion

4.8.1 Fluorescence microscopy

Thermo-mechanical characterization of the coarse aggregates (Table 4-4) and the bulk matrix (Figure 4-9) showed that all four aggregates had a CTE significantly lower than that of the matrix (i.e., $\alpha_1 < \alpha_2$), and this difference increases with the age of the matrix. Based on the proposed two-phase micromechanical model, these results suggest that upon heating, the expected microcracks are more likely to be oriented similar to those in Figure 3b because the tensile stresses will develop in the radial direction. This presumption was confirmed based on fluorescence microscope observation of TC specimens of all experimental points considered. The microcracks were distributed primarily along the ITZ surrounding the aggregates, as shown in the micrographs (Figures 4-10a to 4-10f) for all aggregate types and time-temperature cycles imposed. Dark field (DF) images of the same micrograph for each fluorescence picture are included to aid in phase identification.

Dark Field (DF)	TC Series	Fluorescence (FITC)
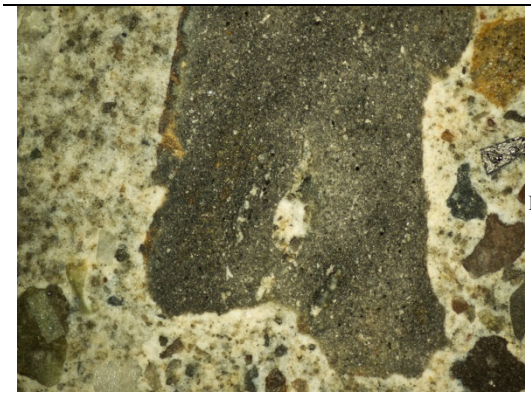	a) LA-1	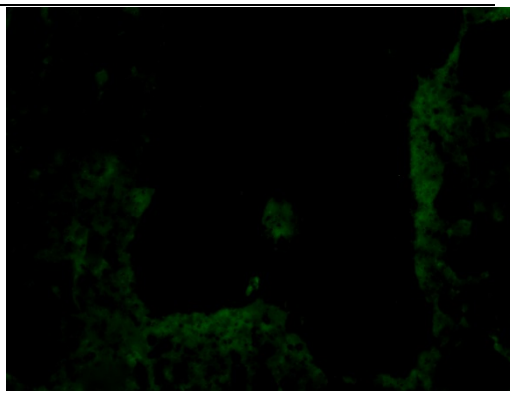
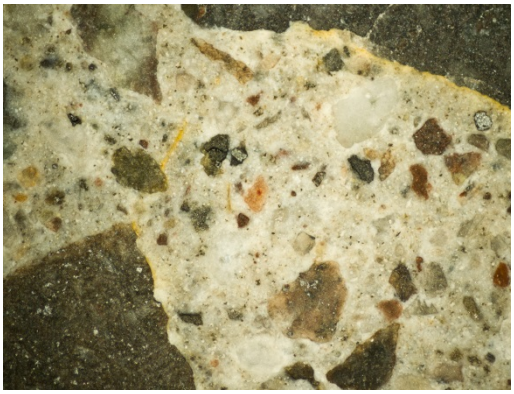	b) CA-1	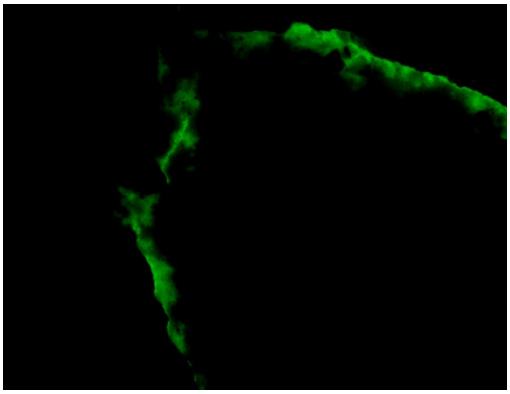
	c) SA-1	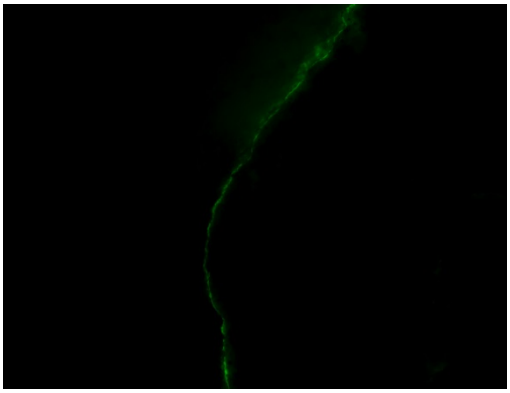

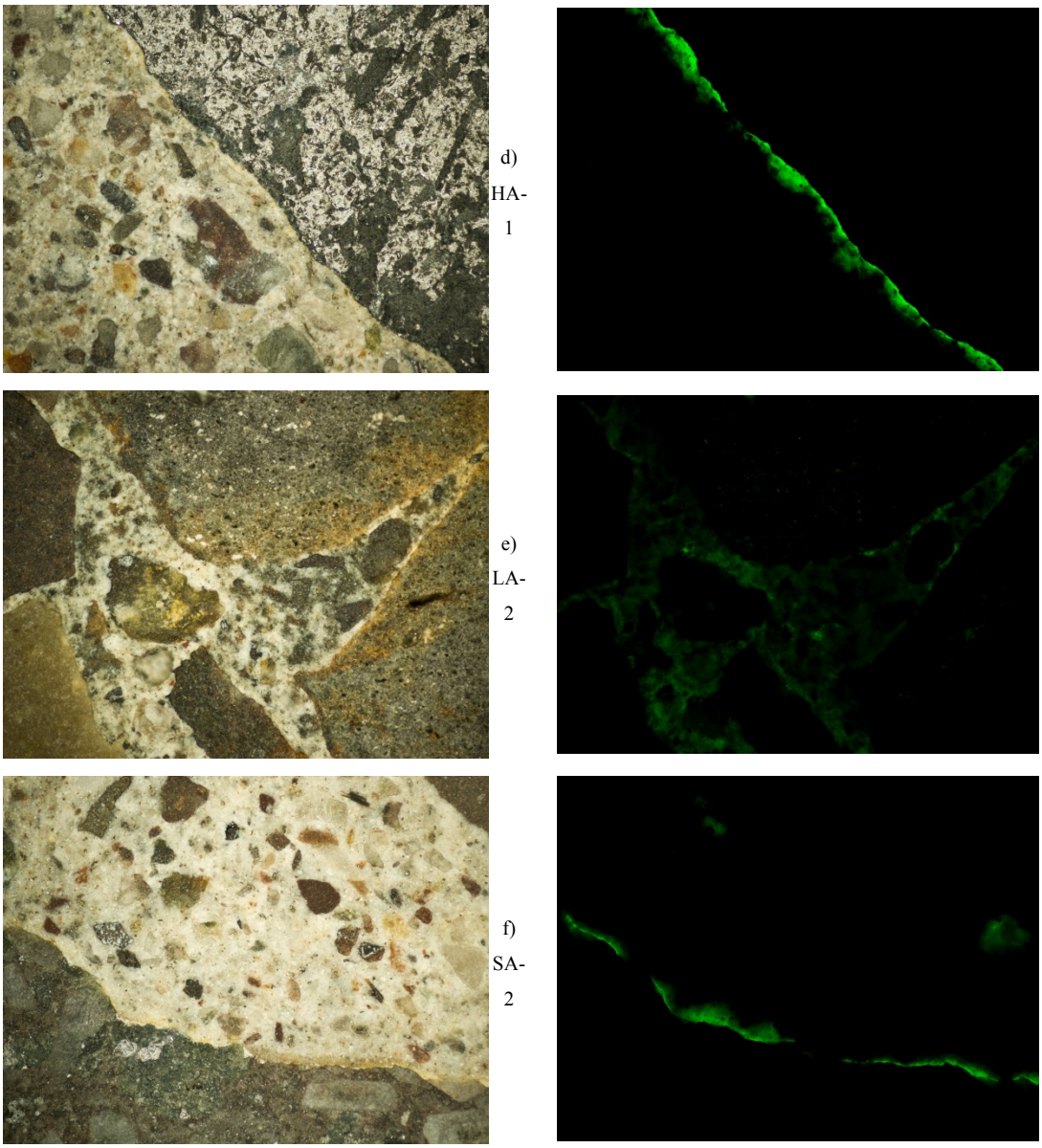

Figure 4-10: Dark field (DF) and fluorescence images of microcracks observed on the ITZ on all experimental series (a-to-f).

To assure that the microcracks observed in Figure 4-10 were in fact due to thermal stresses and not due to drying shrinkage or artifacts that occurred during sample preparation, careful observations of TE samples were conducted. The presence of

microcracks was significantly lower compared with that of the TC samples, as shown in Figure 4-11.

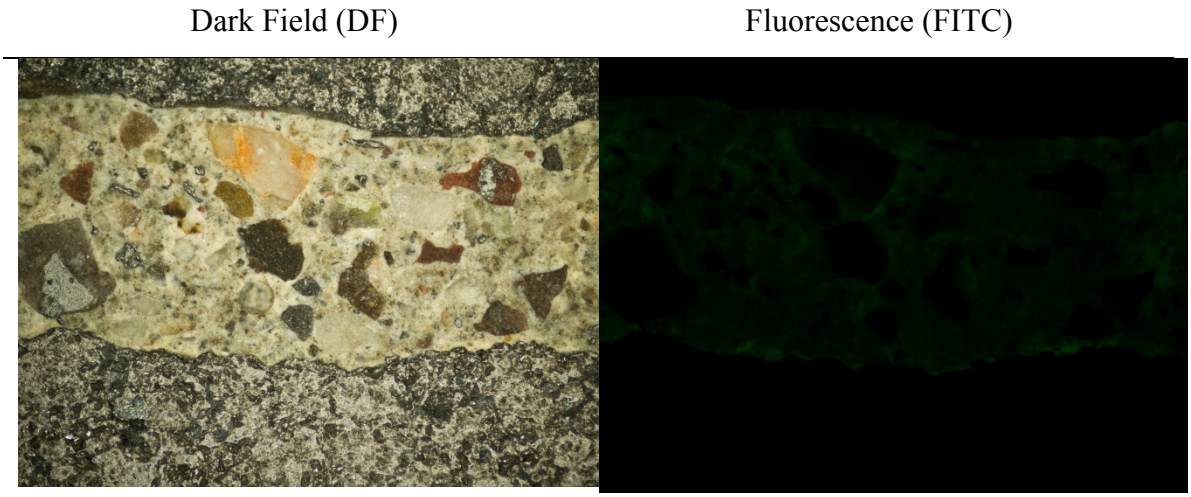

Figure 4-11: Dark field (DF) and fluorescence images of the ITZ zone in samples not subjected to thermal stresses.

Fluorescence microscopy observations confirmed the presence of microcracks at different levels and extensions in the TC samples. The presence of incremental damage due to time-temperature cycles validates the need for statistical analysis of the influence of such damage on the mechanical and transport properties (compressive strength, elastic modulus, and electrical resistivity) and the use of mechanical parameters in the two-phase micromechanical model.

In addition to the thermal stresses and damage, it should be noted that a lower quality and higher porosity CSH matrix would have been generated due to the increased rate of reaction in the TC samples. Thus, the overall damage to the concrete is due to the increased thermal stresses and increased matrix porosity.

4.8.2 Compressive Strength

The results of the compressive strength tests are shown in Figure 4-12 and are divided into two charts (a and b) according to the experimental program design: one shows the iso-thermal strain and the other displays the iso-stiffness. The hatched bars show the TE results, and the overlapped grey bars present the TC results. The gap between the gray and the green-dashed bars represents the strength loss due to thermally induced microcracks.

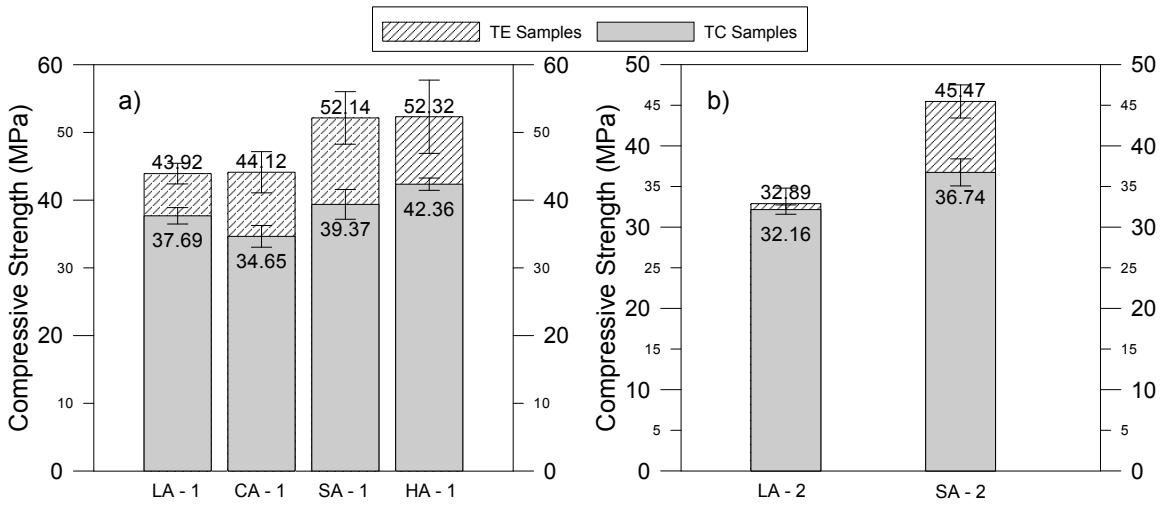

Figure 4-12: Compressive strength results of TC and TE specimens: a) High aggregate thermal expansion level; b) Low aggregate thermal expansion level. Error bars represent the standard deviation of the average of three samples.

Statistically significant strength losses were observed in all of the high aggregate expansion series (Figure 4-12a). A greater relative strength loss was observed in the SA-1 specimens attributed to the high CTE mismatch combined with a relatively high elastic modulus of this aggregate, which leads to an increased deformation of the matrix and a high maximum interaction pressure (P) value. It is interesting to note that a high stiffness aggregate such as the HA will not necessarily lead to high thermal stresses between the aggregate and the bulk matrix because the value of P is determined not only by the elastic modulus of the aggregate but also by its CTE. Particularly in the HA case,

its high elastic modulus is compensated to a certain extent with the reduced CTE mismatch between the HA and the bulk matrix. This situation yields a lower value of P compared with that of the SA and CA. In the same way, although the LA has a higher CTE mismatch compared with HA, its stiffness is significantly lower, resulting in the lowest computed maximum *P* value. All of these theoretical derivations based on aggregate and bulk matrix characterizations are observed in the compressive strength results.

Figure 4-12b shows that no significant strength losses were observed in the LA-2 specimens, which imply that the thermal stresses generated were lower than the developing tensile strength of the matrix, and thus, significant microcracking did not occur during the thermal cycle.

To correlate the experimental results with the theoretical derivations from the micromechanical model, two reference parameters were selected. The interaction pressure *P,* due to the direct relationship between this value and the stresses in both phases and its ease of computation, making it suitable to be used as a practical index of thermal damage. In addition, the radial deformation of the bulk matrix ε_{r2} was selected because tensile stresses will occur primarily in this direction according to the model (Figure 4-3b).

The average compressive strength performance ratios were computed by dividing the average strength of the TC specimens into the corresponding average strength of the TE specimens for each of the six experimental points. These ratios are a numerical representation of the strength losses for which a ratio of 1 implies no decrement in compressive strength of TC specimens compared with that of the TE specimens. The plots of TC/TE compressive strength ratios against their corresponding maximum *P* (Figure 4-13a) or ε_{r2} (Figure 4-13b) values achieved during the time-temperature cycles were analyzed, and a non-linear trend was observed.

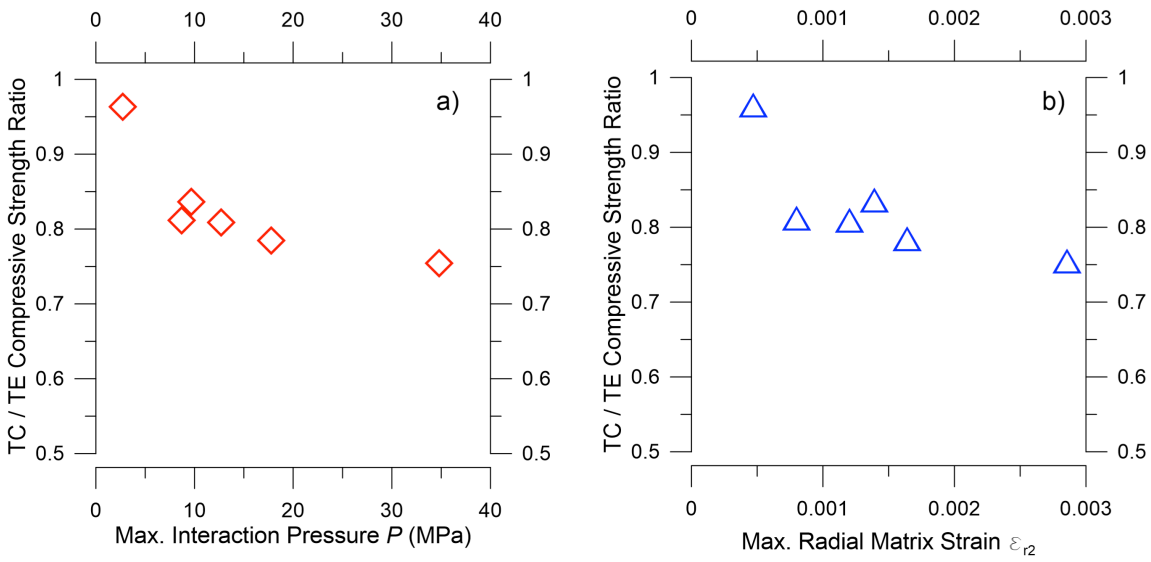

Figure 4-13: a) TC/TE compressive strength ratios correlated with *P* values; b) TC/TE compressive strength ratios correlated with $\boldsymbol{\varepsilon_{r2}}$ values.

It is interesting to note that the computed ε_{r2} values are consistent with the strains that cement paste and concrete are able to withstand before rupture. In the case of SA-1, which presented the most pronounced loss in strength, the maximum radial matrix strains were close to 0.003 mm/mm, suggesting that the maximum strain capacity on average of the matrix was overcome. The non-linear behavior of the compressive strength loss trend could be attributed to presence of the ITZ, neglected in the proposed model. The quasi-brittle behavior of concrete under compression is attributed to multiple microcrack development on the ITZ (Scrivener et al., 2004). In addition, formation of microcracks is not uniform over the loading range (Lim, Gowripalan, & Sirivivatnanon, 2000).Thus, the relationship between *P* and compressive strength is expected to be non-linear.

4.8.3 Dynamic elastic modulus

The results of measurements of the dynamic elastic modulus are presented in Figure 4-14 using the same data distribution described for compressive strength.

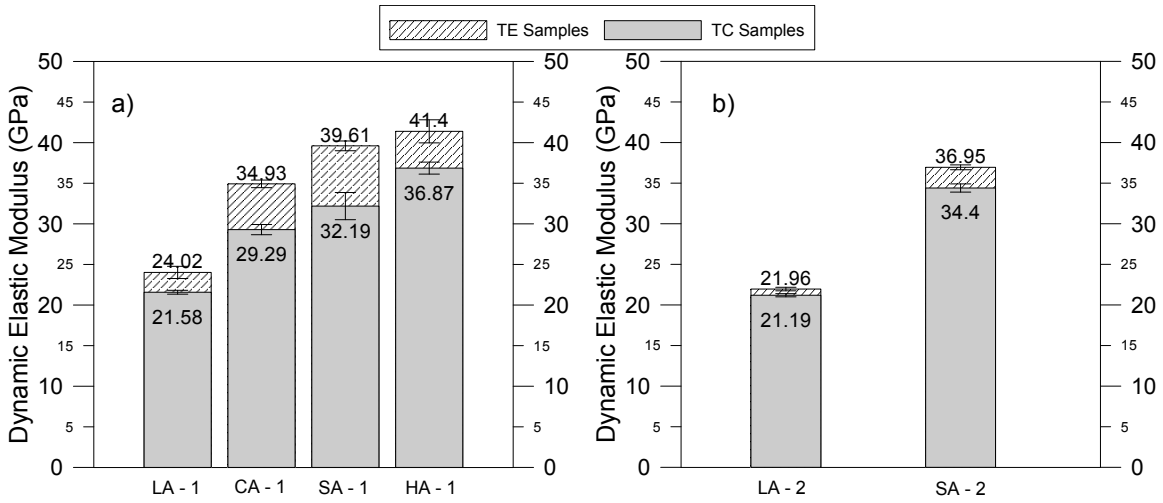

Figure 4-14: Dynamic elastic modulus results of TC and TE specimens: a) High aggregate thermal expansion level; b) Low aggregate thermal expansion level. Error bars represent the standard deviation of the average of three samples.

Consistent with the findings for compressive strength, larger elastic modulus losses for the TC concrete specimens were observed in SA-1 and CA-1. Statistically significant differences between the corresponding TC and TE results were observed in all of the high aggregate expansion series (Figure 4-14a) and only in the SA-2 specimens in the low aggregate expansion level (Figure 4-14b).

Similar to the compressive strength results, the average elastic modulus performance ratios were computed by dividing the average elastic modulus of TC specimens into the corresponding average result of the TE specimens for each of the six experimental points. Plots of the TC/TE elastic modulus ratios against their corresponding maximum *P* (Figure 4-15a) and ε_{r2} (Figure 4-15b) values achieved during the thermal cycle were studied. In this case, a linear trend was observed between the elastic modulus losses represented by the ratios and the maximum P and ε_{r2}.

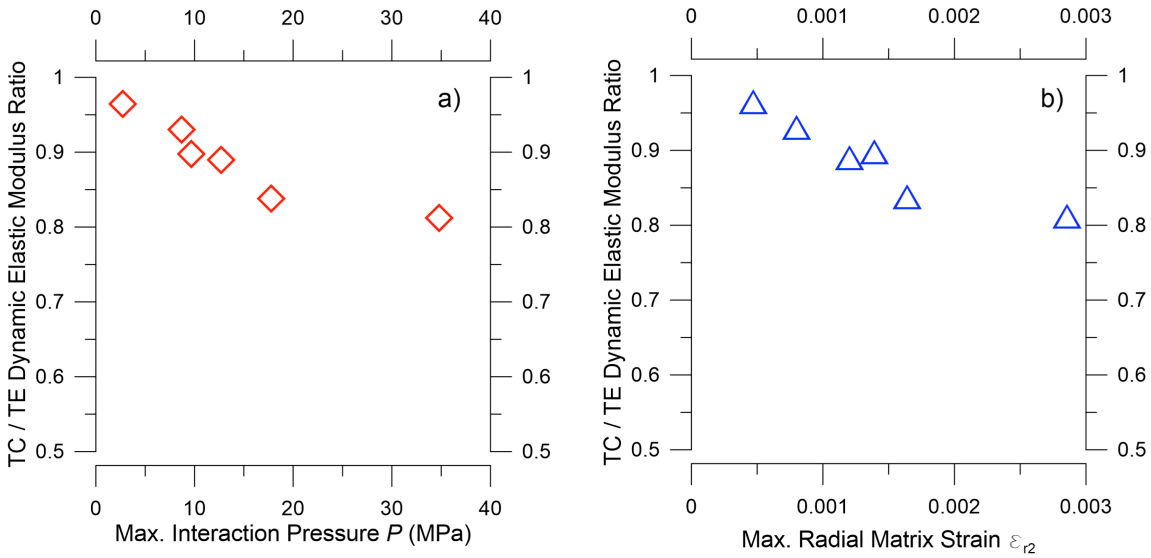

Figure 4-15: a) TC/TE elastic modulus ratios correlated with *P* values; b) TC/TE elastic modulus ratios correlated with $\boldsymbol{\varepsilon_{r2}}$ values. Error bars represent the standard deviation of the average of three samples.

4.8.4 Electrical resistivity

The electrical resistivity tests were intended as an indication of concrete percolation due to microcrack propagation. This and other common permeability tests, i.e., the ASTM C1202 rapid chloride penetration test, are based on the assumption that a variation in electrical current passing through the concrete specimen can be attributed to pore and microcrack interconnection and thus to a higher concrete permeability (Corral, Arredondo, Almaral, & Gómez, 2013; Konin et al., 1998b; Riding, Poole, Schindler, Juenger, & Folliard, 2009; Saraswathy & Song, 2007). For this reason, the inclusion of a conductive material inside the concrete could lead to misleading results because an increase in the current passing through concrete could be attributed not only to increased permeability but also to the presence of the conductive material. The HA aggregates have a high iron content, which is evidenced in its pronounced ferromagnetic behavior, and therefore, the electrical resistivity results do not apply to the HA specimens.

The results of electrical resistivity measurements are presented in Figure 4-16 using the same data distribution described for the compressive strength and dynamic elastic

modulus. As expected, the electrical resistivity values of the HA-1 specimens are significantly lower than those of other specimens containing non-conductive aggregates. Because the bulk matrix is the same in all concrete specimens considered in this study, the difference is attributed to the conductive characteristics of this particular aggregate type.

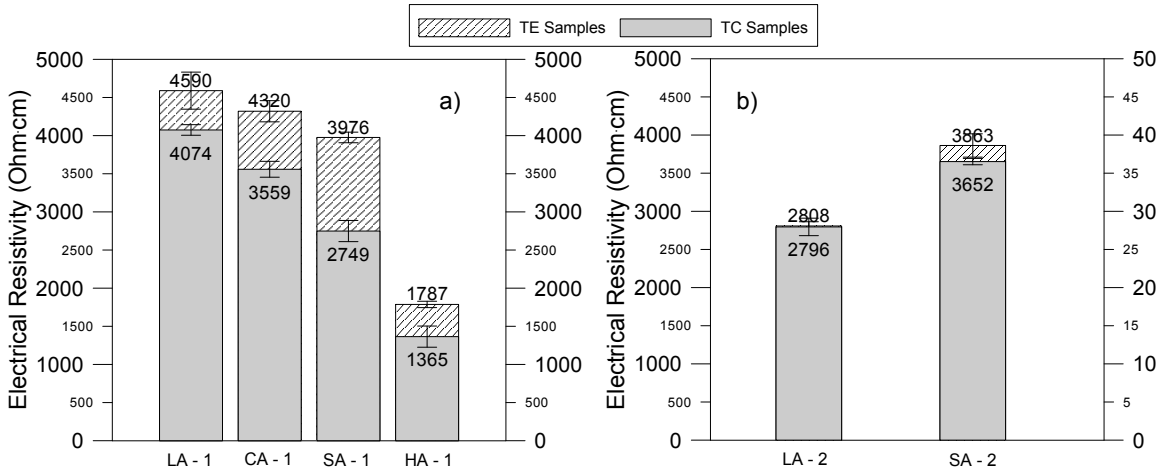

Figure 4-16: Electrical resistivity results of TC and TE specimens: a) High aggregate thermal expansion level; b) Low aggregate thermal expansion level.

As observed from the mechanical properties, the major relative permeability increases are observed in the SA-1 and CA-1 specimens (Figure 4-16a). For the low aggregate expansion series (Figure 4-16b), no statistically significant difference was observed in LA-2, and a slight increase in permeability was measured in the SA-2 specimens subjected to a time-temperature cycle. Due to the conductive character of the HA aggregate, the results cannot be attributed only to an increased permeability. The aggregate proportion in each particular 10x20 cm cylinder, which might vary due to the compaction procedure (Moreno, Zunino, Paul, & Lopez, 2014), could affect the results of this particular specimen group. For this reason, these results were excluded from the statistical comparison between the electrical resistivity ratios and maximum P and ε_{r2} values; these results are shown on Figure 4-17a and 4-17b, respectively, and a linear

trend was observed between the resistivity losses represented by the ratios and the maximum P and ε_{r2}.

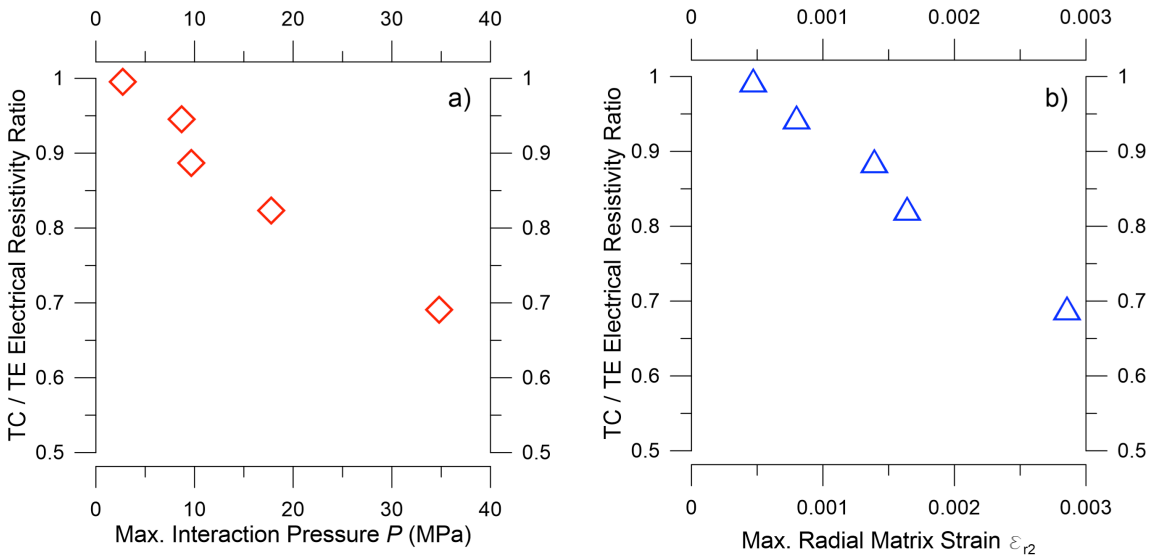

Figure 4-17: a) TC/TE electrical resistivity ratios correlated with *P* values; b) TC/TE electrical resistivity ratios correlated with $\boldsymbol{\varepsilon_{r2}}$ values.

4.9 Conclusions

Thermal stresses are generated in early-age concrete due to heat release from the ongoing cement hydration. Because concrete is a complex mixture of different constituents, thermo-mechanical mismatches occur, which generate differential expansion between the concrete phases, resulting in stresses. These stresses occur when the cementitious matrix begins to develop stiffness and thus restricts the expansion of the concrete phases. In addition, the matrix tensile strength undergoes early stages of development, leaving the concrete prone to microcracking and damage due to this effect.

The objective of this study was to understand the driving mechanical factors that control the thermal stress generation in the interface between the aggregate and the bulk matrix. A two-phase (aggregates and bulk matrix) micromechanical model was proposed to

predict the thermal stresses based on thermo-mechanical mismatches between concrete phases. Two main mismatches were identified: CTE mismatch and elastic mismatch. Extensive characterization of the concrete phases was carried out to ensure proper modeling of the thermal stresses and thus enable the comparison of these predictions with the observed performance under experimental conditions. These conditions were intended to damage the concrete using time-temperature cycles imposed in a controlled laboratory environment. Based on the experimental measurements and theoretical calculations, the following conclusions can be stated:

1. A simplified two-phase concrete model proved to be sufficiently accurate for prediction of damage to concrete from the thermal stresses generated due to differential thermal expansion of its phases. Additionally, the non-complex form of the expressions derived from this model makes it suitable for application to thermal cracking risk assessment in real structures.
2. The interaction pressure P proved to be a good parameter for estimating the thermal cracking risk expressed as the deterioration of key mechanical parameters in the design and durability properties, i.e., compressive strength, modulus of elasticity, and permeability. To accurately apply the proposed model and compute P, a careful thermo-mechanical characterization (CTE and modulus of elasticity) of the concrete phases should be carried out.
3. Fluorescence microscopy was demonstrated as a valuable tool for evaluating the presence and morphology of microcracking in concrete. This approach is particularly relevant to application and correlation of observed damage in concrete with thermal stress models due to concrete experiments and other early-age phenomena that could induce damage, i.e., autogenous shrinkage. The observation of non-exposed specimens confirmed that the generated microcracks were attributable to the time-temperature cycles.
4. Considering the high variability in the thermo-mechanical properties of aggregates of natural origin, such as those used in this study, the model is able to produce an order of magnitude of the expected deterioration of the considered

concrete properties. Although alternatives to measuring the CTE and stiffness of coarse aggregates were presented in this study, the inherent difficulties in measuring these properties in aggregates of irregular shape poses additional challenges to the development of new testing methods for accurate measurement of these parameters in a more simple and direct manner.

The elastic approach used in this study neglects the time-dependent behavior in cement paste, i.e., creep and stress relaxation, and thus, it tends to overestimate the stresses in the ITZ. However, the strain and interaction pressure P calculations allowed for a good estimate of the cracking risk.

Further research is required to assess the effects of cement substitutions, the use of admixtures, variations in the mixture proportions, and other design properties on the thermo-mechanical parameters. Future work is needed to understand and develop new methodologies that reduce the thermal cracking risk at the design stage and to address the thermo-mechanical compatibility orientation, rather than mitigating heat release at the construction site.

4.10 Acknowledgements

The authors greatly acknowledge funding provided by FONDECYT, project Nº1120817 and the support provided by CEDEUS, CONICYT/FONDAP 15110020. The authors also recognize Cementos Polpaico, CAP Minería, DICTUC S.A., Sebastián Calderón and Mauricio Guerra for their contributions to this research project.

4.11 References

Abdel-Jawad, Y. a. (2006). The maturity method: Modifications to improve estimation of concrete strength at later ages. *Construction and Building Materials*, *20*(10), 893–900. doi:10.1016/j.conbuildmat.2005.06.022

ACI 207-2R. (2007). *Report on Thermal and Volume Change Effects on Cracking of Mass Concrete*.

ACI 224.1R. (2007). *Causes , Evaluation , and Repair of cracks in Concrete Structures*.

ACI 231R. (2010). *Report on Early-Age Cracking : Causes , Measurement , and Mitigation*.

Alexander, M. G. (1996). Aggregates and the Deformation Properties of Concrete. *ACI Materials Journal*, *93*(6).

ASTM C1074. (2004). Standard Practice for Estimating Concrete Strength by the Maturity Method. doi:10.1520/C1074-04.2

ASTM C215. (2008). Standard Test Method for Fundamental Transverse , Longitudinal , and Torsional Resonant Frequencies of Concrete Specimens. doi:10.1520/C0215-08.2

Barcelo, L., Moranville, M., & Clavaud, B. (2005). Autogenous shrinkage of concrete: a balance between autogenous swelling and self-desiccation. *Cement and Concrete Research*, *35*(1), 177–183. doi:10.1016/j.cemconres.2004.05.050

Bentz, D. P. (2008). A review of early-age properties of cement-based materials. *Cement and Concrete Research*, *38*(2), 196–204. doi:10.1016/j.cemconres.2007.09.005

Bentz, D. P., Garboczi, E. J., Lu, Y., Martys, N., Sakulich, A. R., & Weiss, W. J. (2013). Modeling of the influence of transverse cracking on chloride penetration into concrete. *Cement and Concrete Composites*, *38*, 65–74. doi:10.1016/j.cemconcomp.2013.03.003

Bentz, D. P., & Jensen, O. M. (2004). Mitigation strategies for autogenous shrinkage cracking. *Cement and Concrete Composites*, *26*(6), 677–685. doi:10.1016/S0958-9465(03)00045-3

Bogue, R. H. (1947). *The chemistry of portland cement* (p. 572). New York: Reinhold.

Bremner, T. W., & Holm, T. A. (1986). Elastic Compatibility and the Behavior of Concrete. *ACI Journal*, *83*(2), 244–250.

Burgreen, D. (1971). *Elements of thermal stress analysis*. London: Arcturus Publishing.

Chancey, R. T., Stutzman, P., Juenger, M. C. G., & Fowler, D. W. (2010). Comprehensive phase characterization of crystalline and amorphous phases of a Class F fly ash. *Cement and Concrete Research*, *40*(1), 146–156. doi:10.1016/j.cemconres.2009.08.029

Chen, H., Yen, T., & Chen, K. (2003). Evaluating Elastic Modulus of Lightweight Aggregate. *ACI Materials Journal*, *100*(2), 108–113.

Chengju, G. (1989). Maturity of concrete: method for predicting early- stage strength. *ACI Materials Journal*, 341–353.

Corral, R., Arredondo, S., Almaral, J., & Gómez, J. (2013). Corrosión por cloruros del acero de refuerzo embebido en concreto con agregado grueso reciclado y materiales cementantes suplementarios. *Revista Ingeniería de Construcción*, *28*(1), 21–35. doi:10.4067/SO718-50732013000100002

Deschutter, G. (2004). Applicability of degree of hydration concept and maturity method for thermo-visco-elastic behaviour of early age concrete. *Cement and Concrete Composites*, *26*(5), 437–443. doi:10.1016/s0958-9465(03)00067-2

Erdem, S., Dawson, A. R., & Thom, N. H. (2012). Influence of the micro- and nanoscale local mechanical properties of the interfacial transition zone on impact behavior of concrete made with different aggregates. *Cement and Concrete Research*, *42*(2), 447–458. doi:10.1016/j.cemconres.2011.11.015

Escadeillas, G., Aubert, J.-E., Segerer, M., & Prince, W. (2007). Some factors affecting delayed ettringite formation in heat-cured mortars. *Cement and Concrete Research*, *37*(10), 1445–1452. doi:10.1016/j.cemconres.2007.07.004

Gallucci, E., Zhang, X., & Scrivener, K. L. (2013). Effect of temperature on the microstructure of calcium silicate hydrate (C-S-H). *Cement and Concrete Research*, *53*, 185–195. doi:10.1016/j.cemconres.2013.06.008

Gowripalan, N., Sirivivatnanon, V., & Lim, C. C. (2000). Chloride diffusivity of concrete cracked in flexure. *Cement and Concrete Research*, *30*(5), 725–730. doi:10.1016/S0008-8846(00)00216-7

Hirsch, T. J. (1962). Modulus of Elasticity of Concrete Affected by Elastic Moduli of Cement Paste Matrix and Aggregate. *ACI Journal*, *59*(3), 427–452.

Holt, E. (2005). Contribution of mixture design to chemical and autogenous shrinkage of concrete at early ages. *Cement and Concrete Research*, *35*(3), 464–472. doi:10.1016/j.cemconres.2004.05.009

Jakobsen, U. H., & Brown, D. R. (2006). Reproducibility of w/c ratio determination from fluorescent impregnated thin sections. *Cement and Concrete Research*, *36*(8), 1567–1573. doi:10.1016/j.cemconres.2006.05.003

Jensen, O. M., & Hansen, P. F. (2001). Autogenous deformation and RH-change in perspective. *Cement and Concrete Research*, *31*(12), 1859–1865.

Konin, A., François, R., & Arliguie, G. (1998). Penetration of chlorides in relation to the microcracking state into reinforced ordinary and high strength concrete. *Materials and Structures*, *31*(5), 310–316.

Lee, K. M., & Park, J. H. (2008). A numerical model for elastic modulus of concrete considering interfacial transition zone. *Cement and Concrete Research*, *38*(3), 396–402. doi:10.1016/j.cemconres.2007.09.019

Lee, Y., Choi, M.-S., Yi, S.-T., & Kim, J.-K. (2009). Experimental study on the convective heat transfer coefficient of early-age concrete. *Cement and Concrete Composites*, *31*(1), 60–71. doi:10.1016/j.cemconcomp.2008.09.009

Lim, C. ., Gowripalan, N., & Sirivivatnanon, V. (2000). Microcracking and chloride permeability of concrete under uniaxial compression. *Cement and Concrete Composites*, *22*(5), 353–360. doi:10.1016/S0958-9465(00)00029-9

Litorowicz, A. (2006). Identification and quantification of cracks in concrete by optical fluorescent microscopy. *Cement and Concrete Research*, *36*(8), 1508–1515. doi:10.1016/j.cemconres.2006.05.011

Maruyama, I., & Teramoto, a. (2012). Effect of water-retaining lightweight aggregate on the reduction of thermal expansion coefficient in mortar subject to temperature histories. *Cement and Concrete Composites*, *34*(10), 1124–1129. doi:10.1016/j.cemconcomp.2012.08.003

Mehta, P. K. (1997). Durability - Critical Issues for the Future. *Concrete International*, *19*(7), 69–76.

Mehta, P., & Monteiro, P. (2005). *Concrete: Microstructure, Properties, and Materials* (3rd ed.). New York: McGraw-Hill Professional.

Moreno, D., Martinez, P., & Lopez, M. (2014). Practical Approach for Assessing Lightweight Aggregate Potential for Concrete Performance. *ACI Materials Journal*, *111*(2), 123–132.

Moreno, D., Zunino, F., Paul, Á., & Lopez, M. (2014). High strength lightweight concrete (HSLC): Challenges when moving from the laboratory to the field. *Construction and Building Materials*, *56*, 44–52. doi:10.1016/j.conbuildmat.2014.01.068

Morris, W., Moreno, E. I., & Sagüés, A. A. (1996). Practical Evaluation of resistivity of concrete in test cylinders using a Wenner array probe. *Cement and Concrete Research*, *26*(12), 1779–1787.

Neville, A. (1995). *Properties of Concrete* (4th Editio., pp. 318–328). Essex: Pearson Education Limited.

Nilsen, A. U., & Monteiro, P. J. M. (1993). Concrete : A three phase material. *Cement and Concrete Research*, *23*, 147–151.

Nilsen, A. U., Monteiro, P. J. M., & Gjcrv, O. E. (1995). Estimation of the elastic moduli of lightweight aggregate. *Cement and Concrete Research*, *25*(2), 276–280.

Noumowe, A. N., Siddique, R., & Debicki, G. (2009). Permeability of high-performance concrete subjected to elevated temperature (600°C). *Construction and Building Materials*, *23*(5), 1855–1861. doi:10.1016/j.conbuildmat.2008.09.023

Pichler, C., Lackner, R., & Mang, H. a. (2007). A multiscale micromechanics model for the autogenous-shrinkage deformation of early-age cement-based materials. *Engineering Fracture Mechanics*, *74*(1-2), 34–58. doi:10.1016/j.engfracmech.2006.01.034

Poole, J. L., Asce, M., Riding, K. A., Juenger, M. C. G., Folliard, K. J., & Schindler, A. K. (2011). Effect of Chemical Admixtures on Apparent Activation Energy of Cementitious Systems. *ASCE Journal of Materials in Civil Engineering*, *23*(12), 1654–1661. doi:10.1061/(ASCE)MT.1943-5533.0000345.

Pourasee, A., Peled, A., Weiss, J., & Asce, M. (2011). Fluid Transport in Cracked Fabric-Reinforced- Cement-Based Composites. *ASCE Journal of Materials in Civil Engineering*, (August), 1227–1238. doi:10.1061/(ASCE)MT.1943-5533.0000289.

Qian, C., & Gao, G. (2012). Reduction of interior temperature of mass concrete using suspension of phase change materials as cooling fluid. *Construction and Building Materials*, *26*(1), 527–531. doi:10.1016/j.conbuildmat.2011.06.053

Riding, K. A., Poole, J. L., Schindler, A. K., Juenger, M. C. G., & Folliard, K. J. (2009). Simplified Concrete Resistivity and Rapid Chloride Permeability Test Method, (105), 1–5.

Samaha, H. R., & Hover, K. C. (1992). Influence of microcracking on the mass transport properties of concrete. *ACI Materials Journal*, *89*(4), 416–424.

Saraswathy, V., & Song, H.-W. (2007). Corrosion performance of rice husk ash blended concrete. *Construction and Building Materials*, *21*(8), 1779–1784.

Saul, A. G. A. (1951). Principles underlying the steam curing of concrete at atmospheric pressure. *Magazine of Concrete Research*, *2*(6), 127–140.

Schindler, A. K. (2004). Effect of Temperature on Hydration of Cementitious Materials. *ACI Materials Journal*, *101*(1), 72–81.

Scrivener, K., Crumbie, A., & Laugesen, P. (2004). The Interfacial Transition Zone (ITZ) Between Cement Paste and Aggregate. *Interface Science*, *12*(4), 411–421.

Selsing, J. (1961). Internal Stresses in Ceramics. *Journal of the American Ceramic Society*, *44*, 419.

Soroushian, P., & Elzafraney, M. (2005). Morphological operations, planar mathematical formulations, and stereological interpretations for automated image analysis of concrete microstructure. *Cement and Concrete Composites*, *27*(7-8), 823–833. doi:10.1016/j.cemconcomp.2004.07.008

Soroushian, P., Elzafraney, M., & Nossoni, A. (2003). Specimen preparation and image processing and analysis techniques for automated quantification of concrete microcracks and voids. *Cement and Concrete Research*, *33*(12), 1949–1962. doi:10.1016/S0008-8846(03)00219-9

Spragg, R. P., Castro, J., Nantung, T., Paredes, M., & Weiss, J. (2012). Variability Analysis of the Bulk Resistivity Measured Using Concrete Cylinders. *Advances in Civil Engineering Materials*, *1*(1), 1–17. doi:10.1520/ACEM104596.

Tank, R. C., & Carino, N. J. (1991). Rate Constant Functions for Strength Development of Concrete. *ACI Materials Journal*, *88*(1), 74–83.

Taylor, H. F. ., Famy, C., & Scrivener, K. . (2001). Delayed ettringite formation. *Cement and Concrete Research*, *31*(5), 683–693. doi:10.1016/S0008-8846(01)00466-5

Trtik, P., & Bartos, P. J. M. (1999). Micromechanical properties of cementitious composites. *Materials and Structures*, *32*, 388–393.

Wang, K., Jansen, D. C., Shah, S. P., & Karr, A. F. (1997). Permeability study of cracked concrete. *Cement and Concrete Research*, *27*(3), 381–393.

Xiao, J., Li, W., Sun, Z., Lange, D. a., & Shah, S. P. (2013). Properties of interfacial transition zones in recycled aggregate concrete tested by nanoindentation. *Cement and Concrete Composites*, *37*, 276–292. doi:10.1016/j.cemconcomp.2013.01.006

Yang, Z., Weiss, W. J., & Olek, J. (2006). Water Transport in Concrete Damaged by Tensile Loading and Freeze – Thaw Cycling. *ASCE Journal of Materials in Civil Engineering*, (June), 424–434.

Yi, S.-T., Moon, Y.-H., & Kim, J.-K. (2005). Long-term strength prediction of concrete with curing temperature. *Cement and Concrete Research*, *35*(10), 1961–1969. doi:10.1016/j.cemconres.2005.06.010

Zhang, M. ., Tam, C. ., & Leow, M. . (2003). Effect of water-to-cementitious materials ratio and silica fume on the autogenous shrinkage of concrete. *Cement and Concrete Research*, *33*(10), 1687–1694. doi:10.1016/S0008-8846(03)00149-2

Zhang, Z., Olek, J., & Diamond, S. (2002). Studies on delayed ettringite formation in early-age , heat-cured mortars I . Expansion measurements , changes in dynamic modulus of elasticity , and weight gains. *Cement and Concrete Research*, *32*(11), 1729–1736.

Zhou, C., Huang, B., Ph, D., Asce, M., Shu, X., & Asce, A. M. (2013). Micromechanical Model for Predicting Coefficient of Thermal Expansion of Concrete. *Journal of Materials in Civil Engineering*, *25*(September), 1171–1180. doi:10.1061/(ASCE)MT.1943-5533.0000663.

Zhu, W., & Bartos, P. J. . (2000). Application of depth-sensing microindentation testing to study of interfacial transition zone in reinforced concrete. *Cement and Concrete Research*, *30*(8), 1299–1304. doi:10.1016/S0008-8846(00)00322-7

5 DECOUPLING THE PHYSICAL AND CHEMICAL EFFECTS OF SUPPLEMENTARY CEMENTITIOUS MATERIALS ON STRENGTH AND PERMEABILITY: A MULTI-SCALE APPROACH

Franco Zunino and Mauricio Lopez

ABSTRACT

Supplementary cementitious materials (SCMs) represent an alternative for the industry sustainability by reducing cement contents without significant compromises of mechanical properties and enhancing durability. The SCMs play a dual role during hydration: a physical effect promoting nucleation and cement hydration and a chemical effect through pozzolanic activity. Rice husk ash (RHA) and natural pozzolans (NP) were evaluated in compressive strength and durability tests on a multi-scale experimental program.. RHA contributed more importantly to strength than NP which is well explained by its prominent chemical effect (78%) assessed by isothermal calorimetry and produced by it high amorphous silica content. Both RHA and NP produced significant reductions in concrete's permeability, which is mostly explained by the chemical effect. Decoupling physical and chemical effect of a SCM allows for optimization of its manufacturing process.

Keywords: sustainability, supplementary cementitious materials, rice husk ash, natural pozzolans, isothermal calorimetry, durability.

5.1 Introduction

Cement industry has faced new environmentally related challenges in the last decades, such as energy consumption and CO_2 emission reductions (Schneider et al., 2011). Developments in these topics has derived in the exploration and use of supplementary cementitious materials (SCMs) to reduce cement content in concrete mixes (Espinoza-Hijazin, Paul, & Lopez, 2012; Jain, 2012; Karim, El-Hadj, Abdelkader, & Rachid, 2010; Lara et al., 2011; Lothenbach et al., 2011), and seek for enhanced durability of the material in order to increase service life of concrete structures (Corral et al., 2013; Mehta, 1997).

Rice husk ash (RHA) is obtained from agricultural wastes, and has been widely investigated (Mehta, 1977; Yu et al., 1999; M. H. Zhang, Lastra, & Malhotra, 1996). World rice production rose to around 722 billion tones in 2011 (Food and Agriculture Organization of the U.N., 2011). The main uses of rice husks are as fuel for the paddy milling process (Rodríguez de Sensale, 2006) and electricity power plants (Chungsangunsit et al., 2005). Effects of rice husk ash on concrete strength ((Givi, Rashid, Aziz, & Salleh, 2010; Khan, Mohan, & Taylor, 1985a; Mehta, 1977; Rodríguez de Sensale, 2006; Zain, Islam, Mahmud, & Jamil, 2011; M. H. Zhang et al., 1996)) and durability ((A L G Gastaldini et al., 2007; A.L.G. Gastaldini, Isaia, Saciloto, Missau, & Hoppe, 2010; Givi et al., 2010; Saraswathy & Song, 2007; Sensale, 2010)) is well documented in the literature. RHA reactivity depends mainly on the particle size distribution ((Cordeiro, Toledo Filho, Tavares, Fairbairn, & Hempel, 2011; Givi et al., 2010; Zain et al., 2011)) and the burning temperature and time of the husks (Della, Kühn, & Hotza, 2002; Nair et al., 2008; Zain et al., 2011).

Natural pozzolans (NP) from volcanic origin had been used in chilean blended cements since the 1960's decade. While chemical and physical properties vary depending on the pozzolan source, performance in compressive strength and durability has been studied in different places where this material is available (Bondar, Lynsdale, Milestone, Hassani,

& Ramezanianpour, 2011; Celik, Meral, Mancio, Mehta, & Monteiro, 2013; Kaid et al., 2009; Pourkhorshidi, Najimi, Parhizkar, Jafarpour, & Hillemeier, 2010).

The effects of SCMs can be analyzed as two non-divisible contributions, occurring simultaneously, in a cementitious system:

1. *Chemical contribution*, referred as pozzolanic effect, which relates to the formation of hydration products from the portlandite (CH) produced during cement hydration and the amorphous silica phases present in the supplementary cementitious material (Lothenbach et al., 2011; Mehta & Monteiro, 2005). Rate of reaction depends on particle size (finer materials have more specific surface to react) and amorphous silica, water and CH availability.
2. *Physical contribution*, referred as filler effect, related to changes in particle spacing and surface availability for hydration products nucleation (Lawrence et al., 2003; Lothenbach et al., 2011).

As stated in the literature (Lawrence et al., 2003; Lothenbach et al., 2011), filler effect can be decomposed as a dual opposing physical interaction of the inert material with the cementitious matrix (Cyr et al., 2005). First, the dilution effect, which is equivalent to an increase in the water-to-cement (w/c). Since the filler does not produce hydrates, at the same water-to-solids ratio w/c increases generating more space between solid particles for hydration product formation. The second effect, related to the additional surface added by fine inert material particles, which acts as nucleation sites for hydration products (Lothenbach et al., 2011), referred as heterogeneous nucleation effect.

While several studies have characterized natural pozzolan and rice husk ash effects on compressive strength and permeability of concrete separately ((Bondar et al., 2011; Cordeiro et al., 2011; Feng, Yamamichi, Shoya, & Sugita, 2004; A L G Gastaldini et al., 2007; A.L.G. Gastaldini et al., 2010; Kaid et al., 2009; Mehta, 1977; Pourkhorshidi et al., 2010; Rao, M Subba. James, 1986; Saraswathy & Song, 2007; Sensale, 2010; Zain et al., 2011)), there is lack of investigations considering and comparing both materials

under the same testing conditions. In addition, physical and chemical effects are commonly not distinguished and the results are reported as overall performance of the corresponding supplementary cementitious material. Since particle size distribution affects chemical reactivity and physical interaction of the addition material, so a deep characterization of its performance requires assessing both contributions separately.

This paper assesses RHA and NP performance with an accent in chemical and physical interactions. In addition, a multi-scale (cement paste, mortar and concrete) approach and testing program is presented.

5.2 Materials and Methods

In order to assess the physical (filler) and chemical (pozzolanic) effects of SCMs accurately, two kinds of materials were used in this study. First, chemically inert filler was intended to be a reference of the physical interaction of the particles on cement hydration and its influence on the measured properties considered. Secondly, SCMs, containing amorphous silica phases, were evaluated and compared under the same experimental program. Since these materials exhibit both behaviors simultaneously (filler and pozzolanic), inert filler is used to assess the chemical contribution of the SCMs by allowing an estimate of the physical component by itself.

5.2.1 Material manufacture and characterization

Type I ordinary Portland cement (OPC) conforming to ASTM C150 was used in all tests conducted in this study.

Rice hush ask (RHA) was manufactured from 24 Kg of locally obtained rice husks. Husks were burnt under controlled conditions in two steps: first, in an industrial furnace at 600ºC for 4 hours in batches of approximately 6 Kg. Second, the ash produced was re-burnt at 700ºC for 3 hours in batches of approximately 50 g in small crucibles using a

laboratory furnace. The procedure was based on previous research that showed that optimal silica production was achieved heating rice husks at 700ºC for 6 hours (Della et al., 2002) and allowed achieving uniformity in the combustion process and remove any remaining organic matter.

Natural pozzolan (NP) from volcanic origin was obtained from a local blended cement manufacturer. This variety of pozzolans has been used in chilean cements as SCMs for decades, and were considered in this study as a comparative performance reference of a widely used SCM in local concrete industry.

Inert filler was obtained by crushing in a jar mill graded siliceous sand conforming to ASTM C778, using steel balls as grinding media. This sand was selected instead of commercial concrete filler due to its high quartz content and therefore its non-pozzolanic nature (Lawrence et al., 2003; Lothenbach et al., 2011). Two particle sizes distribution were obtained: coarse filler by grinding sand for 3 days in the jar mill (FILL3), and fine filler by reprocessing the coarse filler in a smaller jar mill for one week (FILL7). This was done to have comparative particle size distribution (PSD) boundaries for all the SCM's considered in this study, in order to compare physical and chemical interactions.

RHA and NP were ground prior to use in a jar mill for 1 hour to achieve a uniform particle size distribution. Chemical composition of OPC, RHA and NP was measured using XRF and is presented as oxides on Table 5-1. High amounts of SiO_2 were identified in both SCMs, but it is especially high on RHA. In addition, PSD was measured in all the materials used.

Table 5-1: Chemical composition of OPC, NP and RHA.

Composition as oxides (%)	OPC	RHA	NP
SiO_2	11.3	84.20	66.97
Al_2O_3	3.29	0.56	13.51
Fe_2O_3	3.33	1.13	1.82
CaO	73.9	1.38	3.33
Na_2O	0.48	0.38	3.87
K_2O	0.36	4.30	3.32
MnO	0.18	0.62	0.08
TiO_2	0.31	0.04	0.24
MgO	<0.01	0.56	0.65
P_2O_5	0.10	0.99	0.14
LOI	2.68	5.05	6.06
Specific gravity	3.184	2.158	2.432

Thermogravimetric analysis (TGA/DTG) of the materials was conducted under a 50 mL/min nitrogen flux up to 1000ºC. DTG results are presented in Figure 5-1, were no significant decomposition is observed on the inter filler, which is consistent with a mainly quartz composition and suggest high chemical stability. The weight loss of RHA around 100ºC is attributed to humidity water loss. A clear decarbonation peak is shown on the OPC plot slightly above 700ºC.

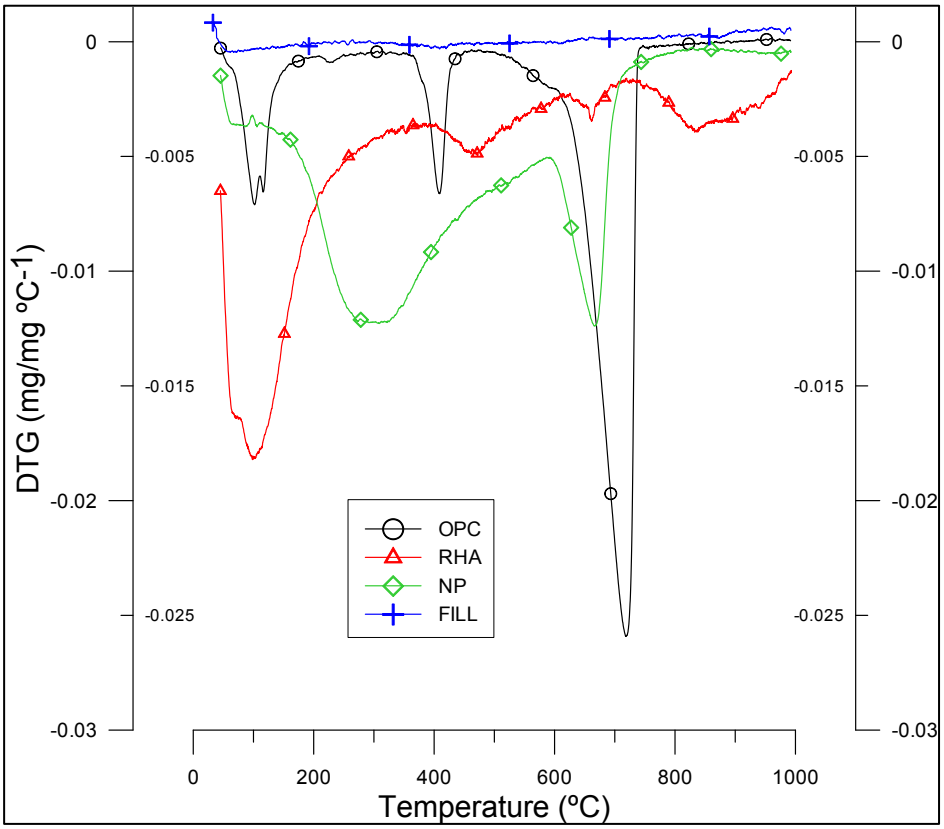

Figure 5-1: Differential thermogravimetric (DTG) curves of OPC, NP, RHA and inert filler (FILL).

5.2.2 X-Ray Diffraction

Quantitative X-Ray diffraction (QXRD) analysis was performed to determinate the mineral composition of RHA and NP. Test was carried out between 10-75º 2θ at 0.02º per second sampling rate. Commercially available software (EVA and TOPAS) was employed for phase identification and Rietveld refinement, respectively. Fluorite was selected as internal standard to account or the amorphous fraction and correct Rietveld results, based on the procedure proposed by Chancey et al. (Chancey et al., 2010).

5.2.3 Isothermal calorimetry

Isothermal calorimetry is a widely used technique to characterize hydration y blended cement systems (Pane & Hansen, 2005; Xu, Hu, Ruiz, Wang, & Ge, 2010). In this particular study, tests were conducted using a TAM Air Isothermal Calorimeter to assess the impact of the different SCMs and inert filler in the hydration kinetics. . Cement pastes with water-to-cementitious materials ratio by weight (W/CM) of 0.5 in all cases. Replacement levels of 20% by weight of OPC by RHA, NP, FILL3 and FILL7 were used. Tests were carried out at 23ºC for 7 days. Each mixture was measured in duplicate samples.

5.2.4 Compressive strength

The impact of the different SCMs was also measured from the mechanical point of view by means of compressive strength. Such assessment was performed at two different scales: cement paste and mortars. Cement pastes were used to evaluate the effects of a broad range of OPC-by-SCMs replacement levels in pure cementitious matrix environment, while mortar mixtures were used for assessing the interaction between the SCM matrix and aggregates.

5.2.4.1 Cement paste

Paste mixtures were made using 0-10-20-30-50-75% OPC-by-SCM replacement levels by weight, considering substitutions of the four materials under study (RHA, NP, FILL3 and FILL7). Cubic specimens of 2 cm were used, at constant W/CM ratio of 0.5 in all cases. Specimens were removed from molds after one day of curing and stored in sealed bags in a 20±3ºC and 95% RH chamber until time of testing. Compressive strength tests were conducted at 7, 28 and 90 days, with a constant 1800 N/s load rate in all cases.

In order to compare the observed SCM effects on strength with porosity variations of the cement matrix, 100% OPC pastes were tested in the same conditions with W/CM ratios of 0.4, 0.45, 0.5, 0.55 and 0.6. This allows expressing SCM's positive/negative impacts on compressive strength as equivalent quantities of cement addition/subtraction, or equivalently, as a variation of W/CM ratio.

5.2.4.2 Mortar

Mortar mixtures were made with 0-10-20-30% OPC-by-SCM replacement levels by weight. RHA and NP were used in the whole experimental spectra, while FILL3 substitution was made at the central level of replacement (20%) only to have an estimate of filler effect on compressive strength at this scale. Cubic specimens of 5 cm were made, using constant W/CM ratio of 0.5 in all cases. Also, some adjustment were made to keep cementitious paste (OPC + SCM + mixing water) volume constant in all mixtures, and therefore, the paste-to-aggregate ratio constant. Standard graded sand conforming to ASTM C778 was used in all mortar mixtures. Specimens were removed from molds after one day of curing and stored submerged in tap water inside a 20±3ºC and 95% RH chamber until time of testing. Compressive strength tests were conducted at 3, 7, 28 and 90 days, with a constant 1800 N/s load rate in all cases. Mixture designs of mortar series are detailed in Table 5-2.

Table 5-2: Mixture proportions of mortar specimens.

Level (%)	SCM ID	W/CM	OPC (Kg/m^3)	Mixing Water (Kg/m^3)	SCM (Kg/m^3)	Std. Sand (Kg/m^3)
0	0	0.5	504.1	252.0	0	1562.6
10	RHA	0.5	445.5	247.5	49.5	1562.6
	NP	0.5	448.3	249.1	49.8	1562.6
20	RHA	0.5	389.0	243.1	97.2	1562.6
	NP	0.5	393.8	246.2	98.5	1562.6

	FILL3	0.5	397.2	248.3	99.3	1562.6
30	RHA	0.5	334.4	238.9	143.3	1562.6
	NP	0.5	340.7	243.3	146.0	1562.6

5.2.5 Durability

The effect of the different SCMs was measured from a durability perspective on concrete specimens. For this purposes, 0-10-20-30% OPC-by-SCM replacement levels by weight were considered for RHA and NP. As in mortar series, FILL3 was used in the central level of replacement. Similarly to the mortars, some adjustment were made to keep cementitious paste (OPC + SCM + mixing water) volume constant in all mixtures, and therefore, the paste-to-aggregate ratio constant. . Four 10-by-20 cm cylinder specimens were made at each substitution level, at constant 0.5 W/CM ratio. A commercial superplasticizer admixture was used in a 0.8% of cementitious materials by weight dosage to improve workability. Specimens were kept in molds until one day of age, after which were cured submerged in tap water in a 20±3ºC and 95% RH chamber until 90 days age, when all durability tests were performed. Mixture proportions can be found on Table 5-3.

Table 5-3: Mixture proportions of concrete specimens for durability testing.

Level (%)	SCM ID	W/ CM	OPC (Kg/m^3)	Mixing Water (Kg/m^3)	SCM (Kg/m^3)	Fine Sand (Kg/m^3)	Coarse Sand (Kg/m^3)	Coarse Agg. (Kg/m^3)
0	-	0.5	350.0	175.0	0	185.0	647.0	1036.1
10	RHA	0.5	309.4	171.9	34.4	185.0	647.0	1036.1
	NP	0.5	311.3	173.0	34.6	185.0	647.0	1036.1
20	RHA	0.5	270.1	168-8	67.5	185.0	647.0	1036.1
	NP	0.5	273.5	170.9	68.4	185.0	647.0	1036.1
	FILL3	0.5	275.8	172.4	68.9	185.0	647.0	1036.1

30	RHA	0.5	232.2	165.9	99.5	185.0	647.0	1036.1
	NP	0.5	236.6	169.0	101.4	185.0	647.0	1036.1

5.2.5.1 Chloride ion penetration

Electrical chloride ion penetration test were performed according to ASTM C1202 standard. Two 51 mm thick slices coming from two different concrete cylinders were tested for each of the concrete mixtures.

5.2.5.2 Electrical resistivity

Electrical resistivity was measured in two 10 by 20 cm cylinder specimens for each mixture based on the axial-measurement method described by Spragg et al. (Spragg et al., 2012), to compare changes in concrete pore percolation due to filler and pozzolanic effects of SCMs. In this method, two stainless steel plates are placed at the ends of the 10-by-20 cm cylinder and connected to the same surface resistivity meter used in the Wenner probe apparatus (Morris et al., 1996). Electrical resistance values obtained are normalized by the cross sectional area to length ratio of the cylinder to calculate bulk resistivity of the specimen. Specimens were stored submerged in water during all curing period and tested in saturated condition.

This method was selected due to its complete non-destructive character, as well as its simplicity and ability to produce inmediate results and consistently throughout subsequent measurements. In addition, Spragg et al. showed that there is a linear correlation between measurements using this method and values obtained using the standard Wenner probe method (Spragg et al., 2012).

5.3 Results and Discussion

5.3.1 Particle Size Distribution (PSD)

Results of PSD analysis are presented in Figure 5-2.

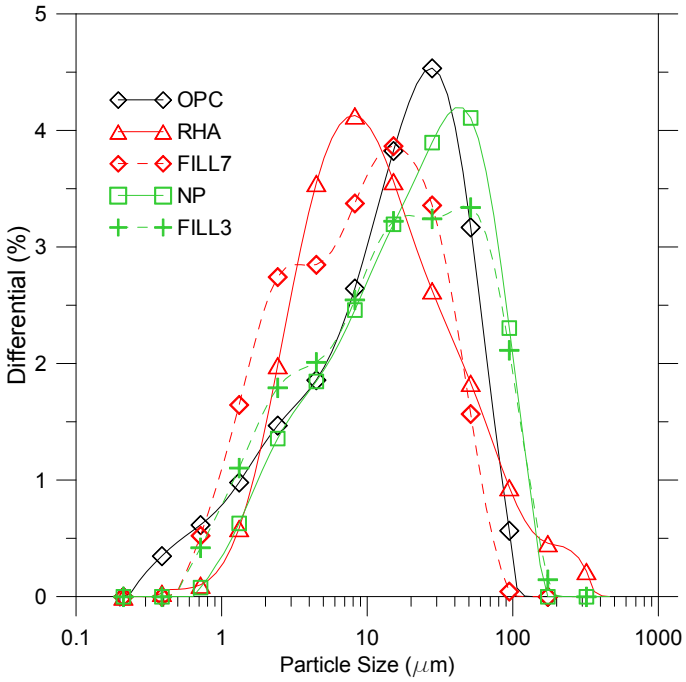

Figure 5-2: Particle size distributions of RHA, NP, OPC, coarse and fine inert fillers (FILL3 and FILL7 respectively).

As seen in the figure, FILL3 has a similar PSD to NP while FILL7 is closer to RHA. Both inert fillers represent good approximations to the SCMs physical characteristics from a particle size perspective. FILL3 and FILL7 are good boundaries to RHA from a PSD perspective, allowing a more accurate measurement of chemical contribution of this SCM. All the materials exhibit PSD in the range of the particles of OPC, allowing comparison of these materials in similar conditions of exposed surface to react.

5.3.2 X-Ray Diffraction

Diffraction patterns are presented in Figure 5-3 and Table 5-4, respectively. They include main peaks and crystalline phase composition, along with amorphous material content.

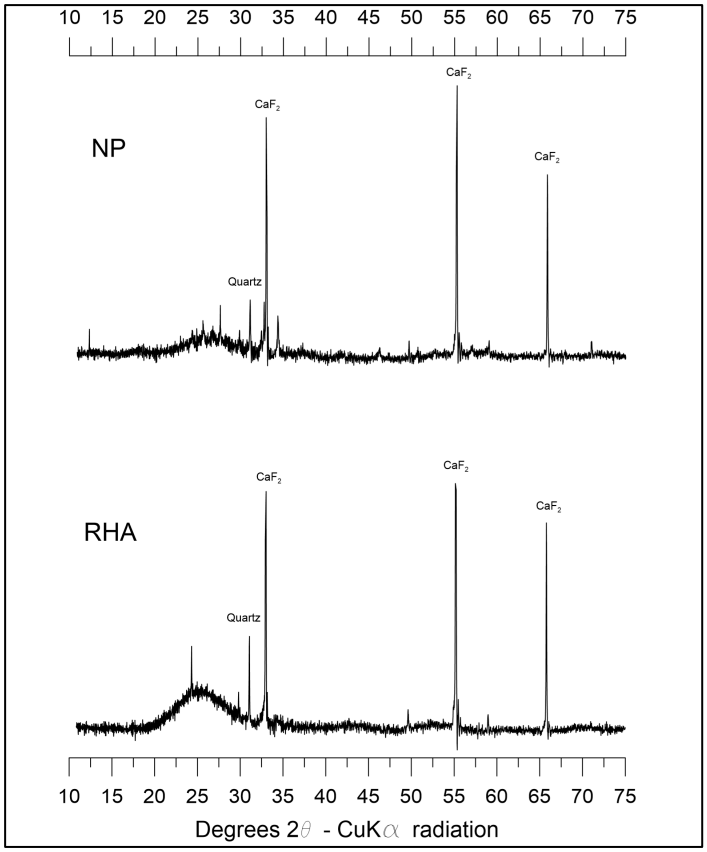

Figure 5-3: X-Ray diffraction pattern of RHA and NP used for Rietveld refinement.

Table 5-4: QXRD analysis of RHA and NP, including computed amorphous content based on internal standard correction procedure.

Mineral Name	NP (% by wt.)	RHA (% by wt.)
Quartz	1.2	1.5
Albite	1.3	0.4

Oligoclase	1.7	0.6
Sanidine	0.4	1.4
Fluorite (I.S.)	11.9	11.7
Andesine	0.9	0.4
Anhydrite	0.1	0.3
Actinolite	0.3	0.0
Calcite	2.4	3.1
Beta C_2S	0.0	0.6
Amorphous	80.0	79.9

I.S. = Internal Standard

Rietveld refinement results were achieved with a goodness of fit (GOF) indicator of 1.2 and a Rexp of 3.0, which shows good agreement between experimental data and Rietveld computed pattern and good data quality, respectively.

Both RHA and NP show an important amount of amorphous phases around 80% and a relatively low amount of Quartz around 1.5%. When comparing this with the XRF results shown in Table 5-1, it can be concluded that most of the total SiO_2 phases exists as amorphous forms of silica. Therefore RHA, having more amorphous silica, would exhibit a higher chemical activity than NP. Additionally, RHA might exhibit higher activity due to the presence of beta C2S that can be formed during it manufacturing at 700°C and remain at ambient temperature without a stabilizer if beta C_2S crystals are sufficiently small (Taylor, 1997). These two differences suggest that RHA might yield higher mechanical and physical performance than NP when used as SCM in concrete.

5.3.3 Isothermal Calorimetry

The heat flow results show a slight acceleration of the hydration reaction when finer materials are added into the sample, and is attributed to the physical effect of the SCMs

in the hydration of OPC (Cyr et al., 2005; Cyr, Lawrence, & Ringot, 2006). This physical effect can be clearly appreciated in the total heat plots (Figure 5-4a), where even chemically inert materials (FILL3 and FILL7) exhibit a higher heat release in time than OPC.

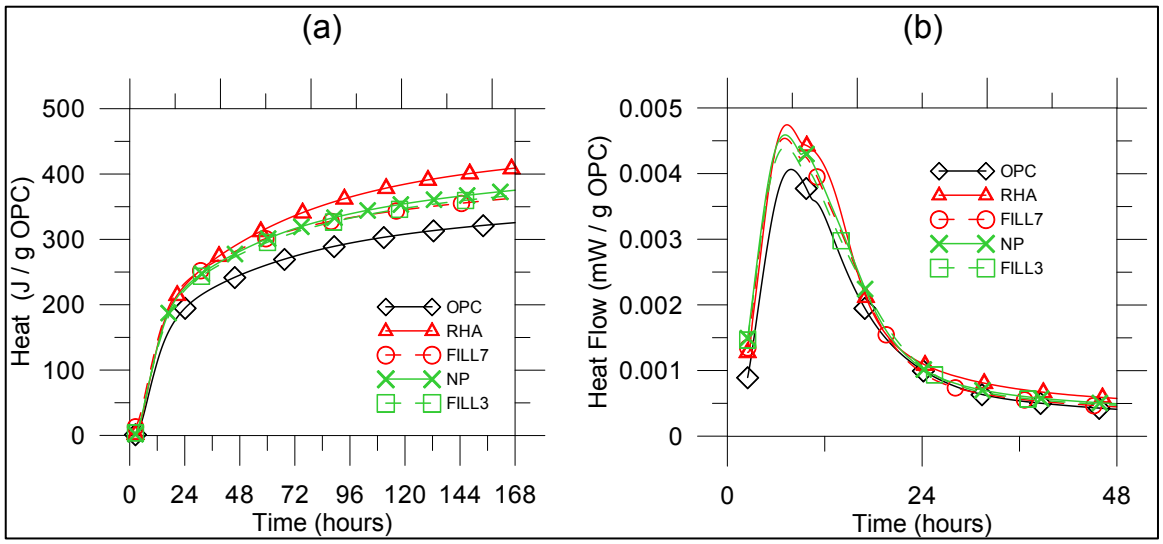

Figure 5-4: Heat flow and total heat of W/CM 0.5 pastes containing 20% of RHA, NP, FILL3 and FILL7.

Chemical interactions can be observed for RHA and NP even at this early stage of hydration, based on the differences with the inert fillers. Since the particle size distribution of FILL7 is similar to RHA and FILL3 is similar to NP (Figure 5-1), the differences in heat released between these pairs are an estimate of the chemical activity of the pozzolanic material. RHA heat evolution (Figure 5-4b) shows clear differences with FILL7, which suggests a significantly higher chemical reactivity of this material at early ages. This can be attributed to the relatively high amorphous silica content. On the contrary, for the NP, chemical reactivity is almost negligible during the first 7 days, since FILL3 and NP het plots are very similar. This can be attributed to the coarser PSD of NP, which can delay pozzolanic reaction.

5.3.4 Compressive Strength

5.3.4.1 Compressive Strength on W/CM 0.5 pastes

Results of compressive strength test of paste specimens are shown on Figure 5-5 a, b and c for 7, 28 and 90 days age, respectively. They are expressed as ratios using W/CM 0.5 100% OPC mixture as reference, which is also represented graphically by a bold horizontal gray line. Porosity variations are represented as horizontal lines and corresponds to the 100% OPC mixes with W/CM variation according to the experimental program. This allows a comparison of the effect of SCM replacement with changes in W/CM in a 100% OPC paste. Therefore, SCM overall reactivity can be expressed as expected performance as a certain OPC added mass.

RHA pastes show a very early strength development compared to the other series ((Figure 5a). That is, it exhibits R_{SCM}/R_{OPC} ratios of 1.25 to 1.50 even at high replacement levels. It can be concluded that these results are the effect of physical and chemical interactions of RHA during hydration, as observed with isothermal calorimetry.

FILL7 and FILL3 series, exhibit very low R_{SCM}/R_{OPC} ratios ranging between 0.10 and 0.80 meaning that the physical interactions are low during the first 7 days. Since FILL7 and FILL3 are boundaries to RHA from a PSD perspective (Figure 5-1), the large differences in the R_{SCM}/R_{OPC} ratios suggest that a considerable pozzolanic reaction going on in the RHA series during the first 7 days.. This is explained by the high amount of amorphous material found in XRD analysis. This agrees with previous findings that RHA can be as reactive as silica fume (Khan, Mohan, & Taylor, 1985b), another SCM with a very high amorphous silica content.

FILL7 shows a higher level of hydration activation than FILL3 paste as expected from the calorimetry results. Since the substitution level is the same in both series with inert filler, the activation observed can be attributed to differences in PSD only; thus, to

hydration enhancement as extra space is available and the filler surface acts as nucleation sites for clinker phases (Lawrence et al., 2003; Lothenbach et al., 2011).

NP results reflect negligible pozzolanic activity during the first 7 days showing R_{SCM}/R_{OPC} ratios below the inert series (FILL7 and FILL3) suggesting a lower acceleration of hydration due to filler effect. This low chemical activity is also appreciated in the total heat release of NP compared to FILL3 and OPC (Figure 5-3b), which can be attributed to the coarser PSD of NP compared to FILL3 and FILL7, as seen in Figure 1, which delayed pozzolanic reaction of the amorphous silica phases.

At 28 days age (Figure 5-5b), the behavior of the RHA series still outperforms that of 100% OPC; however, the ongoing hydration of OPC tends to reduce initial differences. For instance, at 75% replacement level, the specimens exhibit R_{SCM}/R_{OPC} ratio below 1.0 and the maximum R_{SCM}/R_{OPC} ratio decreased form 1.5 at 7 days to 1.25 at 28 days. NP starts to develop pozzolanic activity, which is clear at replacement levels higher than 50%, where this pozzolanic reactivity becomes noticeable when compared to the series exhibiting only physical interactions (FILL3 and FIIL7).

Results at 90 days of age conform the same trend observed between 7 and 28 days. That it the ongoing hydration of OPC keeps reducing the differences in R_{SCM}/R_{OPC} ratios between RHA and 100% OPC even though RHA series still outperforms 100%OPC for replacement levels up to 50% (Figure 5-5c). Also, NP continues to show pozzolanic activity improving its performance compared to the inert series.

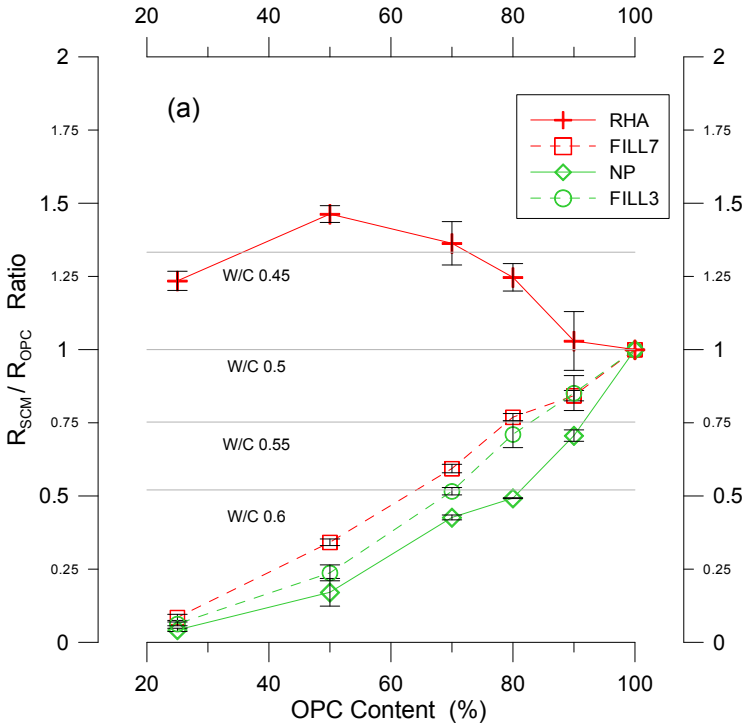
(a)
RHA
FILL7
NP
FILL3
W/C 0.45
W/C 0.5
W/C 0.55
W/C 0.6
R_{SCM} / R_{OPC} Ratio
OPC Content (%)
20
40
60
80
100
0
0.25
0.5
0.75
1
1.25
1.5
1.75
2

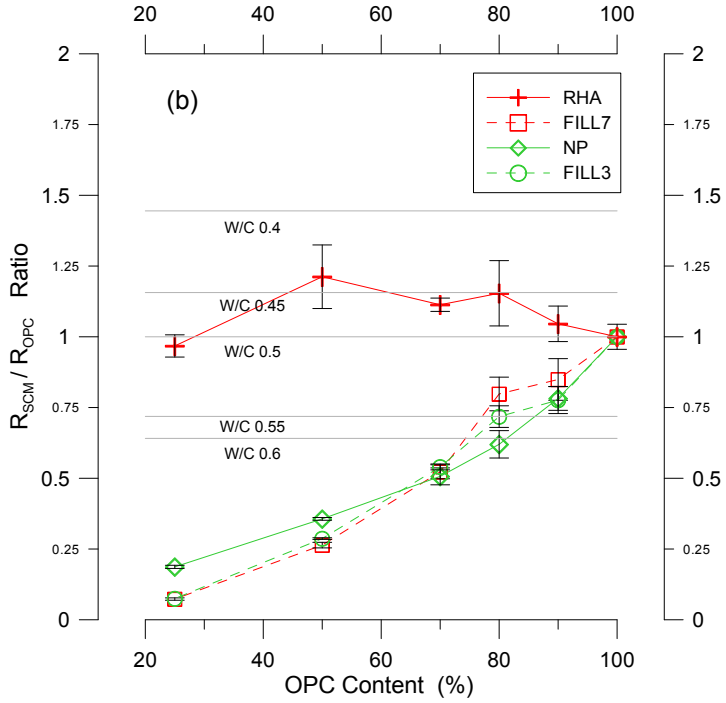
(b)
RHA
FILL7
NP
FILL3
W/C 0.4
W/C 0.45
W/C 0.5
W/C 0.55
W/C 0.6
R_{SCM} / R_{OPC} Ratio
OPC Content (%)
20
40
60
80
100
0
0.25
0.5
0.75
1
1.25
1.5
1.75
2

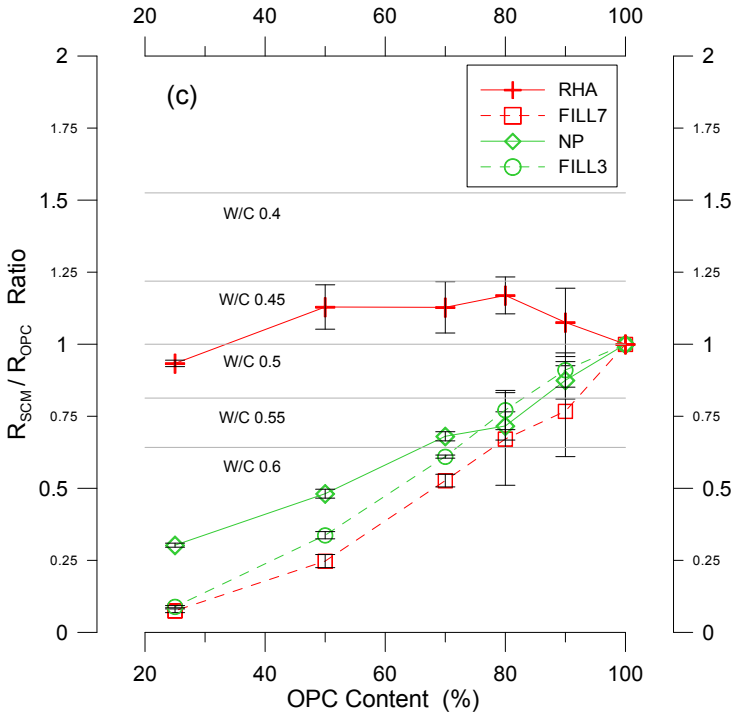

Figure 5-5: Compressive strength ratios (referred to a 100% OPC mixture basis) versus OPC content in mixtures at 7 (a), 28 (b) and 90 (c) days of age.

The sizable differences in R_{SCM}/R_{OPC} ratios between RHA and NP can be explained based on the differences in PSD and amorphous silica content and size as derived from PSD and WRD analyses. The smaller particle size of RHA compared to NP provides a stronger physical effect accelerating hydration, and the higher amorphous silica present in RHA compared to NP explains a larger chemical reactivity.

The strength gain produced by the use of SCMs allows important cement reductions while maintaining or even improving mechanical performance. For instance, additional 13% by mass of cement (at w/c of 0.5) would be needed to obtain the same 7-days compressive strength of the 50% RHA mixture, which is equivalent to a w/c reduction below 0.45 (Figure 5-5a). Similarly, at the same age the incorporation of 20% by mass of NP is equivalent to increasing w/c up to 0.6, thus, 25% of additional OPC should be added to the mixture to reach the same levels of compressive strength than the 100%

OPC mixture. In this matter, RHA is more efficient as OPC replacement if strength is the design parameter.

The chemical and physical contribution of each SCM to compressive strength can be approximated as the difference between the strength obtained by the SCM and the result of the PSD-matching inert filler at the same corresponding age and substitution level. Using this approach, it can be concluded that RHA performance is dominated by its chemical effect at all ages, while NP contributes mainly physically at early-ages and develops pozzolanic activity at later ages (Figure 5-5a to 5-5c).

5.3.4.2 Compressive Strength of Mortar

Compressive strength of mortar shows similar trends than those found in the paste (see R_{SCM}/R_{OPC} ratios in Figure 5-6). That is, the series containing RHA as cement replacement exhibit in general a better performance that those with 100% OPC. The series containing NP exhibit a lower performance than those containing RHA and 100% OPC, but still exhibit improvements with respect to those having inert fillers only. The R_{SCM}/R_{OPC} ratios shown at the mortar level are in general lower than those observed at the paste level. This can be attributed to the presence of the fine aggregate and the interfacial transition zone.

R_{SCM}/R_{OPC} ratio of the RHA mortars reached approximately 1.2 at 28 and 90 days; however, at the age of 3 days the opposite is observed for the three replacement levels (10, 20 and 30%). This low performance can be attributed to a low availability of portlandite from cement hydration present at such early age to properly activate the pozzolanic reaction. Even though during the first few days, the filler effect is predominant (Lothenbach et al., 2011), RHA does show pozzolanic effect as it R_{SCM}/R_{OPC} ratio is higher than that produced by the mixture with the inert filler of

comparable PSD. This fact is also observed in the isothermal calorimetry results (Figures 5-3a and 5-3b).

At later ages (i.e., 28 and 90 days), when more portlandite is available, RHA mixtures exhibited an increment in compressive strength at all levels of substitution reaching R_{SCM}/R_{OPC} ratios of about 1.2, with statistically equivalent results at 90 days for the 3 replacement levels. These results are consistent with the high reactivity observed at the paste level and in agreement with those reported before for RHA mortar (Feng et al., 2004; Mehta, 1977).

Regarding NP mortars, replacement levels of 20 and 30% showed R_{SCM}/R_{OPC} ratios ranging from 0.8 to 1.0 at 28 and 90 days. This low reactivity of NP was also observed in cement pastes in a wider range of replacement levels. As concluded at the paste level, the relatively low performance of NP might be attributed to a low amorphous silica content and coarser PSD.

At 20 % of substitution and 3 days of age, NP mixtures over performed mixtures with inert filler (FILL3) indicating a relevant pozzolanic activity. Nevertheless, at 28 and 90 days, results of NP inert filler mixtures are statistically equivalent indicating that after reaching a certain level of cement hydration the pozzolanic activity of NP is negligible.

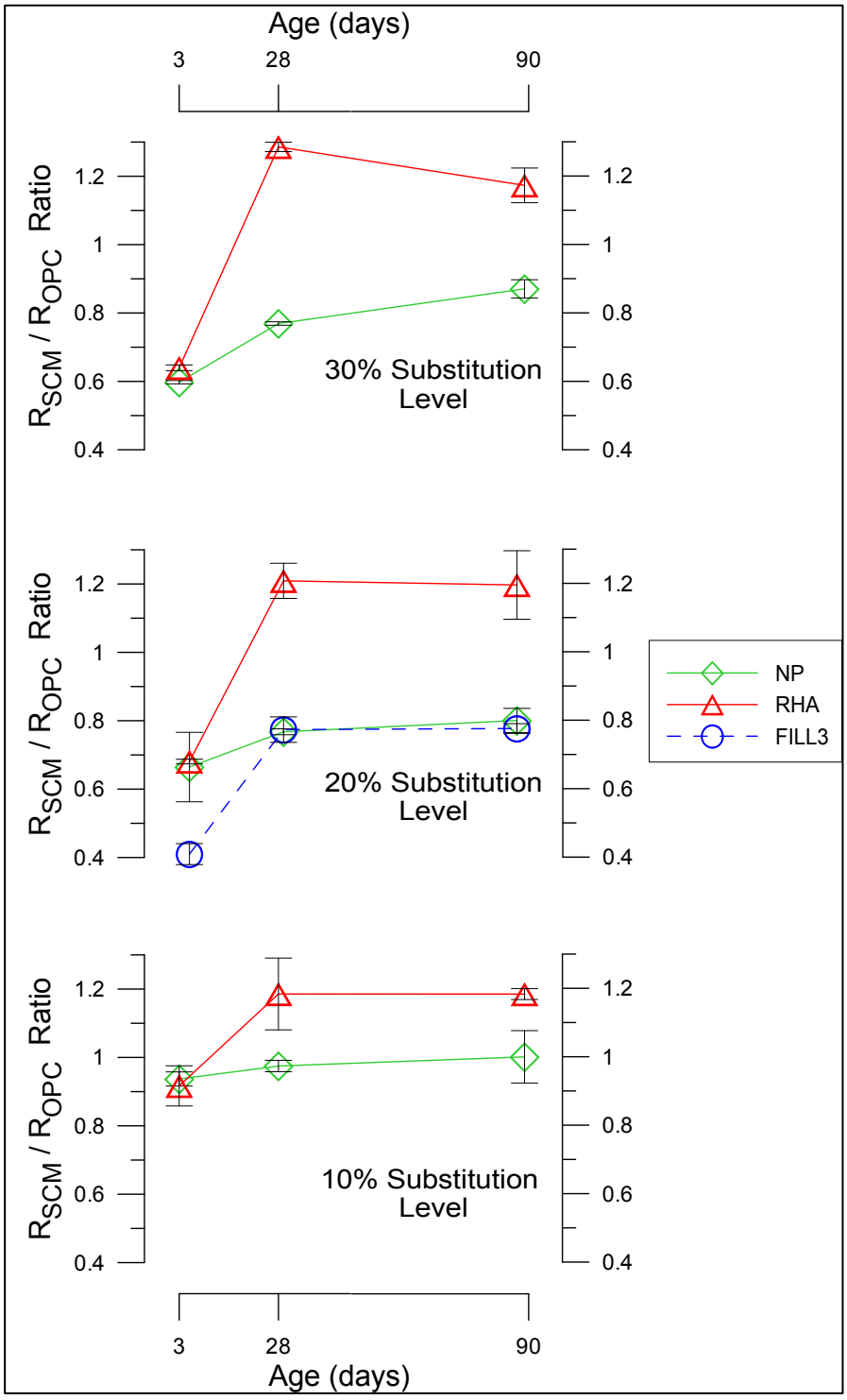

Figure 5-6: Compressive strength ratios of mortar (referred to a 100% OPC mixture basis) mixtures with 10-20-30 percent SCM replacement levels.

5.3.5 Durability

5.3.5.1 Chloride ion

The effect of cement replacement by the SCMs was assessed at the concrete levels using rapid chloride ion penetration test (RCPT) at 90 days of age (Figure 5-7). Results are expressed as ratios of total charge passed on each SCM mixture over the total charge passed on the 100% OPC control mixture (which performance is represented 1.0 ratio value). ASTM C1202 performance classification is also shown. A ration below 1.0 R_{SCM}/R_{OPC} ratio represents, consequently, a better performance compared to the reference mixture.

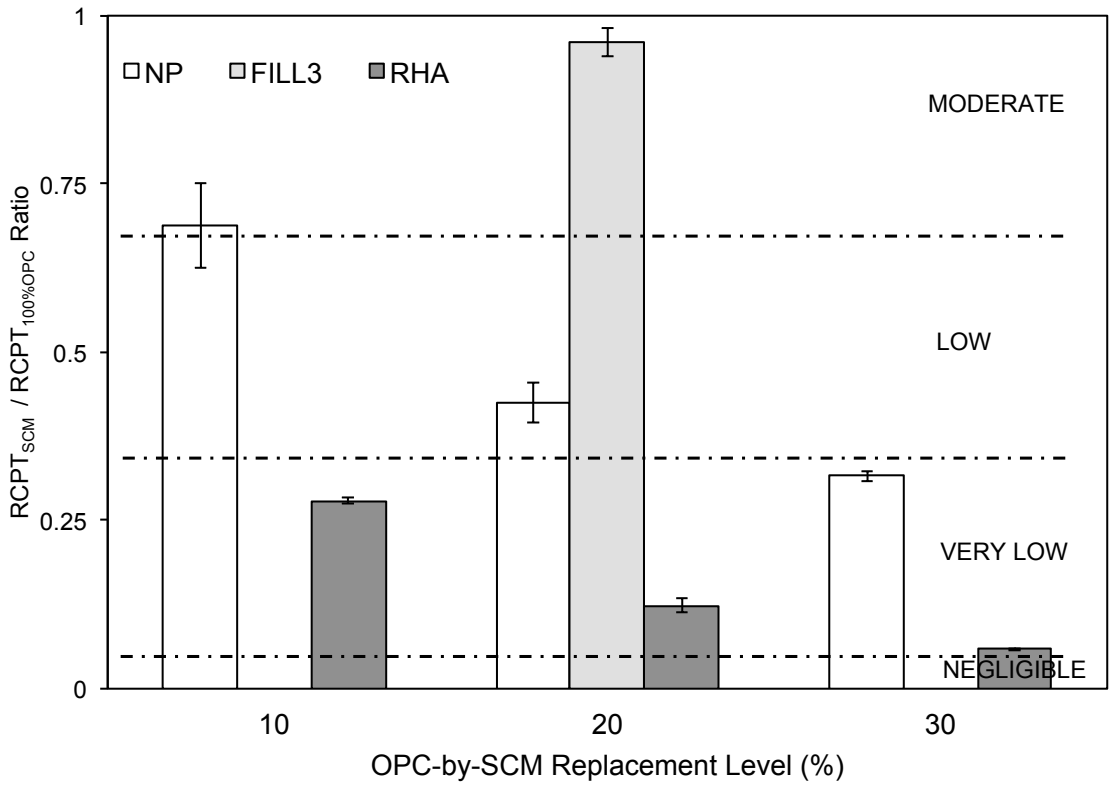

Figure 5-7: Chloride ion penetration results, expressed as ratios with 100% OPC mixture as reference.

There is a clear trend in chloride permeability reduction as chemically replacement level of SCM (RHA and NP) increases. The performance of RHA mixtures, in this matter, is statistically better than NP, reducing from a moderate permeability of the reference mixture to an almost negligible and a $RCPT_{SCM}/RCPT_{OPC}$ ratio of 0.06 result with 30% replacement. This behavior has been previously reported in several studies (A L G Gastaldini et al., 2007; A.L.G. Gastaldini et al., 2010; Saraswathy & Song, 2007), and is an expression of the high pozzolanic activity of rice husk ash, and has been attributed to a reduction of the interfacial transition zone (ITZ) width, porosity and portlandite content (M. H. Zhang et al., 1996).

NP mixtures show $RCPT_{SCM}/RCPT_{OPC}$ ratios ranging from 0.7 to 0.3; reaching for a replacement level of 30% a very low permeability according to ASTM C1202. This is worth to note considering that compressive strength suggested a relatively low gain with using NP. Performance of NP mixture is also better than that of inert filler (FILL3), suggesting that the improvement in permeability is not only due to a physical effect but also to a pozzolanic activity.. RCPT gives a more sensitive assessment than compressive strength when assessing the SCM effect in cement based materials.

As stated by Taylor, replacements of OPC by inert materials, as in this case, does not lower the degree of hydration needed to reach pore depercolation and thus, cannot reduce the overall permeability (Taylor, 1997). This is evident from $RCPT_{SCM}/RCPT_{OPC}$ ratios close to 1.0 shown by FILL3 mixture.

5.3.5.2 Electrical resistivity

The effect of cement replacement by the SCMs in durability was also assessed at the concrete level using electrical resistivity (Table 5-5), where an increased in pore depercolation produces an increase in the electrical resistivity of specimens in saturated condition. Experimental results reveal consistent findings made with electrical resistivity

compared to RCPT. This can be attributed to the similarity of both tests, as the mechanism of measurement is physically equivalent and based on electrical properties of the material. While the sample size and preconditioning varies on each test, the main mechanism that controls concrete behavior in both tests can be reduced to pore connectivity.

Table 5-5: Electrical resistivity of concrete samples at 90 days age.

Replacement Level (%)	SCM ID	Ω Mean Resistivity (Ohm·cm)	Std. Deviation (Ohm·cm)
0	-	9523	139
10	RHA	29649	1388
	NP	11977	547
20	RHA	60868	1388
	NP	21245	56
	FILL3	9179	69
30	RHA	120264	2083
	NP	26900	833

Electrical resistivity of RHA mixtures increased approximately 3, 6 and 12 times that of 100% OPC mixtures with replacement levels of 10, 20, and 30%, respectively. Electrical resistivity of NP mixtures increased 2 and 3 times with replacement levels of 20 and 30% respectively. The use of inert filler at 20% replacement reduced electrical resistivity indicating an increase in permeability which is similar to the findings obtained in RCPT and capillary absorption tests, reaffirming the analysis presented by Taylor (Taylor, 1997).

Strong correlation was found between the electrical resistivity and RCPT results. In addition, this correlation extends to the $RCPT_{SCM}/RCPT_{OPC}$ and $\Omega_{OPC}/\Omega_{SCM}$ ratios

(Figure 5-8). This allows using each one of these tests in an almost equivalent manner to compare several substitution levels and also, several substitution materials.

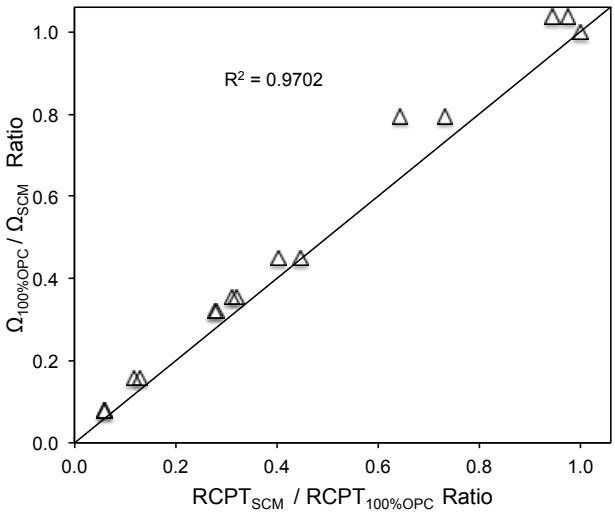

Figure 5-8: ASTM C1202 chloride penetration ratios versus electrical resistivity ratios, showing strong correlation on results of these tests over the complete spectra of SCMs and substitution levels.

The electrical resistivity method offers clear benefits over the ASTM C1202 method. The main advantages are related to a simplified sample preparation and conditioning, strongly reduced time of testing and the possibility to use the same specimen to monitor variations of measurements over the time.

5.4 Conclusions

Sustainability is and will be one of the major concerns regarding concrete technology and future developments. The use of SCMs had been and still is one of the primary alternatives in use to reduce carbon emissions and embodied energy and to improve durability of the concrete structures. The use of this materials sets new challenges for researchers, in order to understand the interactions occurring in cementitious systems

containing this materials in order to optimize the production and use of SCM, and at the same time achieving strength and durability required by the industry..

This paper presented the characterization of RHA and NP, a promising SCM produced from agricultural wastes and a widely used material in chilean cements respectively, in a multi-scale approach considering the paste, mortar and concrete levels. Characterization covered chemical and physical interaction assessment, strength at cement paste and mortar mixtures and durability testing on concrete samples.

The chosen methodology, using inert fillers with different particle size distributions, allowed for separating the physical and chemical effects of the two SCMs under study. Thus, improving the understanding of the contributions of the SCMs.

The main conclusions of this study are:

1. The better performance of RHA compared to NP can be attributed both to its pozzolanic reactivity due to higher amounts of amorphous silica phases, and to the hydration acceleration related to its finer PSD.

2. Even considering the relatively low contribution of NP to strength, the reductions in permeability of NP and RHA in concrete were considerable using three different testing methods. The improvements in permeability achieved with NP and RHA, were more pronounced as replacement level increased up to 30%. Inert filler showed an inability to reduce pore connectivity in all test results obtained. These findings evidenced the lower but not negligible pozzolanic potential of NP, as expected from XRD results.

3. Replacement of OPC by RHA produced increases up to 50% in early age strength and 25% at later ages. It also produced important reductions in permeability at 90 days of age. The contribution of RHA to compressive strength is explained in a 22% to it physical effect and 78% to its chemical effect at 90 days age and 50% replacement level.

Likewise, the RHA contribution to permeability if mostly due to the chemical effects since mixtures containing inert filler presented similar or higher permeability than that having 100% OPC.

4. Replacement of OPC by NP produced reductions in early strength, which are reduced at later ages. Nevertheless, the use of NP produced considerable reductions in permeability at 90 days. The contribution of NP to strength can be attributed in 70% to physical effect and 30% to chemical effect at 90 days age and 50% replacement level. Its contribution to permeability can be solely explained by the chemical effect.

5. While RHA was calcined under controlled conditions to maximize the presence of amorphous and thus, greatly enhance its chemical effect, NP is a natural product from volcanic origin where no controlled temperature cycle is involved. Therefore, an increase of the NP effect on concrete properties would depend only on its physical effect by further reducing its PSD.

6. A proper use of more sophisticated characterization techniques such as XRF, XRD, Rietveld analysis, PSD, Calorimetry, can predict the potential of a SCM and thus help optimizing the SCM performance by changing the burning, cooling and grinding processes during manufacturing.

7. The effects of a particular SCM in concrete properties does not only depend on the physical and chemical characteristics of the SCM but also on the particular property under study. That is, the effect of a SCM on compressive strength does not adequately predict its effect on permeability and independent assessment need to be performed.

5.5 References

Bondar, D., Lynsdale, C. J., Milestone, N. B., Hassani, N., & Ramezanianpour, a. a. (2011). Effect of heat treatment on reactivity-strength of alkali-activated natural pozzolans. *Construction and Building Materials*, *25*(10), 4065–4071.

Celik, K., Meral, C., Mancio, M., Mehta, P. K., & Monteiro, P. J. M. (2013). A comparative study of self-consolidating concretes incorporating high-volume natural pozzolan or high-volume fly ash. *Construction and Building Materials*.

Chancey, R. T., Stutzman, P., Juenger, M. C. G., & Fowler, D. W. (2010). Comprehensive phase characterization of crystalline and amorphous phases of a Class F fly ash. *Cement and Concrete Research*, *40*(1), 146–156.

Chungsangunsit, T., Gheewala, S. H., & Patumsawad, S. (2005). Environmental Assessment of Electricity Production from Rice Husk : A Case Study in Thailand. *International Energy Journal*, *6*(1).

Cordeiro, G. C., Toledo Filho, R. D., Tavares, L. M., Fairbairn, E. D. M. R., & Hempel, S. (2011). Influence of particle size and specific surface area on the pozzolanic activity of residual rice husk ash. *Cement and Concrete Composites*, *33*(5), 529–534.

Corral, R., Arredondo, S., Almaral, J., & Gómez, J. (2013). Corrosión por cloruros del acero de refuerzo embebido en concreto con agregado grueso reciclado y materiales cementantes suplementarios. *Revista Ingeniería de Construcción*, *28*(1), 21–35.

Cyr, M., Lawrence, P., & Ringot, E. (2005). Mineral admixtures in mortars. *Cement and Concrete Research*, *35*(4), 719–730.

Cyr, M., Lawrence, P., & Ringot, E. (2006). Efficiency of mineral admixtures in mortars: Quantification of the physical and chemical effects of fine admixtures in relation with compressive strength. *Cement and Concrete Research*, *36*(2), 264–277.

Della, V. P., Kühn, I., & Hotza, D. (2002). Rice husk ash as an alternate source for active silica production. *Materials Letters*, *57*(4), 818–821.

Espinoza-Hijazin, G., Paul, Á., & Lopez, M. (2012). Concrete Containing Natural Pozzolans : New Challenges for Internal Curing. *Journal of Materials in Civil Engineering*, *24*, 981–988.

Feng, Q., Yamamichi, H., Shoya, M., & Sugita, S. (2004). Study on the pozzolanic properties of rice husk ash by hydrochloric acid pretreatment. *Cement and Concrete Research*, *34*(3), 521–526.

Food and Agriculture Organization of the U.N. (2011). *FAOSTAT* (p. <http://faostat.fao.org>).

Gastaldini, A. L. G., Isaia, G. C., Gomes, N. S., & Sperb, J. E. K. (2007). Chloride penetration and carbonation in concrete with rice husk ash and chemical activators. *Cement and Concrete Composites*, *29*(3), 176–180.

Gastaldini, A. L. G., Isaia, G. C., Saciloto, A. P., Missau, F., & Hoppe, T. F. (2010). Influence of curing time on the chloride penetration resistance of concrete containing rice husk ash: A technical and economical feasibility study. *Cement and Concrete Composites*, *32*(10), 783–793.

Givi, A. N., Rashid, S. A., Aziz, F. N. A., & Salleh, M. A. M. (2010). Assessment of the effects of rice husk ash particle size on strength, water permeability and workability of binary blended concrete. *Construction and Building Materials*, *24*(11), 2145–2150.

Hall, C. (1989). Water sorptivity of mortars and concretes: a review. *Magazine of Concrete Research*, *41*(147), 51–61.

Jain, N. (2012). Effect of nonpozzolanic and pozzolanic mineral admixtures on the hydration behavior of ordinary Portland cement. *Construction and Building Materials*, *27*(1), 39–44.

Kaid, N., Cyr, M., Julien, S., & Khelafi, H. (2009). Durability of concrete containing a natural pozzolan as defined by a performance-based approach. *Construction and Building Materials*, *23*(12), 3457–3467.

Karim, E., El-Hadj, K., Abdelkader, B., & Rachid, B. (2010). Analysis of Mortar Long-Term Strength with Supplementary Cementitious Materials Cured at Different Temperatures. *ACI Materials Journal*, (Jul-Aug 2010), 323–331.

Khan, M. ., Mohan, K., & Taylor, H. F. . (1985a). Pastes of tricalcium silicate with rice husk ash. *Cement and Concrete Research*, *15*(1), 89–92.

Khan, M. ., Mohan, K., & Taylor, H. F. . (1985b). Pastes of tricalcium silicate with rice husk ash. *Cement and Concrete Research*, *15*(1), 89–92.

Lara, R. C., Antoni, M., Díaz, A. A., Scrivener, K., Fernando, J., & Hernández, M. (2011). Estudio de la adición de arcillas calcinadas en la durabilidad de hormigones. *Revista Ingeniería de Construcción*, *26*(1), 25–40.

Lawrence, P., Cyr, M., & Ringot, E. (2003). Mineral admixtures in mortars-- effect of inert materials on short-term hydration. *Cement and Concrete Research*, *33*(12), 1939–1947.

Lothenbach, B., Scrivener, K., & Hooton, R. D. (2011). Supplementary cementitious materials. *Cement and Concrete Research*, *41*(12), 1244–1256.

Mehta, P. K. (1977). Properties of blended cements made from rice husk ash. *ACI Journal*, 440–442.

Mehta, P. K. (1997). Durability - Critical Issues for the Future. *Concrete International*, *19*(7), 69–76.

Mehta, P., & Monteiro, P. (2005). *Concrete: Microstructure, Properties, and Materials* (3rd ed.). New York: McGraw-Hill Professional.

Morris, W., Moreno, E. I., & Sagüés, A. A. (1996). Practical Evaluation of resistivity of concrete in test cylinders using a Wenner array probe. *Cement and Concrete Research*, *26*(12), 1779–1787.

Nair, D. G., Fraaij, A., Klaassen, A. A. K., & Kentgens, A. P. M. (2008). A structural investigation relating to the pozzolanic activity of rice husk ashes. *Cement and Concrete Research*, *38*(6), 861–869.

Pane, I., & Hansen, W. (2005). Investigation of blended cement hydration by isothermal calorimetry and thermal analysis. *Cement and Concrete Research*, *35*(6), 1155–1164.

Pourkhorshidi, a. R., Najimi, M., Parhizkar, T., Jafarpour, F., & Hillemeier, B. (2010). Applicability of the standard specifications of ASTM C618 for evaluation of natural pozzolans. *Cement and Concrete Composites*, *32*(10), 794–800.

Rao, M Subba. James, J. (1986). Reaction product of lime and silica from rice husk ash. *Cement and Concrete Research*, *16*(c), 67–73.

Rodríguez de Sensale, G. (2006). Strength development of concrete with rice-husk ash. *Cement and Concrete Composites*, *28*(2), 158–160.

Saraswathy, V., & Song, H.-W. (2007). Corrosion performance of rice husk ash blended concrete. *Construction and Building Materials*, *21*(8), 1779–1784.

Schneider, M., Romer, M., Tschudin, M., & Bolio, H. (2011). Sustainable cement production—present and future. *Cement and Concrete Research*, *41*(7), 642–650.

Sensale, G. R. De. (2010). Effect of rice-husk ash on durability of cementitious materials. *Cement and Concrete Composites*, *32*, 718–725.

Spragg, R. P., Castro, J., Nantung, T., Paredes, M., & Weiss, J. (2012). Variability Analysis of the Bulk Resistivity Measured Using Concrete Cylinders. *Advances in Civil Engineering Materials*, *1*(1), 1–17.

Taylor, H. (1997). *Cement chemistry* (2nd ed.). London: Thomas Telford.

Xu, Q., Hu, J., Ruiz, J. M., Wang, K., & Ge, Z. (2010). Isothermal calorimetry tests and modeling of cement hydration parameters. *Thermochimica Acta*, *499*(1-2), 91–99.

Yu, Q., Sawayama, K., Sugita, S., Shoya, M., & Isojima, Y. (1999). The reaction between rice husk ash and Ca(OH)2 solution and the nature of its product. *Cement and Concrete Research*, *29*(1), 37–43.

Zain, M. F. M., Islam, M. N., Mahmud, F., & Jamil, M. (2011). Production of rice husk ash for use in concrete as a supplementary cementitious material. *Construction and Building Materials*, *25*(2), 798–805.

Zhang, M. H., Lastra, R., & Malhotra, V. M. (1996). Rice-husk ash paste and concrete: Some aspects of hydration and the microstructure of the interfacial zone between the aggregate and paste. *Cement and Concrete Research*, *26*(6), 963–977.

6 GENERAL CONCLUSIONS

Thermal stresses are generated in early-age concrete due to heat release from the ongoing cement hydration. Because concrete is a complex mixture of different constituents, thermo-mechanical mismatches occur, which generate differential expansion between the concrete phases, resulting in stresses. These stresses occur when the cementitious matrix begins to develop stiffness and thus restricts the expansion of other concrete phases. In addition, the matrix tensile strength undergoes early stages of development, leaving the concrete prone to microcracking and damage due to this effect.

The objective of this study is to understand the driving mechanical factors that control the thermal stress generation in the interface between the aggregate and the bulk matrix. A two-phase (aggregates and bulk matrix) micromechanical model is proposed to predict the thermal stresses based on thermo-mechanical mismatches between concrete phases. Two main mismatches are identified: CTE mismatch and elastic mismatch.

In a second research stage, alternatives to reduce heat of hydration release are explored from a multi-scale approach. Rice husk ash and natural pozzolans are used as supplementary cementitious materials, and property assessment is carried out considering impacts on engineering properties and durability of the material.

As presented in Section 4, damage in measures of compressive strength of concrete samples exposed to early age time-temperature cycles were over 20%, which is comparable to w/c variation impact of strength. The presence of microcracks was verified using fluorescence microscopy. In addition, increases n permeability were measured in consistency with computed thermal stress magnitude. This verifies hypothesis 1.

A simplified two-phase concrete model proved to be sufficiently accurate for prediction of damage to concrete from the thermal stresses generated due to differential thermal

expansion of its phases. Additionally, the simplicity of this model makes it suitable for application to thermal cracking risk assessment in real structures. In addition, the interaction pressure *P* proved to be a good parameter for estimating the thermal cracking risk expressed as the deterioration of key mechanical parameters in the design and durability properties, i.e., compressive strength, modulus of elasticity, and permeability. To accurately apply the proposed model and compute P, a careful thermo-mechanical characterization (CTE and modulus of elasticity) of the concrete phases should be carried out. In this matter, hypothesis 2 is verified.

Rice husk ash exhibited higher chemical activity than natural pozzolans, evidenced in compressive strength development on cement pastes and mortar, and isolated from physical interaction using isothermal calorimetry and strength results from mixtures using chemically inert filler replacements. Both materials proved to be effective on reducing heat of hydration generation while maintaining engineering properties between acceptable ranges and improving durability. These findings, described in detail in Section 5, verifies hypothesis 3.

The high performance of rice husk ash can is attributed both to its highly pozzolanic reactivity and to the hydration acceleration related to its fine PSD. In mortar, and optimum replacement level of 20% of OPC by rice husk ash was observed.

Further research is required to assess the effects of the use of supplementary cementitious materials, such as rice husk ash and natural pozzolans, and other design properties on the thermo-mechanical parameters considered in the proposed micromechanical model. Future work is needed to understand and develop new methodologies that reduce the thermal cracking risk at the mixture design stage and to address the thermo-mechanical compatibility orientation, rather than mitigating heat release at the construction site, which has been the leading strategy in the last decades. This would allow reducing construction site cost related to heat dissipation and also, improve strength and durability of the final concrete placed on site.

Based on the thermo-mechanical approach presented on this thesis, an insightful understanding of mixture design parameters on CTE and modulus of elasticity of the cementitious matrix is required to conform the design to the thermo-mechanical properties of the available aggregates. With these parameters, a thermo-mechanical design of the concrete mixture can be performed *a-priori* based on the proposed stress model, and impacts of variation on mixture proportions on strength, modulus of elasticity and permeability of the resultant concrete may be estimated from a thermal cracking risk perspective. In combination with finite element modeling (FEM) software available to predict the peak temperature that can be expected on a certain concrete element given dosage parameter, a complete thermo-mechanical optimization process may be performed.

Inherent limitations of the presented micromechanical model should be considered prior to use and extrapolation of the presented results to new scenarios. First, the presence of the ITZ is neglected in the model; thus, it overestimates the strength of the matrix and its ability to withstand thermal stresses. In addition, the variability of thermo-mechanical properties of aggregates and cementitious matrix are not considered. This could be included in the model on its present form by turning the focus from a discrete stress value orientation to a potential stress expected range conceptualization. Finally, the model is not able to predict matrix cracking and to establish the moment of cracking occurrence, and thus, it should be only considered as a guide to estimate cracking risk rather than a predictive tool.

REFERENCES

Abdel-Jawad, Y. a. (2006). The maturity method: Modifications to improve estimation of concrete strength at later ages. *Construction and Building Materials*, *20*(10), 893–900. doi:10.1016/j.conbuildmat.2005.06.022

ACI. (2007). *ACI224R - Causes, Evaluation, and Repair of Cracks in Concrete Structures*. Farmington Hills, MI.

ACI 207-2R. (2007). *Report on Thermal and Volume Change Effects on Cracking of Mass Concrete*.

ACI 224.1R. (2007). *Causes , Evaluation , and Repair of cracks in Concrete Structures*.

ACI 231R. (2010). *Report on Early-Age Cracking : Causes , Measurement , and Mitigation*.

ACI 318M. (2011). *Building Code Requirements for Structural Concrete*.

Alexander, M. G. (1996). Aggregates and the Deformation Properties of Concrete. *ACI Materials Journal*, *93*(6).

Alqallaf, H. J., & Alawadhi, E. M. (2013). Concrete roof with cylindrical holes containing PCM to reduce the heat gain. *Energy and Buildings*, *61*, 73–80. doi:10.1016/j.enbuild.2013.01.041

ASTM C1074. (2004). Standard Practice for Estimating Concrete Strength by the Maturity Method. doi:10.1520/C1074-04.2

ASTM C150. (2009). *Standard specification for Portland Cement*.

ASTM C215. (2008). Standard Test Method for Fundamental Transverse , Longitudinal , and Torsional Resonant Frequencies of Concrete Specimens. doi:10.1520/C0215-08.2

Barcelo, L., Moranville, M., & Clavaud, B. (2005). Autogenous shrinkage of concrete: a balance between autogenous swelling and self-desiccation. *Cement and Concrete Research*, *35*(1), 177–183. doi:10.1016/j.cemconres.2004.05.050

Bentz, D. P. (1995). A Three-Dimensional Cement Hydration and microstructure program. I. Hydration Rate, heat of hydration, and chemical shrinkage.

Bentz, D. P. (2008). A review of early-age properties of cement-based materials. *Cement and Concrete Research*, *38*(2), 196–204. doi:10.1016/j.cemconres.2007.09.005

Bentz, D. P., Garboczi, E. J., Lu, Y., Martys, N., Sakulich, A. R., & Weiss, W. J. (2013). Modeling of the influence of transverse cracking on chloride penetration into concrete. *Cement and Concrete Composites*, *38*, 65–74. doi:10.1016/j.cemconcomp.2013.03.003

Bentz, D. P., & Jensen, O. M. (2004). Mitigation strategies for autogenous shrinkage cracking. *Cement and Concrete Composites*, *26*(6), 677–685. doi:10.1016/S0958-9465(03)00045-3

Bentz, D. P., & Turpin, R. (2007). Potential applications of phase change materials in concrete technology. *Cement and Concrete Composites*, *29*(7), 527–532. doi:10.1016/j.cemconcomp.2007.04.007

Bogue, R. H. (1947). *The chemistry of portland cement* (p. 572). New York: Reinhold.

Bondar, D., Lynsdale, C. J., Milestone, N. B., Hassani, N., & Ramezanianpour, a. a. (2011). Effect of heat treatment on reactivity-strength of alkali-activated natural

pozzolans. *Construction and Building Materials*, *25*(10), 4065–4071. doi:10.1016/j.conbuildmat.2011.04.044

Bremner, T. W., & Holm, T. A. (1986). Elastic Compatibility and the Behavior of Concrete. *ACI Journal*, *83*(2), 244–250.

Burgreen, D. (1971). *Elements of thermal stress analysis*. London: Arcturus Publishing.

Cabeza, L. F., Castellón, C., Nogués, M., Medrano, M., Leppers, R., & Zubillaga, O. (2007). Use of microencapsulated PCM in concrete walls for energy savings. *Energy and Buildings*, *39*(2), 113–119. doi:10.1016/j.enbuild.2006.03.030

Celik, K., Meral, C., Mancio, M., Mehta, P. K., & Monteiro, P. J. M. (2013). A comparative study of self-consolidating concretes incorporating high-volume natural pozzolan or high-volume fly ash. *Construction and Building Materials*. doi:10.1016/j.conbuildmat.2013.11.065

Chancey, R. T., Stutzman, P., Juenger, M. C. G., & Fowler, D. W. (2010). Comprehensive phase characterization of crystalline and amorphous phases of a Class F fly ash. *Cement and Concrete Research*, *40*(1), 146–156. doi:10.1016/j.cemconres.2009.08.029

Chen, H., Yen, T., & Chen, K. (2003). Evaluating Elastic Modulus of Lightweight Aggregate. *ACI Materials Journal*, *100*(2), 108–113.

Chengju, G. (1989). Maturity of concrete: method for predicting early- stage strength. *ACI Materials Journal*, 341–353.

Chungsangunsit, T., Gheewala, S. H., & Patumsawad, S. (2005). Environmental Assessment of Electricity Production from Rice Husk : A Case Study in Thailand. *International Energy Journal*, *6*(1).

Cordeiro, G. C., Toledo Filho, R. D., Tavares, L. M., Fairbairn, E. D. M. R., & Hempel, S. (2011). Influence of particle size and specific surface area on the pozzolanic activity of residual rice husk ash. *Cement and Concrete Composites*, *33*(5), 529–534. doi:10.1016/j.cemconcomp.2011.02.005

Corral, R., Arredondo, S., Almaral, J., & Gómez, J. (2013). Corrosión por cloruros del acero de refuerzo embebido en concreto con agregado grueso reciclado y materiales cementantes suplementarios. *Revista Ingeniería de Construcción*, *28*(1), 21–35. doi:10.4067/SO718-50732013000100002

Cyr, M., Lawrence, P., & Ringot, E. (2005). Mineral admixtures in mortars. *Cement and Concrete Research*, *35*(4), 719–730. doi:10.1016/j.cemconres.2004.05.030

Cyr, M., Lawrence, P., & Ringot, E. (2006). Efficiency of mineral admixtures in mortars: Quantification of the physical and chemical effects of fine admixtures in relation with compressive strength. *Cement and Concrete Research*, *36*(2), 264–277. doi:10.1016/j.cemconres.2005.07.001

Della, V. P., Kühn, I., & Hotza, D. (2002). Rice husk ash as an alternate source for active silica production. *Materials Letters*, *57*(4), 818–821.

Deschutter, G. (2004). Applicability of degree of hydration concept and maturity method for thermo-visco-elastic behaviour of early age concrete. *Cement and Concrete Composites*, *26*(5), 437–443. doi:10.1016/s0958-9465(03)00067-2

E.P.A., U. S. (2007). Industrial processes GHG emission. *Greenhouse Gas Production Report*.

EN206. (2002). *Concrete: Specification, performance, production & conformity*.

Erdem, S., Dawson, A. R., & Thom, N. H. (2012). Influence of the micro- and nanoscale local mechanical properties of the interfacial transition zone on impact behavior of concrete made with different aggregates. *Cement and Concrete Research*, *42*(2), 447–458. doi:10.1016/j.cemconres.2011.11.015

Escadeillas, G., Aubert, J.-E., Segerer, M., & Prince, W. (2007). Some factors affecting delayed ettringite formation in heat-cured mortars. *Cement and Concrete Research*, *37*(10), 1445–1452. doi:10.1016/j.cemconres.2007.07.004

Espinoza-Hijazin, G., Paul, Á., & Lopez, M. (2012). Concrete Containing Natural Pozzolans : New Challenges for Internal Curing. *Journal of Materials in Civil Engineering*, *24*, 981–988. doi:10.1061/(ASCE)MT.1943-5533.0000421.

Feng, Q., Yamamichi, H., Shoya, M., & Sugita, S. (2004). Study on the pozzolanic properties of rice husk ash by hydrochloric acid pretreatment. *Cement and Concrete Research*, *34*(3), 521–526.

Fernandes, F., Manari, S., Aguayo, M., Santos, K., Oey, T., Wei, Z., … Sant, G. (2014). On the Feasibility of Using Phase Change Materials (PCMs) to Mitigate Thermal Cracking in Cementitious Materials. *Cement and Concrete Composites*. doi:10.1016/j.cemconcomp.2014.03.003

Food and Agriculture Organization of the U.N. (2011). *FAOSTAT* (p. <http://faostat.fao.org>).

Gallucci, E., Zhang, X., & Scrivener, K. L. (2013). Effect of temperature on the microstructure of calcium silicate hydrate (C-S-H). *Cement and Concrete Research*, *53*, 185–195. doi:10.1016/j.cemconres.2013.06.008

Gastaldini, A. L. G., Isaia, G. C., Gomes, N. S., & Sperb, J. E. K. (2007). Chloride penetration and carbonation in concrete with rice husk ash and chemical activators. *Cement and Concrete Composites*, *29*(3), 176–180.

Gastaldini, A. L. G., Isaia, G. C., Saciloto, A. P., Missau, F., & Hoppe, T. F. (2010). Influence of curing time on the chloride penetration resistance of concrete containing rice husk ash: A technical and economical feasibility study. *Cement and Concrete Composites*, *32*(10), 783–793. doi:10.1016/j.cemconcomp.2010.08.001

Givi, A. N., Rashid, S. A., Aziz, F. N. A., & Salleh, M. A. M. (2010). Assessment of the effects of rice husk ash particle size on strength, water permeability and workability of binary blended concrete. *Construction and Building Materials*, *24*(11), 2145–2150.

Gowripalan, N., Sirivivatnanon, V., & Lim, C. C. (2000). Chloride diffusivity of concrete cracked in flexure. *Cement and Concrete Research*, *30*(5), 725–730. doi:10.1016/S0008-8846(00)00216-7

Hirsch, T. J. (1962). Modulus of Elasticity of Concrete Affected by Elastic Moduli of Cement Paste Matrix and Aggregate. *ACI Journal*, *59*(3), 427–452.

Holt, E. (2005). Contribution of mixture design to chemical and autogenous shrinkage of concrete at early ages. *Cement and Concrete Research*, *35*(3), 464–472. doi:10.1016/j.cemconres.2004.05.009

Hughes, B. P., & Videla, C. (1992). Design criteria for early-age bond strength in reinforced concrete. *Materials and Structures*, *25*, 445–463.

I.N.N. (1968). *NCh148.Of68 : Cemento – Terminología , clasificación y especificaciones generales*.

Jain, N. (2012). Effect of nonpozzolanic and pozzolanic mineral admixtures on the hydration behavior of ordinary Portland cement. *Construction and Building Materials*, *27*(1), 39–44. doi:10.1016/j.conbuildmat.2011.08.006

Jakobsen, U. H., & Brown, D. R. (2006). Reproducibility of w/c ratio determination from fluorescent impregnated thin sections. *Cement and Concrete Research*, *36*(8), 1567–1573. doi:10.1016/j.cemconres.2006.05.003

Jensen, O. M., & Hansen, P. F. (2001). Autogenous deformation and RH-change in perspective. *Cement and Concrete Research*, *31*(12), 1859–1865.

Jeong, S.-G., Jeon, J., Cha, J., Kim, J., & Kim, S. (2013). Preparation and evaluation of thermal enhanced silica fume by incorporating organic PCM, for application to concrete. *Energy and Buildings*, *62*, 190–195. doi:10.1016/j.enbuild.2013.02.053

Kaid, N., Cyr, M., Julien, S., & Khelafi, H. (2009). Durability of concrete containing a natural pozzolan as defined by a performance-based approach. *Construction and Building Materials*, *23*(12), 3457–3467. doi:10.1016/j.conbuildmat.2009.08.002

Karadeniz, Z. H., & Kumlutas, D. (2007). A numerical study on the coefficients of thermal expansion of fiber reinforced composite materials. *Composite Structures*, *78*(1), 1–10. doi:10.1016/j.compstruct.2005.11.034

Karim, E., El-Hadj, K., Abdelkader, B., & Rachid, B. (2010). Analysis of Mortar Long-Term Strength with Supplementary Cementitious Materials Cured at Different Temperatures. *ACI Materials Journal*, (Jul-Aug 2010), 323–331.

Khan, M. ., Mohan, K., & Taylor, H. F. . (1985a). Pastes of tricalcium silicate with rice husk ash. *Cement and Concrete Research*, *15*(1), 89–92.

Khan, M. ., Mohan, K., & Taylor, H. F. . (1985b). Pastes of tricalcium silicate with rice husk ash. *Cement and Concrete Research*, *15*(1), 89–92.

Konin, A., François, R., & Arliguie, G. (1998a). Analysis of progressive damage to reinforced ordinary and high performance concrete in relation to loading. *Materials and Structures*, *31*(1), 27–35.

Konin, A., François, R., & Arliguie, G. (1998b). Penetration of chlorides in relation to the microcracking state into reinforced ordinary and high strength concrete. *Materials and Structures*, *31*(5), 310–316.

Lara, R. C., Antoni, M., Díaz, A. A., Scrivener, K., Fernando, J., & Hernández, M. (2011). Estudio de la adición de arcillas calcinadas en la durabilidad de hormigones. *Revista Ingeniería de Construcción*, *26*(1), 25–40.

Lawrence, P., Cyr, M., & Ringot, E. (2003). Mineral admixtures in mortars-- effect of inert materials on short-term hydration. *Cement and Concrete Research*, *33*(12), 1939–1947. doi:10.1016/S0008-8846(03)00183-2

Lee, K. M., & Park, J. H. (2008). A numerical model for elastic modulus of concrete considering interfacial transition zone. *Cement and Concrete Research*, *38*(3), 396–402. doi:10.1016/j.cemconres.2007.09.019

Lee, Y., Choi, M.-S., Yi, S.-T., & Kim, J.-K. (2009). Experimental study on the convective heat transfer coefficient of early-age concrete. *Cement and Concrete Composites*, *31*(1), 60–71. doi:10.1016/j.cemconcomp.2008.09.009

Lim, C. ., Gowripalan, N., & Sirivivatnanon, V. (2000). Microcracking and chloride permeability of concrete under uniaxial compression. *Cement and Concrete Composites*, *22*(5), 353–360. doi:10.1016/S0958-9465(00)00029-9

Litorowicz, A. (2006). Identification and quantification of cracks in concrete by optical fluorescent microscopy. *Cement and Concrete Research*, *36*(8), 1508–1515. doi:10.1016/j.cemconres.2006.05.011

Lothenbach, B., Scrivener, K., & Hooton, R. D. (2011). Supplementary cementitious materials. *Cement and Concrete Research*, *41*(12), 1244–1256. doi:10.1016/j.cemconres.2010.12.001

Maruyama, I., & Teramoto, a. (2012). Effect of water-retaining lightweight aggregate on the reduction of thermal expansion coefficient in mortar subject to temperature histories. *Cement and Concrete Composites*, *34*(10), 1124–1129. doi:10.1016/j.cemconcomp.2012.08.003

Mehta, P. K. (1977). Properties of blended cements made from rice husk ash. *ACI Journal*, 440–442.

Mehta, P. K. (1997). Durability - Critical Issues for the Future. *Concrete International*, *19*(7), 69–76.

Mehta, P., & Monteiro, P. (2005). *Concrete: Microstructure, Properties, and Materials* (3rd ed.). New York: McGraw-Hill Professional.

Moreno, D., Martinez, P., & Lopez, M. (2014). Practical Approach for Assessing Lightweight Aggregate Potential for Concrete Performance. *ACI Materials Journal*, *111*(2), 123–132.

Moreno, D., Zunino, F., Paul, Á., & Lopez, M. (2014). High strength lightweight concrete (HSLC): Challenges when moving from the laboratory to the field. *Construction and Building Materials*, *56*, 44–52. doi:10.1016/j.conbuildmat.2014.01.068

Morris, W., Moreno, E. I., & Sagüés, A. A. (1996). Practical Evaluation of resistivity of concrete in test cylinders using a Wenner array probe. *Cement and Concrete Research*, *26*(12), 1779–1787.

Mostafa, N. Y., Mohsen, Q., El-Hemaly, S. A. S., El-Korashy, S. A., & Brown, P. W. (2010). High replacements of reactive pozzolan in blended cements: Microstructure and mechanical properties. *Cement and Concrete Composites*, *32*(5), 386–391. doi:10.1016/j.cemconcomp.2010.02.003

Mukhopadhyay, A. K., & Zollinger, D. G. (2009). Development of Dilatometer Test Method to Measure Coefficient of Thermal Expansion of Aggregates. *Journal of Materials in Civil Engineering*, (December), 781–788.

Nair, D. G., Fraaij, A., Klaassen, A. A. K., & Kentgens, A. P. M. (2008). A structural investigation relating to the pozzolanic activity of rice husk ashes. *Cement and Concrete Research*, *38*(6), 861–869.

Neithalath, N., Persun, J., & Hossain, A. (2009). Hydration in high-performance cementitious systems containing vitreous calcium aluminosilicate or silica fume. *Cement and Concrete Research*, *39*(6), 473–481. doi:10.1016/j.cemconres.2009.03.006

Neville, A. (1995). *Properties of Concrete* (4th Edition, pp. 318–328). Essex: Pearson Education Limited.

Nilsen, A. U., & Monteiro, P. J. M. (1993). Concrete : A three phase material. *Cement and Concrete Research*, *23*, 147–151.

Nilsen, A. U., Monteiro, P. J. M., & Gjcrv, O. E. (1995). Estimation of the elastic moduli of lightweight aggregate. *Cement and Concrete Research*, *25*(2), 276–280.

Noumowe, A. N., Siddique, R., & Debicki, G. (2009). Permeability of high-performance concrete subjected to elevated temperature (600°C). *Construction and Building Materials*, *23*(5), 1855–1861. doi:10.1016/j.conbuildmat.2008.09.023

Pane, I., & Hansen, W. (2005). Investigation of blended cement hydration by isothermal calorimetry and thermal analysis. *Cement and Concrete Research*, *35*(6), 1155–1164. doi:10.1016/j.cemconres.2004.10.027

Pavoine, a., Brunetaud, X., & Divet, L. (2012). The impact of cement parameters on Delayed Ettringite Formation. *Cement and Concrete Composites*, *34*(4), 521–528. doi:10.1016/j.cemconcomp.2011.11.012

Pichler, C., Lackner, R., & Mang, H. a. (2007). A multiscale micromechanics model for the autogenous-shrinkage deformation of early-age cement-based materials. *Engineering Fracture Mechanics*, *74*(1-2), 34–58. doi:10.1016/j.engfracmech.2006.01.034

Pomianowski, M., Heiselberg, P., Jensen, R. L., Cheng, R., & Zhang, Y. (2014). A new experimental method to determine specific heat capacity of inhomogeneous concrete material with incorporated microencapsulated-PCM. *Cement and Concrete Research*, *55*, 22–34. doi:10.1016/j.cemconres.2013.09.012

Poole, J. L., Asce, M., Riding, K. A., Juenger, M. C. G., Folliard, K. J., & Schindler, A. K. (2011). Effect of Chemical Admixtures on Apparent Activation Energy of Cementitious Systems. *ASCE Journal of Materials in Civil Engineering*, *23*(12), 1654–1661. doi:10.1061/(ASCE)MT.1943-5533.0000345.

Pourasee, A., Peled, A., Weiss, J., & Asce, M. (2011). Fluid Transport in Cracked Fabric-Reinforced- Cement-Based Composites. *ASCE Journal of Materials in Civil Engineering*, (August), 1227–1238. doi:10.1061/(ASCE)MT.1943-5533.0000289.

Pourkhorshidi, a. R., Najimi, M., Parhizkar, T., Jafarpour, F., & Hillemeier, B. (2010). Applicability of the standard specifications of ASTM C618 for evaluation of natural pozzolans. *Cement and Concrete Composites*, *32*(10), 794–800. doi:10.1016/j.cemconcomp.2010.08.007

Qian, C., & Gao, G. (2012). Reduction of interior temperature of mass concrete using suspension of phase change materials as cooling fluid. *Construction and Building Materials*, *26*(1), 527–531. doi:10.1016/j.conbuildmat.2011.06.053

Rao, M Subba. James, J. (1986). Reaction product of lime and silica from rice husk ash. *Cement and Concrete Research*, *16*(c), 67–73.

Riding, K. A., Poole, J. L., Schindler, A. K., Juenger, M. C. G., & Folliard, K. J. (2009). Simplified Concrete Resistivity and Rapid Chloride Permeability Test Method, (105), 1–5.

Rodríguez de Sensale, G. (2006). Strength development of concrete with rice-husk ash. *Cement and Concrete Composites*, *28*(2), 158–160.

Samaha, H. R., & Hover, K. C. (1992). Influence of microcracking on the mass transport properties of concrete. *ACI Materials Journal*, *89*(4), 416–424.

Saraswathy, V., & Song, H.-W. (2007). Corrosion performance of rice husk ash blended concrete. *Construction and Building Materials*, *21*(8), 1779–1784.

Saul, A. G. A. (1951). Principles underlying the steam curing of concrete at atmospheric pressure. *Magazine of Concrete Research*, *2*(6), 127–140.

Schindler, A. K. (2004). Effect of Temperature on Hydration of Cementitious Materials. *ACI Materials Journal*, *101*(1), 72–81.

Schneider, M., Romer, M., Tschudin, M., & Bolio, H. (2011). Sustainable cement production—present and future. *Cement and Concrete Research*, *41*(7), 642–650. doi:10.1016/j.cemconres.2011.03.019

Scrivener, K., Crumbie, A., & Laugesen, P. (2004). The Interfacial Transition Zone (ITZ) Between Cement Paste and Aggregate. *Interface Science*, *12*(4), 411–421.

Scrivener, K. L., & Nonat, A. (2011). Hydration of cementitious materials, present and future. *Cement and Concrete Research*, *41*(7), 651–665. doi:10.1016/j.cemconres.2011.03.026

Selsing, J. (1961). Internal Stresses in Ceramics. *Journal of the American Ceramic Society*, *44*, 419.

Sensale, G. R. De. (2010). Effect of rice-husk ash on durability of cementitious materials. *Cement and Concrete Composites*, *32*, 718–725. doi:10.1016/j.cemconcomp.2010.07.008

Siddique, R. (2008). *Waste Materials and By-Products in Concrete*. *Control*. Berlin: Springer.

Soroushian, P., & Elzafraney, M. (2005). Morphological operations, planar mathematical formulations, and stereological interpretations for automated image analysis of concrete microstructure. *Cement and Concrete Composites*, *27*(7-8), 823–833. doi:10.1016/j.cemconcomp.2004.07.008

Soroushian, P., Elzafraney, M., & Nossoni, A. (2003). Specimen preparation and image processing and analysis techniques for automated quantification of concrete microcracks and voids. *Cement and Concrete Research*, *33*(12), 1949–1962. doi:10.1016/S0008-8846(03)00219-9

Spragg, R. P., Castro, J., Nantung, T., Paredes, M., & Weiss, J. (2012). Variability Analysis of the Bulk Resistivity Measured Using Concrete Cylinders. *Advances in Civil Engineering Materials*, *1*(1), 1–17. doi:10.1520/ACEM104596.

Tank, R. C., & Carino, N. J. (1991). Rate Constant Functions for Strength Development of Concrete. *ACI Materials Journal*, *88*(1), 74–83.

Taylor, H. (1997). *Cement chemistry* (2nd ed.). London: Thomas Telford.

Taylor, H. F. ., Famy, C., & Scrivener, K. . (2001). Delayed ettringite formation. *Cement and Concrete Research*, *31*(5), 683–693. doi:10.1016/S0008-8846(01)00466-5

Trtik, P., & Bartos, P. J. M. (1999). Micromechanical properties of cementitious composites. *Materials and Structures*, *32*, 388–393.

Wang, K., Jansen, D. C., Shah, S. P., & Karr, A. F. (1997). Permeability study of cracked concrete. *Cement and Concrete Research*, *27*(3), 381–393.

Xiao, J., Li, W., Sun, Z., Lange, D. a., & Shah, S. P. (2013). Properties of interfacial transition zones in recycled aggregate concrete tested by nanoindentation. *Cement and Concrete Composites*, *37*, 276–292. doi:10.1016/j.cemconcomp.2013.01.006

Xu, Q., Hu, J., Ruiz, J. M., Wang, K., & Ge, Z. (2010). Isothermal calorimetry tests and modeling of cement hydration parameters. *Thermochimica Acta*, *499*(1-2), 91–99. doi:10.1016/j.tca.2009.11.007

Yang, Z., Weiss, W. J., & Olek, J. (2006). Water Transport in Concrete Damaged by Tensile Loading and Freeze – Thaw Cycling. *ASCE Journal of Materials in Civil Engineering*, (June), 424–434.

Yi, S.-T., Moon, Y.-H., & Kim, J.-K. (2005). Long-term strength prediction of concrete with curing temperature. *Cement and Concrete Research*, *35*(10), 1961–1969. doi:10.1016/j.cemconres.2005.06.010

Yu, Q., Sawayama, K., Sugita, S., Shoya, M., & Isojima, Y. (1999). The reaction between rice husk ash and Ca(OH)2 solution and the nature of its product. *Cement and Concrete Research*, *29*(1), 37–43.

Zain, M. F. M., Islam, M. N., Mahmud, F., & Jamil, M. (2011). Production of rice husk ash for use in concrete as a supplementary cementitious material. *Construction and Building Materials*, *25*(2), 798–805.

Zhang, M. ., Tam, C. ., & Leow, M. . (2003). Effect of water-to-cementitious materials ratio and silica fume on the autogenous shrinkage of concrete. *Cement and Concrete Research*, *33*(10), 1687–1694. doi:10.1016/S0008-8846(03)00149-2

Zhang, M. H., Lastra, R., & Malhotra, V. M. (1996). Rice-husk ash paste and concrete: Some aspects of hydration and the microstructure of the interfacial zone between the aggregate and paste. *Cement and Concrete Research*, *26*(6), 963–977.

Zhang, Z., Olek, J., & Diamond, S. (2002). Studies on delayed ettringite formation in early-age , heat-cured mortars I . Expansion measurements , changes in dynamic modulus of elasticity , and weight gains. *Cement and Concrete Research*, *32*(11), 1729–1736.

Zhou, C., Huang, B., Ph, D., Asce, M., Shu, X., & Asce, A. M. (2013). Micromechanical Model for Predicting Coefficient of Thermal Expansion of Concrete. *Journal of Materials in Civil Engineering*, *25*(September), 1171–1180. doi:10.1061/(ASCE)MT.1943-5533.0000663.

Zhu, W., & Bartos, P. J. . (1997). Assessment of interfacial microstructure and bond properties in aged grc using a novel microindentation method. *Cement and Concrete Research*, *27*(11), 1701–1711.

Zhu, W., & Bartos, P. J. . (2000). Application of depth-sensing microindentation testing to study of interfacial transition zone in reinforced concrete. *Cement and Concrete Research*, *30*(8), 1299–1304. doi:10.1016/S0008-8846(00)00322-7

APPENDICES

APPENDIX A: DRAFT RESULTS – THERMOMECHANICAL ASSESMENT OF CONCRETE MICROCRACKING (PAPER 1)

Table A- 1: Compressive strength results, iso-strain series ($\boldsymbol{\alpha_1 \Delta T}$ constant).

Sample	Aggregate	Diameter [cm]	Load [ton]	Strength [MPa]
1	Calcareous	9.88	12.07	15.44
2	Calcareous	9.854	13.8	17.75
3	Calcareous	9.54	14.39	19.74
4	Calcareous	9.843	10.57	13.62
5	Calcareous	9.809	25.25	32.77
8	Calcareous	9.904	27.42	34.90
9	Calcareous	9.827	28.34	36.64
11	Calcareous	9.883	26.83	34.30
1	Lutita Exp.	9.99	29.54	36.96
2	Lutita Exp.	10	27.7	34.59
3	Lutita Exp.	9.84	30.23	38.98
5	Lutita Exp.	9.86	29.2	37.50
7	Lutita Exp.	9.87	28.54	36.58
4	Lutita Exp.	9.9	6.92	8.82
6	Lutita Exp.	9.93	6.49	8.22
10	Lutita Exp.	9.97	6.48	8.14
8	Lutita Exp.	9.826	35.53	45.95
11	Lutita Exp.	9.927	33.82	42.85
12	Lutita Exp.	9.913	33.82	42.97
9	Lutita Exp.	9.914	33.93	43.10
13	Lutita Exp.	9.839	35.41	45.67
1	Magnetite	9.9	32.04	40.82
2	Magnetite	9.86	33.29	42.76
3	Magnetite	9.92	33.56	42.58
5	Magnetite	9.99	33.91	42.43
7	Magnetite	9.92	34.05	43.20
4	Magnetite	9.9	5.22	6.65
6	Magnetite	9.84	5.66	7.30
10	Magnetite	9.835	5.67	7.32
11	Magnetite	9.803	43.63	56.69
12	Magnetite	9.933	43.14	54.59
13	Magnetite	9.835	42.07	54.31
8	Magnetite	9.86	33.42	42.92
9	Magnetite	9.901	41.67	53.08

1	Siliceous	9.9	32.23	41.06
2	Siliceous	9.875	30.21	38.68
3	Siliceous	9.85	27.89	35.89
5	Siliceous	9.82	30.9	40.01
7	Siliceous	9.8	31.71	41.23
4	Siliceous	9.85	2.87	3.69
6	Siliceous	9.8	2.79	3.63
10	Siliceous	9.93	2.79	3.53
8	Siliceous	9.865	40.97	52.57
11	Siliceous	9.841	43.7	56.34
13	Siliceous	9.955	42.57	53.64
9	Siliceous	9.869	35.73	45.81
12	Siliceous	9.907	41.16	52.36

Table A- 2: Compressive strength results, iso-stiffness series ($\mathbf{E_1}$ constant).

Sample	Aggregate	Diameter [cm]	Load [ton]	Strength [MPa]
1	Siliceous	10.377	31.65	36.70
2	Siliceous	10.386	30.22	34.98
3	Siliceous	10.523	25.15	28.36
5	Siliceous	10.319	33.24	38.98
7	Siliceous	10.42	31.559	36.29
4	Siliceous	10.315	8.54	10.02
6	Siliceous	10.3	9.08	10.69
10	Siliceous	9.808	7.48	9.71
14	Siliceous	10.312	10.07	11.82
8	Siliceous	10.247	39.08	46.47
9	Siliceous	10.315	36.26	42.55
11	Siliceous	10.389	40.88	47.29
12	Siliceous	10.352	37.88	44.14
13	Siliceous	10.369	40.37	46.88
1	Lutita Exp.	10.288	26.79	31.60
2	Lutita Exp.	10.267	27.24	32.27
3	Lutita Exp.	10.266	26.76	31.70
5	Lutita Exp.	10.255	27.1	32.18
7	Lutita Exp.	10.328	28.23	33.05
4	Lutita Exp.	9.802	4.29	5.58
6	Lutita Exp.	10.302	4.61	5.42
10	Lutita Exp.	10.287	4.8	5.66
14	Lutita Exp.	9.9	4.76	6.06
8	Lutita Exp.	10.356	26.62	30.99
9	Lutita Exp.	10.324	30.06	35.21

11	Lutita Exp.	10.425	26.86	30.86
12	Lutita Exp.	9.78	25.57	33.38
13	Lutita Exp.	9.887	26.62	34.00

Table A- 3: Dynamic elastic modulus results, iso-strain series ($\alpha_1 \Delta T$ constant).

Sample	Agg	Thermal Cycle	Transverse frecuency		Longitudinal Frecuency		Torsional Frecuency		Dynamic Poisson Ratio
			n [Hz]	Dynamic E [Gpa]	n [Hz]	Dynamic E [Gpa]	n [Hz]	Dynamic G [Gpa]	
1	Calcareous	Thermal Cycle 1	3339.84	28.24	6230.47	29.41	3652.34	11.95	0.22
2	Calcareous	Thermal Cycle 1	3417.97	30.08	6269.53	29.93	3671.88	12.14	0.23
3	Calcareous	Thermal Cycle 1	3359.38	28.60	6230.47	29.49	3652.34	11.99	0.23
4	Expanded Shale	E T	3398.44	24.78	6171.88	24.52	3339.84	8.50	0.44
5	Expanded Shale	E T	3330.84	22.82	6113.28	23.56	3554.69	9.42	0.25
6	Expanded Shale	E T	3338.84	24.29	6132.81	24.13	3339.84	8.47	0.43
1	Expanded Shale	Thermal Cycle 1	3144.53	21.41	5820.31	21.75	3444.70	9.01	0.21
1	Magnetite	E T	3496.09	41.41	6523.44	42.26	3750.00	16.52	0.28
2	Magnetite	E T	3535.16	42.19	6582.03	42.90	3789.06	16.82	0.28
3	Magnetite	E T	3496.09	40.83	6256.51	38.78	3691.41	15.97	0.21
4	Magnetite	Thermal Cycle 1	3300.78	36.54	6113.28	36.78	3522.14	14.44	0.21
5	Magnetite	Thermal Cycle 1	3274.74	35.54	6152.34	36.96	3574.22	14.76	0.25
6	Magnetite	Thermal Cycle 1	3339.84	37.83	6132.81	37.54	3554.69	14.92	0.26
1	Siliceous	Thermal Cycle 1	3535.16	32.93	6503.91	33.30	3808.59	13.51	0.23
2	Siliceous	Thermal Cycle 1	3535.16	33.33	6484.38	33.05	3769.53	13.21	0.25
3	Siliceous	Thermal Cycle 1	3359.38	29.17	6367.19	31.34	3710.94	12.59	0.24

4	Siliceous	E T	3808.59	39.21	7031.25	39.68	4062.50	15.67	0.27
5	Siliceous	E T	3847.66	40.43	7070.31	40.11	4082.03	15.82	0.27
6	Siliceous	E T	3808.59	38.81	7031.25	39.39	4062.50	15.56	0.27

Table A- 4: Dynamic elastic modulus results, iso-stiffness series ($\mathbf{E_1}$ constant).

Probeta	**Agg**	**Ciclo térmico**	**Transverse frecuency**		**Longitudinal Frecuency**		**Torsional Frecuency**		**Dynamic Poissons Ratio**
			n [Hz]	**Dynamic E [Gpa]**	**n [Hz]**	**Dynamic E [Gpa]**	**n [Hz]**	**Dynamic G [Gpa]**	
1	Expanded Shale	T. E.	3203.13	21.72	5878.91	21.70	3437.50	8.78	0.24
2	Expanded Shale	T. E.	3242.19	21.99	5917.97	22.28	3476.56	9.09	0.22
3	Expanded Shale	T. E.	3222.66	21.95	5917.97	22.11	3437.50	8.83	0.25
1	Expanded Shale	Thermal Cycle 1	3105.47	21.08	5703.13	20.91	3300.78	3300.78	0.26
2	Expanded Shale	Thermal Cycle 2	3105.47	21.04	5742.19	21.35	3339.84	8.55	0.25
3	Expanded Shale	Thermal Cycle 3	3164.06	21.22	5839.84	21.56	3378.91	8.54	0.26
1	Siliceous	T. E.	3750.00	37.07	6894.53	37.17	4003.91	14.83	0.25
2	Siliceous	T. E.	3710.31	36.38	6875.00	36.83	3945.31	14.35	0.28
3	Siliceous	T. E.	3750.00	37.07	6875.00	37.18	3984.38	14.77	0.26
1	Siliceous	Thermal Cycle 1	3652.34	34.27	6718.75	35.14	3886.72	13.91	0.26
2	Siliceous	Thermal Cycle 2	3632.81	33.36	6660.16	34.27	3847.66	13.53	0.27

3	Siliceous	Thermal Cycle 3	3632.81	34.32	6679.69	35.05	3867.19	13.90	0.26

Table A- 5: CTE measurements of cementitious matrix, used to compute thermal interaction pressure *P*.

Edad [días]	T° Amb. [°C]	T° peak [°C]	deltaT [°C]	dm0 [mm]	dmf [mm]	dp0 [mm]	dpf [mm]	L_0[mm]	Lf [mm]	delta L [mm]	CTE
2	25.70	49.33	23.63	0.428	0.522	0.702	0.734	253.726	253.788	0.062	1.03396E-05
2	25.70	49.40	23.70	0.462	0.552	0.702	0.734	253.760	253.818	0.058	9.64398E-06
3	23.60	48.80	25.20	0.182	0.26	0.74	0.744	253.442	253.516	0.074	1.15865E-05
3	23.60	49.13	25.53	0.19	0.264	0.74	0.74	253.450	253.524	0.074	1.14349E-05
4	24.90	48.87	23.97	0.324	0.392	0.734	0.73	253.590	253.662	0.072	1.18466E-05
4	24.90	48.97	24.07	0.278	0.344	0.734	0.73	253.544	253.614	0.07	1.14717E-05
4	24.90	48.97	24.07	0.23	0.296	0.734	0.73	253.496	253.566	0.07	1.14739E-05
5	23.20	49.33	26.13	0.152	0.22	0.744	0.734	253.408	253.486	0.078	1.17782E-05
5	23.20	49.33	26.13	0.448	0.512	0.744	0.734	253.704	253.778	0.074	1.11612E-05
6	23.63	49.50	25.87	0.48	0.548	0.744	0.738	253.736	253.810	0.074	1.12748E-05
6	23.63	49.53	25.90	0.176	0.248	0.744	0.738	253.432	253.510	0.078	1.18832E-05
9	23.53	49.03	25.50	0.176	0.254	0.746	0.744	253.430	253.510	0.08	1.23792E-05
9	23.53	49.10	25.57	0.326	0.398	0.746	0.744	253.580	253.654	0.074	1.14141E-05
11	23.90	49.70	25.80	0.264	0.336	0.74	0.734	253.524	253.602	0.078	1.19249E-05
11	23.90	49.70	25.80	0.218	0.288	0.74	0.734	253.478	253.554	0.076	1.16213E-05
13	24.53	48.80	24.27	0.128	0.202	0.734	0.73	253.394	253.472	0.078	1.26849E-05
13	24.53	48.93	24.40	0.428	0.504	0.734	0.738	253.694	253.766	0.072	1.16314E-05
13	24.53	49.00	24.47	0.464	0.538	0.734	0.738	253.730	253.800	0.07	1.12759E-05
16	24.37	48.70	24.33	0.162	0.238	0.744	0.744	253.418	253.494	0.076	1.23246E-05
16	24.37	48.93	24.57	0.166	0.236	0.744	0.744	253.422	253.492	0.07	1.12437E-05

16	24.40	49.00	24.60	0.304	0.382	0.744	0.744	253.560	253.638	0.078	1.25049E-05
18	24.13	48.13	24.00	0.258	0.33	0.748	0.74	253.510	253.590	0.08	1.31487E-05
18	24.17	48.23	24.07	0.212	0.288	0.748	0.744	253.464	253.544	0.08	1.31147E-05
18	24.20	48.33	24.13	0.136	0.208	0.748	0.744	253.388	253.464	0.076	1.24283E-05
20	23.90	49.50	25.60	0.43	0.524	0.748	0.758	253.682	253.766	0.084	1.29345E-05
20	24.00	49.50	25.50	0.462	0.56	0.748	0.762	253.714	253.798	0.084	1.29836E-05
20	24.03	49.56	25.53	0.16	0.254	0.748	0.762	253.412	253.492	0.08	1.23671E-05
23	23.37	49.97	26.60	0.16	0.248	0.748	0.748	253.412	253.500	0.088	1.30549E-05
23	23.43	50	26.57	0.294	0.386	0.748	0.748	253.546	253.638	0.092	1.36582E-05
23	23.47	50	26.53	0.254	0.342	0.748	0.748	253.506	253.594	0.088	1.30829E-05
39	26.05	44.1	18.05	0.152	0.21	0.748	0.746	253.404	253.464	0.06	1.31178E-05
39	25.95	43.5	17.55	0.452	0.51	0.748	0.746	253.704	253.764	0.06	1.34756E-05
39	25.95	42.7	16.75	0.116	0.172	0.748	0.746	253.368	253.426	0.058	1.36666E-05
44	25.55	46.95	21.40	0.142	0.214	0.746	0.748	253.396	253.466	0.07	1.29088E-05
44	25.5	45.5	20.00	0.286	0.354	0.746	0.748	253.540	253.606	0.066	1.30157E-05
44	25.5	46.25	20.75	0.238	0.308	0.746	0.748	253.492	253.560	0.068	1.29279E-05
58	22.65	51.1	28.45	0.39	0.486	0.748	0.734	253.642	253.752	0.11	1.52437E-05
58	22.6	48.85	26.25	0.12	0.21	0.748	0.736	253.372	253.474	0.102	1.5336E-05
66	22.95	54.85	31.90	0.396	0.502	0.736	0.736	253.660	253.766	0.106	1.30998E-05
66	23.05	53.55	30.50	0.236	0.344	0.736	0.736	253.500	253.608	0.108	1.39684E-05
66	23.05	53.05	30.00	0.138	0.242	0.736	0.736	253.402	253.506	0.104	1.36805E-05

APPENDIX B: FLUORESCENCE MICROSCOPY SAMPLE PREPARATION PROCEDURE.

PROYECTO FONDECYT Nº1120817

PROTOCOLO DE PREPARACIÓN DE MUESTRAS DE MICROSCOPÍA

El procedimiento que se describe pretende prepara muestras de hormigón para observación de micro-grietas y defectos de microestructura utilizando la técnica de fluorescencia en microscopios ópticos de luz reflejada. Dentro de las consideraciones de este procedimiento, está que las muestras han sido dañadas por un ciclo térmico controlado y por ende, no deben ser sometidas a temperatura una vez finalizado dicho ciclo en ninguna etapa de la preparación.

Reactivos

- Resina epóxica LR White, grado Hard
- Fluoresceína sódica (FITC)
- Alcohol isopropílico al 98%
- Alcohol etílico desnaturalizado al 96%
- Acetona pura, grado técnico

Extracción y almacenamiento de muestras

Las muestras serán extraídas de cilindros de 5 cm de diámetro por 10 cm de altura de hormigón, sometidas al ciclo térmico en condición sellada. El proceso de extracción consta de las siguientes etapas:

1. Remover el material de sellado de las probetas, y almacenar inmediatamente sumergidas en alcohol etílico puro (no potable) o acetona.
2. Cortar secciones de 1 cm de altura de los cilindros usando una sierra de baja velocidad, a revoluciones no mayores a 180 rpm, y utilizando un disco diamantado para corte de cerámicos. Utilizar como lubricante durante el corte alcohol isopropílico puro o acetona.
3. Una vez cortada la sección deseada, almacenar nuevamente sumergida en alcohol etílico puro o en acetona para asegurar que la hidratación no prosigue.
4. Reemplazar el alcohol o acetona de almacenamiento periódicamente para garantizar que se mantiene libre de agua.

Preparación para Impregnación

1. Remover las secciones previamente cortadas del alcohol o acetona de almacenamiento, colocarlas en vasos de precipitado individuales, cubrir con alcohol isopropílico puro y someter a baño de ultrasonido por 10 minutos. Si el disco queda completamente paralelo al fondo del vaso, voltearlo pasados 5 minutos de sonificación. El baño de ultrasonido debe realizarse en los vasos con alcohol, los cuales a su vez se encuentran insertos en el tanque lleno de agua del equipo. No utilizar temperatura durante el proceso.
2. Una vez finalizado el proceso de ultrasonido, remover las muestras de los vasos, enjuagar con alcohol isopropílico limpio y secar con aire comprimido o al ambiente. No reutilizar el alcohol isopropílico de limpieza más de 3 veces para evitar que se sature de partículas de polvo retiradas de las muestras.
3. Volver a almacenar las muestras limpias hasta el momento de la impregnación.

Impregnación con resina y fluorocromo

1. Remover las muestras del alcohol de almacenamiento, dejar evaporar al ambiente por 10 minutos.
2. Colocar las muestras en un desecador y someter a un vacío de 740 mm Hg por 1 hora para retirar los residuos de alcohol y aire que hayan quedado al interior de las muestras.
3. Sin eliminar el vacío del desecador (pero con la bomba apagada para evitar que la resina ingrese a ella), dejar ingresar la resina de impregnación al desecador, previamente combinada con el fluorocromo (FITC como fluoresceína sódica en dosis de 0,05g FITC / 100g resina). Mantener saturando en vacío las muestras por 15 minutos. El nivel de resina debe superar el nivel de las muestras por al menos 0,5 cm de altura.
4. Permitir el ingreso de aire al desecador con las muestras, y mantener saturando en resina por otros 15 minutos.
5. Retirar las muestras con ayuda de una pinza. Volver a almacenar la resina sobrante en refrigerador.
6. Colocar las muestras saturadas de resina sobre un portaobjeto de vidrio.
7. Someter los portaobjetos con las muestras a radiación ultravioleta en la banda UV-A (785 nm) por al menos 48 horas para asegurar que la resina cure adecuadamente. No utilizar temperatura o aceleradores químicos para incrementar la tasa de reacción.

Almacenamiento

1. Retirar las muestras del sistema de curado UV. Almacenar en un disecador sobre un plato de porcelana, con abundante medio de retención de humedad (sílica gel), con indicador de saturación.
2. Reemplazar la sílica gel periódicamente cada vez que su sistema de alerta indique que es necesario. La sílica puede ser usada un número indeterminado de veces, y puede recuperarse con un proceso de secado al horno a 100ºC hasta que recupere su color de indicación de estado seco.

APPENDIX C: DRAFT RESULTS – MULTI-SCALE ASSESSMENT OF SUPPLEMENTARY CEMENTITIOUS MATERIALS (PAPER 2)

Table C- 1: Compressive strength results, 100% OPC paste series.

		7 DIAS			28 DIAS			90 DIAS		
SERIE		*Probeta 1*	*Probeta 2*	*Probeta 3*	*Probeta 1*	*Probeta 2*	*Probeta 3*	*Probeta 1*	*Probeta 2*	*Probeta 3*
W/C 0.4	**Dim. 1**	19.82	19.7	19.77	19.65	19.57	19.7	19.86	19.91	19.79
	Dim. 2	19.15	19.42	19.53	19.68	19.62	20.01	19.91	20.12	19.99
	Masa	15.14	15.25	15.42						
	Promedio	19.485	19.56	19.65	19.665	19.595	19.855	19.885	20.015	19.89
	Área Carga	379.665 225	382.593 6	386.122 5	386.712 225	383.964 025	394.221 025	395.413 225	400.600 225	395.612 1
	Carga (kN)	21	19.3	19	24	20.3	25.7	26.8	27.4	31.3
	Resistencia (Mpa)	55.3118 8694	50.4451 7211	49.2071 8166	62.0616 5321	52.8695 3641	65.1918 5525	67.7771 9688	68.3973 6548	79.1179 0362

		7 DIAS			28 DIAS			90 DIAS		
SERIE		*Probeta 1*	*Probeta 2*	*Probeta 3*	*Probeta 1*	*Probeta 2*	*Probeta 3*	*Probeta 1*	*Probeta 2*	*Probeta 3*
W/C 0.45	**Dim. 1**	20.2	19.64	19.2	19.63	19.5	19.41	19.53	19.89	19.39
	Dim. 2	19.89	19.87	20.07	19.61	19.59	19.67	19.87	20.29	20.03
	Masa	14.56	14.7	14.4						
	Promedio	20.045	19.755	19.635	19.62	19.545	19.54	19.7	20.09	19.71
	Área Carga	401.802 025	390.260 025	385.533 225	384.944 4	382.007 025	381.811 6	388.09	403.608 1	388.484 1
	Carga (kN)	12.4	12.8	14.4	18.9	19.8	16.5	21.5	23.4	22.8
	Resistencia (Mpa)	30.8609 694	32.7986 4495	37.3508 6645	49.0979 9961	51.8315 0755	43.2150 3066	55.3995 2073	57.9770 3267	58.6896 6066

		7 DIAS			28 DIAS			90 DIAS		
SERIE		*Probeta 1*	*Probeta 2*	*Probeta 3*	*Probeta 1*	*Probeta 2*	*Probeta 3*	*Probeta 1*	*Probeta 2*	*Probeta 3*
W/C 0.5	**Dim. 1**	20.07	19.79	19.77	19.67	19.72	19.57	19.94	19.95	19.8
	Dim. 2	19.73	19.82	20.18	20.19	19.53	19.58	19.85	19.9	20.05
	Masa	14.22	14.25	14.45						
	Promedio	19.9	19.805	19.975	19.93	19.625	19.575	19.895	19.925	19.925
	Área Carga	396.01	392.238 025	399.000 625	397.204 9	385.140 625	383.180 625	395.811 025	397.005 625	397.005 625
	Carga (kN)	10.2	9.5	10.3	18.2	17.8	12.5	20.5	16.8	11.5

	Resistencia (Mpa)	25.7569 2533	24.2199 8734	25.8144 959	45.8201 7996	46.2168 8507	32.6216 9114	51.7923 9259	42.3167 8078	28.9668 4398
			7 DIAS			28 DIAS			90 DIAS	
SERIE		*Probeta 1*	*Probeta 2*	*Probeta 3*	*Probeta 1*	*Probeta 2*	*Probeta 3*	*Probeta 1*	*Probeta 2*	*Probeta 3*
W/C 0.55	**Dim. 1**	19.52	19.91	20.24	19.05	19.68	19.59	19.95	19.55	19.55
	Dim. 2	19.87	20.15	19.49	19.81	19.62	19.74	19.55	20	20.2
	Masa	14.1	13.96	14.01						
	Promedio	19.695	20.03	19.865	19.43	19.65	19.665	19.75	19.775	19.875
	Área Carga	387.893 025	401.200 9	394.618 225	377.524 9	386.122 5	386.712 225	390.062 5	391.050 625	395.015 625
	Carga (kN)	7.2	7.2	8.1	9.3	12.7	12.4	16.4	13	15.6
	Resistencia (Mpa)	18.5618 1869	17.9461 2126	20.5261 6805	24.6341 3672	32.8911 1616	32.0651 8749	42.0445 4414	33.2437 7758	39.4921 087
			7 DIAS			28 DIAS			90 DIAS	
SERIE		*Probeta 1*	*Probeta 2*	*Probeta 3*	*Probeta 1*	*Probeta 2*	*Probeta 3*	*Probeta 1*	*Probeta 2*	*Probeta 3*
W/C 0.6	**Dim. 1**	19.94	19.83	19.64	18.82	19.8	19.58	19.5	19.8	19.95
	Dim. 2	19.36	20.23	19.95	19.91	18.97	19.76	20.05	20	19.65
	Masa	13.3	13.34	13.59						
	Promedio	19.65	20.03	19.795	19.365	19.385	19.67	19.775	19.9	19.8
	Área Carga	386.122 5	401.200 9	391.842 025	375.003 225	375.778 225	386.908 9	391.050 625	396.01	392.04
	Carga (kN)	5.5	5.1	4.9	11.4	8.5	10.4	12.7	10.5	12.4
	Resistencia (Mpa)	14.2441 8416	12.7118 3589	12.5050 395	30.3997 3856	22.6197 2471	26.8797 1251	32.4766 1348	26.5144 8196	31.6294 2557

Table C- 2: Compressive strength results, FILL3 paste series.

			7 DIAS			28 DIAS			90 DIAS	
SERIE		*Probeta 1*	*Probeta 2*	*Probeta 3*	*Probeta 1*	*Probeta 2*	*Probeta 3*	*Probeta 1*	*Probeta 2*	*Probeta 3*
10%	**Dim. 1**	19.62	19.87	19.61	19.86	20.05	19.97	19.86	19.85	19.88
	Dim. 2	20.07	20.01	19.99	19.99	20.06	20.07	20.01	19.9	19.91
	Masa	14.21	14.4	14.19						
	Promedio	19.845	19.94	19.8	19.925	20.055	20.02	19.935	19.875	19.895
	Área Carga	393.8240 25	397.6036	392.04	397.0056 25	402.2030 25	400.8004	397.4042 25	395.0156 25	395.8110 25
	Carga (kN)	8.9	8.6	7.7	13.5	12.2	13	15.8	17.2	17.9

	Resistencia (Mpa)	22.59892601	21.62958283	19.64085297	34.00455598	30.33293944	32.43509737	39.75800 71	43.54258139	45.22360134
		0.8945	0.8561	0.7774	0.8183	0.7300	0.7806	0.8449	0.9254	0.9611

		7 DIAS			28 DIAS			90 DIAS		
SERIE		*Probeta 1*	*Probeta 2*	*Probeta 3*	*Probeta 1*	*Probeta 2*	*Probeta 3*	*Probeta 1*	*Probeta 2*	*Probeta 3*
20%	**Dim. 1**	19.91	19.96	19.68	20.05	20	19.98	19.96	19.9	20.16
	Dim. 2	20.22	20.21	19.92	20.01	20.14	20.16	20.19	20.05	19.92
	Masa	14.28	14.22	13.93						
	Promedio	20.065	20.085	19.8	20.03	20.07	20.07	20.075	19.975	20.04
	Área Carga	402.604225	403.407225	392.04	401.2009	402.8049	402.8049	403.005625	399.000625	401.6016
	Carga (kN)	8.1	8.1	7.1	12.5	12.4	11.1	15.3	15.3	13.1
	Resistencia (Mpa)	20.11901 39	20.07896 611	18.11039 69	31.15646 052	30.78413 396	27.55676 507	37.96473 064	38.34580 46	32.61939 195
		0.7964	0.7948	0.7169	0.7498	0.7408	0.6632	0.8068	0.8149	0.6932

		7 DIAS			28 DIAS			90 DIAS		
SERIE		*Probeta 1*	*Probeta 2*	*Probeta 3*	*Probeta 1*	*Probeta 2*	*Probeta 3*	*Probeta 1*	*Probeta 2*	*Probeta 3*
30%	**Dim. 1**	19.97	19.92	19.9	20.04	20.16	19.95	20.12	19.99	20.06
	Dim. 2	19.98	19.93	19.97	20.02	19.98	19.99	19.71	20.13	20.09
	Masa	13.89	14.25	14.15						
	Promedio	19.975	19.925	19.935	20.03	20.07	19.97	19.915	20.06	20.075
	Área Carga	399.000625	397.005625	397.404225	401.2009	402.8049	398.8009	396.607225	402.4036	403.005625
	Carga (kN)	5.9	6.1	5.9	9.7	8.9	8.4	11.5	11.5	11.5
	Resistencia (Mpa)	14.78694426	15.36502159	14.84634442	24.17741336	22.09506389	21.06314203	28.99594177	28.57827316	28.53558185
		0.5853	0.6082	0.5877	0.5818	0.5317	0.5069	0.6162	0.6073	0.6064

		7 DIAS			28 DIAS			90 DIAS		
SERIE		*Probeta 1*	*Probeta 2*	*Probeta 3*	*Probeta 1*	*Probeta 2*	*Probeta 3*	*Probeta 1*	*Probeta 2*	*Probeta 3*
50%	**Dim. 1**	19.97	19.6	19.85	19.98	19.93	19.87	20.07	20.05	20.05
	Dim. 2	19.71	19.94	19.98	20.02	19.81	19.95	19.91	19.99	19.8
	Masa	13.8	13.76	13.83						
	Promedio	19.84	19.77	19.915	20	19.87	19.91	19.99	20.02	19.925
	Área Carga	393.6256	390.8529	396.607225	400	394.8169	396.4081	399.6001	400.8004	397.005625

	Carga (kN)	3.7	3.3	3.2	4.6	4.7	4.9	6.4	6.1	6.5
	Resistencia (Mpa)	9.399795135	8.443074108	8.068435 97	11.5	11.90425233	12.36099868	16.01601201	15.21954569	16.37256399
		0.3721	0.3342	0.3194	0.2768	0.2865	0.2975	0.3404	0.3234	0.3479

		7 DIAS			28 DIAS			90 DIAS		
SERIE		*Probeta 1*	*Probeta 2*	*Probeta 3*	*Probeta 1*	*Probeta 2*	*Probeta 3*	*Probeta 1*	*Probeta 2*	*Probeta 3*
75%	**Dim. 1**	19.68	19.37	19.54	19.59	19.54	20.03	19.46	19.85	19.88
	Dim. 2	19.79	19.82	19.8	20.18	20.17	20	20.21	19.45	19.5
	Masa	13.44	13.65	13.55						
	Promedio	19.735	19.595	19.67	19.885	19.855	20.015	19.835	19.65	19.69
	Área Carga	389.4702 25	383.9640 25	386.9089	395.4132 25	394.2210 25	400.6002 25	393.4272 25	386.1225	387.6961
	Carga (kN)	0.8	0.9	0.8	1.2	1.2	1.3	1.6	1.7	1.6
	Resistencia (Mpa)	2.054072298	2.343969595	2.067670193	3.034799 86	3.043977677	3.245130479	4.066825828	4.402747833	4.126943758
		0.0813	0.0928	0.0818	0.0730	0.0733	0.0781	0.0864	0.0936	0.0877

Table C- 3: Compressive strength results, FILL7 paste series.

		7 DIAS			28 DIAS			90 DIAS		
SERIE		*Probeta 1*	*Probeta 2*	*Probeta 3*	*Probeta 1*	*Probeta 2*	*Probeta 3*	*Probeta 1*	*Probeta 2*	*Probeta 3*
10%	**Dim. 1**	19.43	19.77	19.92	19.5	19.76	19.5	19.2	19.6	19.75
	Dim. 2	19.9	19.91	19.87	19.22	19.22	20.25	19.9	20.05	20.05
	Masa	13.93	14.25	13.97						
	Promedio	19.665	19.84	19.895	19.36	19.49	19.875	19.55	19.825	19.9
	Área Carga	386.7122 25	393.6256	395.8110 25	374.8096	379.8601	395.0156 25	382.2025	393.0306 25	396.01
	Carga (kN)	8.5	8.3	8.5	13.6	12.1	14.9	17	13.2	12
	Resistencia (Mpa)	21.98016885	21.08602693	21.47489449	36.28508982	31.85383 25	37.72002 69	44.47903925	33.58516909	30.30226509
		0.8700	0.8346	0.8500	0.8732	0.7666	0.9078	0.9453	0.7137	0.6440

		7 DIAS			28 DIAS			90 DIAS		
SERIE		*Probeta 1*	*Probeta 2*	*Probeta 3*	*Probeta 1*	*Probeta 2*	*Probeta 3*	*Probeta 1*	*Probeta 2*	*Probeta 3*
20%	**Dim. 1**	19.83	19.95	20.29	19.7	19.84	20.01	19.5	19	19.6

	Dim. 2	20.05	19.2	19.93	20.03	19.79	19.29	19.95	19.95	20
	Masa	14.06	13.69	14.03						
	Promedio	19.83	19.575	20.11	19.865	19.815	19.65	19.725	19.475	19.8
	Área Carga	393.2289	383.180625	404.4121	394.618225	392.6342	386.1225	389.075625	379.275625	392.04
	Carga (kN)	7.2	6.8	7.2	13.7	11.9	13.3	9	14.3	13.3
	Resistencia (Mpa)	18.30994619	17.74619998	17.80362 16	34.71709904	30.30810674	34.44502716	23.13174977	37.70345115	33.92510968
		0.7248	0.7024	0.7047	0.8355	0.7294	0.8289	0.4916	0.8013	0.7210

		7 DIAS			28 DIAS			90 DIAS		
SERIE		*Probeta 1*	*Probeta 2*	*Probeta 3*	*Probeta 1*	*Probeta 2*	*Probeta 3*	*Probeta 1*	*Probeta 2*	*Probeta 3*
30%	**Dim. 1**	19.85	19.82	19.85	19.67	19.83	19.7	19.9	20.1	20.2
	Dim. 2	19.98	20	19.92	19.9	20.17	19.61	20.05	20	20.05
	Masa	13.78	13.7	13.86						
	Promedio	19.915	19.91	19.885	19.785	20	19.655	19.975	20.05	20.125
	Área Carga	396.607225	396.4081	395.413225	391.446225	400	386.319025	399.000625	402.0025	405.015625
	Carga (kN)	5.3	5.2	5	8.1	9.1	8.4	9.5	10.4	10
	Resistencia (Mpa)	13.36334707	13.11779452	12.64499942	20.69249742	22.75	21.74368 71	23.80948651	25.87048588	24.69040546
		0.5290	0.5192	0.5005	0.4980	0.5475	0.5233	0.5060	0.5498	0.5247

		7 DIAS			28 DIAS			90 DIAS		
SERIE		*Probeta 1*	*Probeta 2*	*Probeta 3*	*Probeta 1*	*Probeta 2*	*Probeta 3*	*Probeta 1*	*Probeta 2*	*Probeta 3*
50%	**Dim. 1**	19.87	20.08	20.13	19.73	20.13	20.08	20.02	19.65	19.65
	Dim. 2	20.13	19.73	20.09	19.99	20.1	19.72	19.9	20	20
	Masa	13.58	13.65	13.56						
	Promedio	20	19.905	20.11	19.86	20.115	19.9	19.96	19.825	19.825
	Área Carga	400	396.209025	404.4121	394.4196	404.613225	396.01	398.4016	393.030625	393.030625
	Carga (kN)	2.3	2.5	2.4	4.5	4.4	4.2	5.1	4.2	4.5
	Resistencia (Mpa)	5.75	6.309800742	5.934540534	11.40916932	10.87458276	10.60579278	12.80115341	10.68619017	11.44948946
		0.2276	0.2498	0.2349	0.2746	0.2617	0.2552	0.2720	0.2271	0.2433

		7 DIAS			28 DIAS			90 DIAS		
SERIE		*Probeta 1*	*Probeta 2*	*Probeta 3*	*Probeta 1*	*Probeta 2*	*Probeta 3*	*Probeta 1*	*Probeta 2*	*Probeta 3*

75%	**Dim. 1**	19.52	19.85	20	19.35	19.5	19.41	19.95	20	19.45
	Dim. 2	19.85	20.25	19.99	19.7	19.85	19.72	20	20.05	20.05
	Masa	13.15	13.46	13.41						
	Promedio	19.685	20.05	19.995	19.525	19.675	19.565	19.975	20.025	19.75
	Área Carga	387.4992 25	402.0025	399.8000 25	381.2256 25	387.1056 25	382.7892 25	399.0006 25	401.0006 25	390.0625
	Carga (kN)	0.5	0.7	0.7	1.2	1.1	1.2	1.4	1.3	1.5
	Resistencia (Mpa)	1.290325 161	1.741282 703	1.750875 328	3.147742 233	2.841601 695	3.134884 479	3.508766 434	3.241890 209	3.845537 574
		0.0511	0.0689	0.0693	0.0758	0.0684	0.0754	0.0746	0.0689	0.0817

Table C- 4: Compressive strength results, NP paste series.

		7 DIAS			28 DIAS			90 DIAS		
SERIE		*Probeta 1*	*Probeta 2*	*Probeta 3*	*Probeta 1*	*Probeta 2*	*Probeta 3*	*Probeta 1*	*Probeta 2*	*Probeta 3*
10%	**Dim. 1**	19.93	19.71	19.72	19.91	19.77	19.89	19.93	19.92	20.3
	Dim. 2	20.2	19.89	20.25	19.99	19.93	20.04	19.94	20.18	19.87
	Masa	14.12	14.02	14.2						
	Promedio	20.065	19.8	19.985	19.95	19.85	19.965	19.935	20.05	20.085
	Área Carga	402.6042 25	392.04	399.4002 25	398.0025	394.0225	398.6012 25	397.4042 25	402.0025	403.4072 25
	Carga (kN)	7	7.2	7.1	12.3	12.7	13.7	17.4	15.2	16.9
	Resistencia (Mpa)	17.38680 214	18.36547 291	17.77665 498	30.90432 849	32.23166 19	34.37019 041	43.78413 44	37.81071 013	41.89315 152
		0.6882	0.7269	0.7036	0.7437	0.7757	0.8271	0.9305	0.8035	0.8903

		7 DIAS			28 DIAS			90 DIAS		
SERIE		*Probeta 1*	*Probeta 2*	*Probeta 3*	*Probeta 1*	*Probeta 2*	*Probeta 3*	*Probeta 1*	*Probeta 2*	*Probeta 3*
20%	**Dim. 1**	19.94	19.93	20.03	19.7	19.84	19.87	20	20.08	20.1
	Dim. 2	20.16	20.1	19.71	20.03	20.05	20.08	20.27	20.03	20.35
	Masa	14.07	13.95	13.93						
	Promedio	20.05	20.015	19.87	19.865	19.945	19.975	20.135	20.055	20.225
	Área Carga	402.0025	400.6002 25	394.8169	394.6182 25	397.8030 25	399.0006 25	405.4182 25	402.2030 25	409.0506 25
	Carga (kN)	5	5	4.9	9.8	9.7	11.2	14.2	14.1	12.7
	Resistencia (Mpa)	12.43773 36	12.48127 107	12.41081 625	24.83412 924	24.38392 72	28.07013 147	35.02555 91	35.05692 181	31.04750 176

		0.4923	0.4940	0.4912	0.5977	0.5868	0.6755	0.7444	0.7450	0.6598

		7 DIAS			28 DIAS			90 DIAS		
SERIE		*Probeta 1*	*Probeta 2*	*Probeta 3*	*Probeta 1*	*Probeta 2*	*Probeta 3*	*Probeta 1*	*Probeta 2*	*Probeta 3*
30%	**Dim. 1**	20.09	20.08	20.3	19.92	19.6	19.86	19.94	20	20.02
	Dim. 2	19.87	19.93	20.03	20.12	20.09	20.02	19.94	20.05	20.01
	Masa	13.95	13.65	13.87						
	Promedio	19.98	20.005	20.165	20.02	19.845	19.94	19.94	20.025	20.015
	Área Carga	399.2004	400.2000 25	406.6272 25	400.8004	393.8240 25	397.6036	397.6036	401.0006 25	400.6002 25
	Carga (kN)	4.3	4.4	4.3	8.4	8.8	7.9	12.8	13.1	12.5
	Resistencia (Mpa)	10.77153 229	10.99450 206	10.57479 612	20.95806 292	22.34500 549	19.86903 539	32.19286 747	32.66827 826	31.20317 768
		0.4264	0.4352	0.4186	0.5044	0.5377	0.4782	0.6842	0.6943	0.6631

		7 DIAS			28 DIAS			90 DIAS		
SERIE		*Probeta 1*	*Probeta 2*	*Probeta 3*	*Probeta 1*	*Probeta 2*	*Probeta 3*	*Probeta 1*	*Probeta 2*	*Probeta 3*
50%	**Dim. 1**	19.88	20.4	19.88	20.15	20.03	20.2	20.13	19.99	19.96
	Dim. 2	19.74	20	20.24	19.85	19.83	20.02	20.12	19.94	20.33
	Masa	13.52	13.79	13.54						
	Promedio	19.81	20.2	20.06	20	19.93	20.11	20.125	19.965	20.145
	Área Carga	392.4361	408.04	402.4036	400	397.2049	404.4121	405.0156 25	398.6012 25	405.8210 25
	Carga (kN)	2.5	1.7	1.8	6	5.8	6	9.4	8.7	9.3
	Resistencia (Mpa)	6.370463 879	4.166258 21	4.473121 016	15	14.60203 537	14.83635 134	23.20898 113	21.82632 53	22.91650 611
		0.2522	0.1649	0.1771	0.3610	0.3514	0.3570	0.4932	0.4639	0.4870

		7 DIAS			28 DIAS			90 DIAS		
SERIE		*Probeta 1*	*Probeta 2*	*Probeta 3*	*Probeta 1*	*Probeta 2*	*Probeta 3*	*Probeta 1*	*Probeta 2*	*Probeta 3*
75%	**Dim. 1**	20.11	19.93	20.16	19.93	20.03	20.3	20.08	19.62	20.07
	Dim. 2	20.09	19.99	20.2	20.04	19.98	20.22	20.01	20.1	19.8
	Masa	13.14	13.12	13.29						
	Promedio	20.1	19.96	20.18	19.985	20.005	20.26	20.045	19.86	19.935
	Área Carga	404.01	398.4016	407.2324	399.4002 25	400.2000 25	410.4676	401.8020 25	394.4196	397.4042 25
	Carga (kN)	0.5	0.4	0.4	3.2	3.1	3.1	5.6	5.6	5.8

	Resistencia (Mpa)	1.237593129	1.004012032	0.982240116	8.012013514	7.746126453	7.552362233	13.93721199	14.19807738	14.59471147
		0.0490	0.0397	0.0389	0.1928	0.1864	0.1818	0.2962	0.3017	0.3102

Table C- 5: Compressive strength results, RHA paste series.

		7 DIAS			28 DIAS			90 DIAS		
SERIE		*Probeta 1*	*Probeta 2*	*Probeta 3*	*Probeta 1*	*Probeta 2*	*Probeta 3*	*Probeta 1*	*Probeta 2*	*Probeta 3*
10%	**Dim. 1**	19.74	19.72	19.89	19.74	19.72	19.89	19.7	20.06	20.16
	Dim. 2	19.75	19.85	19.85	19.75	19.85	19.85	19.84	19.84	20.07
	Masa	13.92	14.02	14.13						
	Promedio	19.745	19.785	19.87	19.745	19.785	19.87	19.77	19.95	20.115
	Área Carga	389.865025	391.446225	394.8169	389.865025	391.446225	394.8169	390.8529	398.0025	404.613225
	Carga (kN)	9	10.7	10.9	18.1	16.6	16.4	21.3	17.6	21.5
	Resistencia (Mpa)	23.08491253	27.33453363	27.60773412	46.42632408	42.40684656	41.53824216	54.49620561	44.22082776	53.13716575
		0.9138	1.0820	1.0928	1.1173	1.0206	0.9996	1.1581	0.9398	1.1293

		7 DIAS			28 DIAS			90 DIAS		
SERIE		*Probeta 1*	*Probeta 2*	*Probeta 3*	*Probeta 1*	*Probeta 2*	*Probeta 3*	*Probeta 1*	*Probeta 2*	*Probeta 3*
20%	**Dim. 1**	19.76	19.7	19.72	19.76	19.7	19.72	20.19	20.37	20.27
	Dim. 2	19.8	19.68	19.73	19.8	19.68	19.73	20.15	20.09	19.91
	Masa	13.83	13.79	13.96						
	Promedio	19.78	19.69	19.725	19.78	19.69	19.725	20.17	20.23	20.09
	Área Carga	391.2484	387.6961	389.075625	391.2484	387.6961	389.075625	406.8289	409.2529	403.6081
	Carga (kN)	12.7	11.7	12.4	19.8	19.7	16.5	23	21.1	23
	Resistencia (Mpa)	32.46019664	30.17827623	31.8704108	50.60723571	50.81299502	42.40820792	56.53482336	51.55736221	56.98597228
		1.2848	1.1945	1.2615	1.2179	1.2229	1.0206	1.2015	1.0957	1.2111

		7 DIAS			28 DIAS			90 DIAS		
SERIE		*Probeta 1*	*Probeta 2*	*Probeta 3*	*Probeta 1*	*Probeta 2*	*Probeta 3*	*Probeta 1*	*Probeta 2*	*Probeta 3*
30%	**Dim. 1**	19.76	20.11	19.97	19.76	20.11	19.97	20.33	20.17	20.25
	Dim. 2	19.93	19.7	19.76	19.93	19.7	19.76	19.95	20.06	20.12
	Masa	13.77	13.72	13.84						

	Promedio	19.845	19.905	19.865	19.845	19.905	19.865	20.14	20.115	20.185
	Área Carga	393.8240 25	396.2090 25	394.6182 25	393.8240 25	396.2090 25	394.6182 25	405.6196	404.6132 25	407.4342 25
	Carga (kN)	12.8	13.7	14.3	18	18.1	18.7	18.6	21.3	21.8
	Resistencia (Mpa)	32.50182 616	34.57770 807	36.23755 593	45.70569 304	45.68295 737	47.38757 314	45.85577 226	52.64286 653	53.50556 891
		1.2865	1.3687	1.4344	1.0999	1.0994	1.1404	0.9745	1.1188	1.1371

		7 DIAS			28 DIAS			90 DIAS		
SERIE		*Probeta 1*	*Probeta 2*	*Probeta 3*	*Probeta 1*	*Probeta 2*	*Probeta 3*	*Probeta 1*	*Probeta 2*	*Probeta 3*
50%	**Dim. 1**	19.55	19.86	19.92	19.55	19.86	19.92	20.21	20.22	20.46
	Dim. 2	19.66	19.72	19.72	19.66	19.72	19.72	20.02	20.42	19.99
	Masa	13.16	13.34	13.5						
	Promedio	19.605	19.79	19.82	19.605	19.79	19.82	20.115	20.32	20.225
	Área Carga	384.3560 25	391.6441	392.8324	384.3560 25	391.6441	392.8324	404.6132 25	412.9024	409.0506 25
	Carga (kN)	14.3	14.7	14.2	18	21.8	19.1	20	23.4	21.8
	Resistencia (Mpa)	37.20508 869	37.53407 75	36.14773 12	46.83158 017	55.66278 159	48.62124 407	49.42992 162	56.67198 834	53.29413 688
		1.4727	1.4857	1.4308	1.1270	1.3396	1.1701	1.0505	1.2044	1.1326

		7 DIAS			28 DIAS			90 DIAS		
SERIE		*Probeta 1*	*Probeta 2*	*Probeta 3*	*Probeta 1*	*Probeta 2*	*Probeta 3*	*Probeta 1*	*Probeta 2*	*Probeta 3*
75%	**Dim. 1**	20.57	19.74	19.71	20.57	19.74	19.71	20.43	20.22	20.66
	Dim. 2	19.57	20.04	19.83	19.57	20.04	19.83	20.07	20.42	20.11
	Masa	12.81	12.81	12.52						
	Promedio	20.07	19.89	19.77	20.07	19.89	19.77	20.25	20.32	20.385
	Área Carga	402.8049	395.6121	390.8529	402.8049	395.6121	390.8529	410.0625	412.9024	415.5482 25
	Carga (kN)	12.6	12	12.5	15.6	15.8	16.4	18.2	17.9	18.3
	Resistencia (Mpa)	31.28065 225	30.33274 26	31.98134 132	38.72842 659	39.93811 109	41.95951 981	44.38347 813	43.35164 92	44.03821 001
		1.2382	1.2006	1.2659	0.9320	0.9611	1.0098	0.9432	0.9213	0.9359

Table C- 6: ASTM C-1202 chloride ion penetration test results.

MIX	Charge passed [Coulomb]	Average	St. Dev.
CONTROL	3058.3303 2802.4056	**2930.37**	**180.97**
10% PUZ	1883.4811 2147.6512	**2015.57**	**186.80**
20% PUZ	1185.1382 1310.7984	**1247.97**	**88.86**
30% PUZ	910.0527 940.3914	**925.22**	**21.45**
20% FILL	2856.5358 2769.0082	**2812.77**	**61.89**
10% RHA	825.8681 808.7792	**817.32**	**12.08**
20% RHA	384.2354 341.6786	**362.96**	**30.09**
30% RHA	168.6767 175.0718	**171.87**	**4.52**

Table C- 7: Electrical resistivity results (modified Wenner probe method).

MIX	Resistivity [Omh.cm]	Average	St. Dev.
CONTROL	9424.7780 9621.1275	**9522.95**	**138.84**
10% PUZ	11977.3220 11977.3220	**11977.32**	**0.00**

20% PUZ	21205.7504 21284.2902	**21245.02**	**55.54**
30% PUZ	26310.8385 27488.9357	**26899.89**	**833.04**
20% FILL	9130.2536 9228.4284	**9179.34**	**69.42**
10% RHA	28667.0330 30630.5284	**29648.78**	**1388.40**
20% RHA	59886.6100 61850.1054	**60868.36**	**1388.40**
30% RHA	121736.7153 118791.4722	**120264.09**	**2082.60**

Table C- 8: ASTM C-1585 initial rate of water absorption results.

MIX	Initial Rate of Absorption [mm/s^1/2]	R^2	Average	St. Dev.
CONTROL	0.0023 0.0021	0.99101 0.99093	**0.0022**	**0.0001**
10% PUZ	0.0027 0.0025	0.99107 0.97887	**0.0026**	**0.0001**
20% PUZ	0.0017 0.0022	0.99761 0.99039	**0.0020**	**0.0004**
30% PUZ	0.0018 0.0017	0.99312 0.9898	**0.0018**	**0.0001**
20% FILL	0.0034 0.0032	0.99499 0.99599	**0.0033**	**0.0001**
10% RHA	0.0017 0.0017	0.98623 0.98342	**0.0017**	**0.0000**

20% RHA	0.0018 0.0018	0.97747 0.98957	**0.0018**	**0.0000**
30% RHA	0.0015 0.0012	0.99036 0.99327	**0.0014**	**0.0002**

Table C- 9: ASTM C-1585 secondary rate of water absorption results.

MIX	Secondary Rate of Absorption [mm/s^1/2]	**R^2**	Average	St. Dev.
CONTROL	0.0009 0.0010	0.96418 0.98505	**0.0010**	**0.0001**
10% PUZ	0.0010 0.0009	0.96932 0.97149	**0.0010**	**0.0001**
20% PUZ	0.0006 0.0005	0.97979 0.97488	**0.0006**	**0.0001**
30% PUZ	0.0006 0.0006	0.97172 0.976	**0.0006**	**0.0000**
20% FILL	0.0015 0.0015	0.93981 0.96201	**0.0015**	**0.0000**
10% RHA	0.0005 0.0005	0.9655 0.95711	**0.0005**	**0.0000**
20% RHA	0.0003 0.0004	0.91104 0.98156	**0.0004**	**0.0001**
30% RHA	0.0003 0.0003	0.9764 0.9501	**0.0003**	**0.0000**

APPENDIX D: PAPER 1 OFFICIAL SUBMISSION TO CONSTRUCTION AND BUILDING MATERIALS – JULY 2014

Elsevier Editorial System(tm) for Construction & Building Materials
Manuscript Draft

Manuscript Number:

Title: Thermo-mechanical assessment of concrete microcracking damage due to early-age temperature rise

Article Type: Research Paper

Keywords: temperature, microcracking, micromechanics, degradation, damage, strain effect, coefficient of thermal expansion

Corresponding Author: Dr. Mauricio Lopez, PhD

Corresponding Author's Institution: Pontificia Universidad Catolica de Chile

First Author: Franco Zunino, MSc

Order of Authors: Franco Zunino, MSc; Javier Castro, PhD; Mauricio Lopez, PhD

Abstract: The pursuit of high early-age strength concrete has led to mixtures with higher heat of hydration rates at early ages with produces higher temperatures and an overall increased risk of cracking. This study uses a two-phase micromechanical model to compute thermal stresses based on both coefficient of thermal expansion (CTE) and elastic modulus (E) mismatches between aggregates and the cementitious matrix. Concrete specimens were prepared using four types of aggregates (different CTE and E), and subjected to temperature cycles to generate thermal cracking. Fluorescence microscopy, compressive strength, dynamic elastic modulus, and electrical resistivity were used to characterize the effect of this induced thermal cracking. Experimental results were in agreement with the two-phase model and it was concluded that the interaction pressure (P) between phases could be used to estimate the impact on the mechanical and transportation properties of a temperature gradient at early age.

Suggested Reviewers: Jason Weiss PhD
Jack and Kay Hockema Professor of Civil Eng- and Director of the Pankow Mat Lab, School of Civil Engineering, Purdue University
jweiss@purdue.edu
Possess large experience in this type of research and is the current
chair of the committee Chair ACI231 Properties of Concrete at Early Ages.

Anton Schindler PhD
Professor, Director of Highway Research Center, and Associate Department Chair, Civil Engineering, Auburn University
schinak@auburn.edu
Large experience in the research topic.
Past chair of ACI Committee 231 Properties of Concrete at early ages

Zachary Grasley PhD
Associate Professor , Civil and Environmental Engineering, Virginia Tech
zgrasley@vt.edu
Research experience in early age properties and material science in concrete

Maria Juenger PhD
Associate Professor John A. Focht Centennial Teaching Fellowship in Civil Eng, Civil Engineering,
University of Texas @ Austin
mjuenger@mail.utexas.edu
Research Experience in thermal cracking and material science.

July 17th, 2014

Dr. Michael C. Forde,
Editor-in-Chief,
Construction and Building Materials
ELSEVIER

Dear Dr Forde,

On behalf of my co-authors, Franco Zunino and Javier Castro, I am submitting our manuscript entitled: "Thermo-mechanical assessment of concrete microcracking damage due to early-age temperature rise". In this study we assess thermal cracking damage in concrete and explain it using a simple, but effective thermo-mechanical model. The model estimates stress and strains between aggregates, of different CTE and E, and cement matrix. Based on that, the study helps to explain the detriment in concrete compressive strength, elastic modulus and transport properties wen subjected to thermal stressess.

All authors have read and approved the manuscript. There are no author disclosures. The manuscript has not been published and is not being considered for publication elsewhere in whole or in part, in any language.

Thank you very much for considering our work.

Sincerely,

Mauricio Lopez
Associate Professor
Department of Construction Engineering and Management
School of Engineering
Pontificia Universidad Catolica de Chile

Thermo-mechanical assessment of concrete microcracking damage due to early-age temperature rise

Franco Zunino [a], Javier Castro[b] and Mauricio Lopez[c,d*]

[a] Department of Construction Engineering and Management, *School of Engineering, Pontificia Universidad Catolica de Chile, Vicuña Mackenna 4860, Casilla 306, Correo 22, Santiago, Chile. E-mail: fazunino@ing.puc.cl*
[b] *Faculty of Engineering, Universidad del Desarrollo.*
[c](Corresponding author) Department of Construction Engineering and Management, *School of Engineering, Pontificia Universidad Catolica de Chile*
[d] *Researcher, Center for Sustainable Urban Development (CEDEUS). Pontificia Universidad Catolica de Chile*
Vicuña Mackenna 4860, Casilla 306, Correo 22, Santiago, Chile. E-mail: mlopez@ing.puc.cl
Phone: 562-2-354-4245 Fax: 562-2-354-4806

ABSTRACT

The pursuit of high early-age strength concrete has led to mixtures with higher heat of hydration rates at early ages with produces higher temperatures and an overall increased risk of cracking. This study uses a two-phase micromechanical model to compute thermal stresses based on both coefficient of thermal expansion (CTE) and elastic modulus (*E*) mismatches between aggregates and the cementitious matrix. Concrete specimens were prepared using four types of aggregates (different CTE and *E*), and subjected to temperature cycles to generate thermal cracking. Fluorescence microscopy, compressive strength, dynamic elastic modulus, and electrical resistivity were used to characterize the effect of this induced thermal cracking. Experimental results were in agreement with the two-phase model and it was concluded that the interaction pressure (*P*) between phases could be used to estimate the impact on the mechanical and transportation properties of a temperature gradient at early age.

Keywords: temperature, microcracking, micromechanics, degradation, damage, strain effect, coefficient of thermal expansion

1. Introduction

The main driving force in concrete construction over the last few decades has been construction speed, which has pushed the industry to develop high early-age strength concrete. These mixture designs promote the use of high cement contents, a low water-to-cement ratio (w/c), finer cements, and high-C_3A, contents, among others [1].The resulting materials are commonly referred to as high-strength concretes [2]. Unfortunately, these mixtures are more prone to cracking [3] mainly because they tend to contain a higher paste

fraction and exhibit more pronounced self-desiccation, chemical shrinkage [4], and autogenous shrinkage [2,5].

In addition, the higher cement content per unit volume and the use of finer cements increase both the initial rate and the total released heat of hydration, which can lead to an increase in temperature gradients inside the material. Differential thermal expansion of the concrete constituents may produce stresses and cracking that negatively affect the mechanical properties and durability of concrete [6–9]. These stresses occur in the early stages of the concrete, when it is more vulnerable to cracking [5,10]. Furthermore, the increased temperature that accelerates cement hydration [11], produces lower quality and more porous calcium silicate hydrates (CSH) [12]. Moreover, concrete temperatures greater than 70ºC can induce chemical modifications of the hardened phases and lead to expansion due to delayed ettringite formation (DEF) [13–15].

The ACI committee 207 defines two types of thermal gradients: a "*surface gradient*", which is the difference in temperature between two locations in the concrete element, and a "*mass gradient*", which is the difference in temperature between two periods of time, usually between the internal peak temperature and the annual average ambient temperature [16].

The surface gradient usually generates cracking due to differential expansion between the center and the edges of the structural elements due to differences in temperature at a certain instant [16]. These stresses can occur at early ages due to the heat of hydration release or at later-ages due to ambient temperature variations [17]. Cracking due to mass gradients has its origin in thermo-mechanical mismatches between concrete components, i.e., petrous aggregates and cementitious matrix [18–21], which lead to generation of thermal stresses. These stresses occur at early ages in the interfacial transition zone (ITZ) between the aggregates and cementitious matrix, which exhibits lower strength and higher porosity compared with those of the bulk matrix [22–24]. Thermal stresses at early ages occur simultaneously with other phenomena. It has been demonstrated that if proper curing is ensured, autogenous shrinkage and thermal stresses are the main driving forces in early-age cracking [25].

Although several studies and efforts have been carried out in order to control and mitigate surface gradient effects [26–28], less information is available on mass gradient effects. Moreover, a lack of knowledge of the effects of internal restraint and thermo-mechanical mismatches between concrete phases on key design parameters (i.e., compressive strength and elastic modulus), leads to uncertainty in the actual load-bearing capacity of concrete subjected to high temperatures at early age. Few studies exist in the assessment of permeability of damaged concrete [29–31], which further affects durability, but still not directly related to thermal cracking by mass gradient. Understanding how the aggregate and cementitious matrix properties affect the thermo-mechanical mismatches is crucial in assessment and design of concrete mixtures with reduced microcracking risk for the purpose of ensuring mechanical and durability performance.

2. Objective

The aim of this study is assessment of the impact of thermal stresses on mechanical and transport properties of concrete by imposing early-age "mass gradients" with external time-temperature cycles on specimens with a variety of combinations of the two fundamental

thermo-mechanical parameters (CTE and elastic modulus) of the phases (aggregate and matrix). This approach allows assessment of the effect of these parameters mismatches in the thermal damage of concrete. In addition, this approach facilitates the estimate of expected stress and strain levels using the proposed micromechanical model.

3. Proposed Two-Phase Micromechanical Model

It is widely accepted that concrete is most accurately represented as a three-phase material [23], including the petrous aggregates, cement paste, and the ITZ between them. The ITZ has been described as the explanation for the quasi-ductile behavior of concrete [24], and several studies attempted to characterize and understand this particular phase [32–35]. Despite the recognized relevance of the ITZ in explaining concrete behavior, the inherent difficulties in measuring the mechanical and thermal properties at a micro-scale makes it impractical to fully incorporate the ITZ in models. Advances have been made in this matter using nano-indentation, which consistently shows that the ITZ has higher porosity and lower modulus of elasticity that the bulk matrix. However, most of these studies also verify the high variability of elastic properties of the ITZ, turning the selection of a specific value for modeling less representative and highly inaccurate [32–34,36,37]. For this reason, a widely adopted approach considers concrete as a two-phase material: the coarse petrous aggregates and the bulk matrix of mortar surrounding them. This simplification has been successfully used to model and predict relevant properties of concrete, i.e., elastic modulus and coefficient of thermal expansion [21,38–40].

Due to the composite nature of concrete, understanding the elastic and thermal compatibility of its components is crucial for predicting and modeling concrete behavior with reasonable accuracy [19]. In particular, temperature fluctuations in concrete during cement hydration produce differential strains between the concrete phases and thus the thermally induced stresses that generate microcracking. Assuming a uniform temperature distribution in all concrete phases, the main thermo-mechanical variables that control the magnitude of these stresses are the elastic modulus (E) and the coefficient of thermal expansion (CTE, α) of the aggregates and the matrix [20,21]. The occurrence of differential strains is well explained by the mismatch between the thermo-mechanical parameters of the aggregates and the matrix.

Based on the general formulation presented by Zhou et al. [21], a two-phase model is proposed in this work to assess the thermal stresses between concrete composites in different thermo-mechanical mismatch scenarios. As shown in Figure 1, the micromechanical model consists of a spherical aggregate particle of radius a surrounded by an infinite thickness spherical shell matrix. This model applies a temperature change from T_0 to T_1, which will be denoted as ΔT. This parameter represents the temperature variation of a particular place at two different time periods.

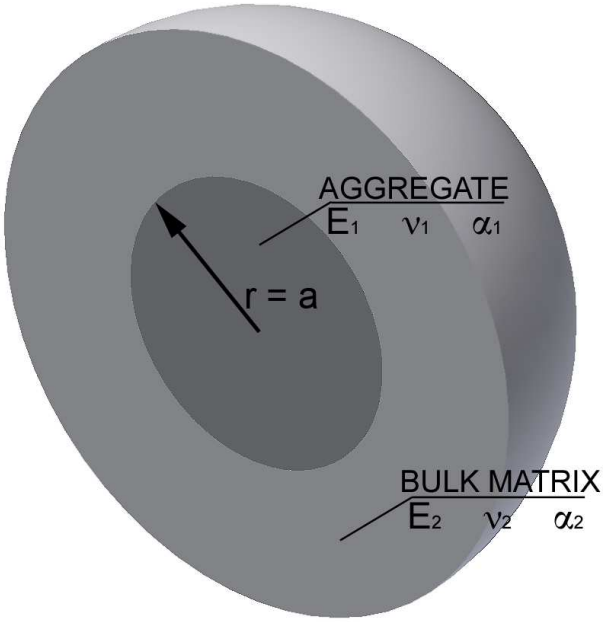

Figure 1. Two-phase model of concrete consisting of an aggregate particle surrounded by an infinite mortar matrix.

Properties and values related to the aggregate and matrix phase will be denoted with the subscripts 1 and 2, respectively. The radial strain (ε_r) and the tangential strain (ε_t) generated in the interface between the aggregate and the bulk matrix are given by [41]:

$$\varepsilon_{ri}=\frac{1}{E_i}(\sigma_{ri}-2\nu_i\sigma_{ti})+\alpha_i\Delta T \quad (1)$$

$$\varepsilon_{ti}=\frac{1}{E_i}((1-\nu_i)\sigma_{ti}-\nu_i\sigma_{ri})+\alpha_i\Delta T \quad (2)$$

where the subscript i refers to the considered phase (1 or 2), σ_r and σ_t are the radial and tangential stress, respectively, and ν_i is the Poisson ratio of phase i. It can be assumed that the differential thermal deformations of the concrete phases are represented by an equivalent thermal interaction pressure (P) present in the interface between them (Figures 2a and 2b). It should be noted that in a 2D formulation at the equator of the spherical aggregate the external shell is equivalent to a cylindrical section. As derived from a simple spherical model of internal radius a and infinite wall thickness with interaction pressure P applied on its cavity (Figure 2b) at a distance r from the center, the stresses are represented as described in [20]:

$$\sigma_{r2} = -2\sigma_{t2} = -P\frac{a^3}{r^3} \quad (3)$$

In this convention, positive values represent tensile stresses. Similarly, for a solid sphere of radius a subjected to an external pressure P (Figure 2a), the radial and tangential stresses are given by:

$$\sigma_{r1} = \sigma_{t1} = -P \quad (4)$$

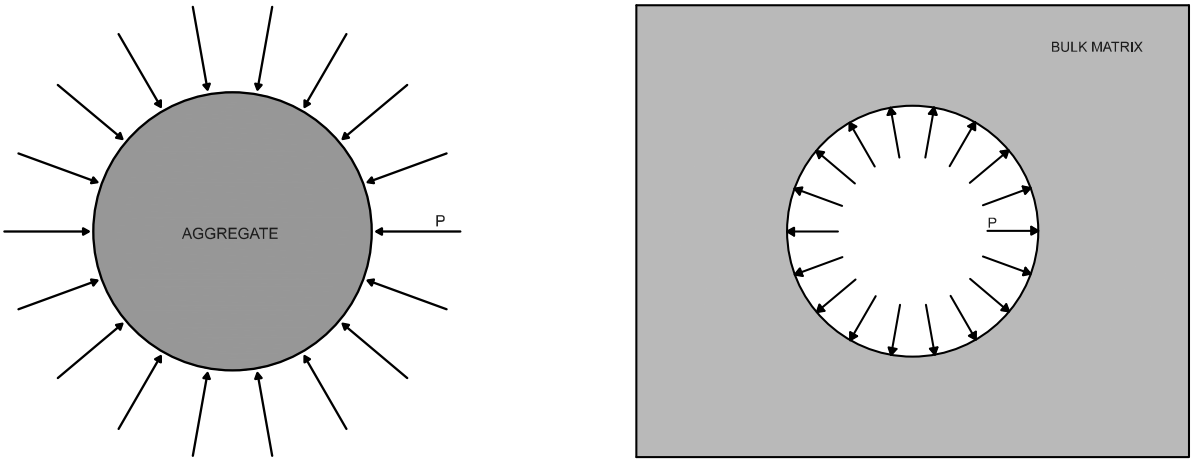

a) b)

Figure 2. a) Solid sphere of radius a with applied external pressure P applied; b) Spherical shell of infinite thickness with internal pressure P.

Substituting Eqs. (3) and (4) into Eqs. (1) and (2) and applying the strain compatibility conditions at $r=a$ ($\varepsilon_{t1}=\varepsilon_{t2}|_{r=a}$), the value of the thermal interaction pressure P is obtained as:

$$P=\frac{\Delta T(\alpha_1-\alpha_2)}{\frac{1+\nu_2}{2E_2}+\frac{1-2\nu_1}{E_1}} \qquad (5)$$

The radial and tangential stress and strain for both phases can be obtained by substituting the obtained value of P into Eqs. (1) through (4).

As expected, Eq. (5) clarifies the linear relationship of P with the CTE mismatch between the aggregate and the matrix represented by the coefficient $(\alpha_1-\alpha_2)$, and the non-linear relationship of P with the elastic mismatch between the aggregate and the matrix represented by E_1 and E_2. From analysis of Eqs. (3) through (5), it can be observed that with a positive value of ΔT (temperature increment), if $\alpha_1>\alpha_2$, tensile stresses are generated in the tangential direction of the second phase (matrix), and thus microcracks are more likely to be generated in the radial direction from the aggregate particle (Figure 3a). Similarly, if $\alpha_1<\alpha_2$, the tensile stresses are oriented in the radial direction in both phases, and microcracks are prone to appear with a tangential orientation between the phases surrounding the aggregate particle (Figure 3b).

The interaction between fine aggregate particles and cement paste is not considered because they are modeled as a unified bulk matrix phase. It has been stated that an ITZ is most likely to occur in the area surrounding large aggregate particles [23]; therefore, microcracks are more likely to occur in the area surrounding large aggregate particles, where a higher porosity and lower strength matrix is observed.

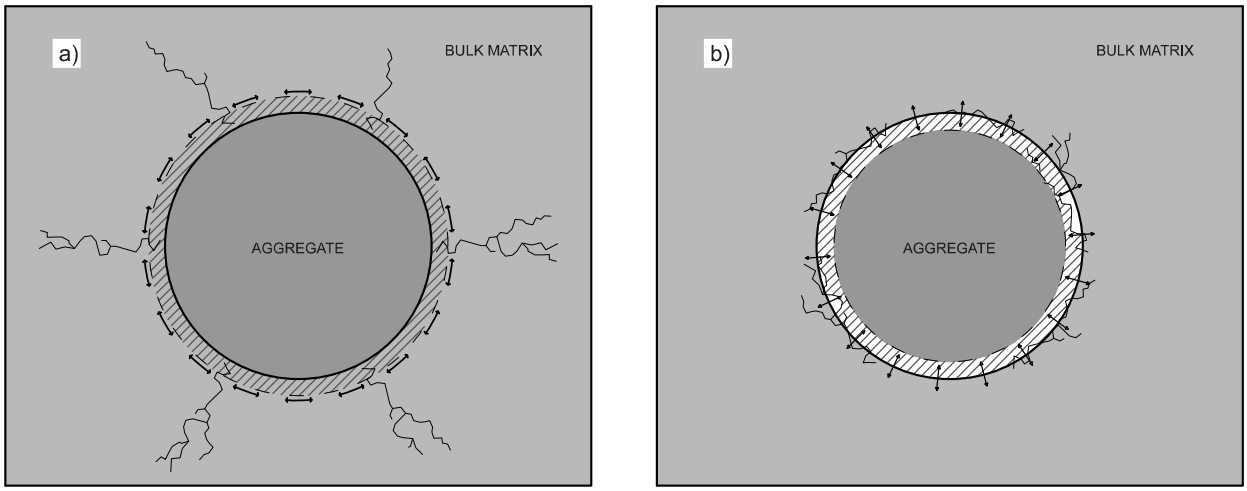

Figure 3. a) Tangential tensile stresses and radial microcracks induced when $\alpha_1>\alpha_2$ and $\Delta T>0$; b) Radial tensile stresses and tangential microcracks induced when $\alpha_1<\alpha_2$ and $\Delta T>0$.

4. Thermal History and Cement Hydration

The time-temperature cycles in concrete, especially at early ages, significantly affect the strength development due to an increase in the hydration reaction rate of cement [1]. For this reason, many researchers have focused their efforts on developing relationships between temperature and strength [42]. In addition, the hydration products generated at accelerated rates due to higher temperatures exhibit a coarser and more porous structure [12], which explains the lower long-term strength reached by concrete cured at higher temperatures [43,44] compare with those cured at 20 ℃.

Saul [45] introduced the maturity concept 60 years ago to account for this effect. According to his research, maturity is the product of temperature cycle ($\theta(t)$) and time (Eq. 6), accounting for a datum temperature (θ_0) below which hydration is unlikely to occur [46,47]:

$$M=\int_0^t (\theta(t)-\theta_0)dt \qquad (6)$$

The ASTM C1074 [48] recommends use of a datum temperature of 0 ºC for Type I Portland cement cured between 0 ºC and 40 ºC. An alternative approach to the maturity function is the equivalent age concept (t_{eq}), defined as the curing time required at a reference temperature (θ_R) to achieve the same maturity level as a concrete that undergoes the actual time-temperature cycle [44,47,49]. The most widely used function for computing equivalent age at a reference temperature θ_R is based on the Arrhenius equation [48,50]:

$$t_{eq}(\theta_R)=\sum_{t=0}^{t} e^{\frac{E_a}{R}\left(\frac{1}{\theta_C}-\frac{1}{\theta_R}\right)} \times \Delta t \qquad (7)$$

where $t_{eq}(\theta_R)$ is the equivalent age at the reference temperature θ_R (K), θ_C (K) is the concrete temperature, Δt is the time interval (days or hours), R is the natural gas constant (8.314 J/mol/K), and E_a is the apparent activation energy (in J/mol), which combines the temperature

sensitivity of the several chemical reactions occurring during cement hydration into one parameter [50]. The same study presents a method used to determine E_a using isothermal calorimetry, which provides a useful tool for accurately modeling the cement hydration kinetics.

5. Experimental Program

The variety of aggregates used in concrete mixtures poses inherent challenges to characterization and engineering of key properties required to improve performance and mechanical behavior in a cementitious matrix [18]. Each type of aggregate type contains a mineralogical composition that conditions the fundamental thermo-mechanical parameters E_1 and α_1, of that particular rock. This fact makes an individual assessment of the CTE and elastic mismatch between the aggregate and the bulk matrix phase impossible because both variables necessarily vary together when the aggregate mineralogy changes.

Temperature variations generate aggregate thermal strain that can be simply denoted as $\alpha_1 \Delta T$, where α_1 is the aggregate CTE. A variation in α_1 changes the thermal stress, increasing or decreasing the CTE mismatch (α_1-α_2) with the matrix. In parallel, a variation in the aggregate elastic modulus E_1 has an non-linear impact on the magnitude of the thermal stress induced by the strains generated due to a temperature change, as shown in Eq. (5). Because E_1 and α_1 are given for a certain aggregate and cannot be varied independently, different time-temperature cycles were used to artificially hold the aggregate thermal strain constant ($\alpha_1 \Delta T$). Thus, the same aggregate expansion scenario can be achieved over a wide range of E_1 values.

Similarly, for a given aggregate, time-temperature cycle adjustments can be used to simulate aggregate thermal strain variations while holding E_1 constant. This goal is achieved by modification of the ΔT term in the $\alpha_1 \Delta T$ expression. The effects of this external handling on the stresses generated between the concrete phases are equivalent to an apparent α_1 modification for a given aggregate of known elastic modulus E_1.

The values of ν_1 and ν_2 were assumed as 0.2 [21]. Because the value of *P* represents a uniform stress in the aggregate and bulk matrix surfaces, the effect of this assumption has low relevance compared with the elastic modulus and CTE mismatches. A representation of the thermo-mechanical experimental design is shown in Figure 4, and details of the considered aggregates will be presented in the Materials and Methods section.

5.1 Design of time-temperature cycles

Four different types of coarse aggregates were selected to explore a wide range of thermo-mechanical properties: expanded shale (LA, lightweight aggregate), calcareous gravel (CA, normalweight aggregate), siliceous gravel (SA, normalweight aggregate), and magnetite (HA, heavyweight aggregate).

Four experimental points were defined in the iso-thermal strain axis, one for each type of aggregate used. Temperature adjustments were chosen accordingly to account for the different α_1 value of each aggregate while holding $\alpha_1 \Delta T$ constant in all cases (determination of aggregate properties will be presented in next section). To explore the effects of the apparent α_1 variation (iso-stiffness axis), the LA and SA were selected due to their significantly different stiffnesses as well as the broad use and availability in the SA case. The experimental points are presented schematically in Figure 4.

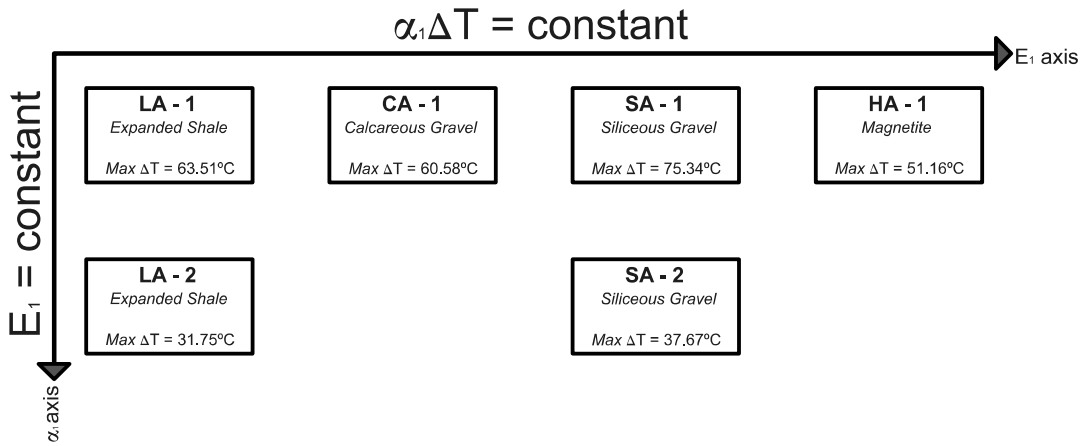

Figure 4. Experimental points explored over a conceptual two-axis thermo-mechanical design.

The time-temperature cycles were based on a real temperature record obtained from a massive concrete foundation. The cooling portion was adjusted to exhibit symmetry with the starting heating ramp, and the general shape of the thermal cycle is shown in Figure 5. The values of T_0, T_1, and T_{MAX} (initial, 1-day, and maximum temperature, respectively) and the aggregate maximum thermal strains are presented in Table 1 for each of the experimental points. Max ΔT was computed as the difference between T_{MAX} and T_0 (20 ºC).

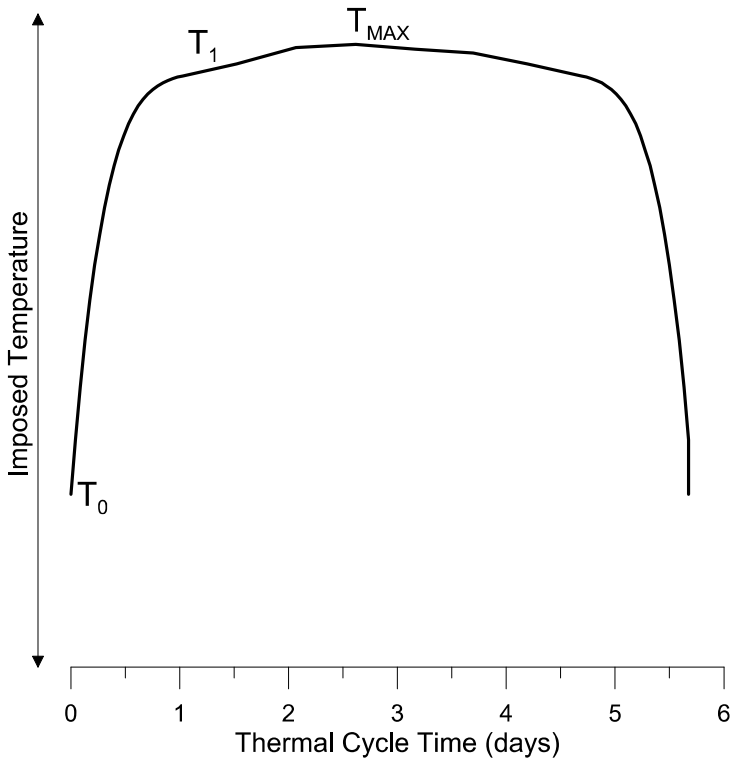

Figure 5. Basic shape of the time-temperature cycle applied to the concrete specimens.

Table 1. Temperature parameters for each experimental point.

Experimental Point	T_1 [ºC]	T_{MAX} [ºC]	Max ΔT [ºC]	Max $\alpha_1 \Delta T$ [$\mu\varepsilon$]
LA – 1	79.4	83.5	63.5	356
CA – 1	76.7	80.6	60.6	356
SA – 1	90.5	95.3	75.3	356
HA – 1	67.9	71.2	51.2	356
LA – 2	49.7	51.8	31.8	178
SA – 2	55.3	57.7	37.7	178

5.2 Concrete mixture proportions

The concrete mixtures were produced using four different types of coarse aggregates. The same base mortar matrix was used for all mixtures and was based on siliceous fine aggregate and Type I ordinary Portland cement (OPC). In all cases, the coarse aggregate volume fraction was 37.5 %, and a water to cement ratio of 0.55 was selected based on the literature to minimize the effects of autogenous shrinkage [5,51–53]. OPC and fine aggregate dosage was fixed at 350 kg/m^3 and 820 kg/m^3, respectively.

Fifteen 10x20 cm cylinders, six 10x10x30 cm prism specimens, and eight 2.5x5.0 cm cylinders were cast for each of the six experimental points studied (Figure 4). The specimens were placed at an environmental chamber for 24 h at (20 ± 3) ºC and covered with plastic sheet to avoid evaporation until removed from the molds.

5.3 Thermal damage testing

After removal from the molds, the specimens were weighed and randomly assigned to the thermal cycle (TC) and equivalent age curing (TE) groups. Five10x20 cm cylinders, three 10x10x30 cm prisms, and four 2.5x5.0 cm cylinders each composed the TC and TE specimen groups.

The TC group refers to specimens subjected to the time-temperature cycles described in Table 1 and were intended to measure the effect of thermal stresses on the concrete properties. The TE group consisted of a set of specimens identical to the TC group and intended to serve as a non-damaged material reference; the specimens in this group were cured at (20 ± 3) ºC for the equivalent age calculated using Eq. (7), and the time-temperature cycle of the TC group. The initial tests on instrumented specimens showed that the maximum temperature gradients between the core and surface (surface gradient) was only 1.5 ºC regardless of the specimen size and shape, which was sufficient to neglect the surface gradient effect and to consider damage produced by a pure mass gradient effect [43]. Specimens from the TC and TE groups were sealed using aluminum tape before undergoing thermal cycles and curing at 20 ºC, respectively. This method proved to be effective in avoiding water losses at high temperatures, which was relevant to avoid the concrete swelling and drying/shrinkage effects present in other curing methods.

5.3.1 Fluorescence microscopy

Fluorescence optical microscopy has been proven as a powerful technique for performing qualitative and quantitative measurements of microcracking in concrete [54–57]. In this study, fluorescence microscopy was used as a tool for qualitative identification of the crack density and morphology in specimens subjected to the time-temperature cycle and the equivalent-age curing. Samples of 1 cm in height were cut from the 2.5x5.0 cm cylinder specimens of the TC and TE groups using a low-speed saw. The samples were cleaned in an ultrasonic bath for 10 min using iso-propanol as cleaning medium. After removal from the bath, the samples were cleaned with compressed air, dried at 35 ºC and 720-mmHg vacuum, and stored under those conditions for 2 h. The samples were finally impregnated using an ultra-low viscosity and high-hardness resin combined with fluorescein (FITC) as a fluorochrome. To avoid additional exposure of the samples to temperatures that could result in unintended microcracking, the resin was cured using UV radiation for 48 h at a laboratory temperature of 20 ºC. After curing, the samples were polished using a standard grinding machine prior to observation. The TE samples were prepared using the same procedure as the TC samples and were intended to provide a reference for cracking generated by the preparation method and other phenomena unrelated to the thermal cycle.

5.3.2 Compressive strength

The compressive strength was measured on 10x20 cm cylinder specimens of each TC and TE group. For the TC and TE specimens, tests were performed after the thermal cycle and equivalent age curing periods, respectively. After completion of electrical resistivity testing, the specimens were also tested for compressive strength. It should be noted that no

significant difference in results were observed between the saturated and non-saturated specimens.

5.3.3 Dynamic elastic modulus

The dynamic elastic modulus was measured on 10x10x30 cm prism specimens of the TC and TE groups according to the ASTM C215 procedure [58]. This method was selected due to its suitability and sensitivity to measurement of concrete damage due to microcracking in freeze-thaw tests. It should be mentioned that the dynamic elastic modulus test is based on measurement of the fundamental resonant frequencies of the specimen and is therefore non-destructive.

5.3.4 Electrical resistivity

The electrical resistivity was measured in 10x20 cm cylinder specimens of the TC and TE groups based on the axial-measurement method described by Spragg et al. [59] to compare changes in the concrete pore percolation due to the presence of microcracks. In this method, two stainless steel plates are placed at the ends of the 10x20 cm cylinder and connected to the same surface resistivity meter used in the Wenner probe apparatus [60]. The obtained electrical resistance values are normalized by the cross-sectional area-to-length ratio of the cylinder to calculate the bulk resistivity of the specimen. Three cylinder specimens were randomly selected, the aluminum tape was removed, and the specimens were submerged in water for 24 h at 20 ºC to achieve saturation of cracks before testing.

6. Materials Characterization

6.1 Cementitious matrix constituents

The Type I OPC chemical composition presented in terms of oxides measured with X-ray fluorescence (XRF) is shown in Table 2, and the particle size distribution (PSD) is presented in Figure 6.

To accurately predict the cement hydration using the Arrhenius equation and calculate the equivalent age (Eq. 7), an accurate measure of the activation energy (E_a) is required. The procedure based on isothermal calorimetry described by Poole et al. [50] was used. The OPC phase composition was determined using X-ray diffraction (XRD) and Rietveld refinement analysis. Fluorite was used as an internal standard to account for the amorphous fraction and to correct the Rietveld results based on the procedure proposed by Chancey et al. [61]. The diffraction pattern with the identified main phases and the phase composition are shown in Figure 7 and Table 3, respectively.

Table 2. Cement chemical characterization.

Composition as oxides (%)	OPC
SiO_2	20.39
Al_2O_3	6.01
Fe_2O_3	3.15
CaO	63.25
Na_2O	0.15
K_2O	0.75
MnO	0.07
TiO_2	0.27
MgO	1.30
P_2O_5	0.08
SrO	0.03
SO_3	2.35
LOI	1.72
Specific gravity (g/cm^3)	3.122

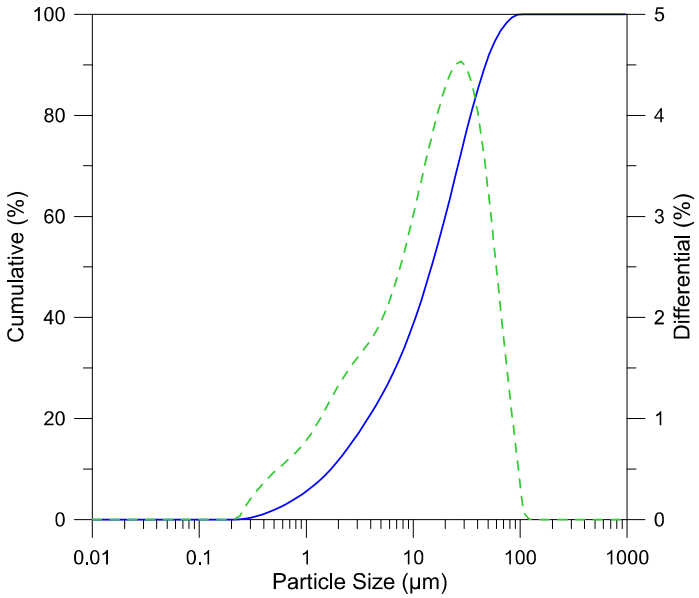

Figure 6. OPC particle size distribution (PSD). The solid line represents the cumulative PSD, and the dashed line corresponds to the differential results.

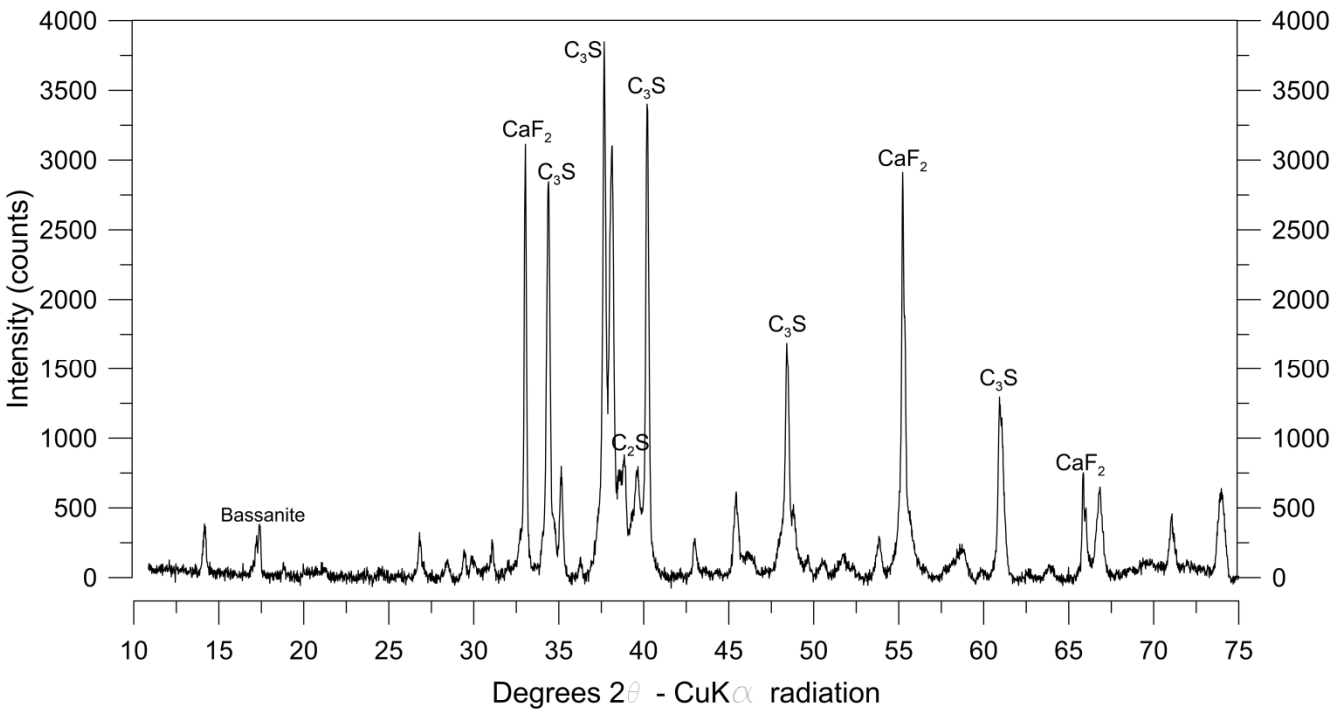

Figure 7. X-ray diffraction pattern of the OPC used for the Rietveld refinement.

Table 3. QXRD analysis of the OPC using the Rietveld refinement and fluorite as an internal standard.

Mineral Name	Formula	Rietveld Presence (% by wt.)
Quartz	SiO_2	1.0
Bassanite	$CaSO_4(H_2O)$	3.1
Anhydrite	$CaSO_4$	1.1
Calcite	$CaCO_3$	1.8
Fluorite (I.S.)	CaF_2	11.5
Lime	$CaCO_3$	0.7
C_3A cubic	$3CaO \cdot Al_2O_3$	8.6
Alpha C_2S	$2CaO \cdot SiO_2$	5.3
Beta C_2S	$2CaO \cdot SiO_2$	1.7
Ferrite (C_4AF)	$4CaO \cdot Al_2O_3 \cdot Fe2O3$	6.8
Alite (C_3S)	$3CaO \cdot SiO_2$	58.4

I.S. = Internal Standard

Isothermal calorimetry tests were carried out using TAM Air isothermal calorimeter at 10 ºC, 20 ºC, 32 ºC and 40 ºC. In all cases, a 0.55 w/c cement paste was used. The maximum heat of hydration (H_u) used to normalize the heat curves and obtain the degree of hydration plots was calculated using the equation proposed by Bogue [62]:

$$H_u = 500 \cdot p_{C_3S} + 260 \cdot p_{C_2S} + 866 \cdot p_{C_3A} + 420 \cdot p_{C_4AF} + 624 \cdot p_{SO_3} + 1186 \cdot p_{FreeCa} + 850 \cdot p_{MgO} \quad (8)$$

where p_x represents the mass ratio of phase x to the total cement material. A commercial non-linear regression package was employed to adjust the model presented in [50] with the obtained degree-of-hydration plots. The computed value for H_u was 460.17 J/g, which is in good agreement with total heat of hydration values reported for numerous other OPC samples [50,62]. The apparent activation energy was subsequently calculated using the equation proposed by Schindler [11], and the resulting value was 45,880 J/mol. This parameter was used to compute the equivalent ages using Eq. (7) for all experimental points. The heat plots together with the regression fit at each temperature and the Arrhenius plot of the applied OPC are presented in Figure 8.

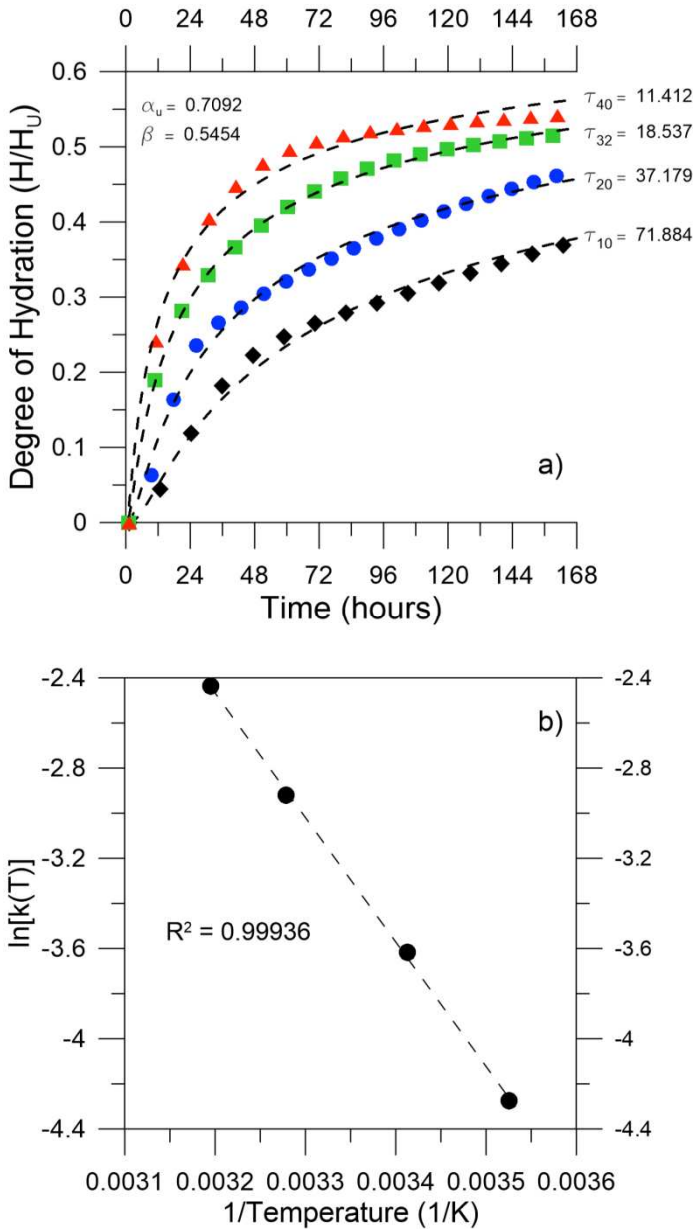

Figure 8. a) Isothermal calorimetry results (dots) and exponential regression (dashed line); b) Arrhenius plot of OPC.

The bulk matrix CTE (α_2) was measured over time using 2.54x2.54x25.4 cm prismatic specimens and a digital length comparator. The applied mixture proportions were the same as those used for concrete but without the coarse aggregate. Because the matrix CTE is influenced by the relative humidity content [63], the specimens were sealed using aluminum tape after removal from the molds. Fifteen specimens were prepared, and three of each type were tested daily from 2 d to 28 d in age and every week up to 66 d. The specimens were heated to 50 ºC, measured in the length comparator (L_{50}), and subsequently cooled to room temperature (T_{LAB}) for a new length measurement (L_{LAB}). The temperature was recorded using a thermocouple embedded within one specimen subjected to the same time-temperature cycle and used exclusively for temperature recording. The CTE of the matrix (α_2) was computed using Eq. (9):

$$\alpha_2 = \frac{\frac{L_{50}-L_{LAB}}{L_{LAB}}}{50-T_{LAB}} \qquad (9)$$

The results for CTE tests of the bulk matrix are presented in Figure 9 in which a clear increasing trend is observed during the first 20 d. This observation is consistent with previous results [63] and is attributed to the reduction in internal relative humidity due to ongoing hydration. However, after 40 d of curing, the CTE change with time stabilizes, presumably due to a reduction in the hydration rate at lower internal relative humidity levels.

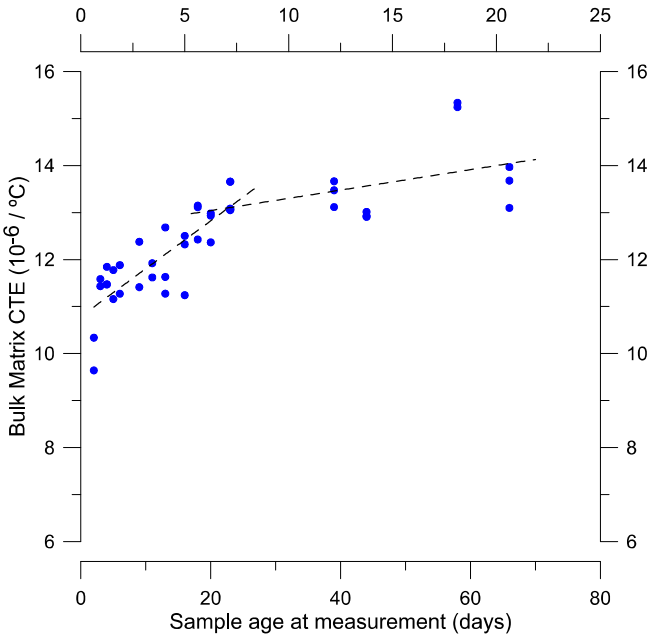

Figure 9. Bulk matrix CTE (α_2) measured over time.

6.2 CTE and E of coarse aggregates

The aggregate CTE (α_1) was measured using thermo-mechanical analysis (TMA) using a TA 943 instrument. Tests were carried out between -20 ºC and 120 ºC in samples with four different grains for each type of aggregate. For the LA aggregate, eight grains were considered in four tests parallel to the cleavage plane and four tests perpendicular to the cleavage plane. The grains were cooled from room temperature (approximately 25 ℃) to -30 ℃ and held until the temperature stabilized. The spe cimen was heated to 130 ℃ at a rate of

5 ℃/min. The test was performed under a load of 1 g (10 mN) and a flow of dry nitrogen at 25 mL/min. If the data showed excessive noise, extreme discontinuities, or outlier behavior due to sample placement or outer vibration, the data collection process was halted, the grain was re-cooled, and the test was restarted. The averages and standard deviations of the measured CTE values are summarized in Table 5.

The aggregate elastic modulus (E_1) of the aggregate grains is difficult to measure due to the irregular shapes that they present. Several composite models were proposed for estimating the concrete elastic modulus based on matrix and aggregate properties [39]. The Hirsch model was selected due to good agreement between the predicted and theoretical values [38]. In this study, the concrete and bulk matrix elastic moduli (E_C and E_m, respectively) were measured to compute the aggregate elastic modulus using Eq. (10) with knowledge of the volume fraction of the aggregate (V_a). The concrete mixtures were assembled following the procedure proposed by Moreno et al. [64] using a V_a equal to 0.4. The x parameter was experimentally adjusted using steel and aluminum chunks as coarse aggregates and was estimated at 0.5. Values for each aggregate type are presented in Table 4:

$$E_C = \frac{1}{x\left[\frac{V_a}{E_1} + \frac{1-V_a}{E_m}\right] + (1-x)\left[\frac{1}{V_a E_1 + (1-V_a)E_m}\right]} \qquad (10)$$

Table 4. Aggregate CTE (α_1) and elastic modulus (E_1) computed using the compound Hirsch model.

Aggregate Type	Specific gravity (SSD) ρ_a	Average α_1 [10^{-6}/ºC]	STD [10^{-6}/ºC]	Average E_1 [GPa]	STD [GPa]
LA	1.628	5.61	0.52	12.48	0.45
CA	2.566	5.88	2.73	50.24	8.37
SA	2.698	4.73	0.74	55.45	2.80
HA	4.220	6.96	0.52	85.70	2.40

7. Results and Discussion

7.1 Fluorescence microscopy

Thermo-mechanical characterization of the coarse aggregates (Table 4) and the bulk matrix (Figure 9) showed that all four aggregates had a CTE significantly lower than that of the matrix (i.e., $\alpha_1 < \alpha_2$), and this difference increases with the age of the matrix. Based on the proposed two-phase micromechanical model, these results suggest that upon heating, the expected microcracks are more likely to be oriented similar to those in Figure 3b because the tensile stresses will develop in the radial direction. This presumption was confirmed based on fluorescence microscope observation of TC specimens of all experimental points considered. The microcracks were distributed primarily along the ITZ surrounding the aggregates, as shown in the micrographs (Figures 10a to 10f) for all aggregate types and time-temperature cycles imposed. Dark field (DF) images of the same micrograph for each fluorescence picture are included to aid in phase identification.

Dark Field (DF)	TC Series	Fluorescence (FITC)
	a) LA-1	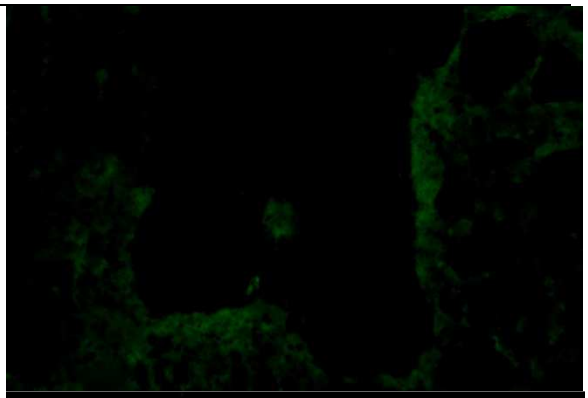
	b) CA-1	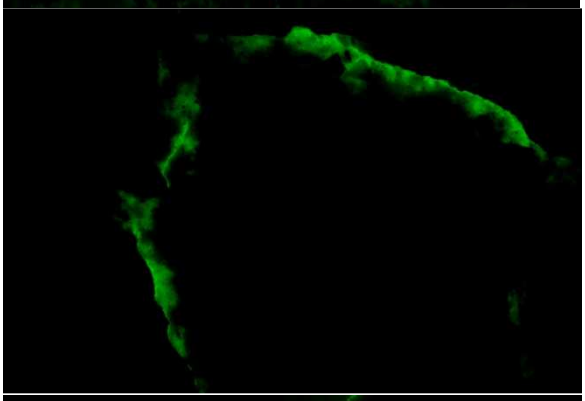
	c) SA-1	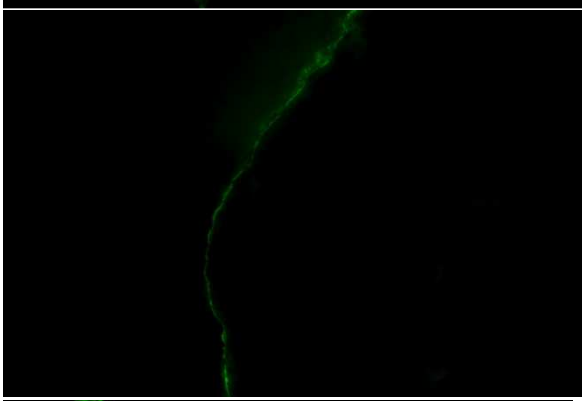
	d) HA-1	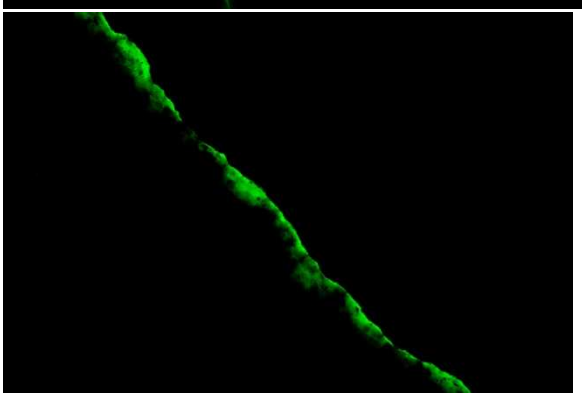

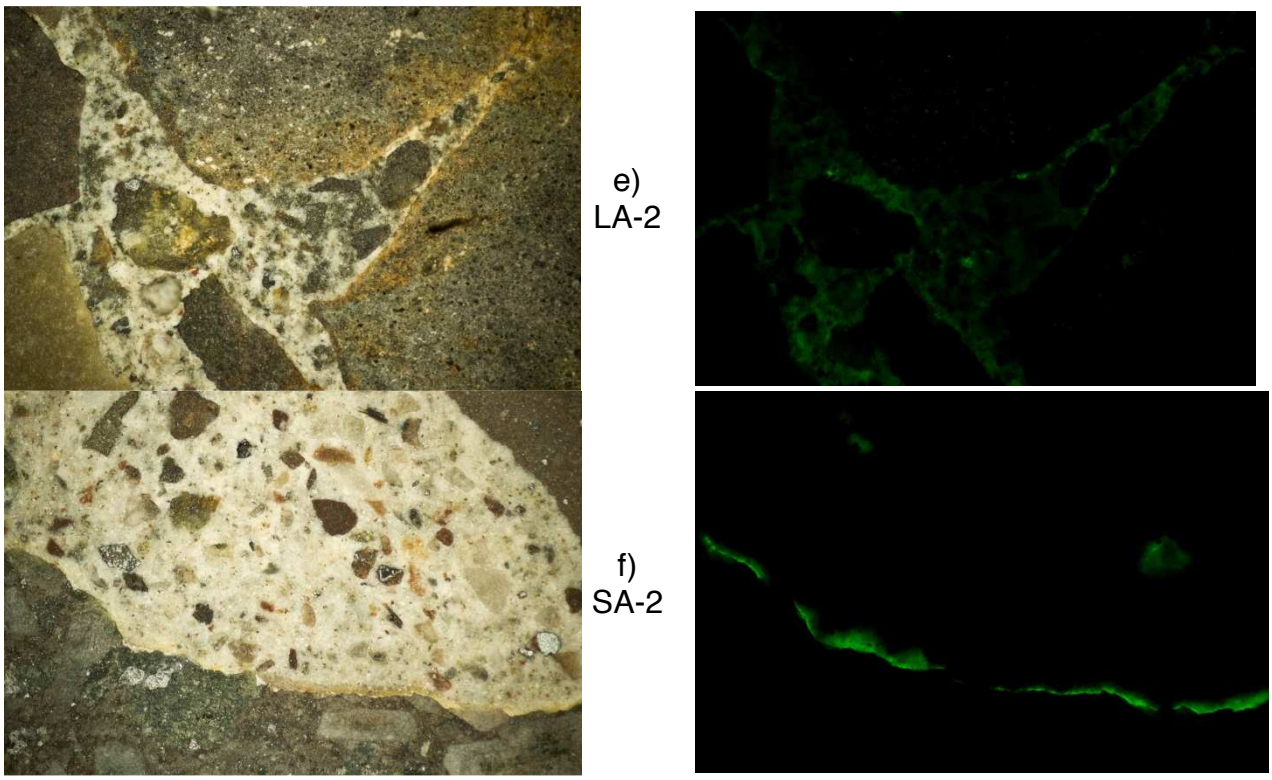

Figure 10. Dark field (DF) and fluorescence images of microcracks observed on the ITZ on all experimental series (a-to-f).

To assure that the microcracks observed in Figure 10 were in fact due to thermal stresses and not due to drying shrinkage or artifacts that occurred during sample preparation, careful observations of TE samples were conducted. The presence of microcracks was significantly lower compared with that of the TC samples, as shown in Figure 11.

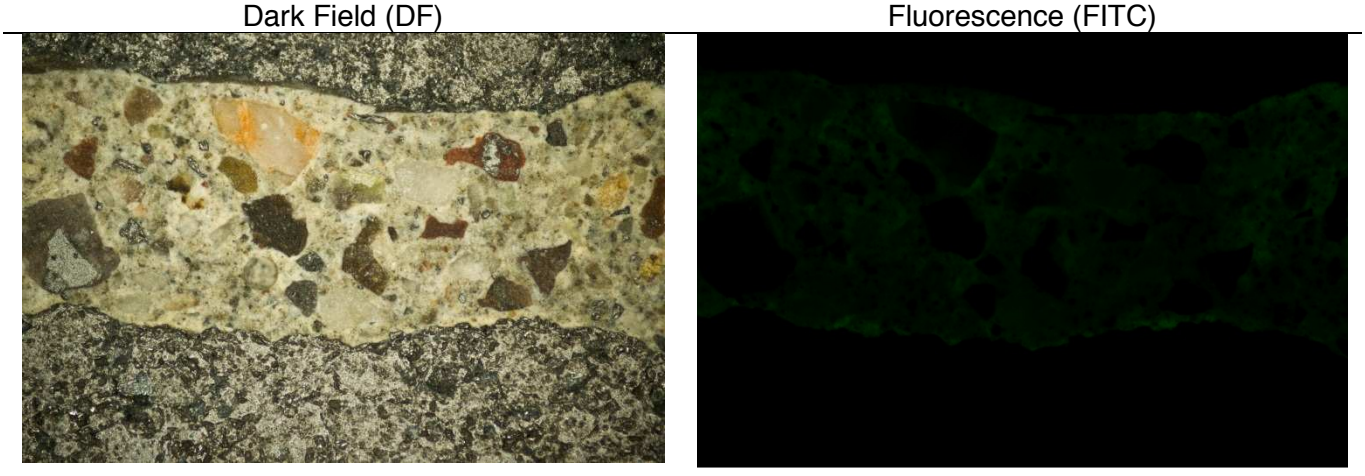

Figure 11. Dark field (DF) and fluorescence images of the ITZ zone in samples not subjected to thermal stresses.

Fluorescence microscopy observations confirmed the presence of microcracks at different levels and extensions in the TC samples. The presence of incremental damage due to time-temperature cycles validates the need for statistical analysis of the influence of such damage on the mechanical and transport properties (compressive strength, elastic modulus, and electrical resistivity) and the use of mechanical parameters in the two-phase micromechanical model.

In addition to the thermal stresses and damage, it should be noted that a lower quality and higher porosity CSH matrix would have been generated due to the increased rate of reaction in the TC samples. Thus, the overall damage to the concrete is due to the increased thermal stresses and increased matrix porosity.

7.2 Compressive Strength

The results of the compressive strength tests are shown in Figure 12 and are divided into two charts (a and b) according to the experimental program design: one shows the iso-thermal strain and the other displays the iso-stiffness. The hatched bars show the TE results, and the overlapped grey bars present the TC results. The gap between the gray and the green-dashed bars represents the strength loss due to thermally induced microcracks.

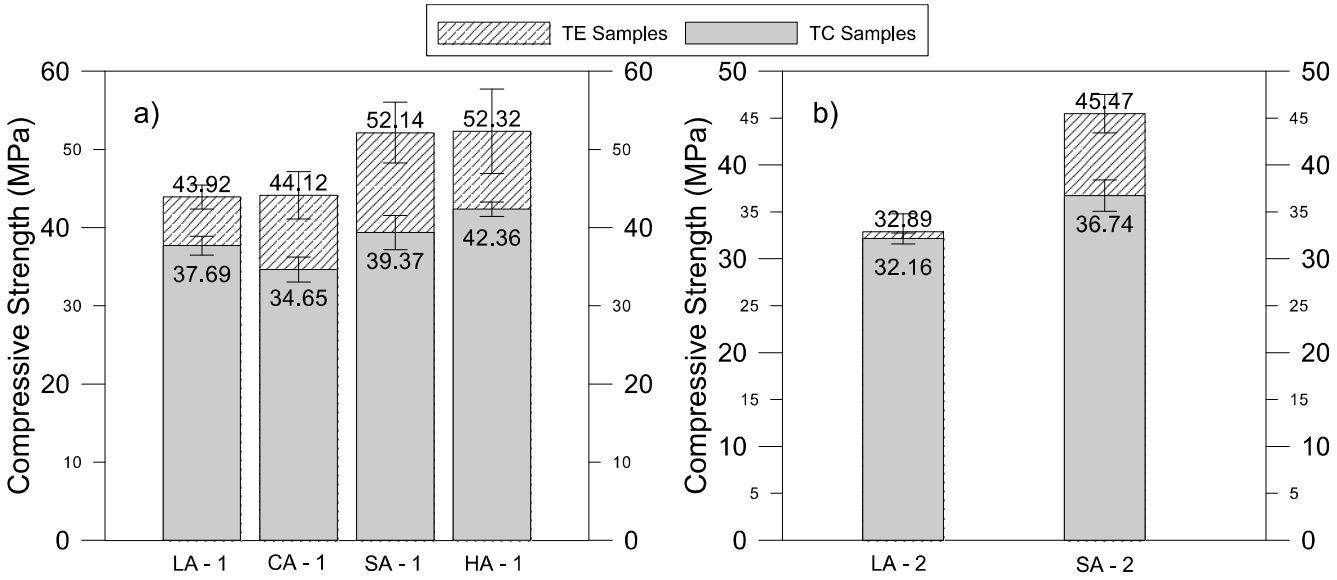

Figure 12. Compressive strength results of TC and TE specimens: a) High aggregate thermal expansion level; b) Low aggregate thermal expansion level. Error bars represent the standard deviation of the average of three samples.

Statistically significant strength losses were observed in all of the high aggregate expansion series (Figure 12a). A greater relative strength loss was observed in the SA-1 specimens attributed to the high CTE mismatch combined with a relatively high elastic modulus of this aggregate, which leads to an increased deformation of the matrix and a high maximum interaction pressure (*P*) value. It is interesting to note that a high stiffness aggregate such as the HA will not necessarily lead to high thermal stresses between the aggregate and the bulk matrix because the value of P is determined not only by the elastic modulus of the aggregate but also by its CTE. Particularly in the HA case, its high elastic modulus is compensated to a

certain extent with the reduced CTE mismatch between the HA and the bulk matrix. This situation yields a lower value of P compared with that of the SA and CA. In the same way, although the LA has a higher CTE mismatch compared with HA, its stiffness is significantly lower, resulting in the lowest computed maximum *P* value. All of these theoretical derivations based on aggregate and bulk matrix characterizations are observed in the compressive strength results.

Figure 12b shows that no significant strength losses were observed in the LA-2 specimens, which imply that the thermal stresses generated were lower than the developing tensile strength of the matrix, and thus, significant microcracking did not occur during the thermal cycle.

To correlate the experimental results with the theoretical derivations from the micromechanical model, two reference parameters were selected. The interaction pressure *P,* due to the direct relationship between this value and the stresses in both phases and its ease of computation, making it suitable to be used as a practical index of thermal damage. In addition, the radial deformation of the bulk matrix ε_{r2} was selected because tensile stresses will occur primarily in this direction according to the model (Figure 3b).

The average compressive strength performance ratios were computed by dividing the average strength of the TC specimens into the corresponding average strength of the TE specimens for each of the six experimental points. These ratios are a numerical representation of the strength losses for which a ratio of 1 implies no decrement in compressive strength of TC specimens compared with that of the TE specimens. The plots of TC/TE compressive strength ratios against their corresponding maximum *P* (Figure 13a) or ε_{r2} (Figure 13b) values achieved during the time-temperature cycles were analyzed, and a non-linear trend was observed.

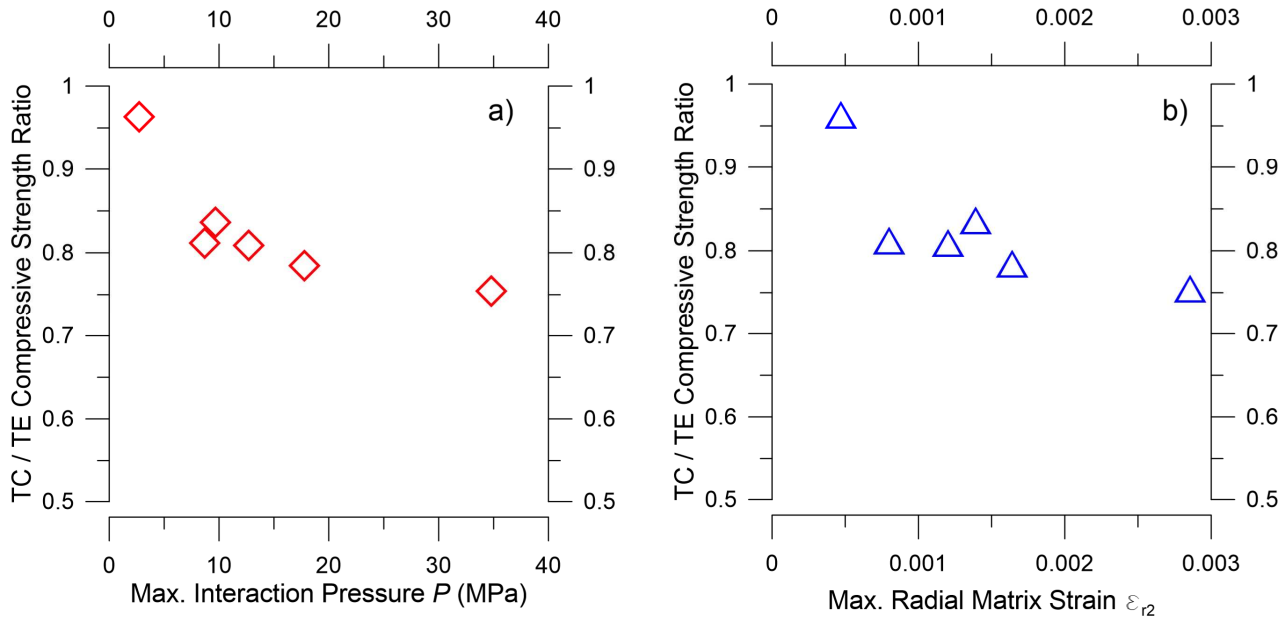

Figure 13. a) TC/TE compressive strength ratios correlated with *P* values; b) TC/TE compressive strength ratios correlated with ε_{r2} values.

It is interesting to note that the computed ε_{r2} values are consistent with the strains that cement paste and concrete are able to withstand before rupture. In the case of SA-1, which presented the most pronounced loss in strength, the maximum radial matrix strains were close to 0.003 mm/mm, suggesting that the maximum strain capacity on average of the matrix was overcome. The non-linear behavior of the compressive strength loss trend could be attributed to presence of the ITZ, neglected in the proposed model. The quasi-brittle behavior of concrete under compression is attributed to multiple microcrack development on the ITZ [24]. In addition, formation of microcracks is not uniform over the loading range [65].Thus, the relationship between *P* and compressive strength is expected to be non-linear.

7.3 Dynamic elastic modulus

The results of measurements of the dynamic elastic modulus are presented in Figure 14 using the same data distribution described for compressive strength.

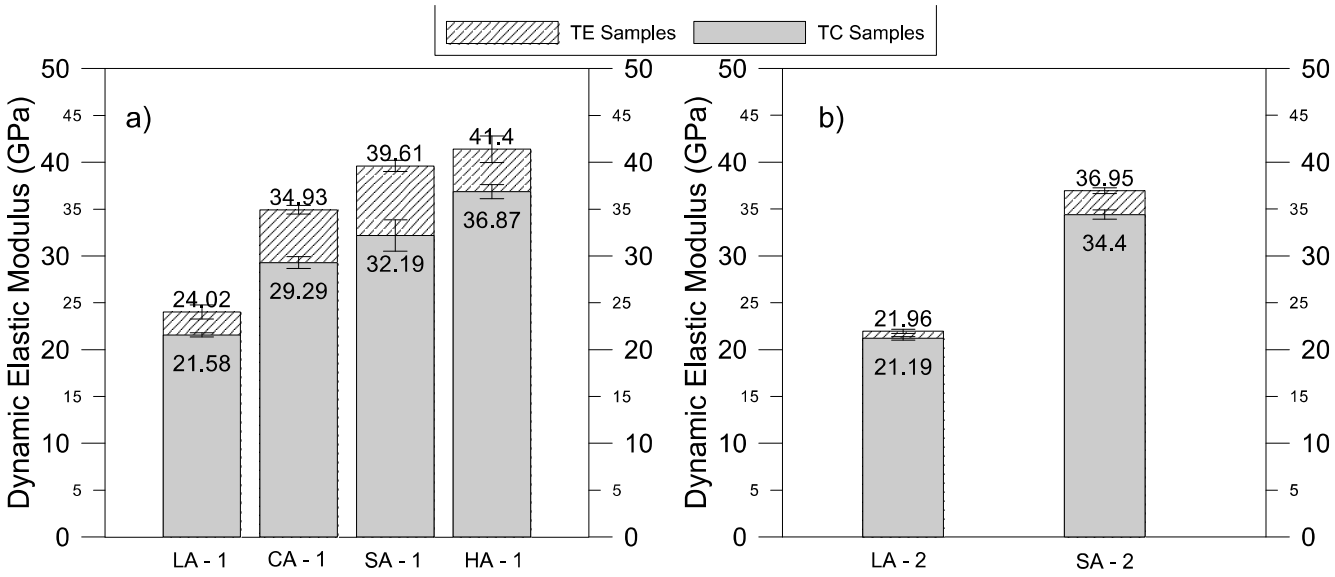

Figure 14. Dynamic elastic modulus results of TC and TE specimens: a) High aggregate thermal expansion level; b) Low aggregate thermal expansion level. Error bars represent the standard deviation of the average of three samples.

Consistent with the findings for compressive strength, larger elastic modulus losses for the TC concrete specimens were observed in SA-1 and CA-1. Statistically significant differences between the corresponding TC and TE results were observed in all of the high aggregate expansion series (Figure 14a) and only in the SA-2 specimens in the low aggregate expansion level (Figure 14b).

Similar to the compressive strength results, the average elastic modulus performance ratios were computed by dividing the average elastic modulus of TC specimens into the corresponding average result of the TE specimens for each of the six experimental points. Plots of the TC/TE elastic modulus ratios against their corresponding maximum *P* (Figure 15a) and ε_{r2} (Figure 15b) values achieved during the thermal cycle were studied. In this case, a linear trend was observed between the elastic modulus losses represented by the ratios and the maximum *P* and ε_{r2}.

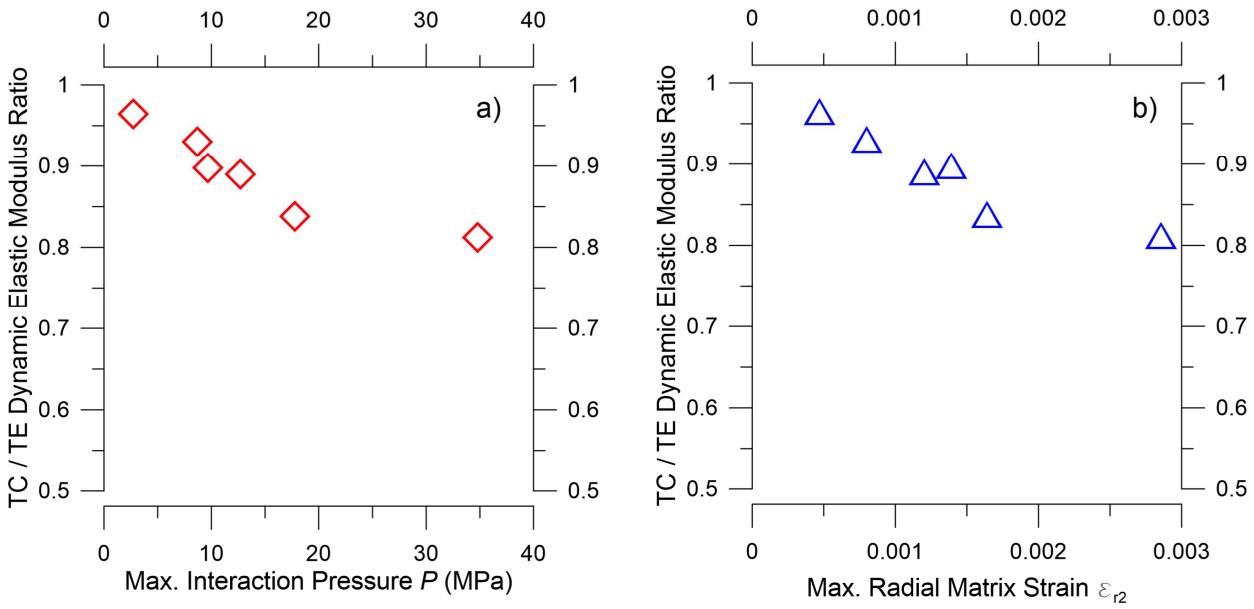

Figure 15. a) TC/TE elastic modulus ratios correlated with *P* values; b) TC/TE elastic modulus ratios correlated with ε_{r2} values.

7.4 Electrical resistivity

The electrical resistivity tests were intended as an indication of concrete percolation due to microcrack propagation. This and other common permeability tests, i.e., the ASTM C1202 rapid chloride penetration test, are based on the assumption that a variation in electrical current passing through the concrete specimen can be attributed to pore and microcrack interconnection and thus to a higher concrete permeability [7,66–68]. For this reason, the inclusion of a conductive material inside the concrete could lead to misleading results because an increase in the current passing through concrete could be attributed not only to increased permeability but also to the presence of the conductive material. The HA aggregates have a high iron content, which is evidenced in its pronounced ferromagnetic behavior, and therefore, the electrical resistivity results do not apply to the HA specimens.

The results of electrical resistivity measurements are presented in Figure 16 using the same data distribution described for the compressive strength and dynamic elastic modulus. As expected, the electrical resistivity values of the HA-1 specimens are significantly lower than those of other specimens containing non-conductive aggregates. Because the bulk matrix is the same in all concrete specimens considered in this study, the difference is attributed to the conductive characteristics of this particular aggregate type.

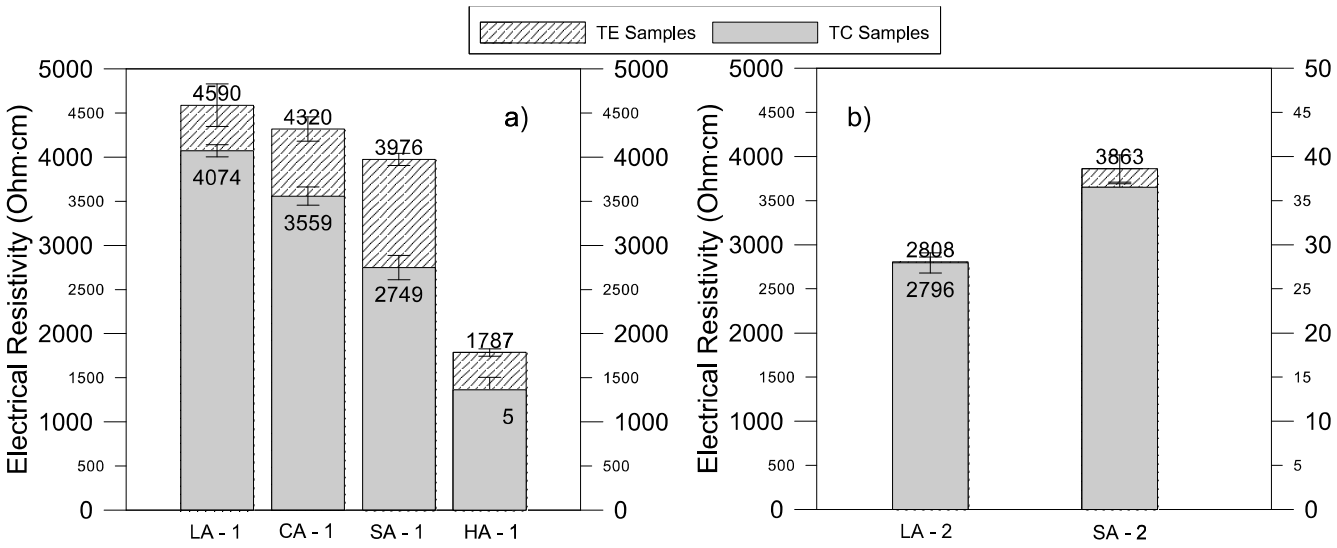

Figure 16. Electrical resistivity results of TC and TE specimens: a) High aggregate thermal expansion level; b) Low aggregate thermal expansion level. Error bars represent the standard deviation of the average of three samples.

As observed from the mechanical properties, the major relative permeability increases are observed in the SA-1 and CA-1 specimens (Figure 16a). For the low aggregate expansion series (Figure 16b), no statistically significant difference was observed in LA-2, and a slight increase in permeability was measured in the SA-2 specimens subjected to a time-temperature cycle. Due to the conductive character of the HA aggregate, the results cannot be attributed only to an increased permeability. The aggregate proportion in each particular 10x20 cm cylinder, which might vary due to the compaction procedure [69], could affect the results of this particular specimen group.

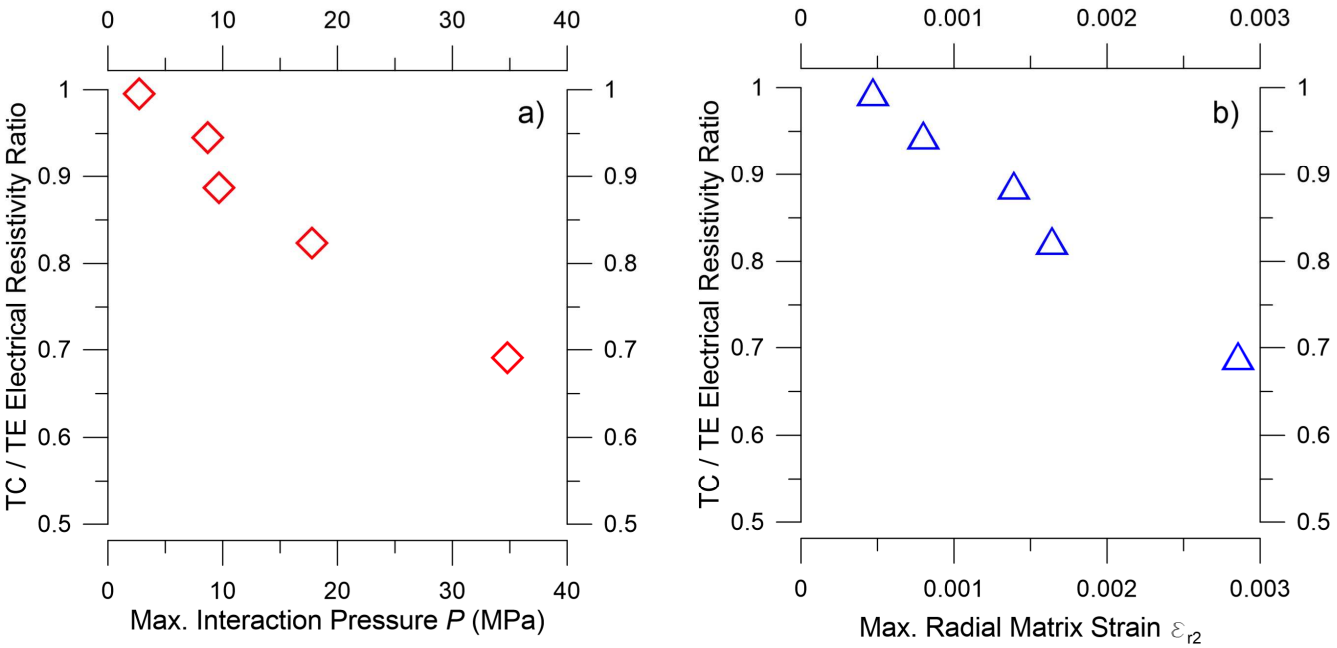

Figure 17 a) TC/TE electrical resistivity ratios correlated with *P* values; b) TC/TE electrical resistivity ratios correlated with ε_{r2} values.

For this reason, these results were excluded from the statistical comparison between the electrical resistivity ratios and maximum P and ε_{r2} values; these results are shown on Figure 17a and 17b, respectively, and a linear trend was observed between the resistivity losses represented by the ratios and the maximum P and ε_{r2}.

8. Conclusions

Thermal stresses are generated in early-age concrete due to heat release from the ongoing cement hydration. Because concrete is a complex mixture of different constituents, thermo-mechanical mismatches occur, which generate differential expansion between the concrete phases, resulting in stresses. These stresses occur when the cementitious matrix begins to develop stiffness and thus restricts the expansion of the concrete phases. In addition, the matrix tensile strength undergoes early stages of development, leaving the concrete prone to microcracking and damage due to this effect.

The objective of this study was to understand the driving mechanical factors that control the thermal stress generation in the interface between the aggregate and the bulk matrix. A two-phase (aggregates and bulk matrix) micromechanical model was proposed to predict the thermal stresses based on thermo-mechanical mismatches between concrete phases. Two main mismatches were identified: CTE mismatch and elastic mismatch.

Extensive characterization of the concrete phases was carried out to ensure proper modeling of the thermal stresses and thus enable the comparison of these predictions with the observed performance under experimental conditions. These conditions were intended to damage the concrete using time-temperature cycles imposed in a controlled laboratory environment. Based on the experimental measurements and theoretical calculations, the following conclusions can be stated:

1. A simplified two-phase concrete model proved to be sufficiently accurate for prediction of damage to concrete from the thermal stresses generated due to differential thermal expansion of its phases. Additionally, the non-complex form of the expressions derived from this model makes it suitable for application to thermal cracking risk assessment in real structures and mixture design procedures based on thermo-mechanical characterization of concrete constituents. Despite it has been shown that the ITZ is the locus of all damage observed, the simplified two-phase model proved to be a reliable approach to estimate the order of magnitude of the impact of thermal cracking on strength, elastic modulus and permeability.
2. The interaction pressure P proved to be a good parameter for estimating the thermal cracking risk expressed as the deterioration of key mechanical parameters in the design and durability properties, i.e., compressive strength, modulus of elasticity, and permeability. To accurately apply the proposed model and compute P, a careful thermo-mechanical characterization (CTE and modulus of elasticity) of the concrete phases should be carried out.
3. Fluorescence microscopy was demonstrated as a valuable tool for evaluating the presence and morphology of microcracking in concrete. This approach is particularly relevant to application and correlation of observed damage in concrete with thermal stress models due to concrete experiments and other early-age phenomena that could induce damage, i.e., autogenous shrinkage. The observation of non-exposed

specimens confirmed that the generated microcracks were attributable to the time-temperature cycles.

4. Considering the high variability in the thermo-mechanical properties of aggregates of natural origin, such as those used in this study, the model is able to produce an order of magnitude of the expected deterioration of the considered concrete properties. Although alternatives to measuring the CTE and stiffness of coarse aggregates were presented in this study, the inherent difficulties in measuring these properties in aggregates of irregular shape poses additional challenges to the development of new testing methods for accurate measurement of these parameters in a more simple and direct manner.

The elastic approach used in this study neglects the time-dependent behavior in cement paste, i.e., creep and stress relaxation, and thus, it tends to overestimate the stresses in the ITZ. However, the strain and interaction pressure P calculations allowed for a good estimate of the cracking risk.

Further research is required to assess the effects of cement substitutions, the use of admixtures, variations in the mixture proportions, and other design properties on the thermo-mechanical parameters. Future work is needed to understand and develop new methodologies that reduce the thermal cracking risk at the design stage and to address the thermo-mechanical compatibility orientation, rather than mitigating heat release at the construction site.

9. Acknowledgements

The authors greatly acknowledge funding provided by FONDECYT, project Nº1120817 and the support provided by CEDEUS, CONICYT/FONDAP 15110020. The authors also recognize Cementos Polpaico, CAP Minería, DICTUC S.A., Sebastián Calderón and Mauricio Guerra for their contributions to this research project.

10. References

[1] P. Mehta, P. Monteiro, Concrete: Microstructure, Properties, and Materials, 3rd ed., McGraw-Hill Professional, New York, 2005.

[2] D.P. Bentz, O.M. Jensen, Mitigation strategies for autogenous shrinkage cracking, Cem. Concr. Compos. 26 (2004) 677–685. doi:10.1016/S0958-9465(03)00045-3.

[3] P.K. Mehta, Durability - Critical Issues for the Future, Concr. Int. 19 (1997) 69–76.

[4] O.M. Jensen, P.F. Hansen, Autogenous deformation and RH-change in perspective, Cem. Concr. Res. 31 (2001) 1859–1865.

[5] E. Holt, Contribution of mixture design to chemical and autogenous shrinkage of concrete at early ages, Cem. Concr. Res. 35 (2005) 464–472. doi:10.1016/j.cemconres.2004.05.009.

[6] N. Gowripalan, V. Sirivivatnanon, C.C. Lim, Chloride diffusivity of concrete cracked in flexure, Cem. Concr. Res. 30 (2000) 725–730. doi:10.1016/S0008-8846(00)00216-7.

[7] A. Konin, R. François, G. Arliguie, Penetration of chlorides in relation to the microcracking state into reinforced ordinary and high strength concrete, Mater. Struct. 31 (1998) 310–316.

[8] H.R. Samaha, K.C. Hover, Influence of microcracking on the mass transport properties of concrete, ACI Mater. J. 89 (1992) 416–424.

[9] K. Wang, D.C. Jansen, S.P. Shah, A.F. Karr, Permeability study of cracked concrete, Cem. Concr. Res. 27 (1997) 381–393.

[10] ACI 231R, Report on Early-Age Cracking□: Causes , Measurement , and Mitigation, 2010.

[11] A.K. Schindler, Effect of Temperature on Hydration of Cementitious Materials, ACI Mater. J. 101 (2004) 72–81.

[12] E. Gallucci, X. Zhang, K.L. Scrivener, Effect of temperature on the microstructure of calcium silicate hydrate (C-S-H), Cem. Concr. Res. 53 (2013) 185–195. doi:10.1016/j.cemconres.2013.06.008.

[13] G. Escadeillas, J.-E. Aubert, M. Segerer, W. Prince, Some factors affecting delayed ettringite formation in heat-cured mortars, Cem. Concr. Res. 37 (2007) 1445–1452. doi:10.1016/j.cemconres.2007.07.004.

[14] H.F.. Taylor, C. Famy, K.. Scrivener, Delayed ettringite formation, Cem. Concr. Res. 31 (2001) 683–693. doi:10.1016/S0008-8846(01)00466-5.

[15] Z. Zhang, J. Olek, S. Diamond, Studies on delayed ettringite formation in early-age , heat-cured mortars I . Expansion measurements , changes in dynamic modulus of elasticity , and weight gains, Cem. Concr. Res. 32 (2002) 1729–1736.

[16] ACI 207-2R, Report on Thermal and Volume Change Effects on Cracking of Mass Concrete, 2007.

[17] ACI 224.1R, Causes , Evaluation , and Repair of cracks in Concrete Structures, 2007.

[18] M.G. Alexander, Aggregates and the Deformation Properties of Concrete, ACI Mater. J. 93 (1996).

[19] T.W. Bremner, T.A. Holm, Elastic Compatibility and the Behavior of Concrete, ACI J. 83 (1986) 244–250.

[20] J. Selsing, Internal Stresses in Ceramics, J. Am. Ceram. Soc. 44 (1961) 419.

[21] C. Zhou, B. Huang, D. Ph, M. Asce, X. Shu, A.M. Asce, Micromechanical Model for Predicting Coefficient of Thermal Expansion of Concrete, J. Mater. Civ. Eng. 25 (2013) 1171–1180. doi:10.1061/(ASCE)MT.1943-5533.0000663.

[22] K.M. Lee, J.H. Park, A numerical model for elastic modulus of concrete considering interfacial transition zone, Cem. Concr. Res. 38 (2008) 396–402. doi:10.1016/j.cemconres.2007.09.019.

[23] A.U. Nilsen, P.J.M. Monteiro, Concrete□: A three phase material, Cem. Concr. Res. 23 (1993) 147–151.

[24] K. Scrivener, A. Crumbie, P. Laugesen, The Interfacial Transition Zone (ITZ) Between Cement Paste and Aggregate, Interface Sci. 12 (2004) 411–421.

[25] D.P. Bentz, A review of early-age properties of cement-based materials, Cem. Concr. Res. 38 (2008) 196–204. doi:10.1016/j.cemconres.2007.09.005.

[26] A.N. Noumowe, R. Siddique, G. Debicki, Permeability of high-performance concrete subjected to elevated temperature (600℃), Constr. Bui ld. Mater. 23 (2009) 1855–1861. doi:10.1016/j.conbuildmat.2008.09.023.

[27] Y. Lee, M.-S. Choi, S.-T. Yi, J.-K. Kim, Experimental study on the convective heat transfer coefficient of early-age concrete, Cem. Concr. Compos. 31 (2009) 60–71. doi:10.1016/j.cemconcomp.2008.09.009.

[28] C. Qian, G. Gao, Reduction of interior temperature of mass concrete using suspension of phase change materials as cooling fluid, Constr. Build. Mater. 26 (2012) 527–531. doi:10.1016/j.conbuildmat.2011.06.053.

[29] A. Pourasee, A. Peled, J. Weiss, M. Asce, Fluid Transport in Cracked Fabric-Reinforced- Cement-Based Composites, ASCE J. Mater. Civ. Eng. (2011) 1227–1238. doi:10.1061/(ASCE)MT.1943-5533.0000289.

[30] Z. Yang, W.J. Weiss, J. Olek, Water Transport in Concrete Damaged by Tensile Loading and Freeze – Thaw Cycling, ASCE J. Mater. Civ. Eng. (2006) 424–434.

[31] D.P. Bentz, E.J. Garboczi, Y. Lu, N. Martys, A.R. Sakulich, W.J. Weiss, Modeling of the influence of transverse cracking on chloride penetration into concrete, Cem. Concr. Compos. 38 (2013) 65–74. doi:10.1016/j.cemconcomp.2013.03.003.

[32] W. Zhu, P.J.. Bartos, Application of depth-sensing microindentation testing to study of interfacial transition zone in reinforced concrete, Cem. Concr. Res. 30 (2000) 1299–1304. doi:10.1016/S0008-8846(00)00322-7.

[33] J. Xiao, W. Li, Z. Sun, D. a. Lange, S.P. Shah, Properties of interfacial transition zones in recycled aggregate concrete tested by nanoindentation, Cem. Concr. Compos. 37 (2013) 276–292. doi:10.1016/j.cemconcomp.2013.01.006.

[34] S. Erdem, A.R. Dawson, N.H. Thom, Influence of the micro- and nanoscale local mechanical properties of the interfacial transition zone on impact behavior of concrete made with different aggregates, Cem. Concr. Res. 42 (2012) 447–458. doi:10.1016/j.cemconres.2011.11.015.

[35] P. Trtik, P.J.M. Bartos, Micromechanical properties of cementitious composites, Mater. Struct. 32 (1999) 388–393.

[36] W. Zhu, P.J.. Bartos, Assessment of interfacial microstructure and bond properties in aged grc using a novel microindentation method, Cem. Concr. Res. 27 (1997) 1701–1711.

[37] X.H. Wang, S. Jacobsen, J.Y. He, Z.L. Zhang, S.F. Lee, H.L. Lein, Application of nanoindentation testing to study of the interfacial transition zone in steel fiber reinforced mortar, Cem. Concr. Res. 39 (2009) 701–715. doi:10.1016/j.cemconres.2009.05.002.

[38] T.J. Hirsch, Modulus of Elasticity of Concrete Affected by Elastic Moduli of Cement Paste Matrix and Aggregate, ACI J. 59 (1962) 427–452.

[39] H. Chen, T. Yen, K. Chen, Evaluating Elastic Modulus of Lightweight Aggregate, ACI Mater. J. 100 (2003) 108–113.

[40] A.U. Nilsen, P.J.M. Monteiro, O.E. Gjcrv, Estimation of the elastic moduli of lightweight aggregate, Cem. Concr. Res. 25 (1995) 276–280.

[41] D. Burgreen, Elements of thermal stress analysis, Arcturus Publishing, London, 1971.

[42] R.C. Tank, N.J. Carino, Rate Constant Functions for Strength Development of Concrete, ACI Mater. J. 88 (1991) 74–83.

[43] A. Neville, Properties of Concrete, 4th Editio, Pearson Education Limited, Essex, 1995.

[44] Y. a. Abdel-Jawad, The maturity method: Modifications to improve estimation of concrete strength at later ages, Constr. Build. Mater. 20 (2006) 893–900. doi:10.1016/j.conbuildmat.2005.06.022.

[45] A.G.A. Saul, Principles underlying the steam curing of concrete at atmospheric pressure, Mag. Concr. Res. 2 (1951) 127–140.

[46] G. Chengju, Maturity of concrete: method for predicting early- stage strength, ACI Mater. J. (1989) 341–353.

[47] G. Deschutter, Applicability of degree of hydration concept and maturity method for thermo-visco-elastic behaviour of early age concrete, Cem. Concr. Compos. 26 (2004) 437–443. doi:10.1016/s0958-9465(03)00067-2.

[48] ASTM C1074, Standard Practice for Estimating Concrete Strength by the Maturity Method, (2004). doi:10.1520/C1074-04.2.

[49] S.-T. Yi, Y.-H. Moon, J.-K. Kim, Long-term strength prediction of concrete with curing temperature, Cem. Concr. Res. 35 (2005) 1961–1969. doi:10.1016/j.cemconres.2005.06.010.

[50] J.L. Poole, M. Asce, K.A. Riding, M.C.G. Juenger, K.J. Folliard, A.K. Schindler, Effect of Chemical Admixtures on Apparent Activation Energy of Cementitious Systems, ASCE J. Mater. Civ. Eng. 23 (2011) 1654–1661. doi:10.1061/(ASCE)MT.1943-5533.0000345.

[51] M.. Zhang, C.. Tam, M.. Leow, Effect of water-to-cementitious materials ratio and silica fume on the autogenous shrinkage of concrete, Cem. Concr. Res. 33 (2003) 1687–1694. doi:10.1016/S0008-8846(03)00149-2.

[52] L. Barcelo, M. Moranville, B. Clavaud, Autogenous shrinkage of concrete: a balance between autogenous swelling and self-desiccation, Cem. Concr. Res. 35 (2005) 177–183. doi:10.1016/j.cemconres.2004.05.050.

[53] C. Pichler, R. Lackner, H. a. Mang, A multiscale micromechanics model for the autogenous-shrinkage deformation of early-age cement-based materials, Eng. Fract. Mech. 74 (2007) 34–58. doi:10.1016/j.engfracmech.2006.01.034.

[54] A. Litorowicz, Identification and quantification of cracks in concrete by optical fluorescent microscopy, Cem. Concr. Res. 36 (2006) 1508–1515. doi:10.1016/j.cemconres.2006.05.011.

[55] P. Soroushian, M. Elzafraney, A. Nossoni, Specimen preparation and image processing and analysis techniques for automated quantification of concrete microcracks and voids, Cem. Concr. Res. 33 (2003) 1949–1962. doi:10.1016/S0008-8846(03)00219-9.

[56] U.H. Jakobsen, D.R. Brown, Reproducibility of w/c ratio determination from fluorescent impregnated thin sections, Cem. Concr. Res. 36 (2006) 1567–1573. doi:10.1016/j.cemconres.2006.05.003.

[57] P. Soroushian, M. Elzafraney, Morphological operations, planar mathematical formulations, and stereological interpretations for automated image analysis of concrete microstructure, Cem. Concr. Compos. 27 (2005) 823–833. doi:10.1016/j.cemconcomp.2004.07.008.

[58] ASTM C215, Standard Test Method for Fundamental Transverse , Longitudinal , and Torsional Resonant Frequencies of Concrete Specimens, (2008). doi:10.1520/C0215-08.2.

[59] R.P. Spragg, J. Castro, T. Nantung, M. Paredes, J. Weiss, Variability Analysis of the Bulk Resistivity Measured Using Concrete Cylinders, Adv. Civ. Eng. Mater. 1 (2012) 1–17. doi:10.1520/ACEM104596.

[60] W. Morris, E.I. Moreno, A.A. Sagüés, Practical Evaluation of resistivity of concrete in test cylinders using a Wenner array probe, Cem. Concr. Res. 26 (1996) 1779–1787.

[61] R.T. Chancey, P. Stutzman, M.C.G. Juenger, D.W. Fowler, Comprehensive phase characterization of crystalline and amorphous phases of a Class F fly ash, Cem. Concr. Res. 40 (2010) 146–156. doi:10.1016/j.cemconres.2009.08.029.

[62] R.H. Bogue, The chemistry of portland cement, Reinhold, New York, 1947.

[63] I. Maruyama, a. Teramoto, Effect of water-retaining lightweight aggregate on the reduction of thermal expansion coefficient in mortar subject to temperature histories, Cem. Concr. Compos. 34 (2012) 1124–1129. doi:10.1016/j.cemconcomp.2012.08.003.

[64] D. Moreno, P. Martinez, M. Lopez, Practical Approach for Assessing Lightweight Aggregate Potential for Concrete Performance, ACI Mater. J. 111 (2014) 123–132.

[65] C.. Lim, N. Gowripalan, V. Sirivivatnanon, Microcracking and chloride permeability of concrete under uniaxial compression, Cem. Concr. Compos. 22 (2000) 353–360. doi:10.1016/S0958-9465(00)00029-9.

[66] K.A. Riding, J.L. Poole, A.K. Schindler, M.C.G. Juenger, K.J. Folliard, Simplified Concrete Resistivity and Rapid Chloride Permeability Test Method, (2009) 1–5.

[67] R. Corral, S. Arredondo, J. Almaral, J. Gómez, Corrosión por cloruros del acero de refuerzo embebido en concreto con agregado grueso reciclado y materiales cementantes suplementarios, Rev. Ing. Construcción. 28 (2013) 21–35. doi:10.4067/SO718-50732013000100002.

[68] V. Saraswathy, H.-W. Song, Corrosion performance of rice husk ash blended concrete, Constr. Build. Mater. 21 (2007) 1779–1784.

[69] D. Moreno, F. Zunino, Á. Paul, M. Lopez, High strength lightweight concrete (HSLC): Challenges when moving from the laboratory to the field, Constr. Build. Mater. 56 (2014) 44–52. doi:10.1016/j.conbuildmat.2014.01.068.

Highlights

- Early-age time-temperature cycles damage observed on a variety of concrete mixtures
- Mismatch between strain in concrete phases as main cause of cracking due to mass gradients
- Simplified two-phase micromechanical model proposed to assess thermal stresses
- Detailed thermo-mechanical characterization of elastic modulus and CTE of phases
- Interaction pressure (P) selected as indicator of thermal cracking damage level

APPENDIX E: PAPER 2 OFFICIAL SUBMISSION TO CEMENT AND CONCRETE COMPOSITES – JUNE 2014

Elsevier Editorial System(tm) for Cement and Concrete Composites

Manuscript Draft

Manuscript Number:

Title: Decoupling the physical and chemical effects of supplementary cementitious materials on strength and permeability: a multi-scale approach

Article Type: Research Paper

Keywords: sustainability, supplementary cementitious materials, rice husk ash, natural pozzolans, isothermal calorimetry, durability

Corresponding Author: Dr. Mauricio Lopez, PhD

Corresponding Author's Institution: Pontificia Universidad Catolica de Chile

First Author: Franco Zunino, MSc

Order of Authors: Franco Zunino, MSc; Mauricio Lopez, PhD

Abstract: Supplementary cementitious materials (SCMs) represent an alternative for the industry to achieve sustainability by reducing cement contents without significant compromises of the mechanical properties and enhancing durability. SCMs play a dual role during hydration: a physical effect promoting nucleation and cement hydration and a chemical effect through pozzolanic activity. Rice husk ash (RHA) and natural pozzolans (NP) were evaluated using compressive strength and durability tests in a multi-scale experimental program. RHA increased the strength more than NP, which is well explained by its prominent chemical effect (78%) assessed by isothermal calorimetry and its high amorphous silica content. Both RHA and NP produced significant reductions in the permeability of the concrete, which is mostly explained by the chemical effect. Decoupling the physical and chemical effects of a SCM allows for optimisation of its manufacturing process.

Cover Letter

June 28th, 2014

Dr. Nemkumar Banthia,
Editor-in-Chief,
Cement and Concrete Composites
ELSEVIER

Dear Dr Banthia,

On behalf of my co-author, Franco Zunino, I am submitting our manuscript entitled: "Decoupling the physical and chemical effects of supplementary cementitious materials in strength and permeability: a multi-scale approach". In this study we assess the effects of OPC-by-SCM substitutions using a multi-scale experimental program (cement paste, mortar and concrete) focused on separating (decoupling) and understanding physical and chemical contributions of rice husk ash and natural pozzolans to strength durability.

All authors have read and approved the manuscript. There are no author disclosures. The manuscript has not been published and is not being considered for publication elsewhere in whole or in part, in any language.

Thank you very much for considering our work.

Sincerely,

Mauricio Lopez
Associate Professor
Department of Construction Engineering and Management
School of Engineering
Pontificia Universidad Catolica de Chile

Decoupling the physical and chemical effects of supplementary cementitious materials on strength and permeability: a multi-scale approach

Franco Zunino[a], Mauricio Lopez[bc]

[a] Department of Construction Engineering and Management, *School of Engineering, Pontificia Universidad Catolica de Chile, Vicuña Mackenna 4860, Casilla 306, Correo 22, Santiago, Chile. E-mail: fazunino@ing.puc.cl*
[b](Corresponding author) Department of Construction Engineering and Management, *School of Engineering, Pontificia Universidad Catolica de Chile*
[c] *Researcher, Center for Sustainable Urban Development (CEDEUS). Pontificia Universidad Catolica de Chile*
Vicuña Mackenna 4860, Casilla 306, Correo 22, Santiago, Chile. E-mail: mlopez@ing.puc.cl
Phone: 562-2-354-4245 Fax: 562-2-354-4806

Abstract

Supplementary cementitious materials (SCMs) represent an alternative for the industry to achieve sustainability by reducing cement contents without significant compromises of the mechanical properties and enhancing durability. SCMs play a dual role during hydration: a physical effect promoting nucleation and cement hydration and a chemical effect through pozzolanic activity. Rice husk ash (RHA) and natural pozzolans (NP) were evaluated using compressive strength and durability tests in a multi-scale experimental program. RHA increased the strength more than NP, which is well explained by its prominent chemical effect (78%) assessed by isothermal calorimetry and its high amorphous silica content. Both RHA and NP produced significant reductions in the permeability of the concrete, which is mostly explained by the chemical effect. Decoupling the physical and chemical effects of a SCM allows for optimisation of its manufacturing process.

Keywords: sustainability, supplementary cementitious materials, rice husk ash, natural pozzolans, isothermal calorimetry, durability

1 Introduction

The cement industry has faced new environmental challenges in the last decades, such as energy consumption and CO_2 emission reductions [1]. Developments addressing these challenges have focused on the exploration and use of supplementary cementitious materials (SCMs) to reduce the cement content in concrete mixes [2–6] and enhance the durability of the material to increase the service life of concrete structures [7,8].

Rice husk ash (RHA) is obtained from agricultural waste, and has been widely investigated [9–11]. World rice production rose to approximately 722 billion tonnes in 2011 [12]. The main uses of rice husks are as fuel for the paddy milling process [13] and electric power plants [14]. Effects of rice husk ash on concrete strength ([9,10,13,15–17]) and durability ([15,18–21]) are well documented in the literature. RHA reactivity mainly depends on the particle size distribution ([15,17,22]) and the burning temperature and time of the husks [17,23,24].

Natural pozzolans (NP) from volcanic origins have been used in Chilean blended cements since the 1960's. While chemical and physical properties vary depending on the pozzolan source,

performance in compressive strength and durability have been studied in different places where this material is available [25–28].

The effects of SCMs can be analysed as two simultaneous, non-divisible contributions occurring in a cementitious system:

1. *Chemical contribution*, referred as the pozzolanic effect, which is related to the formation of hydration products from the portlandite (CH) produced during cement hydration and the amorphous silica phases present in supplementary cementitious material [3,29]. The rate of reaction depends on the particle size (finer materials have more specific surface to react) and the availability of amorphous silica, water and CH.
2. *Physical contribution*, referred to as the filler effect, is related to changes in the particle spacing and surface availability for nucleation of hydration products [3,30].

As stated in the literature [3,30], the filler effect can be decomposed into dual opposing physical interactions of the inert material with the cementitious matrix [31]. First, the dilution effect is equivalent to increasing the water-to-cement ratio (w/c). Because an inert filler does not produce hydration products, the separation between cement particles increases, which makes hydration products less compact at the same water-to-solids ratio. The second effect, related to the additional surface added by the fine inert material particles, provides more nucleation sites for the hydration products [3] and is referred to as the heterogeneous nucleation effect.

While several studies have characterised the effects of natural pozzolan and rice husk ash on the compressive strength and permeability of concrete separately ([9,17–22,25,26,28,32,33]), there is a lack of investigations comparing both materials under the same testing conditions. In addition, the physical and chemical effects are commonly not distinguished, and the results are reported as the overall performance of the corresponding supplementary cementitious material. Because particle size distribution affects chemical reactivity and physical interaction of the addition material, a thorough characterisation of its performance requires assessing both contributions separately.

This paper assesses RHA and NP performance by focusing on the chemical and physical interactions. In addition, a multi-scale (cement paste, mortar and concrete) approach and testing program is presented.

2 Materials and Methods

To assess the physical (filler) and chemical (pozzolanic) effects of SCMs accurately, two types of materials were used in this study. First, chemically inert filler was used as a reference for the physical interaction of particles on cement hydration and its influence on the measured properties. Secondly, SCMs, containing amorphous silica phases, were evaluated and compared in the same experimental program. Because these materials exhibit both behaviours simultaneously (filler and pozzolanic), inert filler is used to assess the chemical contribution of the SCMs by allowing an estimate of the physical component by itself.

2.1 Material manufacture and characterisation

Type I ordinary Portland cement (OPC) conforming to ASTM C150 was used in all tests conducted in this study.

Rice husk ash (RHA) was manufactured from 24 kg of locally obtained rice husks. Husks were burnt under controlled conditions in two steps: in the first step, batches of approximately 6 kg were burned in an industrial furnace at approximately 600ºC for 4 hours; in the second step, the ash produced was re-burnt at 700ºC for 3 hours in batches of approximately 50 g in small crucibles using a laboratory furnace. The two-step procedure was based on previous research that showed that optimal silica production was achieved by heating rice husks at 700ºC for 6 hours [23], which created uniformity in the combustion process and removed any remaining organic matter.

Natural pozzolan (NP) from a volcanic source was obtained from a local blended cement manufacturer. This variety of pozzolans has been used in Chilean cements as SCMs for decades and was considered in this study as a comparative performance reference of a widely used SCM in the local concrete industry.

Inert filler was obtained by crushing mill graded siliceous sand conforming to ASTM C778 in a jar mill using steel balls as the grinding media. This sand was selected instead of commercial concrete filler due to its high quartz content and, therefore, its non-pozzolanic nature [3,30]. Two particle size distributions (PSD) were obtained: coarse filler by grinding sand for 3 days in the jar mill (FILL3), and fine filler by reprocessing the coarse filler in a smaller jar mill for one week (FILL7). This was done to have comparative PSD boundaries for all the SCMs considered in this study so that physical and chemical interactions could be compared.

RHA and NP were ground prior to grinding in a jar mill for 1 hour to achieve a uniform PSD. The chemical composition of the OPC, RHA and NP was measured using XRF and is presented as oxides in Table 1. High amounts of SiO_2 were identified in both SCMs, but it was especially high in the RHA. In addition, the PSD was measured for all the materials used.

Table 1. Chemical composition of the OPC, NP and RHA.

Percentage of oxides (%)	OPC	RHA	NP
SiO_2	11.3	84.20	66.97
Al_2O_3	3.29	0.56	13.51
Fe_2O_3	3.33	1.13	1.82
CaO	73.9	1.38	3.33
Na_2O	0.48	0.38	3.87
K_2O	0.36	4.30	3.32
MnO	0.18	0.62	0.08
TiO_2	0.31	0.04	0.24
MgO	<0.01	0.56	0.65
P_2O_5	0.10	0.99	0.14
LOI	2.68	5.05	6.06
Specific gravity	3.184	2.158	2.432

Thermogravimetric analysis (TGA/DTG) of the materials was conducted under a nitrogen flux, with a temperature ramp up to 1000ºC. The DTG results are presented in Figure 1, were no

significant decomposition is observed for the inert filler, which is consistent with a mainly quartz composition and suggests a high chemical stability. The weight loss of the RHA at approximately 100ºC is attributed to water loss. A clear decarbonation peak is shown on the OPC plot slightly above 700ºC.

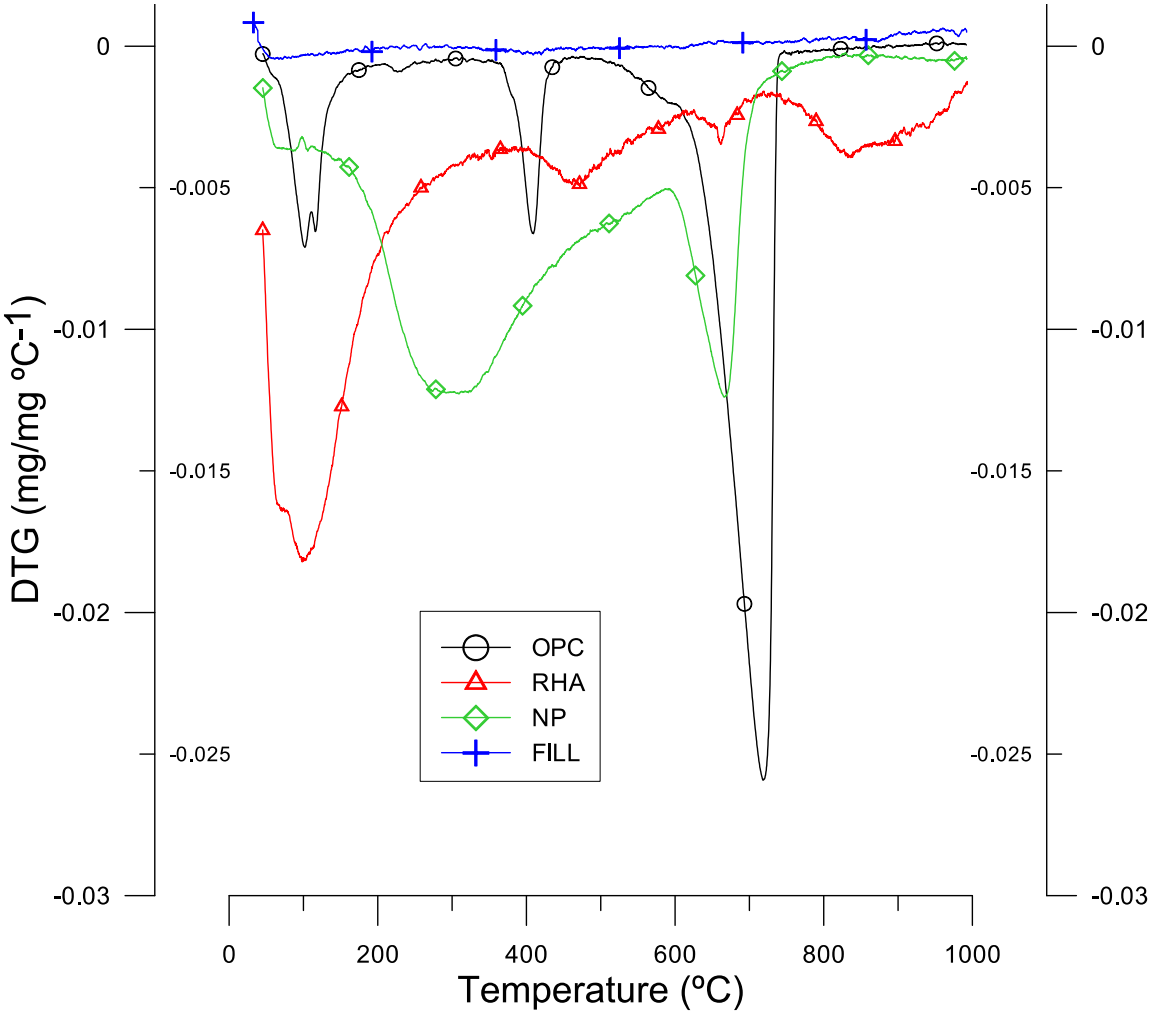

Figure 1. Differential thermogravimetric (DTG) curves of the OPC, NP, RHA and inert filler (FILL).

2.2 X-Ray diffraction

Quantitative X-Ray diffraction (QXRD) analysis was performed to determine the mineral composition of the RHA and NP. Testing was performed between 10-75º 2θ at a 0.02º per second sampling rate. Commercially available software (EVA and TOPAS) was employed for phase identification and Rietveld refinement, respectively. Fluorite was selected as the internal standard to account for the amorphous fraction and correct the Rietveld results, based on the procedure proposed by Chancey et al. [34].

2.3 Isothermal calorimetry

Isothermal calorimetry is a widely used technique to characterise hydration and blended cement systems [35,36]. In this particular study, tests were conducted using a TAM Air Isothermal Calorimeter to assess the impact of different SCMs and inert filler on the hydration kinetics. Cement pastes with water-to-cementitious materials ratio by weight (W/CM) is 0.5 in all cases. The replacement levels of 20% by weight of the OPC by RHA, NP, FILL3 and FILL7 were used. Tests were carried out at 23ºC for 7 days. Duplicate samples were measured for each mixture.

2.4 Compressive strength

The compressive strength was also measured to evaluate the impact of different SCMs on the mechanical behaviour. This assessment was performed at two different scales: cement paste and mortars. Cement pastes were used to evaluate the effects of a broad range of OPC-by-SCMs replacement levels in a pure cementitious matrix environment, while mortar mixtures were used for assessing the interaction between the SCM matrix and aggregates.

2.4.1 Cement paste

Paste mixtures were made using 0, 10, 20, 30, 50 and 75% OPC-by-SCM replacement levels by weight for the four materials studied (RHA, NP, FILL3 and FILL7). Cubic specimens with 2 cm sides were used with a constant W/CM ratio of 0.5 in all cases. Specimens were removed from moulds after one day of curing and stored in sealed bags in a 20 ± 3ºC and 95% Relative Humidity (RH) chamber until the time of testing. Compressive strength tests were conducted at 7, 28 and 90 days with a constant 1800 N/s load rate in all cases.

To compare the observed SCM effects on strength with porosity variations of the cement matrix, 100% OPC pastes were tested in the same conditions with W/CM ratios of 0.4, 0.45, 0.5, 0.55 and 0.6. This allows expressing the SCM's positive/negative impacts on the compressive strength as equivalent quantities of cement addition/subtraction, or as a variation of the W/CM ratio.

2.4.2 Mortar

Mortar mixtures were made with 0, 10, 20 and 30% OPC-by-SCM replacement levels by weight. RHA and NP were used for all cases, while FILL3 substitution was made at the central level of replacement (20%) only to estimate the filler effect on the compressive strength at this scale. Cubic specimens with 5 cm sides were made using a constant W/CM ratio of 0.5 in all cases. Additionally, some adjustments were made to keep the cementitious paste (OPC + SCM + mixing water) volume constant in all mixtures, so that the paste-to-aggregate ratio would not change. Standard graded sand conforming to ASTM C778 was used in all mortar mixtures. Specimens were removed from the moulds after one day of curing and stored submerged in tap water inside a 20 ± 3ºC and 95% RH chamber until time of testing. Compressive strength tests were conducted at 3, 7, 28 and 90 days with a constant 1800 N/s load rate in all cases. Mixture designs of the mortar series are detailed in Table 2.

Table 2. Mixture proportions of the mortar specimens.

Level (%)	SCM ID	W/CM	OPC (kg/m^3)	Mixing Water (kg/m^3)	SCM (kg/m^3)	Std. Sand (kg/m^3)
0	0	0.5	504.1	252.0	0	1562.6
10	RHA	0.5	445.5	247.5	49.5	1562.6

20	NP	0.5	448.3	249.1	49.8	1562.6
	RHA	0.5	389.0	243.1	97.2	1562.6
	NP	0.5	393.8	246.2	98.5	1562.6
	FILL3	0.5	397.2	248.3	99.3	1562.6
30	RHA	0.5	334.4	238.9	143.3	1562.6
	NP	0.5	340.7	243.3	146.0	1562.6

2.5 Durability

The effect of different SCMs on durability was measured using concrete specimens. For this purpose, 0, 10, 20 and 30% OPC-by-SCM replacement levels by weight were considered using RHA and NP. As in the mortar series, FILL3 was used in the central level of replacement. Similarly to the mortars, some adjustments were made to keep the cementitious paste volume (OPC + SCM + mixing water) constant in all mixtures, so that the paste-to-aggregate ratio was constant. Four 10-by-20 cm cylinder specimens were made at each substitution level with a constant 0.5 W/CM ratio. A commercial superplasticiser admixture was used at a weight dosage of 0.8% of cementitious materials to improve workability. Specimens were kept in moulds for one day, and then were cured submerged in tap water in a 20 ± 3ºC and 95% RH chamber until 90 days of age, when all durability tests were performed. Mixture proportions can be found in Table 3.

Table 3. Mixture proportions of the concrete specimens for durability testing.

Level (%)	SCM ID	W/ CM	OPC (kg/m^3)	Mixing Water (kg/m^3)	SCM (kg/m^3)	Fine Sand (kg/m^3)	Coarse Sand (kg/m^3)	Coarse Agg. (kg/m^3)
0	-	0.5	350.0	175.0	0	185.0	647.0	1036.1
10	RHA	0.5	309.4	171.9	34.4	185.0	647.0	1036.1
	NP	0.5	311.3	173.0	34.6	185.0	647.0	1036.1
20	RHA	0.5	270.1	168-8	67.5	185.0	647.0	1036.1
	NP	0.5	273.5	170.9	68.4	185.0	647.0	1036.1
	FILL3	0.5	275.8	172.4	68.9	185.0	647.0	1036.1
30	RHA	0.5	232.2	165.9	99.5	185.0	647.0	1036.1
	NP	0.5	236.6	169.0	101.4	185.0	647.0	1036.1

2.5.1 Chloride ion penetration

The electrical chloride ion penetration test was performed according to the ASTM C1202 standard. Two 51 mm thick slices from two different concrete cylinders were tested for each of the concrete mixtures.

2.5.2 Electrical resistivity

Electrical resistivity was measured using two 10 by 20 cm cylindrical specimens for each mixture based on the axial-measurement method described by Spragg et al. [37] to compare the filler and

pozzolanic effects of the SCMs on concrete pore percolation. In this method, two stainless steel plates are placed at the ends of the 10-by-20 cm cylinder and connected to the same surface resistivity meter used in the Wenner probe apparatus [38]. Electrical resistance values are obtained and normalised by the cross sectional area to length ratio of the cylinder to calculate the bulk resistivity of the specimen. Specimens were stored submerged in water during the whole curing period and tested in a saturated condition.

This method was selected because it is completely non-destructive, simple and able to produce immediate results, as well as consistent results throughout subsequent measurements. In addition, Spragg et al. showed that there is a linear correlation between measurements using this method and values obtained using the standard Wenner probe method [37].

3 Results and Discussion

3.1 Particle Size Distribution (PSD)

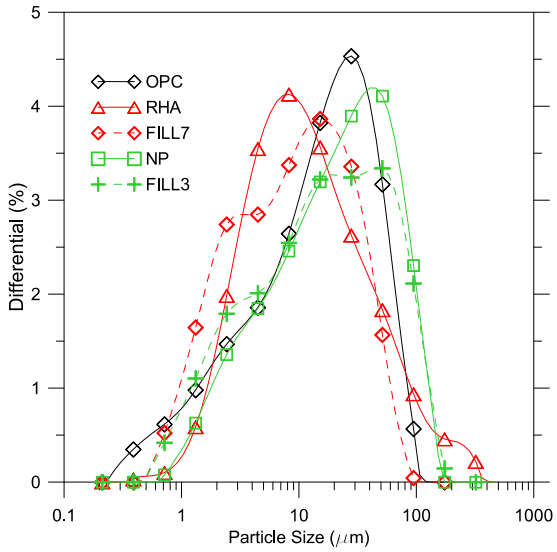

Figure 2. Particle size distributions of the RHA, NP, OPC, coarse and fine inert fillers (i.e., FILL3 and FILL7).

As seen in the figure, FILL3 has a similar PSD to NP while FILL7 is closer to RHA. Both inert fillers represent good approximations of the SCMs physical characteristics from a particle size perspective. FILL3 and FILL7 are good boundaries to the RHA from a PSD perspective, allowing a more accurate measurement of the chemical contribution of this SCM. All the materials have PSDs in a similar range of the particles of the OPC, which allows for comparing these materials with similar conditions of exposed surface.

3.2 X-Ray diffraction

Diffraction patterns are presented in Figure 3 and Table 4. They include the main peaks and crystalline phase composition, along with the amorphous material content.

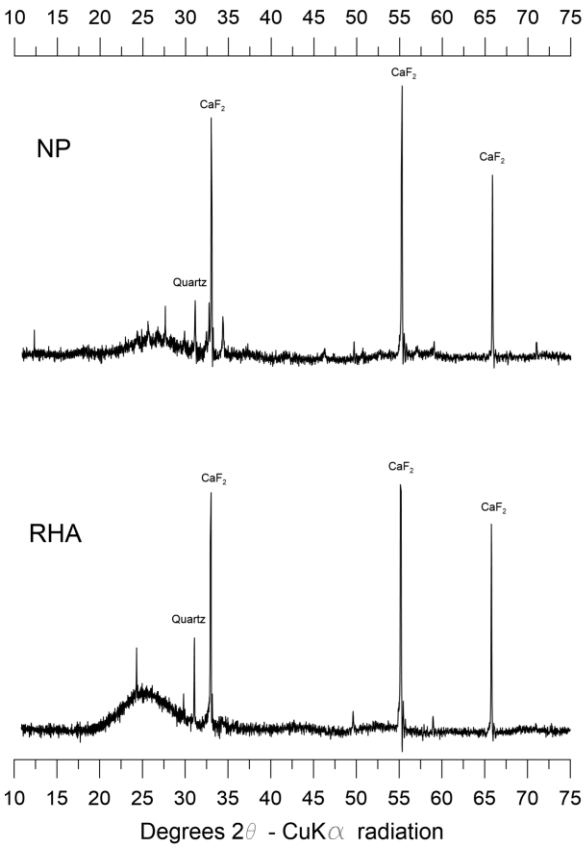

Figure 3. X-Ray diffraction pattern of the RHA and NP used for Rietveld refinement.

Table 4. QXRD analysis of the RHA and NP, including computed amorphous content based on an internal standard correction procedure.

Mineral Name	NP (% by wt.)	RHA (% by wt.)
Quartz	1.2	1.5
Albite	1.3	0.4
Oligoclase	1.7	0.6
Sanidine	0.4	1.4
Fluorite (I.S.)	11.9	11.7
Andesine	0.9	0.4
Anhydrite	0.1	0.3
Actinolite	0.3	0.0
Calcite	2.4	3.1
Beta C_2S	0.0	0.6
Amorphous	80.0	79.9

I.S. = Internal Standard

Rietveld refinement results were achieved with a goodness of fit (GOF) indicator of 1.2 and a Rexp of 3.0, which indicate a good agreement between the experimental data and Rietveld computed pattern and good data quality, respectively.

Both the RHA and NP show a large amount of amorphous phases, approximately 80%, and a relatively small amount of Quartz, approximately 1.5%. When comparing this with the XRF results shown in Table 1, it can be concluded that most of the total SiO_2 phases exists as amorphous forms of silica. Therefore, the RHA, having more amorphous silica, would exhibit a higher chemical activity than the NP. Additionally, the RHA might exhibit higher activity due to the presence of beta C2S that can be formed during manufacturing at 700°C and remain at ambient temperature without a stabiliser if the beta C_2S crystals are sufficiently small [39]. These two differences suggest that the RHA might yield higher mechanical and physical performance than the NP when used as a SCM in concrete.

3.3 Isothermal calorimetry

The heat flow results show a slight acceleration of the hydration reaction when finer materials are added to the sample. This is attributed to the physical effect of the SCMs on the hydration of the OPC [31,40]. This physical effect can be clearly seen in the total heat plots (Figure 4a), where even chemically inert materials (FILL3 and FILL7) exhibit a higher heat release in time than the OPC.

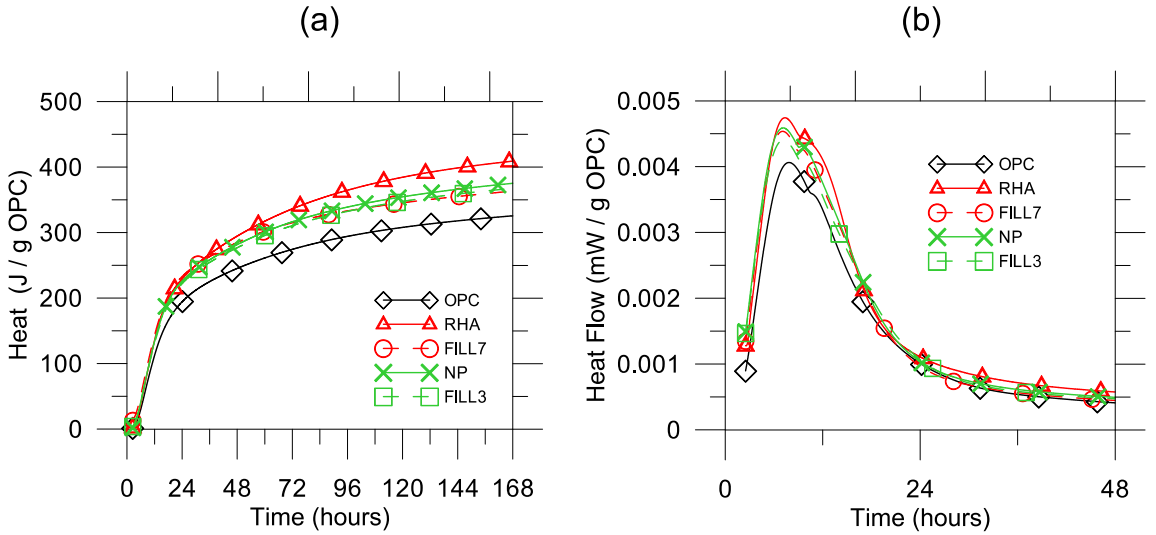

Figure 4. Total heat (a) and heat flow (b) of W/CM 0.5 pastes containing 20% RHA, NP, FILL3 or FILL7.

Chemical interactions can be observed for the RHA and NP even at this early stage of hydration based on the differences between the inert fillers. Because the PSD of FILL7 is similar to RHA and FILL3 is similar to NP (Figure 2), the differences in the heat released between these pairs are an estimate of the chemical activity of the pozzolanic material. The RHA heat evolution (Figure 4b) shows clear differences with FILL7, which suggests a significantly higher chemical reactivity of this material at early ages. This can be attributed to the relatively high amorphous silica content. On the contrary, for the NP, the chemical reactivity is almost negligible during the first 7 days because FILL3 and NP heat plots are very similar. This can be attributed to the coarser PSD of the NP, which can delay the pozzolanic reaction.

3.4 Compressive strength

3.4.1 Compressive strength for the pastes with W/CM ratios of 0.5

Results of the compressive strength test on paste specimens are shown in Figures 5 a, b and c for 7, 28 and 90 days of age, respectively. They are expressed as ratios using the W/CM 0.5 100% OPC mixture as a reference, which is also represented graphically by a bold horizontal grey line. Porosity variations are represented as horizontal lines and corresponds to the 100% OPC mixes with W/CM variation according to the experimental program. This allows for comparing the effect of the SCM replacement with changes in the W/CM in a 100% OPC paste. Therefore, the SCM overall reactivity can be expressed as the expected performance of a given OPC added mass.

RHA pastes show very early strength development compared to the other series (Figure 5a) as exhibited by R_{SCM}/R_{OPC} ratios of 1.25 to 1.50 even at high replacement levels. It can be concluded that these results are the effect of physical and chemical interactions of the RHA during hydration, as observed in isothermal calorimetry.
FILL7 and FILL3 series exhibit very low R_{SCM}/R_{OPC} ratios ranging between 0.10 and 0.80 meaning the physical interactions are low during the first 7 days. Because FILL7 and FILL3 are boundaries to the RHA from a PSD perspective (Figure 2), the large differences in the R_{SCM}/R_{OPC} ratios suggest that a considerable pozzolanic reaction occurs in the RHA series during the first 7 days. The high amount of amorphous material found in the XRD analysis explains this observation. This conclusion agrees with previous findings that RHA can be as reactive as silica fume [41], another SCM with a very high amorphous silica content.

FILL7 shows a higher level of hydration activation than the FILL3 paste, as expected from the calorimetry results. Because the replacement level is the same in both series with inert filler, the activation observed can be attributed to differences in the PSD only; thus, hydration enhancement occurs as extra space is available and the filler surface acts as nucleation sites for clinker phases [3,30].

The NP results reflect negligible pozzolanic activity during the first 7 days showing R_{SCM}/R_{OPC} ratios below the inert series (FILL7 and FILL3) suggesting a lower acceleration of hydration due to the filler effect. This low chemical activity is also observed in the total heat release of the NP compared to FILL3 and OPC (Figure 3b), which can be attributed to the coarser PSD of the NP compared to FILL3 and FILL7, as seen in Figure 2, which delayed the pozzolanic reaction of the amorphous silica phases.

At 28 days age (Figure 5b), the behaviour of the RHA series still outperforms that of 100% OPC; however, the ongoing hydration of the OPC tends to reduce initial differences. For instance, at 75% replacement level, the specimens exhibit a R_{SCM}/R_{OPC} ratio below 1.0 and the maximum R_{SCM}/R_{OPC} ratio decreased form 1.5 at 7 days to 1.25 at 28 days. The NP starts to develop pozzolanic activity, which is clear at replacement levels higher than 50%, where this pozzolanic reactivity becomes noticeable when compared to the series exhibiting only physical interactions (FILL3 and FIIL7).

Results at 90 days of age conform to the same trend observed between 7 and 28 days. The ongoing hydration of the OPC keeps reducing the differences in the R_{SCM}/R_{OPC} ratios between RHA and 100% OPC even though the RHA series still outperforms the 100% OPC for

replacement levels up to 50% (Figure 5c). Additionally, the NP continues to show pozzolanic activity improving its performance compared to the inert series.

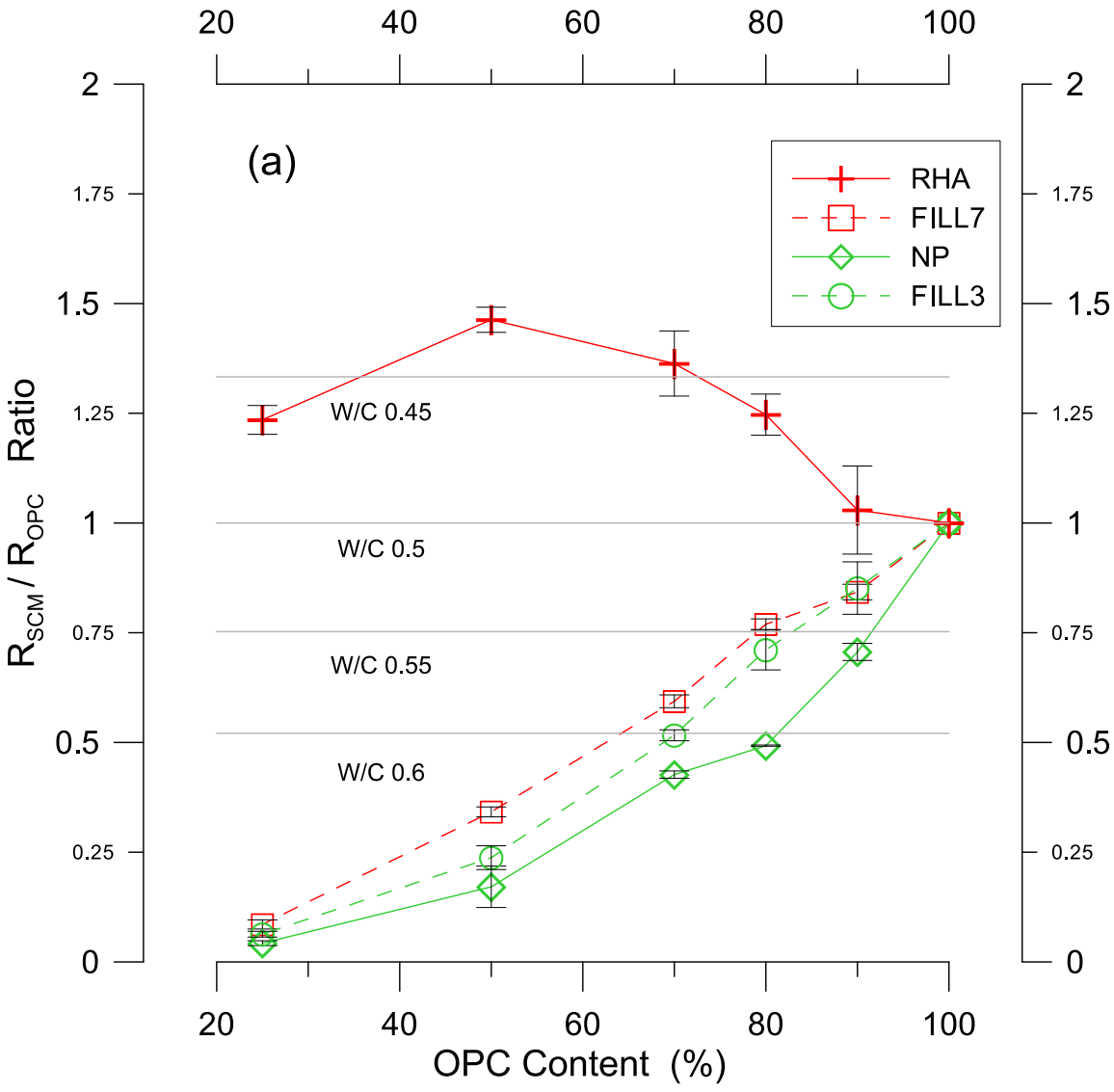

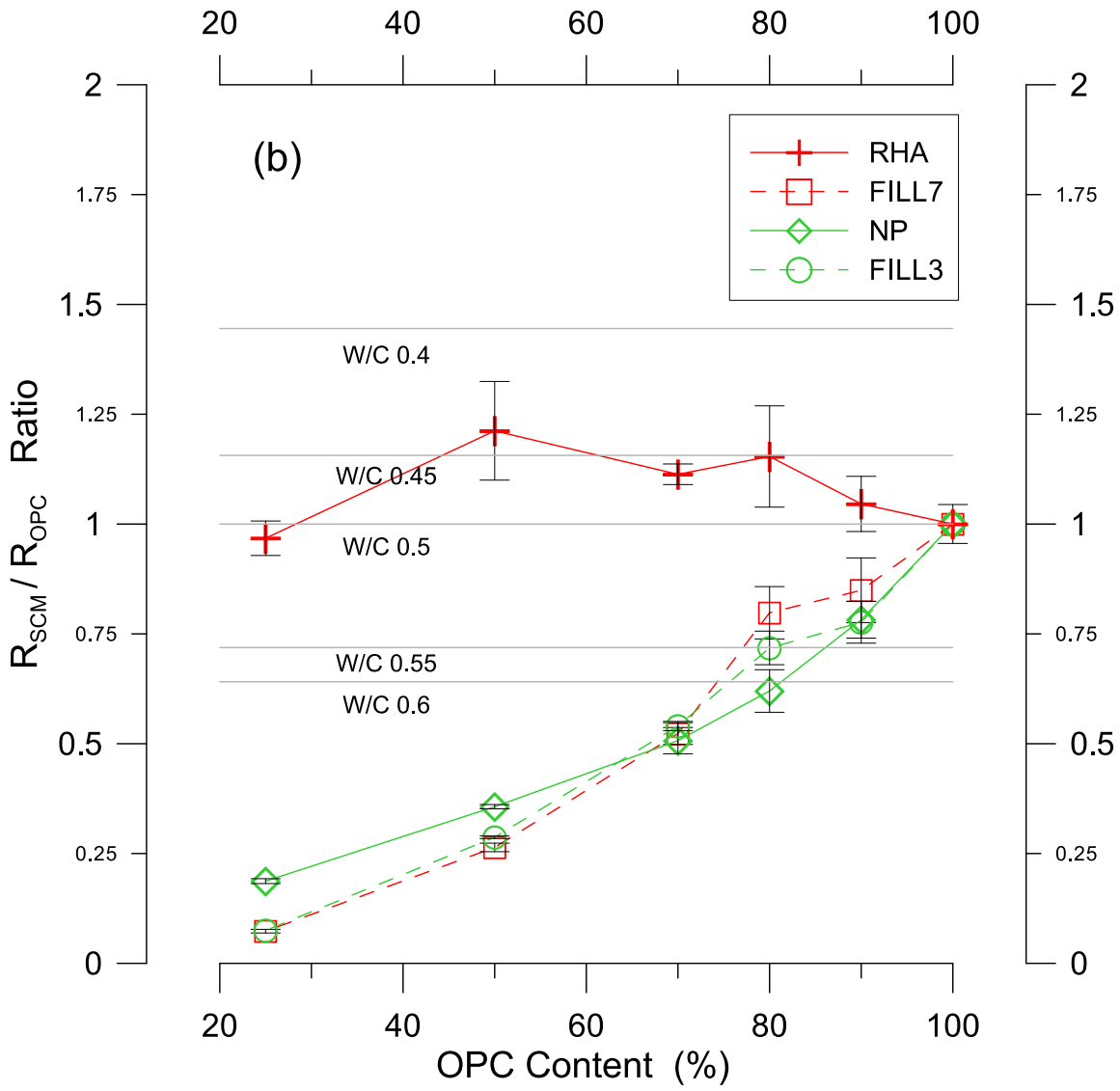
(b)
RHA
FILL7
NP
FILL3
W/C 0.4
W/C 0.45
W/C 0.5
W/C 0.55
W/C 0.6
R_{SCM} / R_{OPC} Ratio
OPC Content (%)
0
0.25
0.5
0.75
1
1.25
1.5
1.75
2
20
40
60
80
100

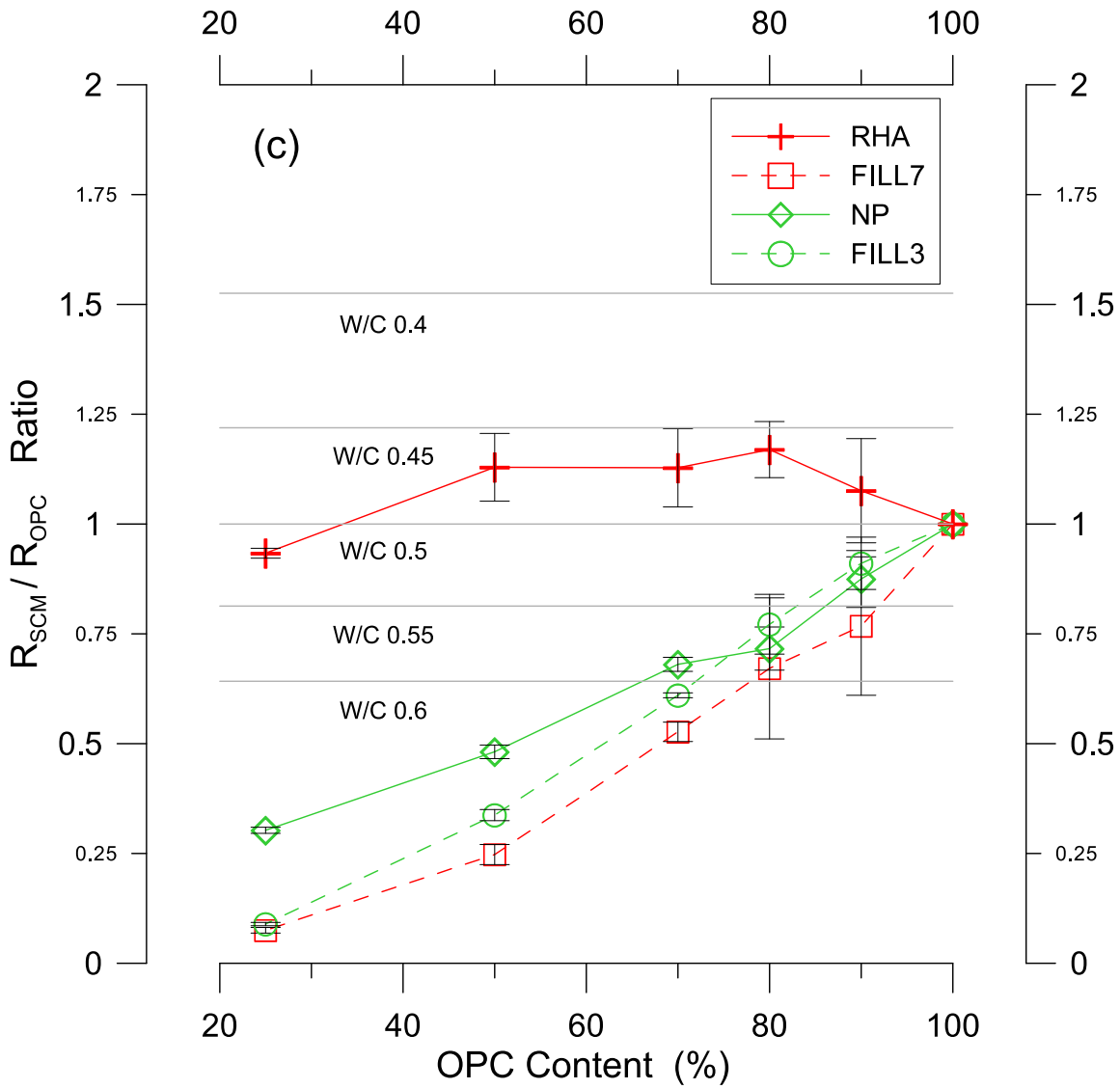

Figure 5. Compressive strength ratios (referenced to the 100% OPC mixture) versus the OPC content in mixtures at (a) 7, (b) 28 and (c) 90 days of age.

The sizable differences in the R_{SCM}/R_{OPC} ratios between the RHA and NP can be explained by the differences in the PSD, amorphous silica content and size as derived from the PSD and WRD analyses. The smaller particle size of RHA compared to NP provides a stronger physical effect accelerating hydration, and the higher amorphous silica present in RHA compared to NP explains the higher chemical reactivity.

The strength gain produced by the use of SCMs allows important cement reductions while maintaining or even improving the mechanical performance. For instance, an additional 13% by mass of cement (equivalent to a w/c reduction below 0.45 in Figure 5a) would be needed to obtain the same 7-day compressive strength as the 50% RHA mixture with a w/cm of 0.5. Similarly, the incorporation of 20% by mass of the NP is equivalent to increasing the w/c up to 0.6. In this matter, RHA is more efficient as an OPC replacement if strength is the design parameter.

The chemical and physical contribution of each SCM to compressive strength can be approximated as the difference between the strength obtained by the SCM and the result of the PSD-matching inert filler at the same corresponding age and substitution level. Using this approach, the RHA performance is dominated by its chemical effect at all ages, while the NP mainly contributes physically at early ages and more chemically at later ages (Figure 5a to 5c).

3.4.2 Compressive strength of mortar

The compressive strength of the mortar show similar trends to those found in the paste (see the R_{SCM}/R_{OPC} ratios in Figure 6). The series containing RHA as the cement replacement in general, performs better that those with 100% OPC. The series containing the NP exhibits a lower performance than those containing the RHA and 100% OPC, but still exhibits improvements with respect to the inert fillers only. The R_{SCM}/R_{OPC} ratios shown at the mortar level are, in general, lower than those observed at the paste level. This can be attributed to the dilution of the cementitious materials by sand [40] combined with the lack of nucleation enhancement due to the coarse PSD of the sand compared to the SCMs and OPC [42].

The R_{SCM}/R_{OPC} ratio of the RHA mortars reached approximately 1.2 at 28 and 90 days; however, at 3 days, the opposite is observed for the three replacement levels (10, 20 and 30%). This low performance can be attributed to a low availability of Portlandite from cement hydration present at such an early age to properly activate the pozzolanic reaction. Although the filler effect is predominant during the first few days[3], the RHA does show the pozzolanic effect, because its R_{SCM}/R_{OPC} ratio is higher than the ratio produced by the mixture with inert filler with a comparable PSD. This fact is also observed in the isothermal calorimetry results (Figures 3a and 3b).

At later ages (i.e., 28 and 90 days), when more Portlandite is available, the RHA mixtures exhibited an incremental increase in the compressive strength at all levels of substitution reaching R_{SCM}/R_{OPC} ratios of approximately 1.2 and reached statistically equivalent results at 90 days for the 3 replacement levels. These results are consistent with the high reactivity observed at the paste level and agree with those previously reported for the RHA mortar [9,32].

Regarding the NP mortars, the replacement levels of 20 and 30% had R_{SCM}/R_{OPC} ratios ranging from 0.8 to 1.0 at 28 and 90 days. The low reactivity of the NP was also observed in cement pastes in a wider range of replacement levels. As concluded at the paste level, the relatively low performance of the NP might be attributed to a low amorphous silica content and coarser PSD.

At 20% substitution and 3 days of age, the NP mixtures performed better than mixtures with inert filler (FILL3) indicating a relevant pozzolanic activity. Nevertheless, at 28 and 90 days, the results for the NP inert filler mixtures are statistically equivalent, which indicates that after reaching a certain level of cement hydration, the pozzolanic activity of the NP is negligible.

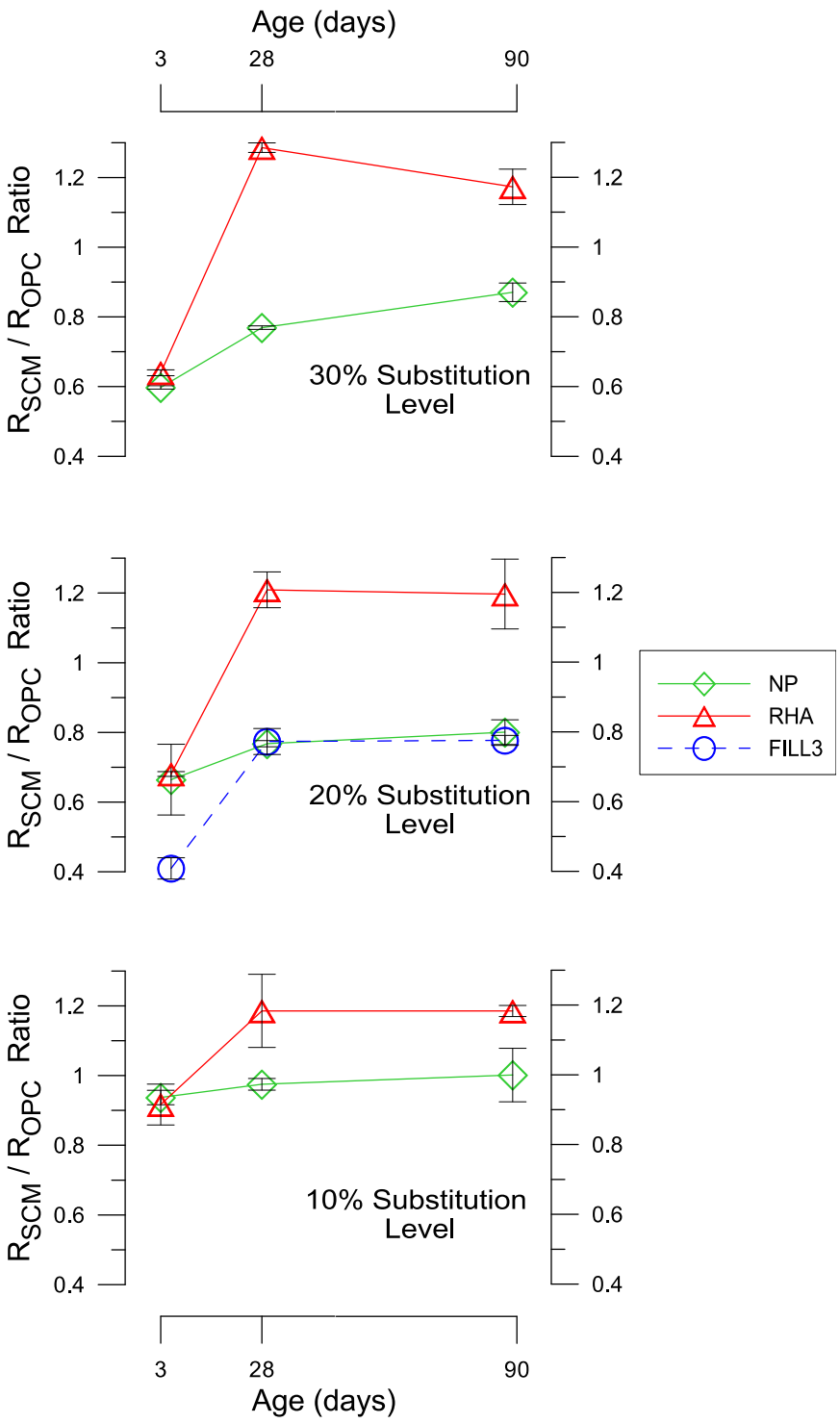

Figure 6. Compressive strength ratios of the mortar mixtures (referenced to the 100% OPC mixture) with 10, 20 and 30 percent SCM replacement levels.

3.5 Durability

3.5.1 Chloride ion penetration

The effect of cement replacement by the SCMs was assessed at the concrete level using the rapid chloride ion penetration test (RCPT) at 90 days of age (Figure 7). Results are expressed as ratios of the total charge passed on each SCM mixture over the total charge passed on the 100% OPC control mixture, so the 100% OPC mixture performance is 1.0. The ASTM C1202 performance classification was also shown. A ratio below the 1.0 R_{SCM}/R_{OPC} ratio represents better performance compared to the reference mixture.

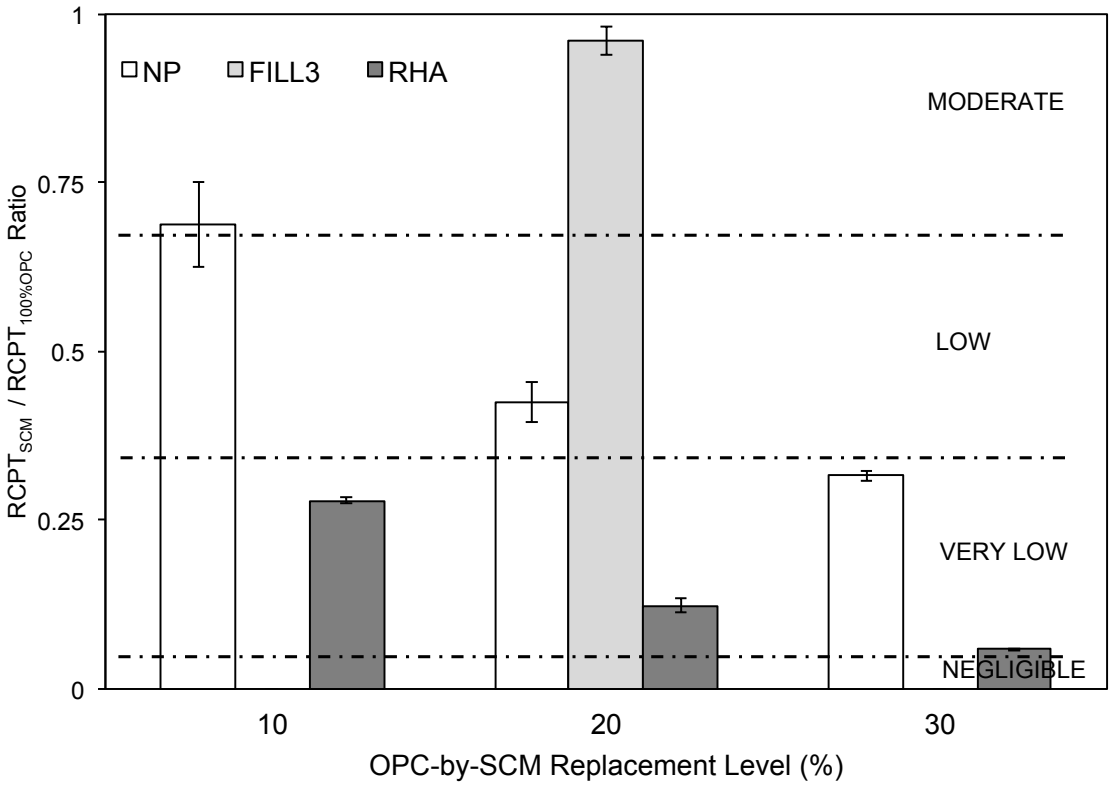

Figure 7. Chloride ion penetration results, expressed as ratios with the 100% OPC mixture as the reference.

There is a clear trend in the chloride permeability reduction as the chemical replacement level of the SCM (RHA and NP) increases. The performance of the RHA mixtures, in this context, is statistically better than the NP, because it reduces the permeability of the reference mixture from moderate to an almost negligible and a $RCPT_{SCM}/RCPT_{OPC}$ ratio of 0.06 with 30% replacement. This behaviour has been previously reported in several studies [18,19,21] and is an expression of the high pozzolanic activity of the rice husk ash, which has been attributed to a reduction of the interfacial transition zone (ITZ) width, porosity and portlandite content [10].

The NP mixtures have $RCPT_{SCM}/RCPT_{OPC}$ ratios ranging from 0.7 to 0.3; a replacement level of 30% results in a very low permeability according to ASTM C1202. This is worth noting that the compressive strength suggested a relatively low gain by using NP. Performance of the NP

mixture is also better than that of inert filler (FILL3), suggesting that the improvement in permeability is not only due to a physical effect but also to pozzolanic activity. The RCPT gives a more sensitive assessment than the compressive strength when assessing the SCM effect in cement based materials.

As stated by Taylor, replacements of the OPC by inert materials, as in this case, does not lower the degree of hydration needed to reach pore de-percolation, so it cannot reduce the overall permeability [39]. This is evident from the $RCPT_{SCM}/RCPT_{OPC}$ ratios close to 1.0 shown by the FILL3 mixture.

3.5.2 Electrical resistivity

The effect of cement replacement by SCMs on the durability was assessed at the concrete level using electrical resistivity (Table 5), where an increase in the pore de-percolation produces an increase in the electrical resistivity of specimens in the saturated condition. Experimental results reveal consistent findings made when comparing the electrical resistivity to the RCPT. This can be attributed to the similarity of both tests, because the mechanism of the measurement is physically equivalent and based on the electrical properties of the material. While the sample size and preconditioning varies for each test, the main mechanism that controls concrete behaviour in both tests can be reduced to pore connectivity.

Table 5. Electrical resistivity of concrete samples at 90 days age.

Replacement Level (%)	SCM ID	Ω Mean Resistivity (Ohm·cm)	Std. Deviation (Ohm·cm)
0	-	9523	139
10	RHA	29649	1388
	NP	11977	547
20	RHA	60868	1388
	NP	21245	56
	FILL3	9179	69
30	RHA	120264	2083
	NP	26900	833

Electrical resistivity of the RHA mixtures increased approximately 3, 6 and 12 times that of the 100% OPC mixtures for replacement levels of 10, 20 and 30%, respectively. Electrical resistivity of the NP mixtures increased 2 and 3 times for replacement levels of 20 and 30%, respectively. The use of inert filler at 20% replacement reduced the electrical resistivity, which indicates an increase in the permeability. This result is similar to the findings obtained in the RCPT and capillary absorption tests, reaffirming the analysis presented by Taylor [39].

A strong correlation was found between the electrical resistivity and RCPT results. In addition, this correlation extends to the $RCPT_{SCM}/RCPT_{OPC}$ and $\Omega_{OPC}/\Omega_{SCM}$ ratios (Figure 8). This allows each of these tests to be used in an almost equivalent manner to compare several substitution levels and substitution materials.

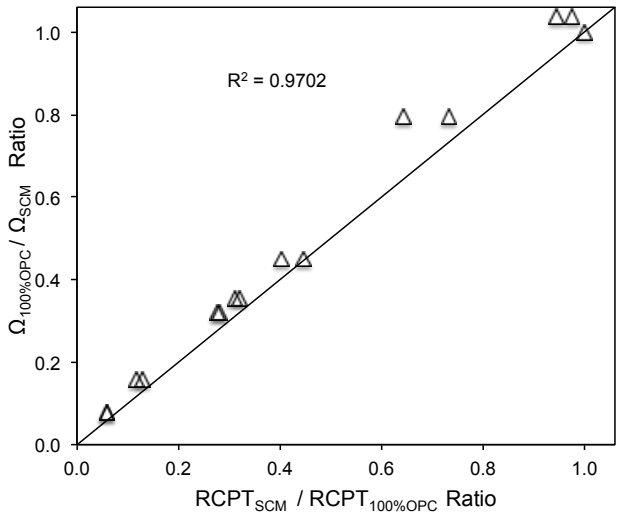

Figure 8. ASTM C1202 chloride penetration ratios versus electrical resistivity ratios, showing a strong correlation between the results of these tests over the complete spectra of SCMs and substitution levels.

The electrical resistivity method offers clear benefits over the ASTM C1202 method. The main advantages are related to a simplified sample preparation and conditioning, greatly reduced testing time and the possibility to use the same specimen to monitor variations of measurements over time.

4 Conclusions

Sustainability is and will continue to be one of the major concerns regarding concrete technology and future developments. The use of SCMs had been and still is one of the primary alternatives to reduce the carbon emissions and embodied energy while improving the durability of concrete structures. The use of these materials creates new challenges for researchers to understand the interactions occurring in cementitious systems containing these materials, to optimise the production and use of SCM and to achieve the strength and durability required by the industry.

This paper presented the characterisation of RHA and NP, a promising SCM produced from agricultural wastes and a widely used material in Chilean cements, respectively, using a multi-scale approach considering the paste, mortar and concrete levels. Characterisation covered chemical and physical interaction assessments, strength of the cement paste and mortar mixtures and durability testing of the concrete samples.

The chosen methodology, using inert fillers with different particle size distributions, allowed for decoupling the physical and chemical effects of the two SCMs studied. This improved the understanding of the contributions of the SCMs.

The main conclusions of this study are:

1. The better performance of RHA compared to NP can be attributed both to its pozzolanic reactivity due to higher amounts of amorphous silica phases and to the hydration acceleration related to its finer PSD.

2. Even considering the relatively low contribution of NP to the strength, reductions in the permeability by using NP and RHA in concrete were considerable using three different testing methods. The improvements in permeability achieved with NP and RHA were more pronounced as the replacement level increased up to 30%. Inert filler showed an inability to reduce the pore connectivity in all test results obtained. These findings showed a lower but non-negligible pozzolanic potential of the NP, as shown in the XRD results.

3. Replacement of the OPC by RHA increased the early age strength up to 50% and 25% for later ages. It also produced important reductions in the permeability at 90 days of age. The contribution of the RHA to the compressive strength is divided into 22% physical effect and 78% chemical effect at 90 days age and 50% replacement level. Likewise, the RHA contribution to permeability is mostly due to the chemical effects because mixtures containing inert filler had similar or higher permeability than mixtures with 100% OPC.

4. Replacement of the OPC by NP produced reductions in the early strength, which are minimised at later ages. Nevertheless, the use of NP produced considerable reductions in the permeability at 90 days. The contribution of NP to the strength can be divided into 70% physical effect and 30% chemical effect at 90 days age and 50% replacement level. Its contribution to permeability can be solely explained by the chemical effect.

5. While the RHA was calcined under controlled conditions to maximise the presence of amorphous and thus, greatly enhance its chemical effect, NP is a natural product with a volcanic origin where no controlled temperature cycle is involved. Therefore, an increase of the NP effect on concrete properties would depend only on its physical effect by further reducing its PSD.

6. Proper use of more sophisticated characterisation techniques such as XRF, XRD, Rietveld analysis, PSD and calorimetry can predict the potential of a SCM, which helps when optimising the SCM performance by changing the burning, cooling and grinding processes during manufacturing.

7. The effects of a particular SCM on concrete properties do not only depend on the physical and chemical characteristics of the SCM but also on the particular property studied. That is, the effect of a SCM on the compressive strength does not adequately predict its effect on the permeability, so independent assessments need to be performed.

5 Acknowledgements

The authors greatly acknowledge funding provided by FONDECYT, project Nº1120817 and the support provided by CEDEUS, CONICYT/FONDAP 15110020. The authors also recognize Javier Castro, Omar Ríos and Mauricio Guerra for their contributions to this research project.

6 References

[1] M. Schneider, M. Romer, M. Tschudin, H. Bolio, Sustainable cement production—present and future, Cem. Concr. Res. 41 (2011) 642–650. doi:10.1016/j.cemconres.2011.03.019.

[2] R.C. Lara, M. Antoni, A.A. Díaz, K. Scrivener, J. Fernando, M. Hernández, Estudio de la adición de arcillas calcinadas en la durabilidad de hormigones, Rev. Ing. Construcción. 26 (2011) 25–40.

[3] B. Lothenbach, K. Scrivener, R.D. Hooton, Supplementary cementitious materials, Cem. Concr. Res. 41 (2011) 1244–1256. doi:10.1016/j.cemconres.2010.12.001.

[4] N. Jain, Effect of nonpozzolanic and pozzolanic mineral admixtures on the hydration behavior of ordinary Portland cement, Constr. Build. Mater. 27 (2012) 39–44. doi:10.1016/j.conbuildmat.2011.08.006.

[5] E. Karim, K. El-Hadj, B. Abdelkader, B. Rachid, Analysis of Mortar Long-Term Strength with Supplementary Cementitious Materials Cured at Different Temperatures, ACI Mater. J. (2010) 323–331.

[6] G. Espinoza-Hijazin, Á. Paul, M. Lopez, Concrete Containing Natural Pozzolans : New Challenges for Internal Curing, J. Mater. Civ. Eng. 24 (2012) 981–988. doi:10.1061/(ASCE)MT.1943-5533.0000421.

[7] P.K. Mehta, Durability - Critical Issues for the Future, Concr. Int. 19 (1997) 69–76.

[8] R. Corral, S. Arredondo, J. Almaral, J. Gómez, Corrosión por cloruros del acero de refuerzo embebido en concreto con agregado grueso reciclado y materiales cementantes suplementarios, Rev. Ing. Construcción. 28 (2013) 21–35. doi:10.4067/SO718-50732013000100002.

[9] P.K. Mehta, Properties of blended cements made from rice husk ash, ACI J. (1977) 440–442.

[10] M.H. Zhang, R. Lastra, V.M. Malhotra, Rice-husk ash paste and concrete: Some aspects of hydration and the microstructure of the interfacial zone between the aggregate and paste, Cem. Concr. Res. 26 (1996) 963–977.

[11] Q. Yu, K. Sawayama, S. Sugita, M. Shoya, Y. Isojima, The reaction between rice husk ash and Ca(OH)2 solution and the nature of its product, Cem. Concr. Res. 29 (1999) 37–43.

[12] Food and Agriculture Organization of the U.N., FAOSTAT, 2011.

[13] G. Rodríguez de Sensale, Strength development of concrete with rice-husk ash, Cem. Concr. Compos. 28 (2006) 158–160.

[14] T. Chungsangunsit, S.H. Gheewala, S. Patumsawad, Environmental Assessment of Electricity Production from Rice Husk : A Case Study in Thailand, Int. Energy J. 6 (2005).

[15] A.N. Givi, S.A. Rashid, F.N.A. Aziz, M.A.M. Salleh, Assessment of the effects of rice husk ash particle size on strength, water permeability and workability of binary blended concrete, Constr. Build. Mater. 24 (2010) 2145–2150.

[16] M.. Khan, K. Mohan, H.F.. Taylor, Pastes of tricalcium silicate with rice husk ash, Cem. Concr. Res. 15 (1985) 89–92.

[17] M.F.M. Zain, M.N. Islam, F. Mahmud, M. Jamil, Production of rice husk ash for use in concrete as a supplementary cementitious material, Constr. Build. Mater. 25 (2011) 798–805.

[18] A.L.G. Gastaldini, G.C. Isaia, N.S. Gomes, J.E.K. Sperb, Chloride penetration and carbonation in concrete with rice husk ash and chemical activators, Cem. Concr. Compos. 29 (2007) 176–180.

[19] A.L.G. Gastaldini, G.C. Isaia, A.P. Saciloto, F. Missau, T.F. Hoppe, Influence of curing time on the chloride penetration resistance of concrete containing rice husk ash: A technical and economical feasibility study, Cem. Concr. Compos. 32 (2010) 783–793. doi:10.1016/j.cemconcomp.2010.08.001.

[20] G.R. De Sensale, Effect of rice-husk ash on durability of cementitious materials, Cem. Concr. Compos. 32 (2010) 718–725. doi:10.1016/j.cemconcomp.2010.07.008.

[21] V. Saraswathy, H.-W. Song, Corrosion performance of rice husk ash blended concrete, Constr. Build. Mater. 21 (2007) 1779–1784.

[22] G.C. Cordeiro, R.D. Toledo Filho, L.M. Tavares, E.D.M.R. Fairbairn, S. Hempel, Influence of particle size and specific surface area on the pozzolanic activity of residual rice husk ash, Cem. Concr. Compos. 33 (2011) 529–534. doi:10.1016/j.cemconcomp.2011.02.005.

[23] V.P. Della, I. Kühn, D. Hotza, Rice husk ash as an alternate source for active silica production, Mater. Lett. 57 (2002) 818–821.

[24] D.G. Nair, A. Fraaij, A.A.K. Klaassen, A.P.M. Kentgens, A structural investigation relating to the pozzolanic activity of rice husk ashes, Cem. Concr. Res. 38 (2008) 861–869.

[25] N. Kaid, M. Cyr, S. Julien, H. Khelafi, Durability of concrete containing a natural pozzolan as defined by a performance-based approach, Constr. Build. Mater. 23 (2009) 3457–3467. doi:10.1016/j.conbuildmat.2009.08.002.

[26] D. Bondar, C.J. Lynsdale, N.B. Milestone, N. Hassani, a. a. Ramezanianpour, Effect of heat treatment on reactivity-strength of alkali-activated natural pozzolans, Constr. Build. Mater. 25 (2011) 4065–4071. doi:10.1016/j.conbuildmat.2011.04.044.

[27] K. Celik, C. Meral, M. Mancio, P.K. Mehta, P.J.M. Monteiro, A comparative study of self-consolidating concretes incorporating high-volume natural pozzolan or high-volume fly ash, Constr. Build. Mater. (2013). doi:10.1016/j.conbuildmat.2013.11.065.

[28] a. R. Pourkhorshidi, M. Najimi, T. Parhizkar, F. Jafarpour, B. Hillemeier, Applicability of the standard specifications of ASTM C618 for evaluation of natural pozzolans, Cem. Concr. Compos. 32 (2010) 794–800. doi:10.1016/j.cemconcomp.2010.08.007.

[29] P. Mehta, P. Monteiro, Concrete: Microstructure, Properties, and Materials, 3rd ed., McGraw-Hill Professional, New York, 2005.

[30] P. Lawrence, M. Cyr, E. Ringot, Mineral admixtures in mortars-- effect of inert materials on short-term hydration, Cem. Concr. Res. 33 (2003) 1939–1947. doi:10.1016/S0008-8846(03)00183-2.

[31] M. Cyr, P. Lawrence, E. Ringot, Mineral admixtures in mortars, Cem. Concr. Res. 35 (2005) 719–730. doi:10.1016/j.cemconres.2004.05.030.

[32] Q. Feng, H. Yamamichi, M. Shoya, S. Sugita, Study on the pozzolanic properties of rice husk ash by hydrochloric acid pretreatment, Cem. Concr. Res. 34 (2004) 521–526.

[33] J. Rao, M Subba. James, Reaction product of lime and silica from rice husk ash, Cem. Concr. Res. 16 (1986) 67–73.

[34] R.T. Chancey, P. Stutzman, M.C.G. Juenger, D.W. Fowler, Comprehensive phase characterization of crystalline and amorphous phases of a Class F fly ash, Cem. Concr. Res. 40 (2010) 146–156. doi:10.1016/j.cemconres.2009.08.029.

[35] I. Pane, W. Hansen, Investigation of blended cement hydration by isothermal calorimetry and thermal analysis, Cem. Concr. Res. 35 (2005) 1155–1164. doi:10.1016/j.cemconres.2004.10.027.

[36] Q. Xu, J. Hu, J.M. Ruiz, K. Wang, Z. Ge, Isothermal calorimetry tests and modeling of cement hydration parameters, Thermochim. Acta. 499 (2010) 91–99. doi:10.1016/j.tca.2009.11.007.

[37] R.P. Spragg, J. Castro, T. Nantung, M. Paredes, J. Weiss, Variability Analysis of the Bulk Resistivity Measured Using Concrete Cylinders, Adv. Civ. Eng. Mater. 1 (2012) 1–17. doi:10.1520/ACEM104596.

[38] W. Morris, E.I. Moreno, A.A. Sagüés, Practical Evaluation of resistivity of concrete in test cylinders using a Wenner array probe, Cem. Concr. Res. 26 (1996) 1779–1787.

[39] H. Taylor, Cement chemistry, 2nd ed., Thomas Telford, London, 1997.

[40] M. Cyr, P. Lawrence, E. Ringot, Efficiency of mineral admixtures in mortars: Quantification of the physical and chemical effects of fine admixtures in relation with compressive strength, Cem. Concr. Res. 36 (2006) 264–277. doi:10.1016/j.cemconres.2005.07.001.

[41] M.. Khan, K. Mohan, H.F.. Taylor, Pastes of tricalcium silicate with rice husk ash, Cem. Concr. Res. 15 (1985) 89–92.

[42] A. Neville, Properties of Concrete, 4th Edition, Pearson Education Limited, Essex, 1995.